Development of SRF monolayer/multilayer thin film materials to increase the performance of SRF accelerating structures beyond bulk Nb

Anne-Marie Valente-Feliciano

UNIVERSITÉ PARIS-SUD

ÉCOLE DOCTORALE 564 :
PHYSIQUE EN ÎLE-DE-FRANCE

Laboratoire : Thomas Jefferson National Accelerator Facility, VA USA

THÈSE DE DOCTORAT

PHYSIQUE

par

Anne-Marie VALENTE-FELICIANO

Development of SRF monolayer/multilayer thin film materials to increase the performance of SRF accelerating structures beyond bulk Nb

Date de soutenance : 30/09/2014

Composition du jury :

Directeur de thèse :	Claire ANTOINE	Directeur de Recherche (CEA-IRFU)
Co-directeur de thèse :	Jean DELAYEN	(Old Dominion University, VA USA)
Rapporteurs :	Pascal BRIOIS	Maître de Conférences (Université de Montbéliard)
	Vincenzo PALMIERI	Professeur (INFN-LNL, Padova Italy)
Examinateurs :	Marin CHABOT	Directeur de Recherche CNRS/IN2P3 (IPN Orsay)

Thèse préparée au
Thomas Jefferson National Accelerator Facility
Accelerator division
SRF R&D Department
23 606 Newport news, VA, USA
This material is based upon work supported
by the U.S. Department of Energy,
Office of Science, Office of Nuclear Physics
under contract DE-AC05-06OR23177.

Abstract

The minimization of cost and energy consumption of future particle accelerators, both large and small, depends upon the development of new materials for the active surfaces of superconducting RF (SRF) accelerating structures. SRF properties are inherently a surface phenomenon as the RF only penetrates the London penetration depth λ, typically between 20 and 400 nm depending on the material. The greatest potential for dramatic new performance capabilities lies with methods and materials which deliberately produce the sub-micron-thick critical surface layer in a controlled way. Thus, two opportunities arise for the use of SRF thin films as single layer superconductor or multilayer Superconductor-Insulator-Superconductor structures:

SRF properties are inherently a surface phenomenon, and when other technological processes are optimized, the fundamental limit to the maximum supportable RF field amplitude is understood to be the field at which the magnetic flux first penetrates into the surface, H_{c1}. Niobium, the material most exploited for SRF accelerator applications, has $H_{c1} \sim 170$ mT, which yields a maximum accelerating gradient of less than 50 MV/m. Thus, new materials must be investigated to push this limit to the desired range. Although many compounds have shown higher critical superconducting transition temperature (T_c), their critical field (H_{c1}) is lower than niobium. To circumvent this issue, a Superconductor/Insulator/Superconductor (S-I-S) multilayer films approach has been proposed to achieve performance in excess of that of bulk Nb. In this system, the critical field is enhanced and the fluxon penetration delayed by using, on top of the Nb surface, a superposition of superconductor layers, each less than a penetration depth in thickness, separated by a dielectric layer a few nanometers thick. For bulk type-II superconducting materials, vortex entry occurs at surface magnetic field H_{c1}. The key aspect of Gurevich's analysis is the recognition that vortex entry is inhibited if the surface layer thickness (d) of the superconductor is less than the penetration depth, λ. The overlayer provides magnetic screening of the underlying Nb with the attenuation factor $\exp(d/\lambda_0)$. The Nb surface can remain in the Meissner state at fields much higher than in bulk due to the increase of the parallel H_{c1} in a thin film. This could potentially lead to further improvement in RF cavity performance using the benefit of the higher-T_c superconductors without being limited by their lower H_{c1}.

Niobium on copper (Nb/Cu) technology for superconducting cavities has proven over the years to be a viable alternative to bulk niobium. However the deposition techniques used for cavities, mainly magnetron sputtering, have not yielded, so far, SRF surfaces suitable for high field performance.

High quality films can be grown using methods of energetic condensation, such as Electron Cyclotron Resonance (ECR) Nb ion source in UHV and High Power Impulse Magnetron Sputtering (HiPIMS) with energetic ions only and neutral atoms significantly blocked. The main advantages of these techniques are the production of higher flux of ions with controllable incident angle and kinetic energy and the absence of macroparticle production.

The project in general, is focusing onto understanding the physics underlying the RF superconductivity in layered structures and developing SRF material films suitable as substrate and S-I-S multilayer structures. In first hand, the primary focus is to understand the physics governing the relationship between growth conditions, film microstructure and RF performance for SRF materials produced by energetic condensation. The deposition by energetic condensation in UHV via ECR and HiPIMS are studied for Nb and B1 superconducting compounds on substrates with various lattice match and surface conditions (in-situ etching, high energy assisted atomic annealing, deposition temperature). The general energy-temperature zone model developed by André Anders is explored to define the optimized coating conditions for films suitable for single layer and multilayer SRF structures. The contribution of both the ion incident energy and the substrate lattice energy on the nucleation of the SRF materials considered, and some insulating materials (AlN and MgO) and the influence of the coating conditions on the resulting materials, superconducting and/or RF properties will be investigated. Attention is be given to minimize the residual stress (intrinsic and thermal) with the choice of lattice match between the film and substrate materials, the coating temperature, and to evaluate the coating methods used in terms of conformality for 3D structures. In second hand, as a proof of concept, the coating conditions developed will be used to prepare multi-layer superconductor/insulator/superconductor (S-I-S) films having high quality factor and high gradient breakthrough potential. A thick Nb film ($> 1\mu$m) could be used as a substrate. Particular attention is given to the interface between superconducting and insulator films. For this work, various material analyses techniques have been used to characterize each type of thin film material: electron backscatter diffraction (EBSD), X-ray diffraction (XRD), high-resolution scanning electron microscopy (SEM), transmission electron microscopy (TEM), stylus and AFM profilometry, secondary ion mass spectroscopy (SIMS), scanning auger microscopy (SAM). Superconducting and RF measurements are also performed (RRR, T_c, and low-temperature SRF sur-

face impedance, SQUID-magnetometry). The insight gained from this project on the physics involved in RF superconductivity of layered structures open the way to enable major reductions in both capital and operating costs associated with future particle accelerators across the spectrum from low footprint compact machines to energy frontier facilities. Realization of quality thin film SRF cavities may dramatically change the cost structure of acceleration systems and significantly improve performance consistency and reliability.

Keywords : Superconducting RF, thin films, niobium, multilayer.

Développement de couches minces de matériaux SRF pour augmenter les performances des structures SRF au-delà du Nb massif

Résumé

La réduction du coût et de la consommation d'énergie de futurs accélérateurs de particules, à grande ou petite échelle, dépend du développement de nouveaux matériaux pour la surface active des structures supraconductrices en radiofréquence (SRF). Les propriétés SRF sont intrinsèquement un phénomène de surface vu que la RF ne pénètre que la profondeur de pénétration, typiquement entre 20 et 400 nm en fonction du matériau. Le plus grand potentiel d'amélioration des performances réside dans le développement de méthodes et de matériaux qui produisent délibérément la surface critique d'épaisseur nanométrique d'une manière contrôlée. Ainsi, deux opportunités se présentent pour l'utilisation de couches minces de matériaux SRF en monocouche ou en structures multicouches supraconducteur-isolant-supraconducteur (S-I-S) :

Les propriétés SRF étant de façon intrinsèque un phénomène de surface, lorsque d'autres procédés technologiques sont optimisés, la limite fondamentale à l'amplitude maximale de champ RF applicable est comprise comme étant le champ H_{c1} où le flux magnétique commence à pénétrer la surface. Le niobium (Nb) est le matériau le plus exploité pour les applications d'accélérateur SRF, pour lequel le champ H_{c1} 170 mT, ce qui donne un gradient de champ accélérateur maximum de moins de 50 MV/m. De nouveaux matériaux doivent donc être développés afin de repousser cette limite plus loin. Bien que de nombreux composés aient une température critique de transition supraconductrice (T_c) supérieure, leur champ critique (H_{c1}) est inférieur à celui de niobium. Pour contourner ce problème, une approche basée sur des multicouches supraconducteur -isolant- supraconducteur (S-I-S) a été proposée par A. Gurevich pour atteindre une performance supérieure à celle du Nb massif. Dans ce système, le champ critique est augmenté et la pénétration des fluxons retardée en utilisant, au-dessus de la surface de Nb, une superposition de couches supraconductrices, d'épaisseur plus faible que la profondeur de pénétration λ, séparées par une couche diélectrique de quelques nanomètres d'épaisseur. Pour des matériaux supraconducteurs de type II, l'entrée des vortex se produit au champ magnétique de surface H_{c1}. L'idée clé de l'analyse de Gurevich est la reconnaissance que l'entrée de vortex est retardée si l'épaisseur de la couche de surface (d) du supraconducteur est inférieure à la profondeur de pénétration, λ. La surcouche fournit un blindage magnétique de la surface de Nb sous-jacente avec un facteur d'atténuation exp (d / λ_0). La surface Nb peut ainsi rester dans l'état Meissner à des champs beaucoup plus élevés que pour le Nb massif du fait de l'augmentation du champ H_{c1} parallèle dans une couche mince. Cela permettrait une amélioration de performances des cavités SRF en profitant de matériaux supraconducteurs à T_c élevée, sans être limité par leur faible H_{c1}. Au cours des années, la technologie niobium sur cuivre (Nb/Cu) pour les cavités supraconductrices a prouvé être une alternative viable au Nb massif. Cependant, les techniques de dépôt utilisées jusqu'à présent, principalement la pulvérisation magnétron, n'ont pas produit des surfaces SRF permettant d'atteindre de bonnes performances à champ élevé.

Des films de haute qualité peuvent être déposés en utilisant des méthodes à condensation énergétique, comme une source ultravide (UHV) d'ions à résonance cyclotron électronique (ECR) et la pulvérisation à magnétron pulsé à haute puissance (HiPIMS) avec uniquement des ions énergétiques, les atomes neutres étant bloqués de manière significative. Les principaux avantages de ces techniques sont la production de flux d'ions importants avec un angle d'incidence et une énergie cinétique contrôlables ainsi que l'absence de production de macro-particules. Le projet se concentre, en général, sur l'étude des phénomènes physiques gouvernant la supraconductivité RF pour des structures en couches et le développement de couches minces de matériaux SRF appropriés sous forme de substrat et de structures multicouches S-I-S. En premier lieu, l'objectif principal est de comprendre la relation entre les conditions de croissance, la microstructure du film et de la performance RF pour les matériaux SRF

produits par la condensation énergétique. Le dépôt par condensation énergétique en ultravide par ECR et HiPIMS est étudié pour le Nb et certain composés B1 supraconducteurs à définir sur des substrats avec accord de maille et des conditions de surface différents. Le modèle de zone énergie-température mis au point par André Anders est exploré afin de définir les conditions de dépôt optimales pour produire des films adéquats pour des applications SRF en monocouche et en structures multicouches. La contribution de l'énergie à la fois des ions incidents et du réseau du substrat sur la nucléation des matériaux SRF considérés et des matériaux diélectriques (AlN et MgO) ainsi que l'influence des conditions de dépôt sur les propriétés structurelles, supraconductrices et/ou RF seront étudiées. Une attention particulière sera accordée à minimiser les contraintes résiduelles (intrinsèque et thermique) avec le choix du substrat et son traitement in-situ avant dépôt ainsi que la température de dépôt. En second lieu, les conditions de dépôt développées sont utilisées, comme preuve de concept, pour préparer des structures multicouches S-I-S ayant le potentiel d'atteindre des gradients de champ élevés. Une couche de Nb épaisse ($> 1\mu$m) peut être utilisée comme substrat. Une attention particulière est accordée à l'interface entre les couches supraconductrices et diélectriques. Pour ce travail, diverses analyses de matériaux techniques ont été utilisées pour caractériser chaque type de matériau : diffraction aux électrons rétrodiffusés (EBSD), diffraction aux rayons X (XRD), MEB à haute résolution, MET, profilométrie, microscopie à force atomique (AFM), SIMS, SAM). Des mesures des propriétés supraconductrices et RF sont également effectuées (RRR, T_c, résistance de surface SRF à basse température, magnétométrie SQUID). La connaissance et les résultats acquis lors de ce projet permettront d'envisager d'importantes réductions dans les coûts de production et d'opération associés aux futurs accélérateurs de particules, qu'ils soient des machines compactes ou des installations à la frontière de l'énergie. La réalisation de couches minces de qualité pour cavités SRF changera radicalement le coût des systèmes d'accélération et améliorera de façon significative leur performance et fiabilité.

Mots-clefs : Supraconductivite RF, couches minces, niobium, multi-couches.

Aknowledgements

The work I performed during the course of my dissertation was extremely interdisciplinary. Along the years, I have been very fortunate to work with people from all backgrounds who were willing to share their knowledge and to help me. I would like to acknowledge their contributions here. First, I want to thank Andrew Hutton, director of the JLab's Accelerator Division for supporting me along the years and pushing me to make this dissertation a reality. This work would not have been possible without the guidance and support of my thesis advisors, Claire Antoine and Jean Delayen and my JLab supervisor Charlie Reece. I have been very lucky to collaborate with Larry Phillips for the past fifteen years. Special thanks go to Joshua Spradlin and Olga Trofimova for their precious help in substrate surface preparation and sample characterization. Thank you both very much. Thank you to our collaborators in the surrounding universities, Prof. Alejandra Lukaszew from the College William & Mary , Fred Stevie, Dale Batchelor, Roberto Gracia from North Carolina State University, Qiguang Yang from Norfolk State University, Lepsha Vuskovic from Old Dominion University. Thank you to Thomas Proslier at ANL, Sarah Aull at CERN, for stimulating conversations and collaborations. Thank you to Grigory Eremeev, Ari Palcewski, Fay Hannon and John Mammosser for their enthusiasm. it is a pleasure to work with you. A thousand thanks to Bonnie Madre and Valerie Brookwalter for letting me vent from time to time. It's time to go to Pearl! This work could not be possible without the precious support of our technical staff. Scott Williams, Teena Harris, Jim Folkie, Chad Wilson, Danny Forehand, Roland Overton, Chris Dreyfuss, Tom Goodman, Tina Menefee, Ken Worland, Aaron Austin, Jared Martin. Gary slack, Robert Martin, Jeff Dail, Jerry Moore, thank you for translating my pitiful drawings into real UHV parts. Very warm thanks go to Carolyn Camp and Erin Smith for their administrative support. I cannot forget my supervisors and friends from CERN who introduced me to SRF thin films years ago: Cristoforo Benvenuti, Pierre Darriulat, Sergio Calatroni, Paolo Chiggiatto, Roberto Russo, Gabriele Orlandi, Giulia Lanza, Jean-Michel Rieubland. Mille grazie a tutti. My family is the foundation of my life. To my parents, aunts, cousins and my extended family, muito obrigada, muchas gracias. Thank you to my friends in Europe and in the US, you know who you are. Candace, Judy, Vanessa, let's go dancing finally. Marie, il est temps d'aller faire un tour en ville. Nathalie and Miguel, vamos hacer los saldos en Milán. Finally, to Ashton Valente-Feliciano: thank you, thank you. Thank you for your love, your support and patience. I love you! Let's work on that dance studio now. Thank you also to the four-legged members of our family, Filou, Rushka and Tyler, who always made sure to not let me forget what is important in life ... feeding them...

Contents

Introduction

Particle accelerators are essential tools in nuclear and high energy physics research. They also have many other applications in the medical, defense fields for example. A key component of the high energy accelerators is the superconducting radio-frequency (SRF) cavity, a resonating electromagnetic structure operated in the microwave regime to impart energy to the charged particles in the beam.

Bulk niobium (Nb) has been the material of choice for SRF cavities for several decades mainly because of it is the elemental material with the highest critical temperature, the highest lower critical magnetic field and with relatively good mechanical properties. Considerable efforts have been devoted in the past years to enhance the performance of Nb bulk cavities which are now reaching the intrinsic limit of the material. Further significant breakthrough in SRF cavity technology can only be achieved by the use of alternative materials and new surface treatments. Since the RF field penetration into a superconducting surface is very shallow, SRF is essentially a surface phenomenon. As such, one can imagine to use thin films as the active superconducting surface. The concept of a thin layer of Nb deposited on the inner surface of a castable cavity structure made of copper (Cu) or aluminum (Al) opens the possibility to dramatically change the cost framework of SRF accelerators by decoupling the active SRF surface from the accelerating structure definition and cooling. The viability of SRF Nb films on Cu (Nb/Cu) technology has been demonstrated with pioneer studies at CERN [1, 2, 3] and the successful implementation of this technology in LEP-2 with 352MHz cavities. Due to defects inherent to the technique used for Nb deposition, the Nb/Cu cavities produced suffered a significant reduction of Q with increasing accelerating gradients [4].

The challenge in developing SRF Nb thin films is to reproduce and go beyond the performance of bulk Nb. While tight correlation with the characterization of real materials has yet to be described, there exists a theoretical framework describing the relevant material parameters of surfaces as they influence SRF properties. Several material factors, highly dependent upon the surface creation conditions, contribute to degraded SRF performance with respect to ideal surfaces. These limiting factors such as intra-granular impurities and lattice defect density, inter-granular impurities and oxidation, surface topography and chemistry, may lead to the reduction of the electron mean free path, thus the reduction of the lower critical field H_{c1}.

Thus, understanding of the film growth dynamics from nucleation to final exposed surface is crucial. The defect density (which determines the electron mean free path) within the RF penetration depth is certainly affected by intragrain contaminants incorporated during the final stage film growth, but it is also strongly affected by the underlying crystal texture, which is in turn developed from the initial film nucleation process, which necessarily is strongly influenced by the substrate. The development of every stage can be expected to depend strongly on the kinetic energy distribution of the arriving Nb ions. Although the thickness submitted to the RF field corresponds to the very top 40 nm of the Nb film, this final surface is dictated from its origin, i.e. the substrate, the interface, and deposition technique (ion energy, substrate temperature /*dots*). By opposition to bulk Nb surfaces, the top Nb film surface is anticipated to be the cleanest. Other superconducting materials with a T_c higher than Nb (9.27 K) have also been of interest for SRF applications. For a superconducting material to be a good candidate for SRF applications, it needs a high T_c and a low resistivity in the normal state to minimize RF losses. Additionally, a high thermodynamic critical field, H_c, and a high lower critical field, H_{c1}, are necessary to maximize accelerating gradients. Although many superconducting compounds have T_c and H_c larger than Nb, their H_{c1} is generally lower than Nb.

Recently, a concept [5] has been proposed to take advantage of these high-T_c superconductors without being penalized by their lower H_{c1}. SRF cavities are coated with alternating superconducting and insulating (SIS) layers with a thickness d smaller than the penetration depth λ so the Meissner state can be retained at a magnetic field much higher than the bulk

H_{c1}. The thin higher-T_c layers provide magnetic screening of the bulk superconducting cavity delaying vortex penetration. The BCS resistance is also strongly reduced because the envisioned superconducting materials (Nb_3Sn, NbTiN ...) have a larger superconducting gap Δ than Nb. With such structures, the cavity quality factor, Q, at 4.2 K could be increased a couple orders of magnitude above Nb values.

The subject of this dissertation is the engineering of Nb films for improved SRF performance and the demonstration of the phenomenology and the development of multi-layered SIS (superconductor-insulator-superconductor) SRF film structures following the concept proposed by Gurevich. The understanding of the dependence of the final RF surface for Nb and multilayer films on the characteristics of the films produced, the nucleation, the diverse deposition parameters, substrate nature, temperature and morphology is of primary importance. The quality of the resultant thin film is heavily influenced by the deposition technique utilized. With the availability of energetic condensation techniques [6], films with a wide range of structure and features potentially relevant to RF performance can be produced. In this context, Nb films have been produced for this work using an Electron Cyclotron Resonance (ECR) Nb ion source in ultra-high vacuum (UHV). The main advantages are the production of a high flux of singly charged ions with controllable kinetic energy and the absence of macro-particle production. For the multilayer structures development, the deposition techniques pursued are reactive magnetron sputtering and high power impulse magnetron sputtering (HiPIMS). Film growth is approached in three phases: Film nucleation on substrate, growth of an appropriate template for subsequent deposition of the final RF surface and deposition of the final surface optimized for minimum defect density.

This dissertation is organized as follows:

- Part I introduces the basics of superconductivity, the state of the art for superconducting RF bulk and Nb/Cu technologies. It introduces a theoretical proposal to enhance the current technologies along with alternate materials to Nb.
- Part II introduces the general phenomenology of film growth and the techniques used in this work to create SRF thin films.
- Part III describes the characterization techniques used for these experimental studies.
- Part IV is dedicated to the results of the development of Nb films via energetic condensation. Exploration of the Structure Zone diagram for ECR plasma deposition.
- Part V presents the fabrication and characterization of multilayer SIS structures based on NbTiN and AlN providing some results towards the RF proof of principle of the proposed model in Part I.
- Finally, part VI summarizes the important results of this dissertation and a roadmap for future work.

Part I

Background

The key component of the high energy accelerators is the superconducting radio-frequency (SRF) cavity which imparts energy to the charged particles in the beam. This part introduces briefly, in chapter I.1 the basics of superconductivity and the superconducting parameters relevant in the RF regime where SRF cavities are operated. It also introduces the concept of multilayer structures based on higher T_c materials proposed to enhance the RF behavior of SRF cavities. A description of the state of the art for bulk Nb and Nb/Cu technologies is treated in chapters I.2 and I.3. Finally, chapter I.4 gives an overview of superconducting materials with higher T_c than Nb that could be considered as potential alternatives to Nb for SRF applications.

Chapter I.1

Superconducting Radio-Frequency

In this chapter, phenomenological aspects of superconductivity are introduced along with some rudimentary theoretical background. For a rigorous treatment, see References [7, 8, 9]. The particular case of superconductivity in the radio-frequency (RF) regime is then addressed along with the parameters relevant to SRF cavities.

I.1.1 Basics of superconductivity

Superconductivity was discovered in 1911 by H. Kamerlingh-Onnes in mercury, lead and tin, when he observed a complete disappearance of the electrical resistance below the material-specific critical temperature T_c. A complete theoretical understanding of classic superconductors was not achieved until Bardeen, Cooper and Schrieffer formulated the first microscopic theory, known as the BCS theory, in the 1950s. Since then, many elements and compounds have been found to possess superconducting properties. Among these superconducting elements, niobium (Nb) has the highest critical temperature and relatively high critical fields, which motivates its choice as a material for superconducting RF cavities.

The behavior of electrical resistivity was among the first problems investigated by Kamerlingh Onnes [10, 11], after he achieved the liquefaction of helium. In 1911, measuring the resistance of a mercury sample as a function of temperature, he found that, at about 4 K, it falls abruptly to a value which he could not distinguish from zero. He called this extraordinary phenomenon superconductivity and the temperature at which it appears the critical temperature T_c.

When a metallic ring is exposed to a changing magnetic field, a current will be induced which attempts to maintain the magnetic flux through the ring at a constant value. For a body with resistance R and self-inductance L, this induced current will decay as

$$I(t) = I(0)e^{(-\frac{Rt}{L})}I(t). \tag{I.1.1}$$

I(t) can be measured with great precision (for example, by observing the torque exerted by the ring upon another, concentric one which carries a known current) and a long series of experiments demonstrates the absence of any detectable decay: the current induced in a superconducting ring will persist indefinitely without dissipation. However, superconductivity is destroyed by the application of a sufficiently large magnetic field. If the current exceeds a critical current, the superconducting state will also be destroyed.

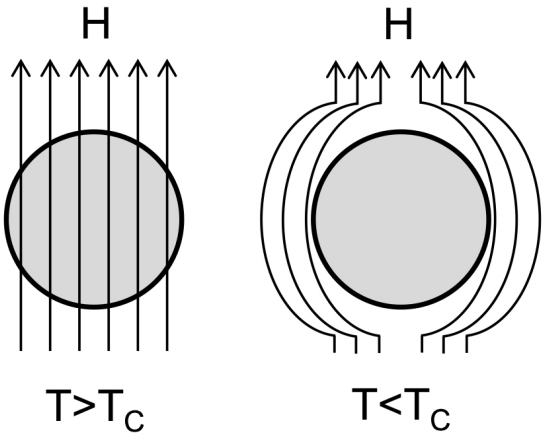

Figure I.1.1: Diagram of the Meissner effect

I.1.1.1 Perfect diamagnetism

If a perfect conductor is placed in a dc external magnetic field H_{ext}, provided that H_{ext} is lower than the critical field, no magnetic flux can penetrate the specimen. Induced surface currents maintain the internal flux, and persist indefinitely. In 1933, Meissner and Ochsenfeld made an important discovery regarding the magnetic behavior of a superconductor compared to a perfect conductor [7, 12, 13]. Their careful measurements of the field distribution around a spherical specimen indicated that regardless of the path of transition the magnetic flux is expelled from the interior of the superconductor and the magnetic field H vanishes. This is called the Meissner effect and shows the reversible character of the superconducting transition.

I.1.1.2 Phenomenological approach with the London equations

In 1935, Fritz and Heinz London examined quantitatively the fundamental fact that a metal in the superconducting state expels magnetic fields. Their analysis starts with the two-fluid model of Gorter and Casimir [14]. The only crucial assumption of this model to consider is that in a superconductor at a temperature T $<$ Tc, only a fraction $n_s(T)$ of the total number of conduction electrons participate in a supercurrent. The quantity n_s(T) is known as the density of superconducting electrons. It approaches the full electrostatic density n as T falls well below T$_c$, but it drops to zero as T rises to T$_c$. The remaining fraction of electrons is assumed to constitute a *normal fluid* of density n-$n_s$that cannot carry an electric current without normal dissipation.

The normal current and the supercurrent are assumed to flow in parallel. Since the supercurrent flows with no resistance, it will carry the entire current induced by any small transitory electric field and the normal electrons will remain quite inert. Normal electrons are therefore ignored in the following discussion (the exact role of the normal electrons will be detailed in § I.1.1.7).

In the presence of an electric field, the superconducting electrons will be freely accelerated without dissipation so that their mean velocity v_s will satisfy

$$m\frac{dV_S}{dt} = -eE \tag{I.1.2}$$

.

The current density carried by these electrons is $j = -eV_S n_S$, Equation I.1.2 can then be written as

$$\frac{dj}{dt} = \frac{n_S e^2}{m} E \tag{I.1.3}$$

.

The above equation is known as the first London equation. Substituting I.1.3 into the Faraday's law of induction,

$$\nabla \times E = -\frac{1}{c}\frac{\partial H}{\partial t} \tag{I.1.4}$$

,

the following relation between current density and magnetic field can be obtained:

$$\frac{\partial}{\partial t}\left(\nabla \times j + \frac{nse^2}{mc} H\right) = 0 \tag{I.1.5}$$

.

This relation, together with the Maxwell equation

$$\nabla \times H = \frac{4\pi}{c} j \tag{I.1.6}$$

,

determines the magnetic fields and current densities that can exist within a perfect conductor. Any static field H determines a static current density j through Equation I.1.6. Since any time independent H and j are trivial solutions of I.1.5, the two equations are consistent with an arbitrary static magnetic field. This is incompatible with the observed behavior of superconductors, which permit no fields in their interior. The London brothers discovered that this characteristic behavior of superconductors could be obtained by restricting the full set of solutions of I.1.5 to those that obey

$$\nabla \times H = \frac{nse^2}{mc} H \tag{I.1.7}$$

.

The Meissner effect requires that the quantity $\nabla \times j + \frac{nse^2}{mc} H$ to be not only independent in time but also to be zero. Equation (I.1.8) is known as the second London equation.

$$\nabla \times j + \frac{nse^2}{mc} H = 0 \tag{I.1.8}$$

.

Equations I.1.6 and I.1.7 imply that

$$\nabla^2 H = \frac{4\pi n_s e^2}{mc^2} H \tag{I.1.9}$$

,

$$\nabla^2 j = \frac{4\pi n_s e^2}{mc^2} j \tag{I.1.10}$$

.

These equations predict that currents and magnetic fields can only exist in superconductors within a certain thickness of the surface layer, λ_L, known as the London penetration depth and given by

$$\lambda_L = \sqrt{\frac{mc^2}{4\pi n_s e^2}} \tag{I.1.11}$$

.

The London penetration depth is temperature dependent and approaches, corresponding to full penetration of the field in the material, as the temperature approaches T_c.

I.1.1.3 Microscopic theory of Bardeen, Cooper and Schrieffer (BCS) - brief description

The microscopic theory of superconductivity was developed by Bardeen, Cooper and Schrieffer in 1957 [15] and is known as the *BCS theory*.

The theory of superconductivity requires a net attractive interaction between electrons in the neighborhood of the Fermi surface. At the low temperature required for superconductivity, lattice vibrations (phonons) are minimal. As such, electrons travelling through a metal can cause a lattice distorsion due to the Coulomb attraction with the positively charged ion cores. This lattice distorsion ceates a small volume with a net positive charge that attracts another electron in the material. Although the direct electrostatic interaction is repulsive, it is possible for the ionic motion to screen the Coulomb interaction, leading to a net attraction between electrons.

The screening by the ionic motion can yield a net attractive interaction between electrons with energies sufficiently close together (roughly separated by less than $barh\omega_D$, a measure of the typical phonon energy). This attraction underlies the theory of superconductivity.

Given that electrons whose energies differ by $O(barh\omega_D)$ can experience a net attraction, the possibility arises that such electrons might form bound pairs in a boson-like state. This pairs are called *Cooper pairs*.

Because Cooper pairs behave like boson, the *Pauli Exclusion Principle* does not apply and the electrons can occupy the same electronic quantum state.

The BCS theory constructs a ground state in which all electrons form bound pairs. Each electron plays a dual role: it provides the necessary restriction on allowed wave vectors (via the exclusion principle) that makes possible the binding of other pairs in spite of the weakness of the attraction and participates itself in one of the bound pairs.

The spatial range of the pair wave functions is defined as the *coherence length* ξ_0. Itis very large compared with the spacing between electrons r_s. A crude estimate of ξ_0 can be:

$$\xi_0 = \frac{\bar{h} v_F}{k_B T_c} \tag{I.1.12}$$

,

ξ_0 is typically of the order of 10^3 Å.

Because Cooper pair lengths are much larger than lattice spacings, they can overlap and interact with each other causing a condensation of boson-like particles.

Although the paired state is energetically favorable below T_c, not all electrons are in the boson ground state when $0 < \mathrm{T} < T_c$, due to the finite probability that some pairs are split by thermal excitations across an energy gap, $2\Delta(\mathrm{T})$. This probability is governed by the Boltzmann factor $exp(\text{-}\Delta(T)/k_B T)$ where $k_B$is the Boltzman constant. Below $\mathrm{T} = T_c/2$, the Cooper pair density n_s (T) is close to n_s $(T = 0)$, and the number of unpaired electrons is given by

$$n_e \approx 2n_s\,(T=0)\exp\ (-\frac{\Delta\,(T)}{k_B T}) \qquad (T < \frac{T_c}{2}) \tag{I.1.13}$$

.

In this temperature range the energy gap $\Delta(\mathrm{T})$ is also close to its zero temperature value.

I.1.1.4 Characteristic figures of merit of superconductivity

Critical temperature

In zero magnetic fields, superconducting ordering sets in at a critical temperature given by

$$k_B T_c = 1.13\bar{h}\omega e^{-\frac{1}{N_0 V_0}} \tag{I.1.14}$$

,

where $N_0$is the density of electronic levels $(g(\epsilon_F))$ for a single spin population in the normal metal $(g(\epsilon_F)/2)$ and V_0 is the effective electrons coupling. No matter how weak V_0 is, the theory predicts a transition, though it may be at an unobservably low temperature.

Superconducting energy gap

The bound state energy E is typically within $\mathrm{k}_B\mathrm{T}_c$ of E_F. Close to the Fermi surface, there exists an energy gap 2Δ corresponding to the energy required for pair breaking. This gap is one way to characterize the superconducting state. The BCS theory predicts a relation between the pairing energy and the critical temperature.

The following formula is predicted for the zero-temperature energy gap:

$$\Delta\,(0) = 2\bar{h}\omega e^{-\frac{1}{N_0 V_0}} \tag{I.1.15}$$

.

The ratio of equations (I.1.14) and (I.1.15) leads to a formula independent of the phenomenological parameters:

$$\frac{\Delta(0)}{k_B T_c} = 1.76 \tag{I.1.16}$$

.

The actual size of the gap is different from one material to another due to the difference in electron-phonon interaction strength. For Nb, the supeconducting energy gap is quite large $(\Delta(0)/\mathrm{k}_B\mathrm{T}_c = 1.9)$ thus its significant interest for SRF applications.

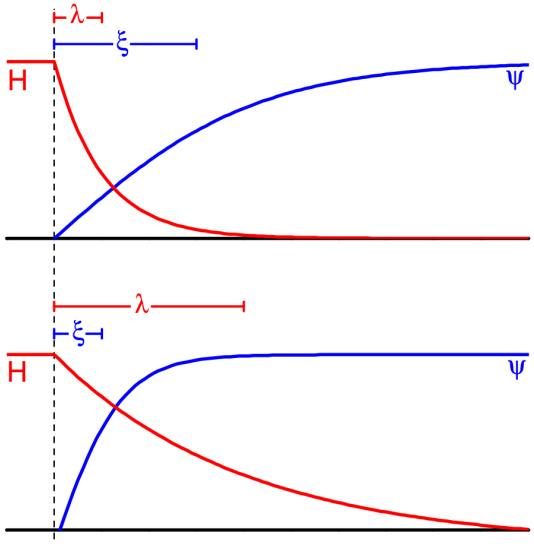

Figure I.1.2: Surface energy for type I and II superconductors

The coherence length and effective penetration depth

The size of a Cooper pair is characterized by the coherence length ξ. Pippard [16] studied the role of scattering impurities:

Based on the evidence that the coherence length depends on the mean free path of electrons in the material with

$$\frac{1}{\xi} = \frac{1}{\xi_0} + \frac{1}{l} \tag{I.1.17}$$

,

he introduced an effective penetration depth to underlines the penetration depth increases with a reduction of the mean free path [17].

$$\lambda_{eff} = \lambda_L \cdot \frac{\xi_0}{\xi} \tag{I.1.18}$$

,

where ξ_0 is the characteristic coherence length of the superconductor. For "clean" superconductors, $l \to \infty$ *so* $\xi = \xi_0$. If $l \ll \xi_0$, then $\xi = l$.

Classes of superconductors and the Ginzburg-Landau parameter

Two classes of classic (low temperature) superconductors exist, known as type I and type II. While the superconducting mechanism is the same in both cases, the surface energy for normal conducting-superconducting boundaries differs, resulting in different behavior for type I and type II superconductors in a magnetic field (figure I.1.2).

For type I superconductors, the surface energy is positive. This class remains in the perfect Meissner state in applied dc fields up to a temperature dependent critical field H_c.

Type II superconductors (such as Nb, NbN, Nb_3Sn ...) are different because the surface energy of a superconducting-normal conducting interface is negative, so that the creation of

interfaces can be energetically favorable. They expel a dc magnetic field completely up to a lower critical field H_{c1}. Rather than quenching above this value, though, they enter what is known as the *mixed state*, where normal conducting cores form in the superconductor. The density of these flux tubes,the so-called *fluxons* or *vortices*, increases with H_{ext} until the entire sample becomes normal conducting at an upper critical field H_{c2} (see § I.1.1.7 for more details).

A method for determining a superconductor type uses the *Ginzburg-Landau (GL) parameter* κ defined as:

$$\kappa = \frac{\lambda_L}{\xi_0}. \tag{I.1.19}$$

The distinction between the two types of superconductors is as follow:

$$\kappa < \frac{1}{\sqrt{2}} \quad TypeI, \tag{I.1.20}$$

$$\kappa > \frac{1}{\sqrt{2}} \quad TypeII. \tag{I.1.21}$$

Critical fields

When electrons condense into Cooper pairs, the resulting superconducting state becomes more highly ordered than the normal-conducting state. Since only those few electrons within $k_B T_c$of the Fermi energy are involved, the entropy difference is small. The free energy in the superconducting state is lower than that in the normal-conducting one. Here free energy is

$$F = U_{int}\left(T\right) - TS \tag{I.1.22}$$

,

where U_{int} is the internal energy and S the entropy. As mentioned earlier, when an external dc magnetic field H_ext is turned on, supercurrents flow in the penetration depth to cancel out the field in the interior. This rises the free energy of the superconducting state.

$$F_s\left(H\right) = F_n = \ F_s\left(H=0\right) + \mu_0 V_s \int_0^{H_c} HdH \tag{I.1.23}$$

Here $V_s$is the superconductor volume. All the flux enters the superconductor at H_c, which is the thermodynamic critical field. The second term in *I.1.3*4 is the work done on the superconductor to establish the screening currents:

$$F_n - F_s\left(H\right) = \frac{\mu_0 V_s H_c^2}{2} \tag{I.1.24}$$

.

The BCS theory leads to an expression for the free energy of electrons in the superconducting state from which various thermodynamic properties, including H_c, can be derived.

In particular one can calculate the zero temperature thermodynamic critical field

$$\frac{\mu_0 H_c^2}{2} = \frac{3\gamma T_c^2}{4\pi^2}\left(\frac{\Delta(0)}{k_B T_c}\right)^2 = 0236\gamma T_c^2 \tag{I.1.25}$$

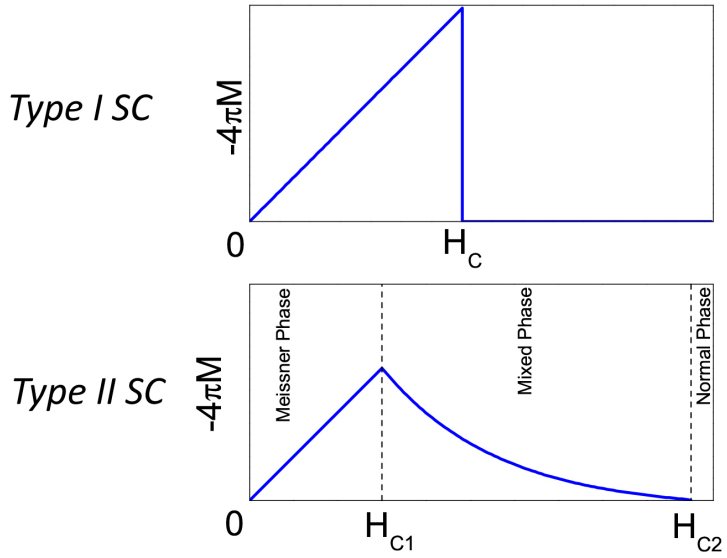

Figure I.1.3: Magnetization as a function of applied field for type I and type II superconductors

.

Here γ is the coefficient of the linear electronic specific heat in the normal state ($(\pi^2/3)k^2{}_B g(\epsilon_F)$). It is important to note that the thermodynamic critical field increases proportionally to T_c. Therefore the higher transition temperature superconductors, such as Nb_3Sn, are interesting for accelerating cavities because of the promise of higher operating fields. Note that γ is related to the electronic density of states and thereby reflects the role of the electronic structure of the material.

The elementary BCS prediction for $H_c(T)$ is often expressed by the empirical law:

$$\frac{H_c(T)}{H_c(0)} = 1 - \left(\frac{T}{T_c}\right)^2 \tag{I.1.26}$$

.

Type I-superconductors remain in the Meissner state until the critical field H_c is reached which forces the material into the normal state.

Type II-superconductors have three phases: the Meissner, mixed and normal states. They are then characterized by two critical fields:

- The lower critical field H_{c1} at which the material transitions from the Meissner state to the mixed state.
- The upper critical field H_{c2} above which the material becomes fully normal.

The generalized magnetic response of both classes of superconductors is represented in figure I.1.3.

Nb is a marginal type II-superconductor for which its critical fields are very close in value.

At zero temperature, ${H_{c1}}^{Nb}$ = 170 mT, ${H_c}^{Nb}$=200 mT, ${H_{c2}}^{Nb}$ = 240 mT.

I.1.2 Superconducting RF

The superconducting accelerating cavities used in accelerators are operated in the RF regime where the superconductor behavior differs from the DC regime.

I.1.2.1 Superconductor surface resistance

Although superconductors do not exhibit any dc resistivity, there are small losses for RF currents. This fact can be explained by a model of interpenetrating normal conducting electrons and superconducting Cooper pairs when T > 0 (the two-fluid model). Collisions between Cooper pairs and lattice defects, impurities or phonons are insufficient to split the pairs and scatter them out of the ground state. Any current carried by these pairs flows without resistance. However, the unpaired electrons can be scattered and dissipate energy. Nevertheless, the dc resistivity of a superconductor is zero because the lossless Cooper pairs current expel any fields in the superconductor. The normal conducting electrons never see an electric field and do not contribute to the current flow.

In the RF case the situation is different. Although Cooper pairs cannot be scattered, they do possess inertia. At microwave frequencies, they no longer screen externally applied fields completely and normal conducting electrons are accelerated. This component of the electron fluid then causes power dissipation. By equation I.1.13, the number of unpaired electrons declines exponentially with temperature and one observes a corresponding decline in the surface resistance of the superconductor.

The application of the two fluid model yields a surface resistance that drops exponentially to zero at $T = 0$.

$$R_s \propto \omega^2 \exp\left(-s\frac{T_c}{T}\right) \qquad (T \leq \frac{T_c}{2}) \tag{I.1.27}$$

.

With T being the working temperature and $T_c$the superconducting transition temperature, [18] the surface resistance can be expressed using the following approximated formula (for T $\leq T_c/2$):

$$\frac{R_s}{R_n} = \frac{1}{\sqrt{2}} \frac{\frac{\sigma_1}{\sigma_n}}{(\frac{\sigma_2}{\sigma_n})^{\frac{3}{2}}} \tag{I.1.28}$$

BCS resistance

In the framework of the BCS theory extension to finite frequencies, Mattis and Bardeen [19] found, for $\bar{h}\omega<2\Delta$, two integral relations for the complex conductivity of a superconductor.

$$\frac{\sigma_1}{\sigma_n} = \frac{2}{\hbar\omega}\int_{\Delta}^{\infty} [f(E) + f(E+\hbar\omega)] g^{+}(E)\, dE \tag{I.1.29}$$

$$\frac{\sigma_2}{\sigma_n} = \frac{1}{\hbar\omega}\int_{\Delta-\hbar\omega,-\Delta}^{\infty} [1 - 2f(E+\hbar\omega)] g^{-}(E)\, dE \tag{I.1.30}$$

$$\text{where} \qquad f(E) = \frac{1}{1+\exp(\frac{E}{k_B T})}$$

and

$$g^{\pm} = \frac{E^2 + \Delta^2 + \bar{h}\omega E}{\sqrt{\pm\left(E^2 - \Delta^2\right)\left(E + \bar{h}\omega\right)^2 - \Delta^2}} \tag{I.1.31}$$

These integrals (σ_1/σ_n and σ_2/σ_n) are easily calculated numerically [20]. In particular, they can be approximated in the normal skin effect regime (for $\bar{h}\omega < 2\Delta$) by two analytical expressions:

$$\frac{\sigma_1}{\sigma_n} = \left[\frac{\frac{2\Delta}{k_B T}}{1 + e^{(\frac{-\Delta}{k_B T})2}}\right] e^{(\frac{-\Delta}{k_B T})} ln\frac{\Delta}{\hbar\omega} \tag{I.1.32}$$

,

$$\frac{\sigma_2}{\sigma_n} = \frac{\pi\Delta}{\omega}\tanh\left(\frac{\Delta}{2k_B T}\right) \tag{I.1.33}$$

.

One can then arrive to the following formula (valid for $T \leq T_c/2$),

$$R_{BCS} = \frac{R_n}{\sqrt{2}}\left(\frac{\hbar\omega}{\pi\Delta}\right)^{\frac{3}{2}}\frac{\sigma_1}{\sigma_n} = A\sqrt{\varrho_n}\frac{e^{\frac{-\Delta}{k_B T}}}{\sqrt{sT_c}T\left(1 + e^{\frac{-\Delta}{k_B T}}\right)^2}\omega^2 ln\frac{\Delta}{\hbar\omega} \tag{I.1.34}$$

,

where A is a material dependent constant. The BCS surface resistance expression is similar to that given by equation I.1.25.

Although Equation I.1.34 is approximated and limited to the dirty superconductors, it clearly shows how low BCS values can be obtained reducing ρ_n and increasing T_c. The BCS theory predicts then that a good candidate for RF applications must be a high $T_c$material but also a good metal in the normal state (lowρ_n).

Residual losses

In practice, the surface resistance never vanishes as shown in figure I.1.4: it is due to the presence of a temperature independent residual term of several nΩ [21]:

$$R_s = R_{BCS}(T) + R_{res} \tag{I.1.35}$$

.

Many reports exist in the literature about the possible origin of the residual resistance: both *physical phenomena* and *accidental mechanisms* (such as particulates, chemical residues or surface defects on the cavity walls) contribute to parasitic losses. Due to the variety of the phenomena involved, it is impossible to give one formula predicting them. Nevertheless, from the literature analysis, we can deduce some interesting information: R_{res} is at least proportional to the square root of ρ_n. Therefore, among two different materials with different ρ_n and T_c values, having the same R_{BCS}, the one with the lower ρ_n should have the smallest residual resistance.

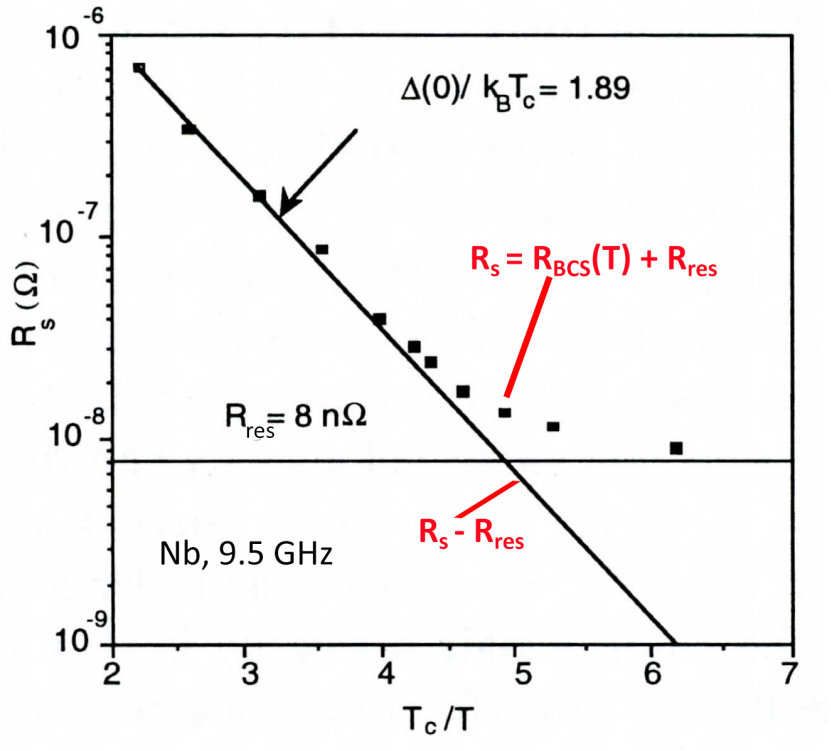

Figure I.1.4: Surface resistance.

I.1.2.2 Superheating magnetic field

In the presence of an external magnetic field, the superconductor/normal-conductor transition is of first order at T_c (H), and is combined with a latent heat due to the entropy discontinuity. The first order phase transition takes place at nucleation centers. Because of the entropy discontinuity and required nucleation centers, there is a possibility for a *superheated* superconducting state to persist metastably at $H > H_c$.

In a type I superconductor, the positive surface energy suggests that, in DC fields, the Meissner state could persist beyond the thermodynamic critical field, up to the superheating field H_{sh}. At this field (figure I.1.5) the surface energy per unit area vanishes:

$$\frac{\mu_0}{2}H_c^2\xi - H_{sh}^2\lambda = 0, \quad H_{sh} = \frac{1}{\sqrt{kGL}}H_c \tag{I.1.36}$$

.

For type II superconductors, it is also possible for the Meissner state to persist metastably above the lower critical field H_{c1}.

The dependence of the superheating critical field on the GL parameter κ has been calculated by solving the GL equations [22] to show that:

$$H_{sh} \approx \frac{0.89}{\sqrt{kGL}}H_c \qquad \kappa \ll 1 \tag{I.1.37}$$

,

$$H_{sh} \approx 1.2H_c \qquad \kappa \approx 1 \tag{I.1.38}$$

,

$$H_{sh} \approx 0.75 H_c \qquad \kappa \gg 1 \tag{I.1.39}$$

.

Because it is theoretically possible to maintain a metastable Meissner state up to H_{sh}, it was expected that the critical RF field was equal to H_{sh} [21] as suggested by some experiments conducted in the pulsed regime [23].

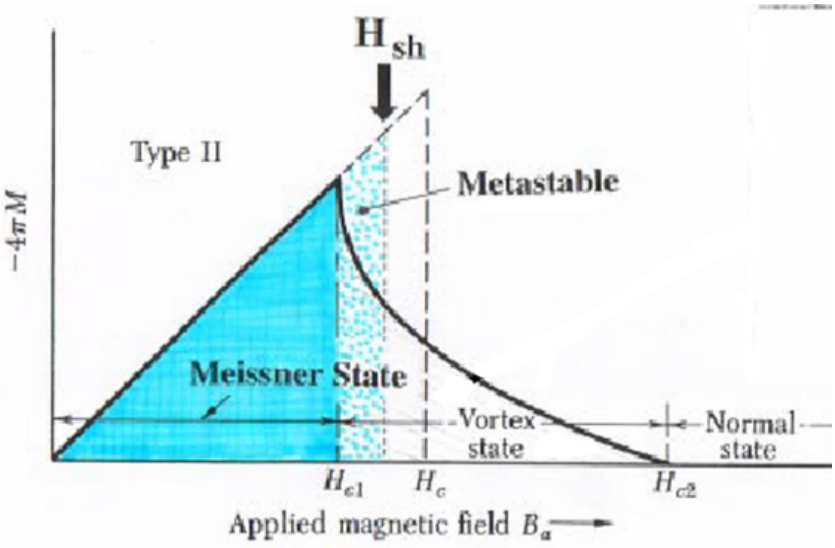

Figure I.1.5: Superheating field

I.1.3 Characteristics of superconducting radiofrequency cavities

Accelerator facilities such as the continuous Electron Beam Accelerator facility (CEBAF) at Jefferson Lab or the Large Hadron Collider (LHC) at CERN, use superconducting resonating cavities that operate in the RF regime. These SRF cavities are preferred over normal conducting cavities because they are capable of higher accelerating gradients and duty cycles with lower RF losses.

SRF cavities are immersed in a superfluid He bath to maintain their temperature well below the material's T_c. A representative cross-section of an SRF cavity is shown in figure I.1.6.

An alternating electric field is present along the direction of propagation for the accelerated charged particle beam. Because the electric field in the cavity is alternating, an associated magnetic field travels parallel to the cavity surface.

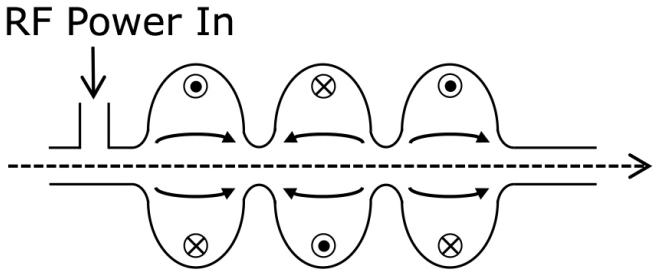

Figure I.1.6: Diagram of an SRF cavity

Accelerating voltage

The accelerating voltage $V_{acc}$of a cavity is determined by considering the motion of a charged particle along the beam axis. For a charge q, by definition

$$V_{acc} = |\frac{1}{q} \times \textit{maximum energy gain possible during transit}| \tag{I.1.40}$$

,

$$V_{acc} = |\int_0^d E_z(\varrho = 0,\ z) e^{\frac{i\omega_0 z}{c}} dz| \tag{I.1.41}$$

,

$$E_{acc} = \frac{V_{acc}}{d} \tag{I.1.42}$$

.

I.1.3.1 Peak surface fields

The magnetic field amplitude is proportional to the magnitude of the applied electric field. So the maximum accelerating field for a given cavity depends on the maximum surface fields it can sustain before vortex penetration diminishes the efficiency of the cavity: the peak surface electric field (E_{pk}) and the peak surface magnetic field (H_{pk}). For TM-type cavities with $\beta = 1$,

$$\frac{E_{pk}}{E_{acc}} = \frac{\pi}{2} = 1.6, \tag{I.1.43}$$

$$\frac{H_{pk}}{E_{acc}} = 30.5\ \frac{Oe}{MV/m}. \tag{I.1.44}$$

I.1.3.2 Power dissipation and quality factor Q

To support the electromagnetic fields, currents flow within a thin surface layer of the cavity walls. A superconductor has a small resistance at RF frequencies so the wall currents dissipate energy. The losses are characterized by the material dependent surface resistance R_s which is defined via the power P_d dissipated per unit area

$$\frac{dP_d}{ds} = \frac{1}{2} R_s |H|^2 \tag{I.1.45}$$

,

where H is the local surface magnetic field.

A common figure of merit for accelerating cavities - or any resonator - is the quality factor, Q (Q-value). The Q-value is a dimensionless measure of the efficiency of a cavity related to the power dissipation as follows:

$$Q = \omega \frac{U}{P_d} \tag{I.1.46}$$

,

where U is the stored energy and P_d is the power dissipated in the cavity walls.

The notation Q_0 denotes an *unloaded Q* which describes only the cavity and not the surrounding components or the beam being accelerated. A *loaded* Q_L would account for beam loss, inter-cavity coupling and other loss mechanisms. Q_0 is large when the cavity stores large amounts of energy and the cavity walls dissipate very little power.

For all cavity modes, the time averaged energy in the electric field equals that in the magnetic field, so the total energy in the cavity is given by

$$U = \frac{1}{2}\mu_0 \int_V |H|^2 dv = \frac{1}{2}\epsilon_0 \int_V |E|^2 dv \tag{I.1.47}$$

,

where the integral is taken over the volume of the cavity. Equation I.1.49 yields the dissipated power

$$P_d = \frac{1}{2} R_s \int_S |H|^2 ds \tag{I.1.48}$$

,

where the integration is taken over the interior cavity surface. By keeping R_S in the integral we have

$$Q_0 = \frac{\omega_0 \mu_0 \int_V |H|^2 dv}{R_s \int_S |H|^2 ds} \tag{I.1.49}$$

.

Q_0 is also frequently written as $Q_0 = \frac{G}{R_s}$where G is the *geometry factor*

$$G = \frac{\omega_0 \mu_0 \int_V |H|^2 dv}{\int_S |H|^2 ds} \tag{I.1.50}$$

For 1.5 GHz cavities, such as for the CEBAF machine at Jefferson Lab, the geometry factor is 290 Ω.

I.1.4 Towards a new SRF BCS R_s theory

A new theoretical analysis of the effective RF surface impedance of a BCS superconductor was developed and presented by B. Xiao *et al.* in 2013 [24, 25, 26]. This work extends the Mattis-Bardeen theory from a perturbative, zero-field limit theory to a full field-dependent theory. The result gives a rather unexpected prediction of decreasing resistance, implying increasing Q_0, for an RF field amplitude over a broadly useful range (figure I.1.7). Remarkably, one finds strong agreement between some of the best performing cavities and the predictions of this theory (figure I.1.8). Further work is underway to examine the applicability of this theory, but the correspondence suggests that the performance benefits obtained via the thermal diffusion of interstitials into the RF surface occur via the shortening of the electron mean free path and the inhibition of parasitic losses, which have yet to be clarified.

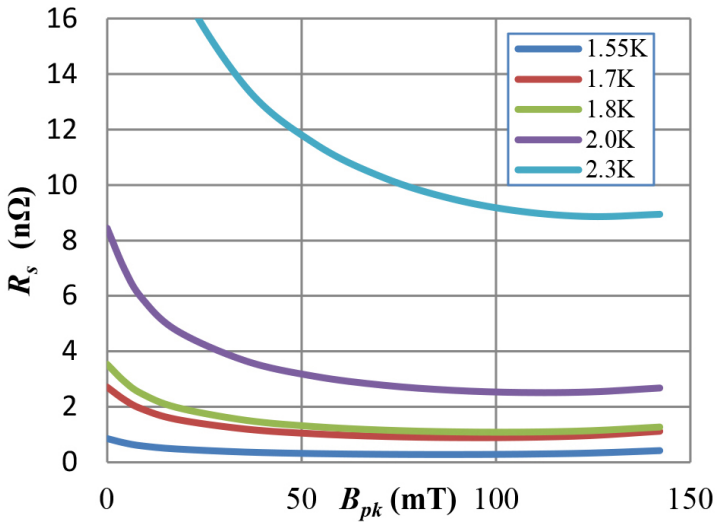

Figure I.1.7: Effective 1.3 GHz surface resistance of standard Nb material parameters at various temperatures of interest [27].

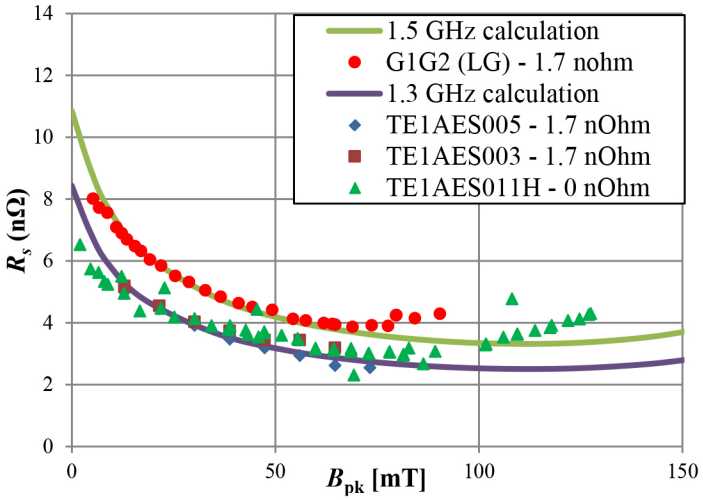

Figure I.1.8: Field-dependent BCS surface resistance at 2.0 K, calculated by Xiao's code and recent very low loss cavity test data from JLab at 1.5 GHz and FNAL at 1.3 GHz prepared by different methods. For the experimental data, $\sim 20\%$ error on R_s and $\sim 5\%$ error on B_{pk} are not shown here [27].

I.1.5 Criteria of choice for superconductors for SRF applications

As seen in section I.1.2, for dirty limit superconductors and for $T<T_c/2$ [28], the BCS surface resistance R_{BCS}, can be expressed as follows:

$$R_{BCS} = \frac{R_n}{\sqrt{2}}\left(\frac{\eta\omega}{\pi\Delta}\right)^{\frac{3}{2}}\frac{\sigma_1}{\sigma_n} = A\sqrt{\rho_n}e^{\frac{\Delta}{K_B T}}\left(1 + O\left(\Delta, \omega, T\right)\right) \quad \text{(I.1.51)}$$

,

where A is a constant weakly dependent on the material, ω is the RF frequency, ρ_n is the normal state conductivity, λ is the penetration depth and T_c the transition temperature.

In equation I.1.55, the dependence of R_{BCS} on ρ_n and T_c represents an immediate criterion for selecting the potential candidates for SRF cavity applications.

As seen in section I.1.2., in practice, the surface resistance at T=0 never vanishes due to a residual surface resistance term which is temperature independent and due to parasitic losses. It is not fully understood yet but believed to be due to intrinsic losses due to non-ideal surface quality, metallic inclusions within the penetration depth, oxides on the surface and grain boundaries. Other contributors are extrinsic losses due to flux trapped during cooling. Due to the wide variety of phenomena, it is impossible to predict these residual losses with one formula. However, from results reported in literature, R_{res} is found empirically to be at least proportional to the normal resistivity $\sqrt{\rho_n}$. Therefore, for a material with the same BCS resistance but different T_c and ρ_n , the lower ρ_n, the lower R_{res}.

The other primary requirement is a high superheating magnetic field H_{sh}, which is of the order of the thermodynamic critical field H_c. H_c increases proportionally to T_c (Equation I.1.36): the higher transition temperature superconductors are interesting for accelerating cavities because of the promise of higher operating fields. To maximize accelerating gradients, a high H_c or H_{sh} and small GL parameter κ are necessary.

I.1.6 A concept to enhance the performance of SRF cavities

In the quest of improving the RF response of SRF cavities, an alternative concept was proposed, a few years ago, by Alexander Gurevich [5] which would allow to take advantage of high-T_c superconductors without being penalized by their lower H_{c1}. The idea is to coat SRF cavities with alternating superconducting and insulating layers (SIS structures) with a thickness d smaller than the penetration depth λ.

If the superconducting film is deposited with a thickness $d << \lambda$, the Meissner state can be retained at magnetic field much higher than bulk H_{c1} as

$$H_{c1} = \frac{2\phi_0}{\pi d^2}\ln(\frac{d}{1.07\xi_0}) for d \ll \lambda \quad \text{(I.1.52)}$$

.

As shown in (figure I.1.10), the strong increase of H_{c1} in films allows to use RF fields higher than the critical field H_c1 of bulk Nb, but lower than those at which the flux penetration at grain boundaries may create a problem. The BCS resistance is also strongly reduced because of the use of superconducting layers with higher gap Δ (Nb_3Sn, NbTiN ...).

Successful magnetic shielding of a Nb cavity can be achieved using superconducting films, tailored to withstand larger magnetic field than bulk Nb, with thin insulating layers to inhibit

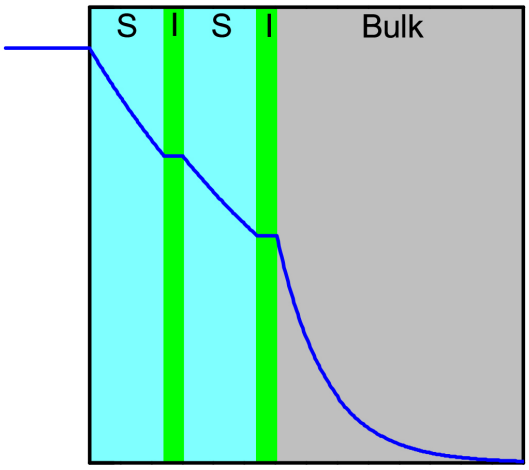

Figure I.1.9: The SIS structure shields the Nb cavity from higher magnetic fields reducing the effective field experienced by the cavity.

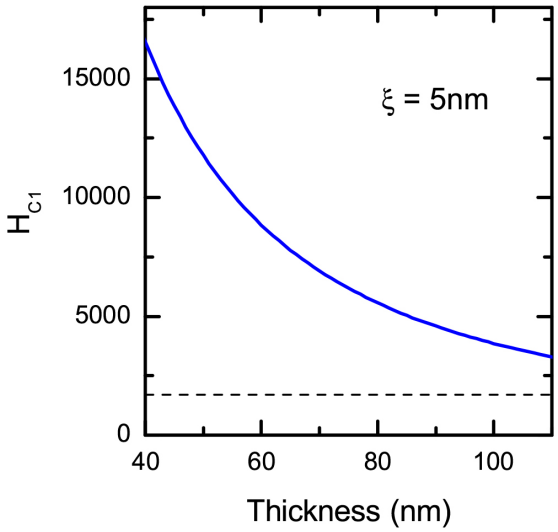

Figure I.1.10: Enhancement of H_{c1} as a function of thickness for superconducting thin film with a coherence length of 5 nm. The dashed line corresponds to ${H_{c1}}^{Nb}$ = 170 mT

vortex penetration. With such structures, Q-values at 4.2 K of two orders of magnitude above Nb values could be achieved.

As an example, a thin Nb_3Sn film of 20 nm in thickness increases H_{c1} for Nb_3Sn to 5.7 T. If a 50 nm Nb_3Sn layer is coated on a bulk Nb cavity with an insulator layer in between, and if the Nb cavity can sustain fields up to 150 mT, this structure could sustain external magnetic field of about 320 mT and therefore could reach accelerating gradient without precedent.

Chapter I.2

Frontiers of bulk Nb based SRF Technology

Based on the fundamental aspects of superconductivity, discussed in Chapter I.1, for a material to be useful in accelerators, the primary requirements are a high transition temperature, T_c, a low ρ_n, and a high superheating critical magnetic field H_{sh}which is of the order of the thermodynamic critical field, H_c. In the early days, lead (Pb), coated on a Cu cavity, has been very useful in early studies and heavy-ion accelerator applications. However, for the past 40 years, the material of choice for superconducting accelerators has been Nb because it has the highest T_c (9.25 K) among all pure metals and the highest lower critical field $H_{c1} \approx$ 180 mT (2 K) among all superconductors. Technical considerations, such as ease of fabrication, and the ability to achieve uniformly good material properties over a large surface area, have also been proven favorable for niobium. High purity niobium is readily available, has a reasonably high thermal conductivity, and is mechanically workable to form cavity shapes. As mentioned earlier, Nb is a marginal type II superconductor, so all the critical fields are very close.

I.2.1 Approach of the intrinsic Nb limit

In the recent years, bulk Nb cavities are approaching their intrinsic limit at $H_{max} = H_{c1}$ (180 mT), with breakdown fields close to the de-pairing limit (50 MV/m) (for a typical elliptical cavity geometry) [29]. The limits of SRF performance obtained with bulk Nb technology is best illustrated by by the curve of their quality factor Q (inversely proportional to the surface resistance) versus the accelerating gradient, measured around 2 K and is represented here with the set of standardized preparation and tests performed at Jefferson Lab as part of the ILC R&D work [30] (figure I.2.1 top).

I.2.2 State of the art for SRF cavity surface processing

In the past two decades, tremendous efforts have been made to exploit to the maximum the capabilities of Nb. Recent progress in Nb cavity material surface modification that yields dramatically lower BCS as well as residual resistance is revolutionizing the community's expectations for the ultimate Nb performance. To realize benefit from these lower losses in practical applications implies also increasing control over other sources of dissipative loss, principally frozen flux from ambient fields and parasitic losses from contamination-derived electronic activity. Technological progress in the 20 years since the design of the TESLA cavity (the most

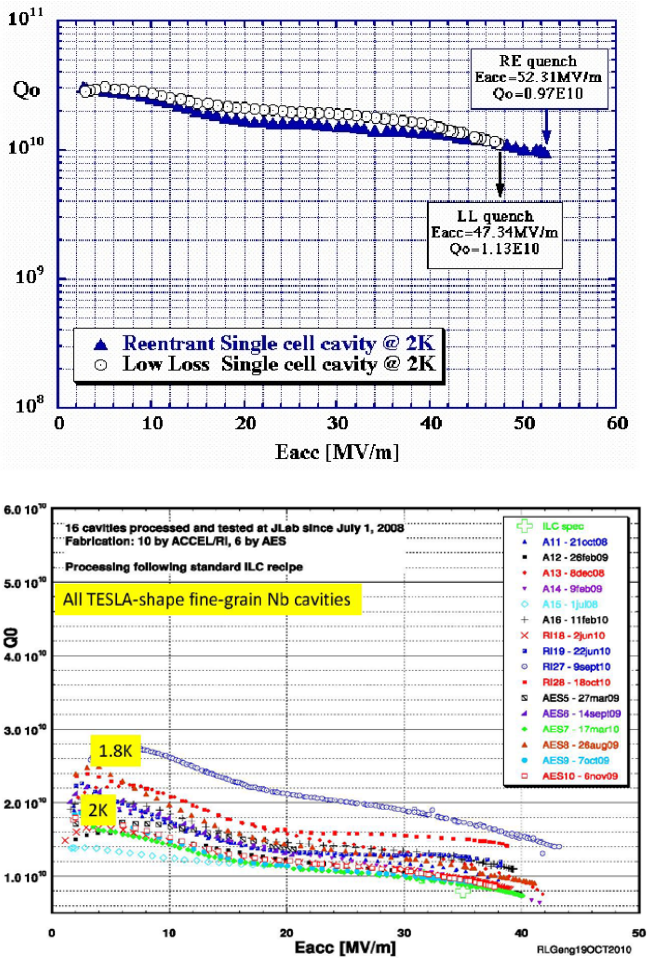

Figure I.2.1: Single cell cavity performance close to the de-pairing limit for bulk Nb (Top) and performance of TESLA-shaped 9-cell fine-grain niobium cavities prepared with 2010 best practices. [30] (bottom) with $E_{acc} = H_{pk}/30.5$.

commonly used cavity shape) allows for use of more efficient cavity shapes. The recent JLAB CEBAF upgrade with the C100 cavity demonstrates that shapes with 13-15% improvement in cryo-watts/MV are now accessible.

I.2.2.1 Surface chemistry and topography-dependent losses

The roughness of a SRF cavity surface can increase RF losses at high surface fields. Various surface treatments are implemented to achieve beneficial smoothness. Electropolishing (EP) rather than chemical etching (BCP) is now the standard process to obtain best-performing finished Nb cavity surfaces. Different treatments modify surface features at various lateral length scales with different mechanisms and rates. However, only recently have analyses begun to establish in detail how the specifics of topographical features directly affect RF performance. It is understood that sharp surface features promote magnetic field enhancement and may initiate local premature transition from superconducting to normal conducting state. Modeling simulations of microscopic field enhancements associated with characteristic BCP and EP surface topography and local Hc transitions have reproduced the non-linear losses that are associated with the high-field Q drop that distinguishes BCP-treated fine grain niobium from EP-treated cavities [31]. The consistent performance of the 80 cavities used in the CEBAF 12 GeV Upgrade cryomodules demonstrated that it is the topography left by the final surface

chemistry step that matters [32, 33, 34, 35].

I.2.2.2 120 °C bake and HF-rinse

The final step in the internationally recognized standard baseline cavity treatment protocol for producing high performance cavities (i.e. European XFEL, ILC-GDE R&D, CEBAF 12 GeV upgrade) is a 120 °C UHV bake for 24 to 48 hours. The 120 °C bake reduces the mean fee path of the electron to a desirable low value and also somewhat increases the energy gap, thereby reducing the BCS resistance by up to a factor of 2 (to ~8 nΩ at operating gradient, 2 K) [36, 63]. However, the 120 °C bake is also usually associated with an increase in residual resistance of a couple of nΩ, making the overall improvement in Q_0 less dramatic. This increase in residual resistance can be reversed reliably by an HF rinse, while maintaining the lower BCS brought by the 120 °C bake. The HF rinse removes the 2 to 4 nm thick oxide layer from the surface (which subsequently regrows), which appears to include the source of the increased residual resistance after the 120 °C bake. This beneficial procedure has been demonstrated on a variety of cavities yielding very low values of residual resistance of ~1 nΩ and thus very high quality factors [38, 39].

I.2.2.3 Multipacting

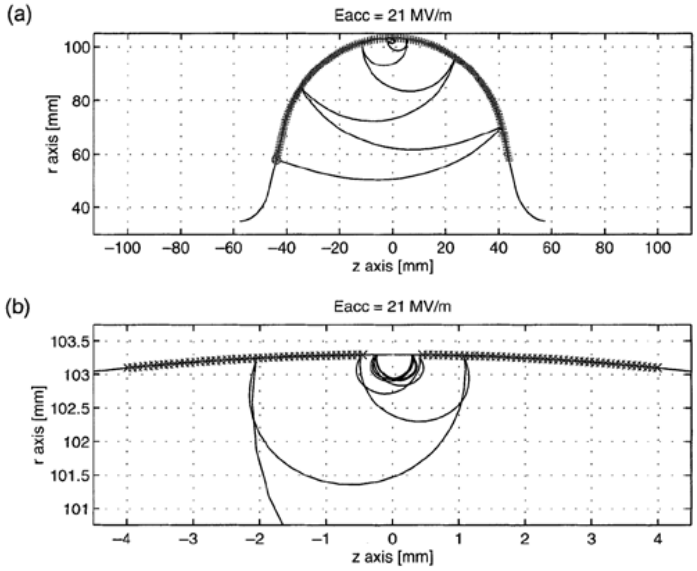

Figure I.2.2: Two-surface multipactor in the TESLA-shape cavity

In SRF cavities, stray electrons can hit the cavity surface, creating secondary electrons. The secondary electrons, which in turn, can be accelerated by RF fields, absorb the RF energy and hit the wall surface creating more secondary electrons. When these secondary electrons happen to hit the same area, the absorbed RF energy heats the surface, thus creating a local hot spot. This not only limits the accelerating gradient, but also creates more RF surface loss, even leading to a possible thermal quench. By adjusting the resonant cavity shape, the multipacting occurrence can be reduced but it can't be totally eliminated. For example, circumstances known to support a multipacting barrier exist in the equator region for the TESLA cavity shape [40]. The electron impact energy is typically low, on the order of 100 eV or less. For the ideal TESLA cavity shape, the center of the barrier is at E_{acc}=21 MV/m. The

boundaries of the multipacting barrier are determined by the secondary electron yield of the surface [41]. Small deviations of the cavity shape from the ideal elliptical geometry (such as the presence of weld underbead) can have dramatic effect on the multipacting occurrence [42].

Practically, multipacting is very sensitive to the surface condition because the secondary electron yield is a sensitive surface property. The local heating of the niobium surface due to electron bombardment can cause the cavity to quench. Although self-recovery after a multipacting induced quench is typical, additional magnetic flux, generated by the thermal current or previously expelled ambient flux, may become trapped in the cavity wall for each occurence [43]. Such additional frozen-in flux leads to an increased residual surface resistance and lower Q_0.

The residual presence of organics on the sensitive surface can dramatically enhance the multipacting occurrence and strength, especially if the design operation gradient is very close to the multipacting barrier.

I.2.2.4 Field emission

Field emission in SRF cavities is another phenomenon with detrimental effects including added heat load to cryogenics and limitation to achievable gradients [44, 45].

Electrons are emitted at highly localized emitter sites, typically where the surface electric field is the highest [46]. When the surface electrical field is strong enough for that small area, the electrons will start to tunnel out of the metal surface to form a steady current (quantum mechanical tunneling effect). The field emission current, described by the Fowler-Nordheim equation, increases exponentially with the surface electric field. A large fraction of field emitted electrons end up hitting the cavity wall, losing their energy in the form of heat, which is removed by evaporating liquid helium. The local temperature rise at the electron impinging site can exceed Tc, causing the cavity to lose the superconducting state (quench).

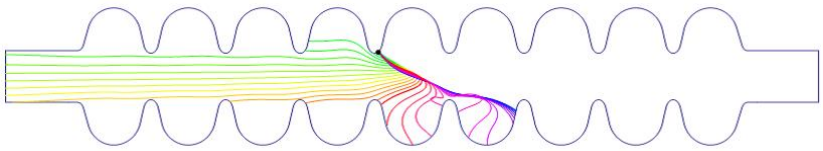

Figure I.2.3: Trajectories of electrons emitted from a cavity wall surface

Some fraction of the field-emitted electrons may move along the cavity axis without hitting its wall, escaping from one cavity and entering the next [47, 48, 49, 50, 51]. These electrons can potentially form a so-called "dark current" detrimental to the beam quality, produce Bremsstrahlung X-rays due to collision with the cavity wall or beam line components, produce energetic γ-rays (in the case of high energy electrons) which in turn produce neutrons through (γ,n) reaction, causing activation of beam line components.

There are a number of sources for field emitters, among them microscopic particulates. These particulates are randomly brought to the cavity surface during the different steps of its preparation (chemical, cleaning, and assembly processes). The significance and strength of electron emission under the RF electric field is highly dependent on the nature of field emitters [43].

Due to their small surface losses, SRF cavities are sensitive to parasitic losses due to field emission. The presence of field emission can severely degrade cavity performance, adding significant dynamic heat load at lower operating gradients.

Significant progress towards field emission elimination has been made in the past two decades with modern-day cavity processing, cleaning procedures [52, 53, 54, 55] and *in-situ* processing techniques for completed cryomodule [56], and helium processing [59, 58]. A detailed summary on the subject can be found in Ref. [21]. Although, "field emission free" vertical testing of SRF cavities is typically demonstrated, field emission can still be encountered in final cavity operation in cryomodules, which can be an issue especially for large-scale accelerators.

I.2.2.5 "Doped" Nb bulk cavities

Recently, a form of doping process have been applied to SRF cavities by diffusing a small concentration Ti and N resulting in RF behavior well described by the recently proposed RF BCS theory (see section I.1.6).

Nb is an excellent getter for various gases such as O, N, and H. Historically, solid-state gettering[1] with titanium (Ti) has been used to post-purify niobium as it has a higher affinity than Nb for these gasses. After the titanification of the niobium surface, several microns are chemically etched to remove the impurities gettered by surface-diffused titanium. This process is beneficial for the increase in RRR of Nb, thus improve the thermal stability of SRF cavities. Recently, a much smaller concentration of Ti (~1 at.%) was thermally diffused in a thin layer on the interior of SRF cavities. The Q showed an increase of a factor of 2 to 4 over the baseline chemically etched cavities (Fig. I.2.4) and with a peak surface magnetic field (Bp) up to ~ 90 mT[2] [59, 58].

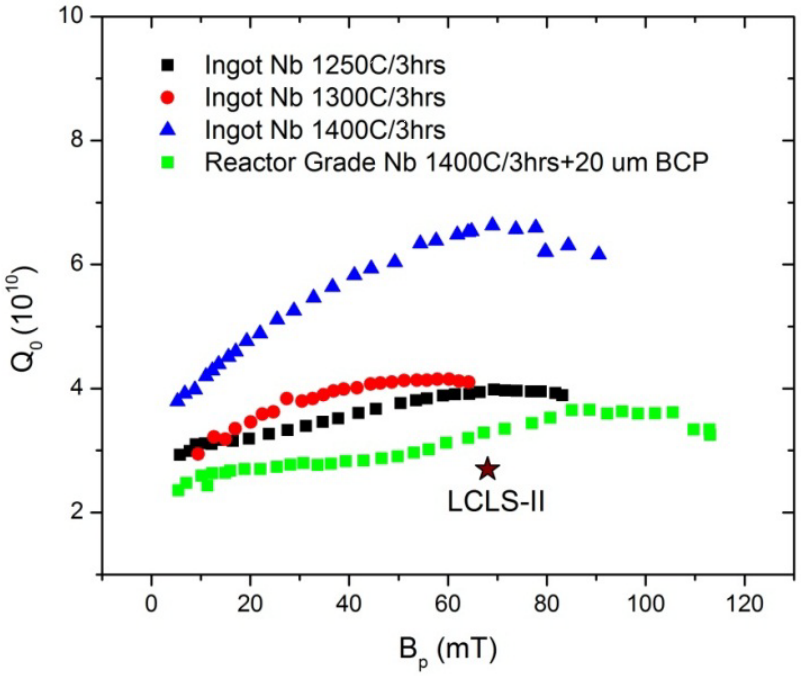

Figure I.2.4: Q_0(2 K) scaled to 1.3 GHz vs B_p for the ingot and reactor grade Nb 1.5 GHz SRF cavities heat treated in the temperature range of 1250-1400 °C.

A similar decrease of the typical residual and BCS resistances, both for single and multi-cell cavities has been reproducibly observed in different institutions by doping the Nb surface with a low concentration of nitrogen [61, 62, 63].The treatment brings improvements of up to a

[1] Solid state gettering is the evaporation of a substance or gettering agent, onto a desired surface, from which the agent may withdraw impurities.

[2] For reference, for a TESLA shaped 1.3 GHz cavity, at $E_{acc} = 16$ MV/m, $B_p = 70$ mT.

factor of 3 at 2 K and 1.8 K compared to standard treatments (figure I.2.5) leading to quality factors of up to ~ 9×10^{10} at 70 mT, 1.8 K. An increased frequency of limitation by quench at ~ 90 mT peak magnetic field was observed and was loosely associated with multipacting. Best initial results were reproducibly seen for a heat treatment at 800 °C for a couple of hours and then exposure ~ 20 mTorr of nitrogen still at 800 °C for 10 minutes, followed by a 7 micron surface removal by EP.

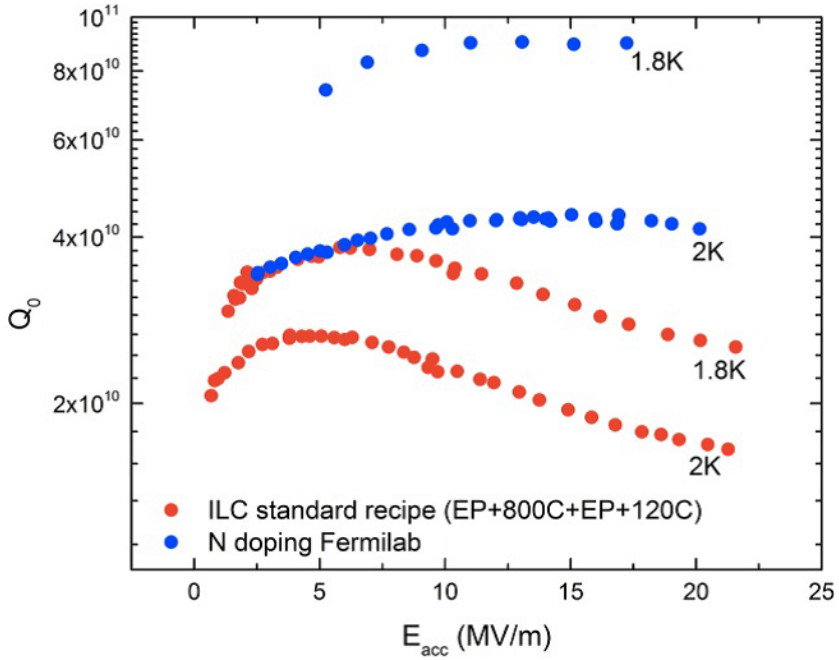

Figure I.2.5: Comparison of performance for a single cell nitrogen treated cavity and ILC R&D treatment at 2 K and 1.8 K.

A possible explanation for the increase of Q of these “doped” cavities with the increasing RF field is the effect of the broadening of the quasi-particle density of states induced by the RF current on the surface resistance in the so-called "dirty limit" ($l << \xi$) [64]. The reduction of the mean free path after the interstitial diffusion can be inferred from curve fits of $Q_0(T)$ data. The diffusion of impurities (N, Ar and Ti) on a cavity surface tends to reduce the RRR of the Nb and change the superconducting behavior towards the “dirty limit”.

I.2.2.6 RF losses from trapped flux

In an effort to exploit to the maximum the present performance of bulk Nb, laboratories are paying close attention to the measurement methods and the associated hardware.

Trapped magnetic flux represents one of the known contributors to the residual resistance R_{res} of superconducting radio frequency (SRF) niobium cavities [65]. For this reason, minimization of trapped flux in niobium cavities has recently been a topic of particular interest, especially in light of its potential impact on cryogenic costs of high duty factor accelerators, i.e., Linac Coherent Lights Source upgrade at SLAC National Accelerator Laboratory (LCLS-II), Energy Recovery Linacs, and a potential upgrade of the European X-ray Free Electron Laser (XFEL). Studies at Helmholtz-Zentrum Berlin (HZB) showed that the details of the cooling procedure affect the amount of trapped flux and thus its associated additional residual surface resistance [66, 67].

In order to derive the maximum benefit from improvements in BCS RF losses and reduction

of other contributions of residual resistance, one must minimize the magnetic field present at the cavity surface during the T_c transition and also manage the cooldown conditions which influence how much of the residual magnetic flux is expelled from the cavity and how much remains trapped in the superconducting surface [68, 69].

Permeability of material used for testing hardware such as end-flanges with RF probes [70, 71, 71], magnetic shielding of vertical dewars used for the RF performance test [72] and ambient magnetic shielding for cryomodules [73, 74], cooldown rate sensitivity [66, 68, 69, 75] and quench induced losses.

Chapter I.3

State of the art of Nb/Cu technology

Due to the very shallow penetration depth of RF fields (only ~40 nm for Nb), SRF properties are inherently a surface phenomenon, involving a material thickness of less than 1 micron. One can then foresee the merits of depositing an Nb film on the inner surface of a castable cavity structure made of copper (Cu) or aluminum (Al). At the system design level, this would exploit the freedom to decouple the active SRF surface from the accelerating structure definition and its cooling, opening the possibility to dramatically change the cost framework of SRF accelerators.

I.3.1 Advantages and disadvantages of Nb Thin Film Cavity

I.3.1.1 Thermal stability

Bulk niobium has a typical heat conductance of about 75 W/mK at 4.2 K if the purity is high, while, for copper, the value is as high as 300 - 2000 W/mK. For a typical hot spot inside a SC cavity, for example a 50 μm size defect, the amount of heat is about 10 mW if the RF magnetic field at the defect area is 400 Oe. It is very easy for the copper substrate cavity to conduct the excessive heat to the helium bath. A more accurate simulation using thermal breakdown model for defects inside the resonant cavity [76] sufficiently illustrates the effect of the defect's size and the niobium purity level (represented by RRR, residual resistivity ratio). As we have seen in the previous section, multipacting and field emission could cause problems to resonant cavities. The large thermal conductivity of copper helps the thin film cavity to be more resilient in those situations.

I.3.1.2 Low cost

The copper is much cheaper than niobium, about 10% of the cost of the niobium. The material itself is not the only cost advantage: it is widely believed that the manufacturing cost associated with copper can be substantially lower than that of niobium.

I.3.1.3 Insensitivity to earth magnetic field trapping

Residual resistance of the niobium surface is caused by many different sources. For an ideally cleaned cavity, the residual resistance can be caused by trapped magnetic flux, hydrogen dissolved in the surface layer, surface oxides and even some surface roughness.

Films showed a further unexpected advantage, in that their surface resistance is almost insensitive to the Earth's magnetic field.

As an order of magnitude the effect is 100 nΩ/Gauss of external magnetic field for bulk Nb, and only 1 nΩ/Gauss for films. This allows for the fabrication of much simpler and cheaper cryostats without the need of complex magnetic shielding of cavities [77, 21].

Dissolved impurities serve as scattering sites for the electrons not condensed into Cooper pairs. These impurities lower the thermal conductivity and thereby limit the maximum tolerable surface magnetic field before the thermal breakdown occurs. Interstitial dissolved impurities in niobium, such as oxygen, carbon, nitrogen or hydrogen have a strong effect on the thermal conductivity and decrease the critical temperature of niobium. For example, oxygen decreases the Tc of Nb by 1 K per *atomic*% [78]. Such losses are exponential and the decrease of the critical temperature with 1 K causes a drastic increase of dissipations.

I.3.1.4 Freedom from undissolved inclusions

During the pressing, rolling and melting, etc., the niobium sheet or the copper sheet will have some kind of micro-inclusions. Typical inclusions can be elements such as steel, nickel and some compound oxides. They do not necessarily decrease the RRR of the metal sheet, but they show up from time to time, even with vigorous etching.

Although they can be well controlled, they do increase the cost for better raw material and also the cost for extra processing during the cavity manufacturing. One simple example is that the inclusions are very easily introduced to the niobium sample from machine tools [79]. Although this kind of inclusions can be etched away, the inclusions caused by precipitation during cooling process can be deep inside the niobium material. That can happen when the amount of some compound dissolved while the Nb is molten exceeds the solubility during cooling. Vacuum deposition of thin film is known to produce excellent surface quality except the possible degradation of performance due to the increased BCS surface resistance.

I.3.1.5 Non-Quadratic RF Losses

At 1.7 K, the BCS component of the surface resistance reduces exponentially and the residual term remains dominant. Although of comparable order of magnitude between sputtered film and bulk at zero-field, the residual resistance had a stronger increase with field in the case of films (see figure I.2.12), thus showing a "slope" in Q (*Q-slope*). This Q-degradation caused by the increased external RF field actually exists in both bulk niobium and in thin film cavities but for the latter, it limits the cavity operation to low field. This anomalous RF loss is known as the *Non-Quadratic Loss (NQL)*, as named by Durand and Weingarten in their pioneer work [80].

Some models predict that such Q-slope is inherent to Nb films due to the limited electron mean free path compared to bulk Nb. This should manifest either in a reduction of H_{c1} and thus nucleation of so-called Abrikosov fluxons [81] in a rather low RF field, effect possibly enhanced by demagnetization due to surface roughness (see section I.3.1.8). Other models suggests that the *Q-slope* could manifest itself in a depression of the superconducting gap due to a reduction of the critical superfluid velocity [82, 84], inducing a direct increase of R_{BCS}. Both phenomena are observed in Nb films. However the estimation of the relevance of one or the other is a priori difficult. It is then of ultimate importance to study in depth the film material properties and their influence on the films RF performance.

I.3.1.6 Impurities

A certain number of impurities can be found in Nb thin films mainly due to the deposition process and the affinity of Nb for O and H. These impurities can then present themselves as scattering centers and then induce RF losses.

In the commonly used magnetron sputtering technique, a sputtering or carrier gas has to be used. Therefore, atoms of this gas are embedded in the film. CERN conducted detailed investigations [74] of the quantity of gas embedded in Nb/Cu films (for Ar, Kr, Xe, Ne and mixtures) and the effect on their SRF performance. The best cavity performances were achieved for films deposited with Kr (See figure I.3.2 further).The quantity of Kr in these films was two orders of magnitude lower than Ar (400 ppm versus 10 ppm).

Hydrogen is found to be a primary source of losses in bulk Nb cavities. Similarly, hydrogen trapped in Nb films is a possible cause of Q degradation. The largest sources of hydrogen are the outgassing from the Nb cathode and the Cu substrate during the deposition process and, of course, the residual hydrogen in the vacuum system. The Nb film hydrogen content and its binding state have been measured at CERN for different coating procedures [85, 86]. Despite the efforts to eliminate the hydrogen sources [87] and the use of non-evaporable getters (NEG) [88], hydrogen reduction was unfortunately not effective.

Though still subject to discussion, oxygen is another suspected source of RF losses [89, 90]. In their analysis of CERN's Nb films data [91], Malev and Weisser proposed that the stimulated desorption mainly contributes to the oxygen and carbon oxide partial pressure to 10^{-7} mbar during the argon discharge sputtering [92]. However, several analyses show that no concentrated oxygen migrate to the grain boundary and the interface of the thin film and its substrate [80].

I.3.1.7 Roughness

Thin films typically replicate the substrate morphology. thus the roughness of the substrate has a strong influence on the roughness of the film. Shadowing effects during film growth may lead to poorly connected Nb film grains, possibly enhanced by a non-normal angle of incidence [93]. Granularity effects have always been seen as a major source of problems in literature, due to possible losses in weak-links [94] or easier penetration of (Josephson) fluxons [82].

I.3.1.8 Inter-grain losses

Another potential source of RF losses is inter-grain losses, a basic effect for fine-grained superconductors. Counter evidence for this mechanism comes from the fact that films grown on oxidized copper have a grain size of 100 nm, but when grown on an oxide-free surface the grain size is of the order of micrometers. However, larger grain sizes do not seem to have any effect in decreasing the Q-slope. Other possibilities are impurities in the film and surface roughness. Irregularities on the substrate can result in film inhomogeneities. The intrinsic defects are believed to be conducting nanometer size junctions which decrease the critical magnetic field of the superconducting thin film and are similar to the intra-granular weak links in the superconductor [80]. The intrinsic defects are also believed to trap the RF magnetic flux contributing significantly to the NQL. To this day, there is no strong evidence showing the presence of O in these intrinsic defects.

I.3.2 State of the art for Nb/Cu coated cavities

Superconducting cavities produced by the magnetron sputtering technology have been successfully used at CERN, and are also employed in several other present or future accelerator facilities, such as ALPI (INFN,Legnaro, Italy) or SOLEIL (St-Aubin, Gif-sur-Yvette, France) for acceleration. Recently a project of sputtered QWR at the China institute for Atomic Energy and then, at CERN, for SOLEIL, started. There are clearly defined sets of accelerator machine parameters where films show a clear advantage compared to bulk niobium, in particular for low frequencies or for operation at 4.2 K. Niobium films have however not yet achieved their potential ultimate performance.

Several innovative developments in coating technology are however under study which may reveal an important path forward. A first simple step towards improving film quality is adding a bias to the classical magnetron configuration for having an ion bombardment during film growth. This should produce smoother films and has been first tested at CERN with no significant changes in RF performance. A further possibility is to create the film using Nb ions, instead of neutrals as in sputtering, attracted to the substrate by a bias, thereby allowing conformal deposition with a normal angle of incidence all along the cavity profile and thus suppressing any shadowing effect during the film growth. The most promising techniques have been selected by different institutions and are under development.

I.3.2.1 Sputtered cavities

CERN LEP-2, LHC experience and R&D on 1.5 GHz Nb/Cu magnetron sputtered cavities

CERN has conducted pioneering studies [1, 2, 3] in the field of SRF Nb films on Cu (Nb/Cu) applied to cavities and successfully implemented this technology in LEP-2 and LHC accelerators.

The LHC machine relies on 16 low impedance Nb/Cu single cell cavities [3]. Good Q vs. E performance curves (figure I.3.1) for LHC cavities [65]

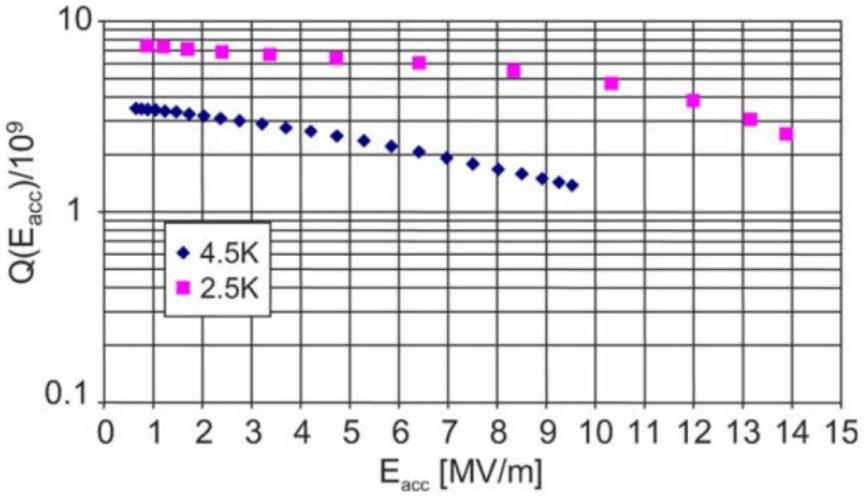

Figure I.3.1: RF performance of LHC cavities

Although 1.5 GHz cavities achieving gradients up around 25 MV/m [4] were produced, these cavities suffered from significant losses resulting in the significant reduction of Q at

accelerating gradients above 15 MV/m. Some of the defects were inherent to the magnetron sputtering technique used to produce these cavities.

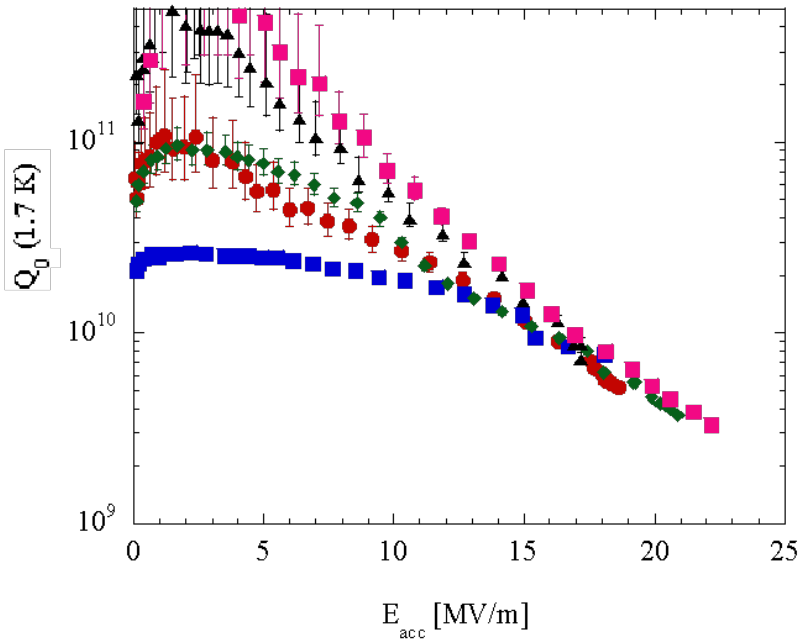

Figure I.3.2: Best RF performance of 1.5 GHz Nb/Cu cavities sputter coated with Kr at CERN

All of these cavities exhibit an increase in Q at very low accelerating field and one cannot help but compare this behavior to the one recently observed for doped bulk Nb cavities and the prediction from the Xiao's extended BCS theory as reported in chapter I.1.

HIE-ISOLDE diode sputtered cavities at CERN

The new HIE-ISOLDE accelerator at CERN requires the production of 32 superconducting cavities (20 high- β and 12 low- β) in order to increase the energy of the rare isotope beam delivered to the experiments [95, 96].

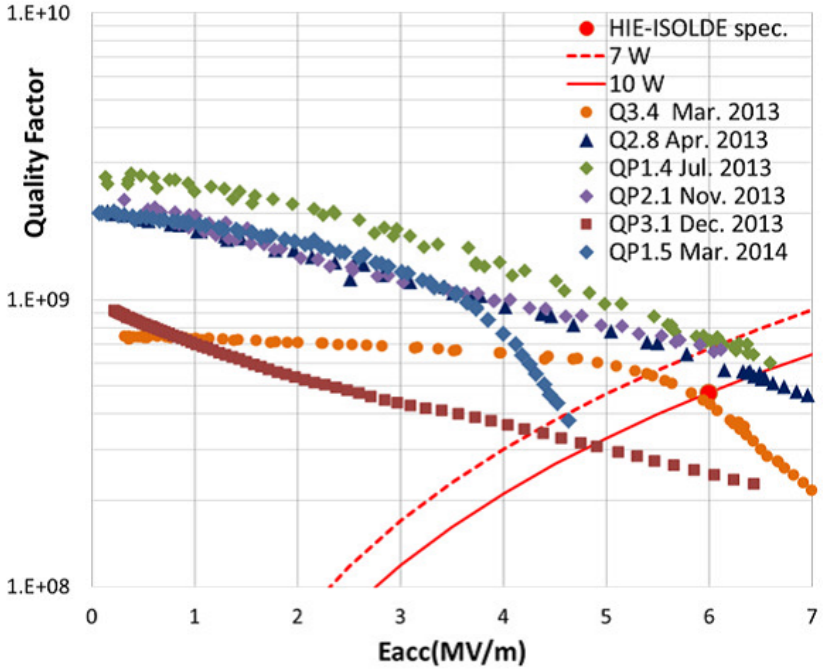

Figure I.3.3: RF performance of HIE-Isolde cavities from [96]

INFN Legnaro ALPI Experience with DC bias sputtered quarter-wave resonators

ALPI is a superconducting linac for heavy ions, in operation at INFN Legnaro (Italy) since 1994 [97]. Originally the sputtered medium β cavities installed in ALPI were Pb plated and only later they were renewed by substituting the original metal coating with a Nb layer deposited by DC bias sputtering.

Since the very beginning of the ALPI project two R&D programs were launched, one on the sputtering of Cu bases with Nb and the other on the realization of bulk Nb cavities [98]. These programs, which proceeded in parallel, brought ALPI to the outstanding result of an accelerating field of higher than 6 MV/m in 1993.

Given the success of the R&D, it was decided, in the second phase of ALPI, to build the higher β section with the Nb/Cu technology. By means of new design details, along with a careful and long setup of the delicate sputtering procedure, the first results were confirmed and exceeded in a number of tests, showing an average accelerating field off-line $E_{acc}>$ 6-8 MV/m at $P_{dissipated}$ = 7 W (with Q0 >6-7x108 at the high field values). The technology has been applied to on-line resonators.

52 quarter wave Nb/Cu resonators (figure I.3.4 from [98]) are currently installed and the success of the development of higher β cavities opened the possibility to apply the sputtering technique to the medium β section as well. By replacing the original Pb layer with a sputtered Nb film the accelerating field exceeds 4 MV/m at 7 W dissipated power.

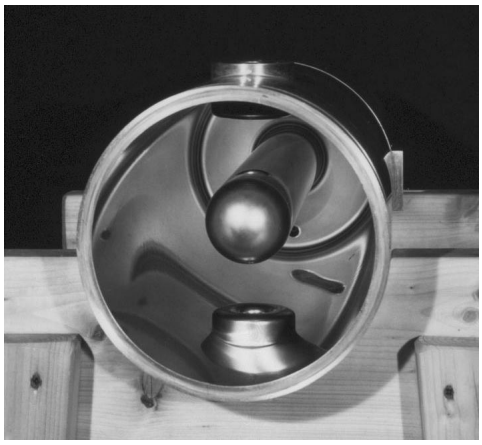

Figure I.3.4: High β Quarter Wave sputtered Resonator reaching 7 MV/m.

I.3.2.2 Vacuum arc coating

INFN Roma and Soltan Institute collaboration

INFN "Roma II" and the Soltan Institute for Nuclear Studies (Poland) formed a few years ago a collaboration to investigate the feasibility of a vacuum arc deposition technique for Nb/cu cavities [99, 100]. In this coating technique (see section II.3.3.2), an electric arc is established over the cathode's surface by a suitable trigger (high voltage or laser pulse). The arc is sustained by an adequate power supply, with the plasma plume containing Nb atoms at such a high density that they are fully ionized. The technique provides a high coating rate, and of course the coating flux can be attracted at the desired energy towards the substrate.

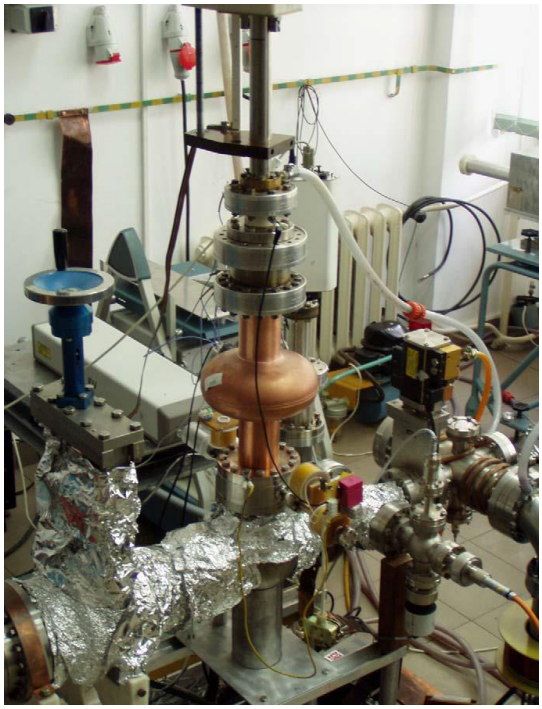

Figure I.3.5: Arc deposition systemm for the ARCO project [99].

A strong disadvantage is however the formation of macro-particles because of the explosive nature of the process. Magnetic filtering and steering of the ion flux is then needed, in order to

remove macro-particles from the flux and to obtain a defect-free coating, adding complexity to the coating system [101]. Nb coatings have been performed on Cu samples and have been fully characterized. An important difference of "energetic" coatings compared to sputtered films is the absence of preferential orientation of the crystallites, whose growth in the case of sputtering is instead dominated by the lattice free energy resulting in a (110) texture. The crystallites are several microns in size, compared to a few hundred nm in the case of sputtering, and completely free from defects and strain, which are major sources of electron scattering in sputtered films. In addition, the depositing energy varies from 10-100 eV. The transition temperature ranged randomly from 8.7 K to 9.26 K [102]. However, the best result on small samples could not be reproduced on larger surfaces.

A filtered UHV arc coating system for RF cavities, using two symmetrical cylindrical arc sources, somewhat similar in geometry to the standard DC magnetron system (figure I.3.6-ARCO cavity deposition system), was built and a couple cavities were coated [244].

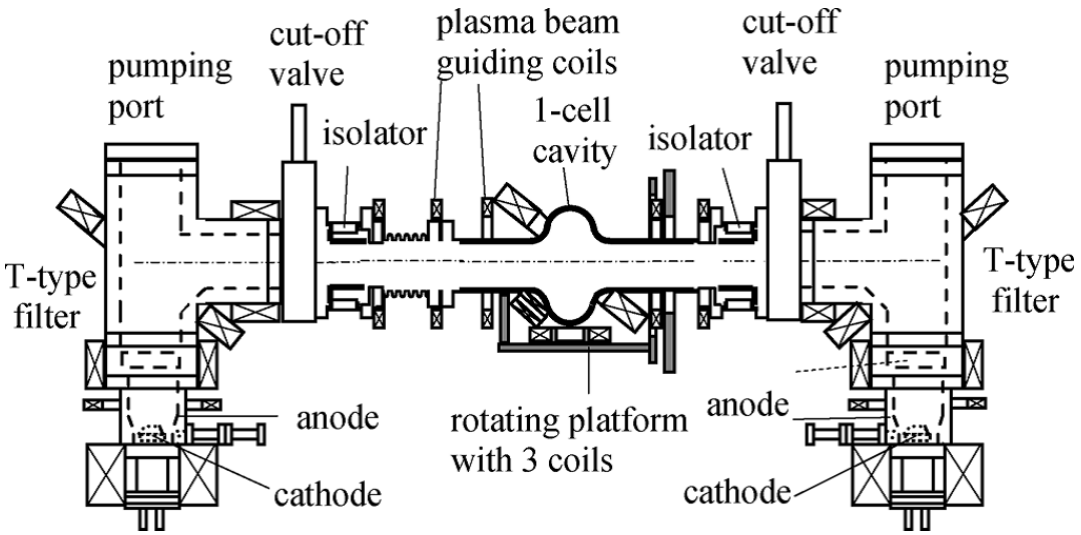

Figure I.3.6: Schematic of the ARCO cavity deposition system equipped with two filtered arc sources.

Coaxial energetic deposition at Alameda Applied Science Corporation

A similar technique, named coaxial energetic deposition (CED^{TM}), has also been implemented by a company in California, Alameda applied sciences, Inc. (AASC). As part of a collaboration with JLab, high RRR Nb films on small samples, mainly MgO, have been produced [104]. First trials on cavities have been performed without much success. These coated cavities suffered from significant delamination of the film from the substrate [105, 106].

I.3.2.3 HiPIMS development for Nb/Cu cavities

HiPIMS is an array of deposition techniques which is seeing extensive development in the industry. The characteristics of the produced films can be of great benefit in the development of Nb film coatings for SRF application (see section II.3.3.3). Beyond Jefferson Lab, Lawrence Berkley National Laboratory (LBNL) and CERN are applying this technique to SRF cavities.

LBNL

The HiPIMS process has been the object of extensive plasma studies applied to a variety of materials at Lawrence Berkley National Lab (LBNL) in the group of Andre Anders [107, 108].

Various experiments are carried out in a general-use chamber to explore the plasma physics and characteristics of the HiPIMS process, especially applied to Nb and other SRF materials. The possibility of "gasless" self-sputtering [109] of Nb, i.e. a HIPIMS mode in which the sputtered atoms satisfy the need for a process gas was explored. Thus no argon (Ar), krypton (Kr) or any other gas is needed, eliminating the issues related to noble gas inclusion, which is a big progress compare to sputtering. Such "gasless" self-sputtering has been demonstrated for HIPIMS using high sputter yield materials such as copper [110]. In the case of Nb [111], the sputter yield is not sufficient to produce enough "niobium gas". Rather, noble process gas is always needed to obtain HIPIMS pulses. This leaded into the exploration of the minimum pressure needed to obtain a HIPIMS Nb discharge [112]. It was found that, due to some "residual plasma" of the previous pulse, the pulse repetition rate is an important parameter that allows pressure reduction while still maintaining a stable and reproducible operation.

Another recent development of the HiPIMS process consists in superimposing a Mid Frequency (MF) discharge in between the HiPIMS pulses to lower the frequency pulses of the HiPIMS pulses. Though they do not depend on MF pulse pattern, the HiPIMS pulses can be spaced as far (or close) in time as desired as long as the MF discharge is present. Conditions are found where the species in the plasma are largely dominated by Nb^+ [113].

Sample studies are in progress for Nb films deposited on Cu and Al. The characteristics such as crystal structure, adhesion to the substrate, T_c, RRR are investigated [111] in the framework of a collaboration between LBNL, ANL and JLab.

In parallel to the exploration of HiPIMS process for the development of SRF materials, a cavity dedicated deposition chamber was designed and built (figure I.3.7). The system is composed of a set of two, movable cylindrical magnetrons, sized for 1.3 GHz cavity deposition. The two magnetrons are mounted on movable arms, as shown on top in figure I.3.7, to uniformly coat the inside of the cavity while slowly traveling through it. Their travel is synchronized by computer-controlled stepper motors. The use of two magnetrons allows the option of biasing the cavity for film optimization. The concept is to use one target as the cathode, and the other as the anode. The polarity of the targets is alternated at a frequency typical for HIPIMS. As a result, the cavity does not participate in the discharge process and can be biased using another, independent power supply. Additionally, the deposition rate can be doubled by using each of the magnetrons at its maximum power rating. This leads to a shorter process time and a reduced incorporation of residual gas contaminants. No cavities have been produced yet.

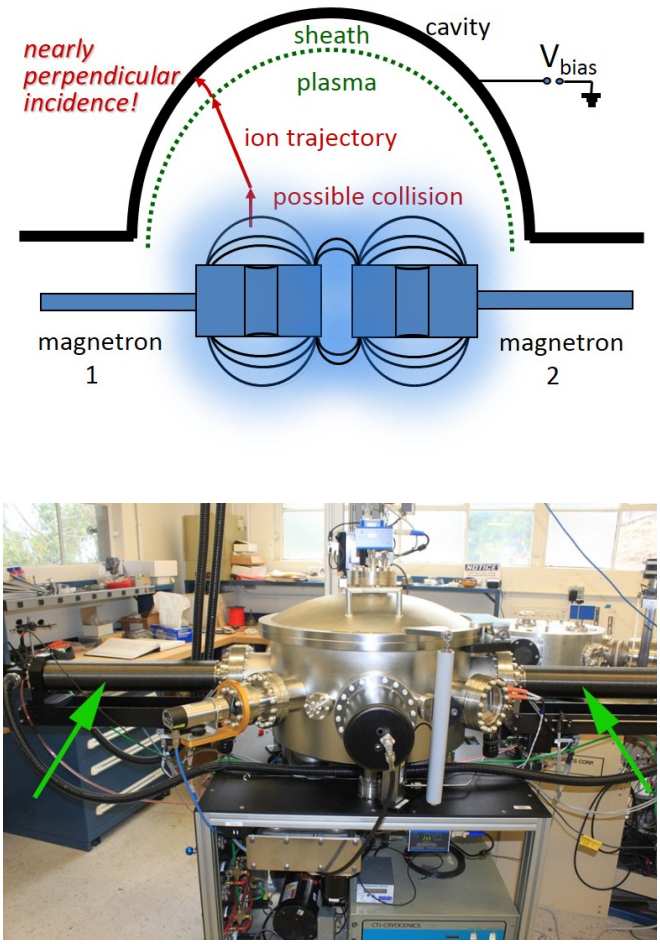

Figure I.3.7: LBNL dual magnetron HiPIMS deposition chamber dedicated to the coating of 1.3 GHz cavities with niobium [111].

CERN

CERN in collaboration with Sheffield Hallam University is conducting studies on HiPIMS plasma with Nb [114] and developing the technique for the coating of 1.5 GHz Nb/Cu cavities.

The HiPIMS coating system described in details in [115] has a vertical cylindrical magnetron configuration (Fig. I.3.8). It is built on the basis of the DC cylindrical magnetron coating system for 1.5 GHz Nb/Cu cavities used in previous studies [74]. It is an all-metal UHV system with the cavity being part of the vacuum system. The base pressure of the system is in the 10^{-10} - 10^{-11} mbar range. The cavity beam pipes are coated in sequential steps by DC magnetron sputtering (dc-MS), while the cell is coated either by HIPIMS or by dc-MS. The coatings are performed in a 10^{-3} mbar range Kr atmosphere.

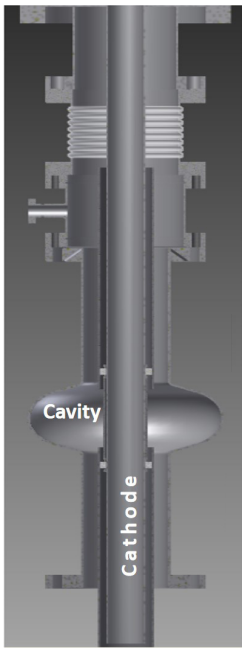

Figure I.3.8: HiPIMS cavity deposition system used at CERN

Some 1.5 GHz Cu cavities have been coated with both HiPIMS and dcMS. figure I.3.9 represents the quality factor curves at 4.2 K and 2.1 K for a dc-MS cavity and HiPIMS cavity, both coated with Kr. These preliminary results show an improvement in the performance of Nb films coated by HiPIMS compared to dc-MS.

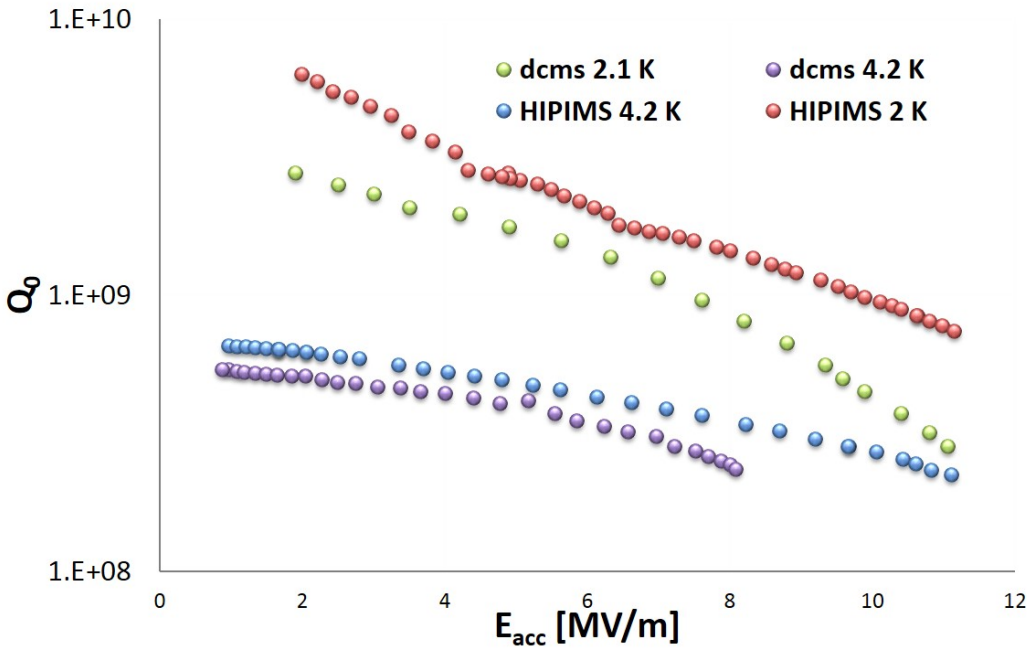

Figure I.3.9: Quality factor of two elliptical single cell cavities, produced by dc-MS and HIPIMS sputtering

Chapter I.4

Materials beyond to Nb

As seen in Chapter I.2, SRF cavities using Nb are reaching RF performances approaching its theoretical limit ($H \sim H_c\,(0) \sim 200$ mT) [5].

Achieving the magnetic field limitation means that no further increase in the accelerating electrical field of bulk Nb cavities can be expected. For further improvement of cavities RF performance, some innovation is needed and one may have to turn to other superconducting materials. The potential benefits of using other materials than Nb would be a higher T_c, a potentially higher critical field H_c, leading to potentially significant cryogenics cost reduction if the cavity operation temperature is 4.2 K or higher. If the thin film route is chosen, the use of substrates with higher thermal conductivity could also lead to substantial cost reduction in cryomodules fabrication (for example, easily castable aluminum or copper, reduction in microphonics).

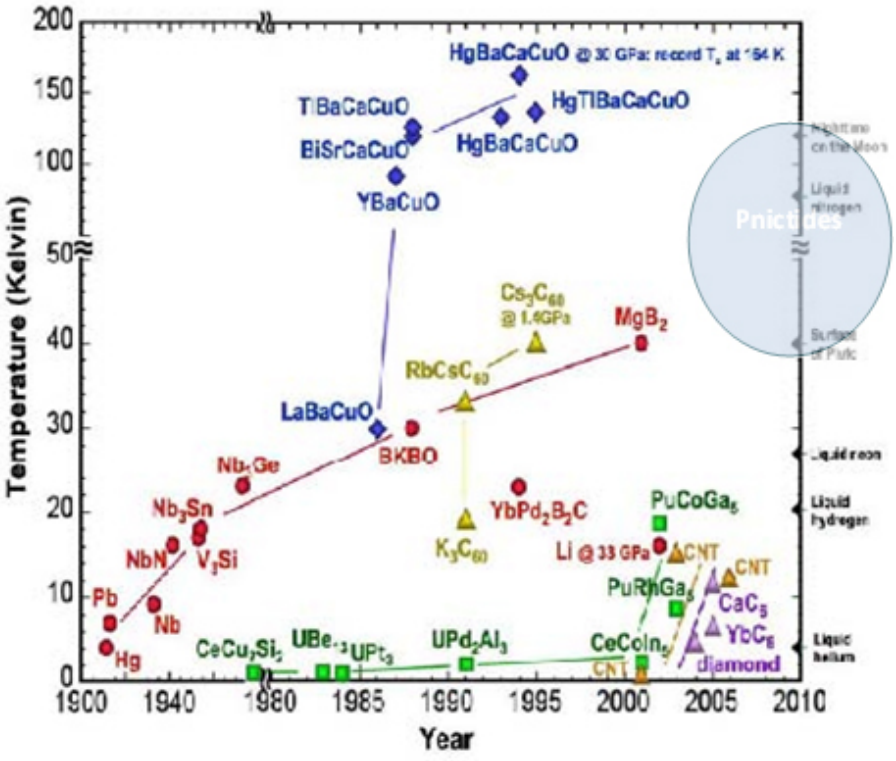

Figure I.4.1: Superconductors transition temperature T_c versus their year of discovery

The realm of superconducting compounds (see figure I.4.1) has been much less explored in the past because of technical complexities that govern compound formation. In looking at candidates, it is important to select a material for which the desired compound phase is stable over a broad composition range. For further improvement of RF cavity performance for future accelerator projects, research interest is renewed towards alternative materials to niobium. This chapter is dedicated to the description of potential candidate materials that can be used as an alternative to Nb.

As seen in section I.1.5, the criteria for a superconducting material to be a good candidate for SRF application i.e. low surface resistance are:

A large superconducting gap Δ, thus a high T_c

A metallic behavior ie a low normal resistivity ρ_0.

A high H_c or H_{sh} and a small GL parameter κ .

Among the thousands of known conventional superconductors, only a limited number of compounds have a critical temperature higher than Nb and present a potential as candidate materials for SRF cavity applications (cf. Table I.4.1). A comprehensive review of the different classes of superconductors for cavity applications has been given by Palmieri [28] a few years ago.

In equation I.1.34, the dependence of R_{BCS} on ρ_n and T_c represents an immediate criterion for selecting the potential candidates for SRF cavity applications. The nomogram represented in figure I.4.2 can then be constructed for different materials at 4.2 K, 500 MHz and for a strong coupling factor of 4 [116]. Materials with different T_c and $\rho_n$having the same $R_{BCS}$are represented by the dotted lines.

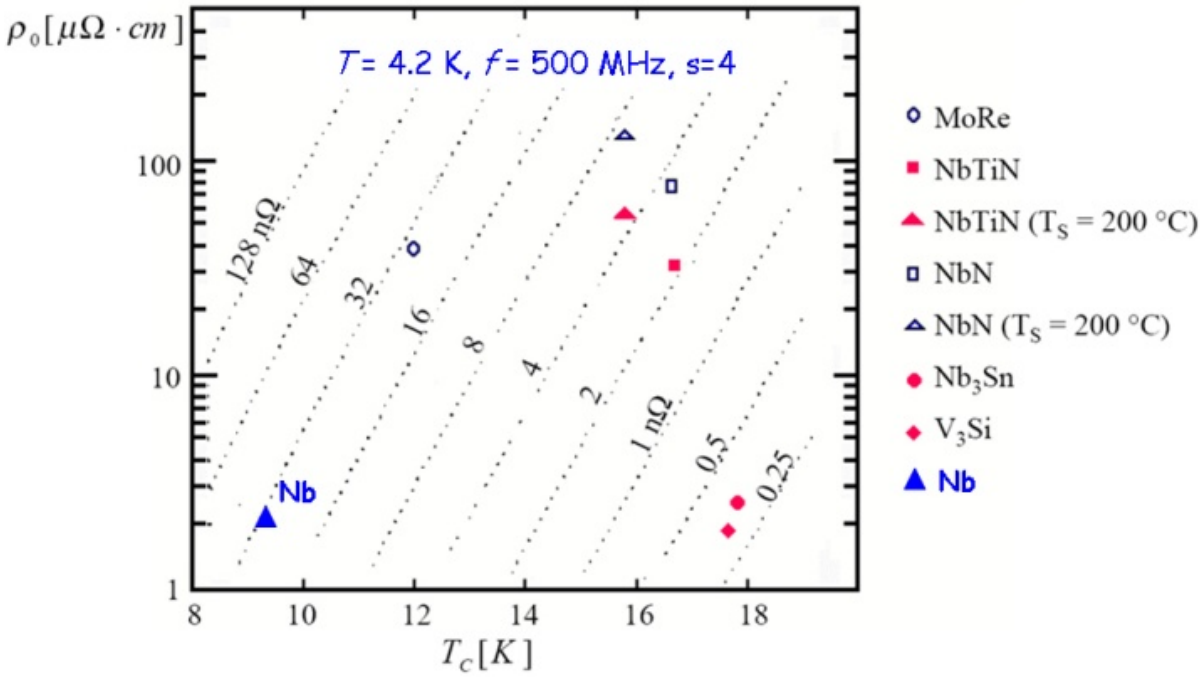

Figure I.4.2: Nomogram calculated for different materials at T=4.2 K, f=500 MHz and s=4 [116]

Table I.4.1: Some superconducting parameters for materials considered for SRF applications.

Material	T_c [K]	$\rho_n(\mu\Omega cm)$	$H_c(0)$ [T]	$H_{c1}(0)$ [T]	$H_{c2}(0)$ [T]	λ [nm]
Nb	9.2	2	0.2	0.17	0.4	40
NbN	16.2	70	0.23	0.02	15	200
NbTiN	17.5	35		0.03		151
Nb_3Sn	18.3	20	0.52	0.04	30	135
V_3Si	17		0.43			
Mo_3Re	15		0.43	0.03	3.5	140
MgB_2	39	0.1		0.03	3.5	40

I.4.1 Nb COMPOUNDS

B1 compounds have a NaCl structure where metallic atoms A form a face centered cubic (fcc) lattice and non-metallic atoms B occupy all the octahedral interstices (figure I.4.3).

These compounds are characterized by the fact that they always have a certain amount of vacancies, usually distributed randomly throughout the lattice [117]. The superconducting properties of B1 compounds are very sensitive to deviation from stoichiometric composition.

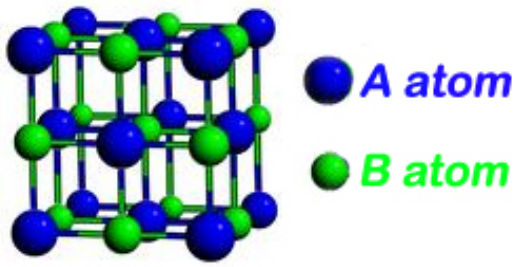

Figure I.4.3: NaCl Structure

Among all the B1 compounds found to be superconductors, only a few nitrides and carbides of the IV, V, VI group transition metals have T_c higher than Nb, as reported in figure I.4.4

B \ A	Sc	Y	La	Ti	Zr	Hf	V	Nb	Ta	Cr	Mo	W	Re
B					3.4	3.1							
C	<1.38	<1.38		3.42	<0.3	<1.20	0.03 3.2*	12	10.35		14.3	10.0	3.4
N	<1.38	<1.4	1.35	5.49	10.7	8.83	8.5	17.3	6.5	<1.28	5.0	<1.38	
P			<1.68										
Sb		<1.02	<1.02										
O				2.0			<0.3	1.39					
S	<0.33	1.9	0.87		3.3								
Se	<0.33	2.5	1.02										
Te		2.05	1.48										

* T_c = 3.2 K was registered in vanadium carbide after implantation of C^+ ions

Figure I.4.4: T_c of B1 compounds [117].

I.4.1.1 NbN

NbN is one of the B1 binary compounds with the highest critical temperature. For this reason, it has been widely tested for SRF cavity applications.

The phase diagram of the binary system Nb-N up to N/Nb=1 includes many different phases [118, 119]. The B1-NbN superconducting phase of interest is the cubic δ-phase for which T_c=17.3 K and the lattice parameter is 4.388 Å. This phase is only thermodynamically metastable at room temperature. T_c is very sensitive to nitrogen stoichiometry.

Various attempts have been made to produce NbN cavities by thermal diffusion [120, 121, 122] or reactive magnetron sputtering. For NbN made by thermal diffusion of N into Nb at 1400 °C followed by rapid quench cooling, surface resistances of 1.3 x 10^{-6} Ω and 1.3 x 10^{-10} Ω were calculated from TE_{011} measurements at 7.9 GHz and respectively at 4.2 K and 1.8 K [123].

NbN was produced by reactive magnetron sputtering [124], even when deposited at relatively low temperature (600 °C), with good superconducting properties (T_c=17 K), a low secondary emission coefficient and very stable surface properties. However, the resistivity of NbN in the normal state was found to be anomalously high (see figure I.4.5) and the residual resistivity ratio (RRR) is very low (~1).

In sputtered films, the δ-phase is often found to be mixed with other phases. The films are columnar, with grains weakly bounded, and separated by strong boundaries consisting of voids, normal conducting areas of Niobium and Niobium-dissolved gas composite phases. Even with no grain boundaries and only the δ-phase present, the resistivity is not so low due to the presence of both metallic and gaseous vacancies randomly distributed in both sublattices, in amount of 1.3% respectively. The equiatomic composition is not $Nb_{1.0}N_{1.0}$ but $Nb_{0.987}N_{0.987}$.

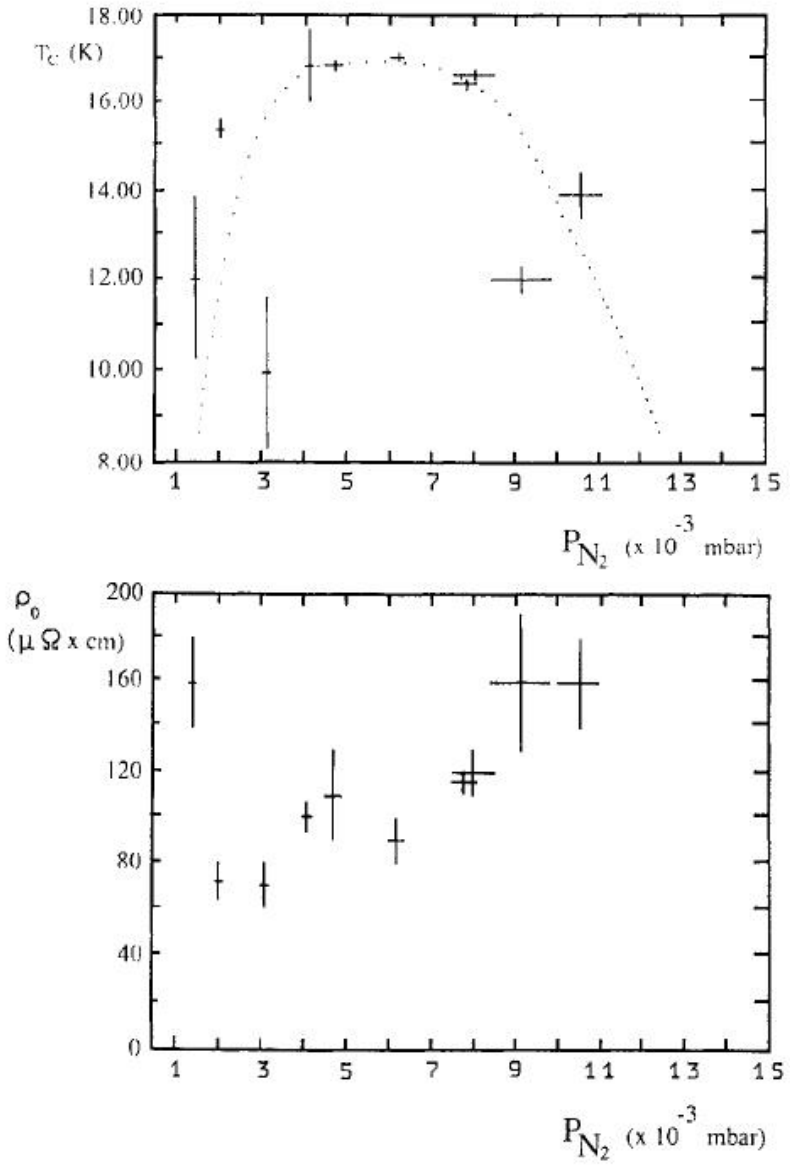

Figure I.4.5: Tc and Resistivity ρ_0 in the normal state as a function of N_2partial pressure P(N_2) for NbN films produced by reactive magnetron sputtering [124].

I.4.1.2 NbTiN

The ternary nitride NbTiN presents all the advantages of NbN but shows more metallic electrical conduction properties with higher titanium (Ti) percentage. Ti is a good nitrogen getter, so the higher is the Ti composition, the lower is the number of vacancies. In contrast with NbN, the B1-TiN phase is stable at room temperature (T_c=5 K and a=4.24 Å). The two nitride phases are completely miscible [125] resulting in a superconducting ternary NbTiN cubic phase which remains thermodynamically stable at room temperature. T_c is slightly higher (17.8 K) but as for NbN, N stoichiometry is critical to obtaining the right superconducting phase.

The commonly used techniques to produce NbTiN are reactive diffusion of NbTi sheets by high temperature heating in nitrogen atmosphere [123, 125] and reactive sputtering [126]. Figure I.4.6 shows T_c and the low-temperature normal resistivity as a function of Ti compo-

sition for NbTiN samples produced by reactive sputtering in Ar/N_2 mixture in a DC Triode Magnetron Sputtering system at 600 °C and 200 °C [127]. The resistivity is found to be lowered with an increasing Ti content.

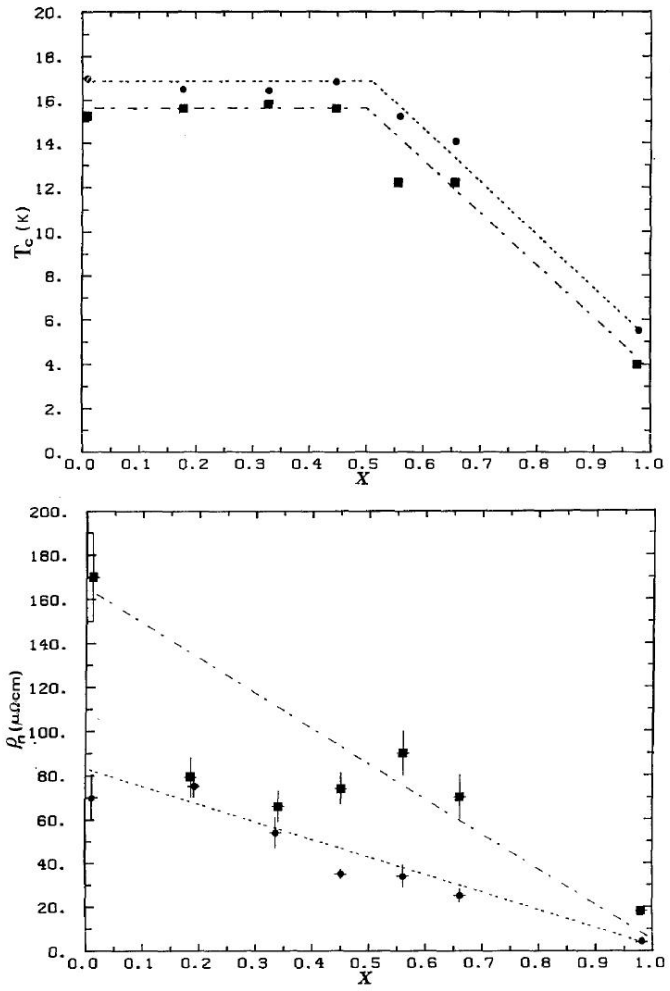

Figure I.4.6: T_c and low-temperature normal state resistivity as a function of the Ti composition X for $(Nb_{1-x}Ti_x)N$ films deposited at $T_{substrate}$=600 °C [126].

NbTiN films were also deposited on copper disks by reactive magnetron sputtering and tested at 4 GHz in a cylindrical TE_{011} cavity at CEA Saclay [128, 129]. The best results show RF fields levels of 35 mT, a low surface resistance (<50 nΩ at 1.6 K) with a small BCS resistance. Additionally, it was observed that the surface resistance decreases when the coating is performed with a bias voltage from -50 V to -100 V. Some attempts were made to deposit 1.5 GHz Cu cavities but no RF measurements were performed due to film blistering on a large area of the cavities.

NbTiN was also investigated at CERN [130, 131] on samples and 1.5 GHz Cu cavities coated by reactive cylindrical magnetron sputtering. The best cavity results were obtained for a thicker film (4.3 μm) and a lower deposition temperature (265 °C). The measured surface resistance was 330 nΩ at 4.2 K, with a Q-value at zero field higher than for bulk Nb cavities. However the maximum accelerating field was limited under 10 MV/m.

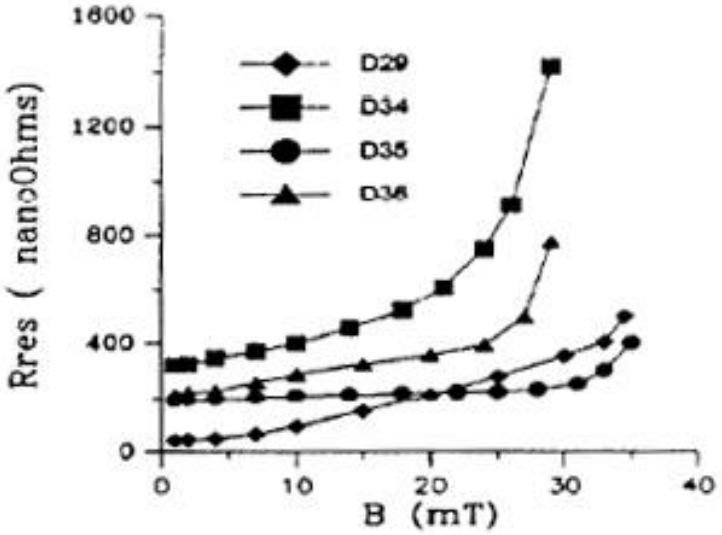

Figure I.4.7: Surface resistance measured at 4 GHz an 1.6 K for NbTiN/Cu films deposited by reactive magnetron sputtering.

I.4.2 A15 compounds

On the basis of the criteria enunciated earlier, some compounds from the A15 class appear to be promising.

A15 materials were first discovered to be superconducting when Hardy and Hulm found that V_3Si had a transition temperature of 17.1 K. In the following year, Nb_3Sn was also discovered with a T_c of 18.1 K by Matthias. These compounds structure is classified as the W_3O or Cr_3Si type. The stoichiometric composition is A_3B: B atoms forms a bcc crystal structure while A atoms arrange themselves in rows parallel to the three crystallographic directions [100], [010], [001].

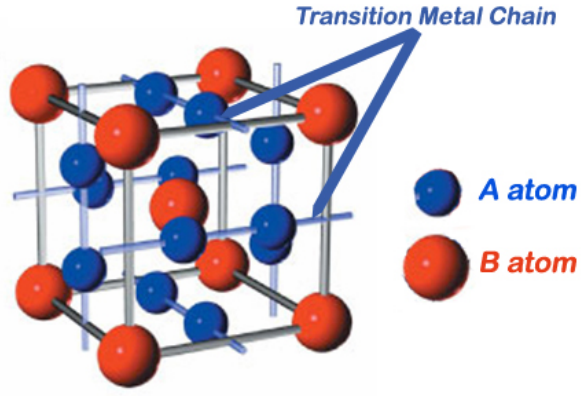

Figure I.4.8: A15 Structure with A_3B composition

The superconducting parameters of most A15 compounds are strongly influenced by the Long-Range crystallographic Order (LRO) degree. All what can affect the LRO must be carefully taken into account. Only a few of these compounds may have a practical interest for RF applications: Nb_3Sn, Nb_3Al, Nb_3Ga, Nb_3Ge, V_3Ga, V_3Si, the Mo_3Re system. A detailed review of A15 compounds for RF applications has been given by Sharma [132].

The A15 phase for the Nb-Sn intermetallics system is in the composition range of 18 to 25 at.% Sn. The superconducting parameters, T_c, Δ, H_{c2}, depend strongly on the Sn content [133]. Close to stoichiometry (24.5at.% Sn) and as a result of perfect ordering in the stoichiometric phase, ρ_n drops below $20\mu\Omega$cm. Therefore, R_{BCS} for Nb_3Sn has the potential to be much lower and Q much higher than for Nb.

A systematic study on Nb_3Sn was carried out at Wuppertal University in the late 80s [134, 135, 136, 137]. In this framework, 1.5 GHz Nb_3Sn cavities were obtained through Sn vapor phase diffusion at high temperature (> 1200 °C). A few microns thick Nb_3Sn films were deposited on the inner surface of Nb cavities exposed to Sn vapor (10^{-3} mbar) in an UHV furnace at temperatures between 1050 and 1250 °C (figure I.4.9). The RF performance of these cavities was measured and compared to bulk Nb cavity performance at 4.2 K and 2 K (figure I.4.9). High Q-values were retained up to a peak field E_{peak} of 15 MV/m before Q-drop occurred. The highest E_{peak} achieved was around 30 MV/m. An attempt was also done with a 5-cell 1.5 GHz cavity which achieved $Q_0 \tilde{} 10^9$ and E_{acc}=7 MV/m (E_{peak}=16 MV/m)with Q=8x10^8.

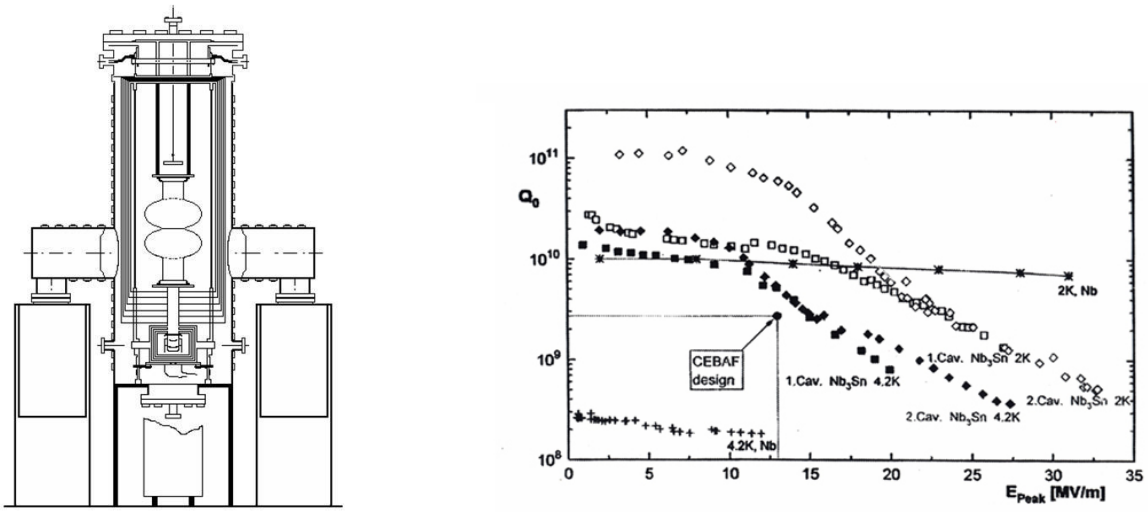

(a) A15setup

(b) My second picture

Figure I.4.9: Vapor diffusion setup for Nb_3Sn formation at Wuppertal University (left) and Q vs. E_{peak} of the 1^{st} two Nb_3Sn coated 1.5 GHz single cell cavities in comparison to pure Nb at 4.2 K and 2 K from CEBAF [137].

In the recent years, regained interest re-emerged in different institutions such as INFN-Legnaro (It), CERN (CH), Cornell University (NY, USA) and JLab.

The investigation of Nb_3Sn for SRF applications resumed at INFN Legnaro, Italy in the group of Prof. V. Palmieri. The liquid surface diffusion process commercially used for producing Nb_3Sn tapes has been modified to produce Nb_3Sn films for SRF applications [138]. The so-called "hybrid liquid diffusion" process [139] produced films with good superconducting properties and T_c=16.8 K (ΔT_c=0.16 K).

A Nb_3Sn program is also on going at Cornell [140], JLab [141] using the Sn vapor diffusion technique. A certain number of cavities have been produced (see figure I.4.10).

Other A15 compound such as V_3Si and Mo_3Re have been investigated as well [143, 144]. But no significant results have been obtained on their RF performance both on samples and in cavities.

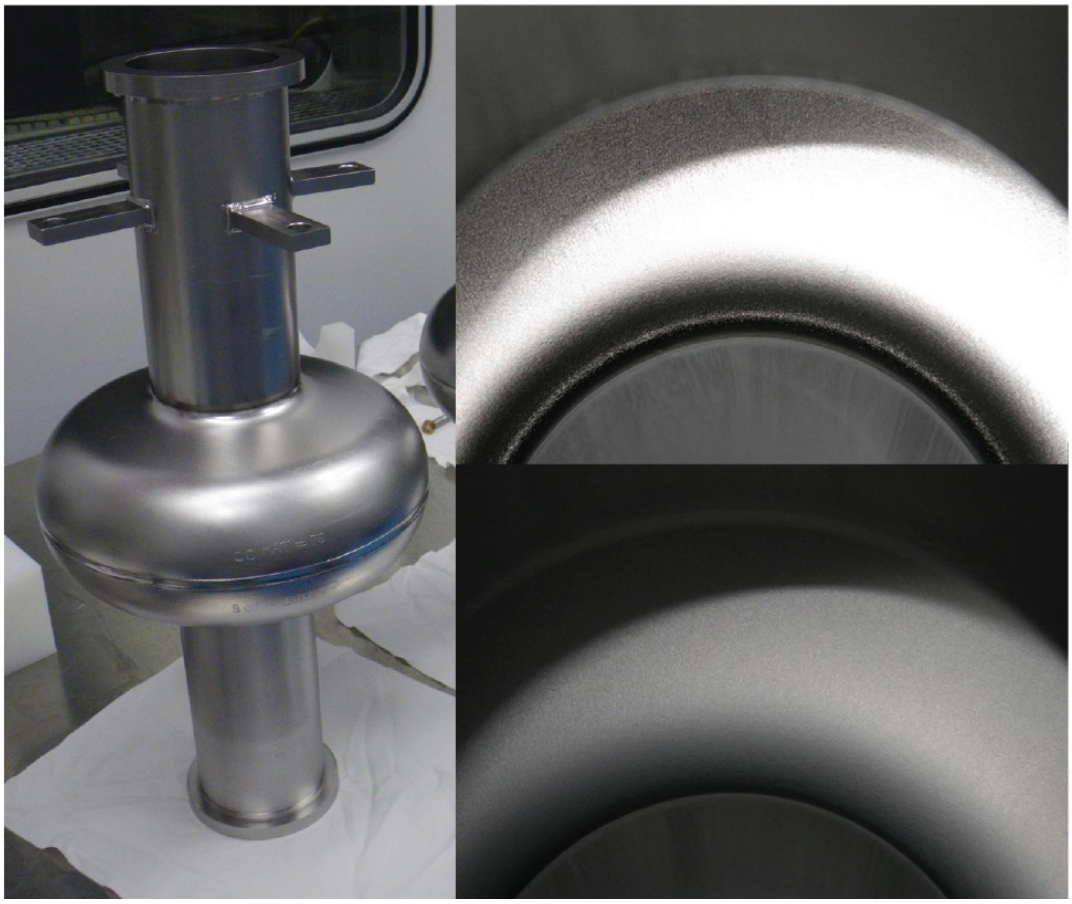

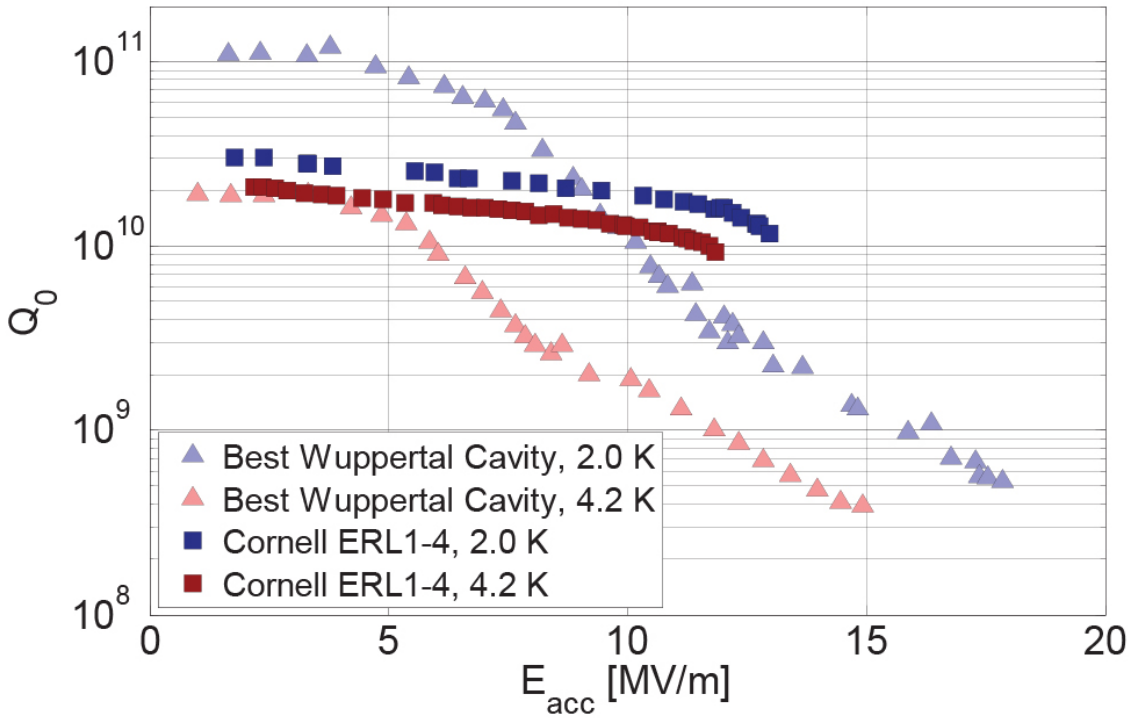

Figure I.4.10: Cornell Nb_3Sn cavity performance compared to the best Wuppertal Nb_3Sn cavity, from [142]

I.4.3 Magnesium Diboride

The superconductivity of MgB_2 has been discovered in 2001 with T_c=39 K [145]. MgB_2 has a hexagonal structure. The graphite-type boron (B) layers are separated by hexagonal close-packed layers of magnesium (Mg).

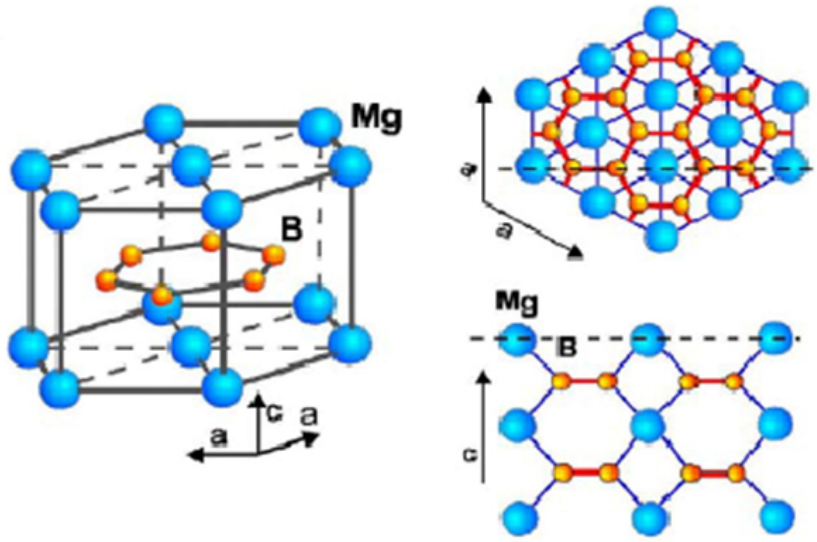

Figure I.4.11: MgB_2 structure

The superconductivity comes from the phonon-mediated cooper pairs production similar to low-T_c superconductors except for the two-gap nature [146] with Δ_p=2.7 meV and Δ_s=6.7 meV (see figure I.4.11).

The RF response has shown lower energy gap behavior. This must be compared to 1.5 meV for Nb, since the resistivity can also be made quite low (best values are $\leq 1\mu\Omega$cm). With a higher $T_c$than Nb, a low resistivity, a larger gap, a higher critical field (see Table reftab:Materials-SRFcandidate), there is room for better performance than Nb.

Different MgB_2 deposition techniques have been developed, among. Some RF performance has been measured. The best results have been obtained with Hybrid Physical Chemical Vapor Deposition (HPCVD) [147] which combines physical and chemical vapor deposition. Films have been deposited on various metal substrates like stainless steel, Nb, TiN and maintained good properties.

RF measurements on such films performed at 7.5 GHz in a TE-011 Nb cavity and represented in figure I.4.12 were also performed [148].

One of the challenges with using MgB_2 for SRF application is the degradation of the film properties with exposure to moisture (resistance goes up and T_c goes down). One way to overcome such degradation during cavity surface cleaning may be to use a cap layer to protect the MgB_2 film.

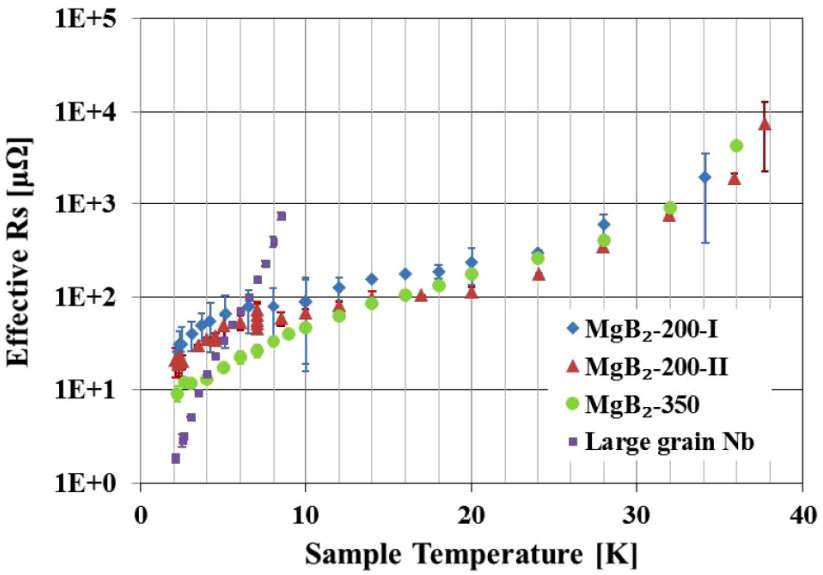

Figure I.4.12: Effective surface resistance versus sample temperature of MgB_2 films on sapphire and of a large grain Nb sample (from [148]).

I.4.4 Oxipnictides

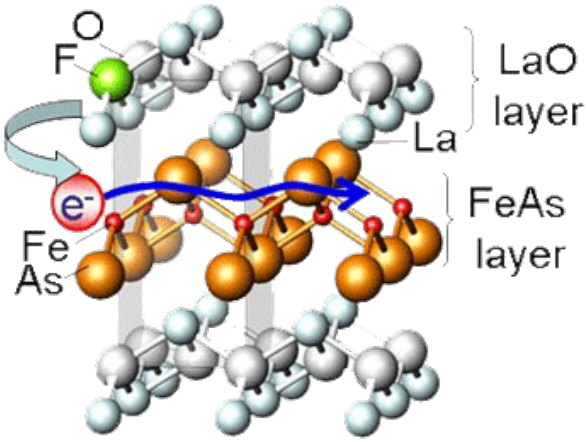

Figure I.4.13: Oxipnictide structure [149]

Recently a new family of superconductors has been discovered, accounting up to a few thousand compounds. They are structured with the oxypnictide base (ReOMPn) where M = Fe, Co, Ni, Pn = As or P, Re = La, Nd, Sm, Pr. These superconductors are layered like High-T_c superconductors (HTS) with T_c ranging from <10 K to 55 K. The superconductivity occurs on the FeAs layer with magnetic pair-breaking Fe^{2+} ions.

Tests in magnetic fields up to 45 T suggest the H_{c2} of $LaFeAsO_{0.89}F_{0.11}$ may be about 64 T. A different La-based material (La0.8K0.2FeAsO0.8F0.2) tested at 6 K predicts H_{c2} up to 122 T.

For s-wave members of the pnictide family, one can expect a much lower R_s at 2 K because Δ_{oxy} = 5-10 meV > Δ_{Nb3Sn}= 3 meV.

These compounds have a high ρ_n ($\sim$ 1 mΩcm $\sim$ 10 ρ_{nMgB2}), a high value of λ (180-250 nm) and low H_{c1} ($\sim$ 10 mT). R_s can be much lower than R_s of Nb_3Sn, but a structure based

on SIS multilayers is necessary.

High quality epitaxial films have been grown via MBE, although only on a small scale ($1cm^2$) [150]. The evaluation of such structures is ongoing in the framework of a collaboration between the University of Wisconsin (WS, USA) and Old dominion University (VA, USA).

I.4.5 SIS MULTILAYER APPROACH FOR SRF CAVITIES- Ongoing experiments

As seen previously (section I.1.6), a few years ago, a concept was proposed by Alexander Gurevich [5] which would allow to take advantage of high-T_c superconductors without being penalized by their lower H_{c1}. The idea is to coat SRF cavities with alternating superconducting and insulating layers (SIS structures) with a thickness d smaller than the penetration depth λ. If the superconducting film is deposited with a thickness d $<<\lambda$, the Meissner state can be retained at magnetic field much higher than bulk H_{c1}. The higher-T_c thin layers provide then magnetic screening of the bulk superconducting cavity without vortex penetration. The strong increase of H_{c1} in films allows to use RF fields higher than the critical field H_c of Nb, but lower than those at which the flux penetration at grain boundaries may create a problem. The BCS resistance is also strongly reduced because of the use of superconducting layers with higher gap Δ (Nb_3Sn, NbTiN ...). With such structures, Q-values at 4.2 K of two orders of magnitude above Nb values could be achieved.

As an example, a thin Nb_3Sn film of 20 nm in thickness increases H_{c1} for Nb_3Sn to 5.7T. If a 50 nm Nb_3Sn layer is coated on a bulk Nb cavity with an insulator layer in between, and if the Nb cavity can sustain fields up to 150 mT, this structure could sustain external magnetic field of about 320 mT and therefore could reach accelerating gradient without precedent.

I.4.5.1 C. Antoine et al., CEA Saclay, France

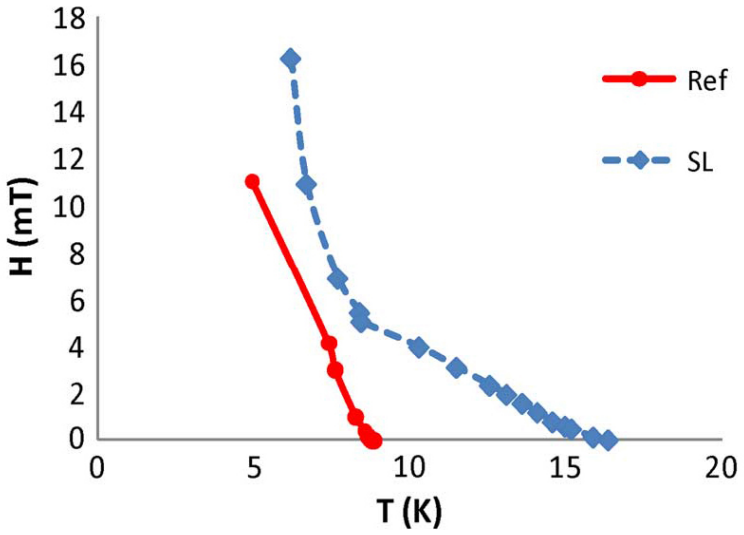

Figure I.4.14: Third harmonic signals in a modified SQUID magnetometer for a Nb film/MgO as a reference (red) and a NbN/MgO structure coated on the reference film from [153].

In this work [151, 152], 25 nm layers of NbN (superconductor) and MgO (insulator) were deposited on 250 nm thick Nb film substrates via magnetron sputtering. The DC magnetization response of the samples was then studied using SQUID and local magnetometry. The results of this work tend to suggest a difference in the magnetization of films due to the presence of a multilayer coating.

I.4.5.2 R. Russo et al., various institutions, Italy

At INFN Roma and Napoli (Italy), alternating 80 nm layers of Nb and Al_2O_3 were deposited on 250 nm thick Nb film substrates via DC and RF magnetron sputtering [100]. The film response was studied using inductive third-harmonic measurements, in which a 1 kHz magnetic field is applied by a "pancake coil" to small and flat multilayer samples. The third-harmonic voltage responses induced by vortex motion in the film is then detected by the same coil. These measurements indicate a clear improvement in H_v (as defined in Section I.4.6.1 - termed B_{c1} on this graph) due to multilayer coatings, as shown in figure I.4.15.

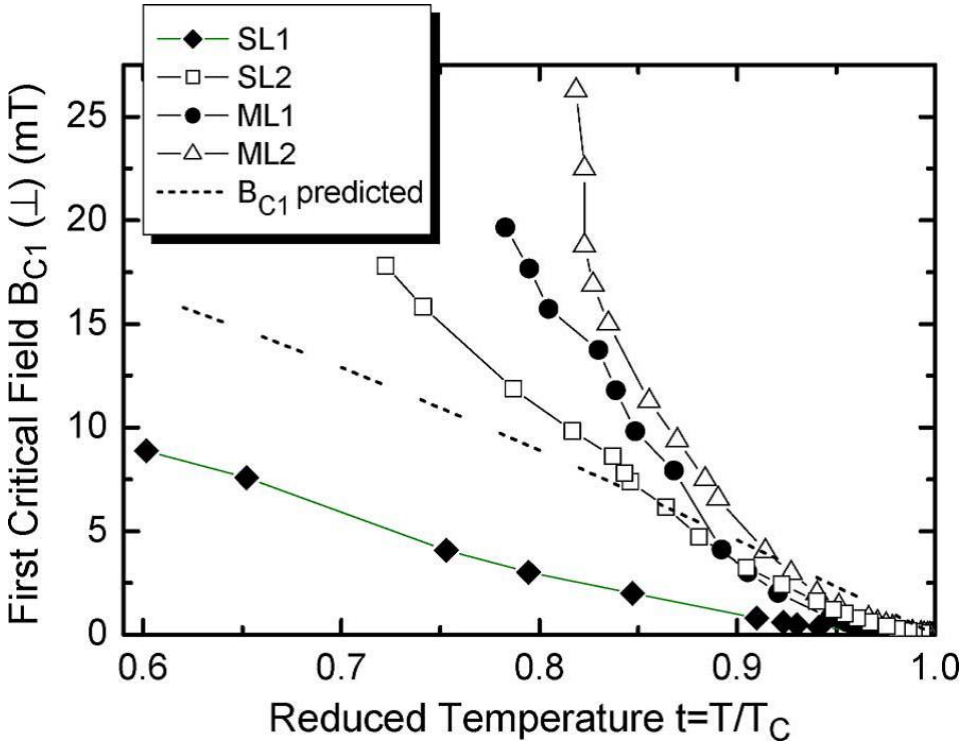

Figure I.4.15: Results from Russo *et al.*, from [100].

I.4.5.3 College William & Mary

H_{C1} measurements were performed for MgB_2 films of different thicknesses and deposited via the HPCVD method mentioned in section I.4.4.2. The results are represented in figure I.4.16 along with expected theoretical curves for lower critical field enhancement for particular coherence lengths (solid lines). Associated error for critical field measurements are on the order of ~ 100 Oe and therefore not represented [154].

The studies described above give interesting indications of the efficacy of multilayer films in postponing the onset of flux penetration. Note, however, that these studies are conducted at DC or at very low (kHz) frequencies, complicating any potential cavity predictions concerning RF surface resistance.

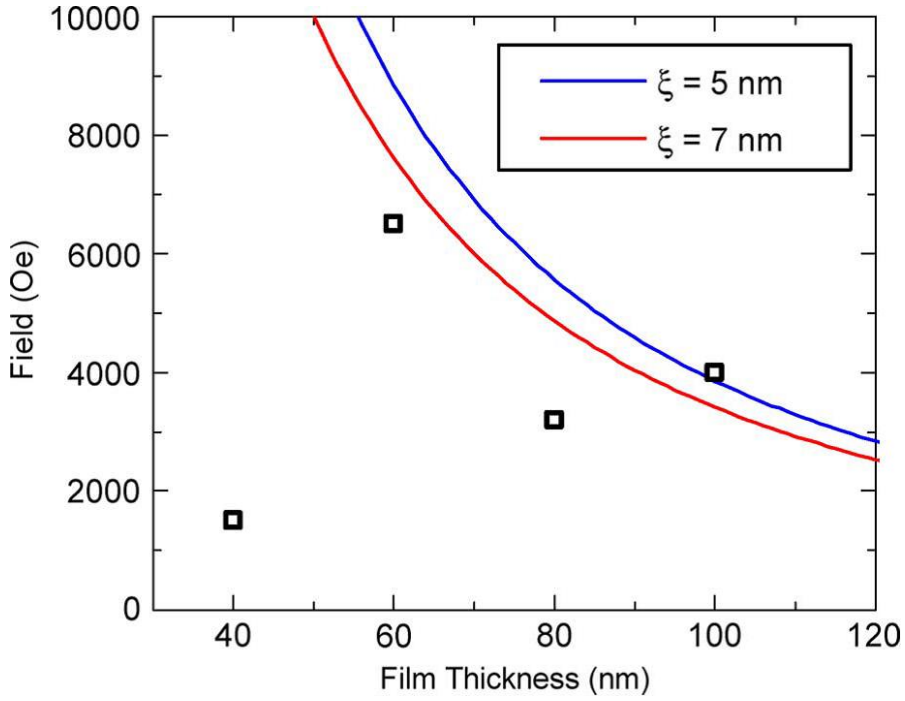

Figure I.4.16: Measured H_{C1} (4 K) as a function of MgB_2 thickness, from [154].

Part II

Thin Film Growth

This section is dedicated to description of the Physical Vapor Deposition (PVD) processes and techniques used in this work. We have mainly explored energetic condensation for Nb films deposition and dc magnetron sputtering (dc-MS), some HiPIMS for NbTiN and AlN based structures. Energetic condensation constitutes an evolution of classical PVD techniques with many common important parameters. In order to develop, control and tailor the properties of thin films, one needs to understand the mechanisms driving the microstructure evolution and the influence of the technique parameters on the film properties. In chapter II.1, some of the fundamental processes, through which the microstructure of a polycrystalline film may evolve during deposition, will be discussed. The discussion is largely descriptive and is primarily based on References [155, 156, 157, 164], where a more thorough treatment of the subject can be found. In chapter II.2, a brief description is given for the conventional deposition techniques, among which reactive dc magnetron sputtering used in the present work for NbN and AlN deposition. Finally, the relationship between important deposition parameters and film microstructure is described in terms of structure zone models. In chapter II.3, the phenomenology of Ionized PVD (IPVD) [160, 161, 162, 163], also called energetic condensation and the associated deposition techniques are introduced. Finally, the approach to film growth followed in this work will be given in chapter II.4.

Chapter II.1

Thin Film Growth - Fundamentals

This chapter is dedicated to the description of the basic phenomena taking place during thin film growth in general. Chapter II.3 will address the phenomena particular to energetic condensation.

In physical vapor deposition (PVD), thin films grow from the gas phase. It is a non-equilibrium process phenomenon governed by a competition between kinetics and thermodynamics. Ionic, molecular or atomic species are produced in the gas phase and transported to the substrate. These species then condense onto the substrate directly (thermal accommodation, binding, surface diffusion) or either by chemical or electrochemical reaction.

During deposition of a thin film, several fundamental kinetic processes exist through which the microstructure evolves. These processes are often classified in three different regimes [164, 217, 167]: (i) the nucleation and island growth regime, (ii) the island impingement and coalescence (interface formation) regime and (iii) the continuous film growth regime (thickening or subsequent growth).

In addition, the structure may also develop or be altered during post-deposition processing, for example due to thermal annealing, where grain growth, recrystallization, defect annihilation etc. are possible structure-developing processes. The way the film structure evolves during the various processes is of course very dependent on the exact processing conditions: choice of materials, deposition rate, deposition and annealing temperatures, ion bombardment etc. Each of these processing conditions affects the diffusivity and mobility in the evolving thin film. Generally, the diffusivity scales with the melting temperature Tm of the material, for which reason the homologous temperature T/T_m is a better indicator of diffusivity than the absolute deposition or annealing temperature T of the deposited material. Furthermore, if the growing film is exposed to energetic particle bombardment additional mobility is supplied to the surface atoms (see chapter II.3).

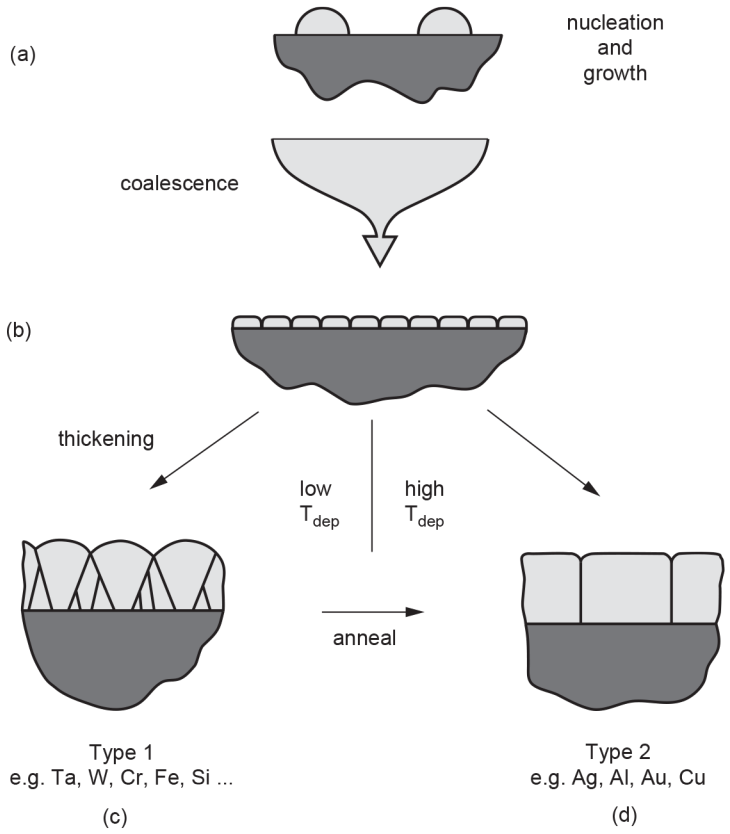

Figure II.1.1: Overview of possible grain structure evolution during deposition of polycrystalline thin film. Island formation and growth leads to impingement of islands to form grain boundaries. The development of grain structure during subsequent film growth is determined largely by surface mobility of adatoms relative to the deposition rate, and by the substrate temperature relative to the melting temperature of the film material. From [158].

II.1.1 Nucleation

Condensation from the vapor involves incident atoms becoming bonded adatoms which diffuse over the film surface until they are trapped at low energy lattice sites.

Several competing processes are then at play [167]. The atoms are continuously depositing on the surface. Depending on their energy and the position at which they hit the surface, they can be re-evaporated from the surface, adsorbed (adatom), form a covalent or ionic bond with a surface atom (chemisorption), form a Van der Waal's bond with a surface atom (physisorption) or migrate on the surface and interact with each other or with the substrate atoms. This atomic odyssey involves four basic processes: shadowing, surface diffusion, bulk diffusion and desorption.

The first three are quantified by the characteristic diffusion and sublimation activation energies (scaling with the melting point). Shadowing arises from the line of sight impingement of arriving toms. The dominance of one or more of these processes as a function of substrate temperature is manifested by different structural morphologies.

Gain growth and coarsening, growth modes

Thin films are formed on a substrate by a process of nucleation and growth.

Nucleation depends on the interaction between the adatoms and the substrate and is affected by the surface mobility of the species, which depends on the substrate temperature, the deposition rate, and the energy of the arriving atoms. The shape of the nuclei depends on the relative interfacial free energies between the film and the substrate γ_{fs}, the film and the vapor γ_{fv}, and the substrate and the vapor γ_{sv} [168]. The interfacial energies balance each other at the interface so that $\gamma_{sv}= \gamma_{fs}+\gamma_{fv}\cos\theta$, where θ is the contact angle, as seen in figure II.1.2.

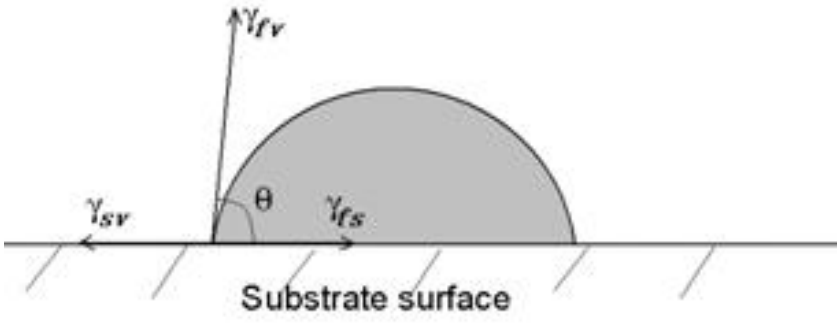

Figure II.1.2: Schematic of a nucleus and the corresponding free energies of the substrate, the film, and the vapor

In conventional (low energy) PVD, during the early stages of thin film growth and depending on whether or not the bonding between similar adatoms is stronger than between adatom and substrate atoms, one of three main growth modes dominates [155]:

- 3-D or island growth mode, also known as Volmer-Weber (VW) mode: The adatoms have a strong affinity with each other (γ_sv$< \gamma_{fv}+\gamma_{fs}$ and $\theta>0$) and build 3-D islands that grow in all directions, including the direction normal to the surface. The growing islands eventually coalesce and form a contiguous and later continuous film.
- 2-D or layer-by-layer growth, also known as *Frank-van der Merwe (FVDM) mode*: The condensing particles have a strong affinity for the substrate atoms ($\gamma_{sv}\geq \gamma_{fv}+ \gamma_{fs}$ and $\theta=0$): they bond to the substrate rather than to each other.
- A mixed mode that starts with 2-D growth that switches into island mode after one or more monolayers; this mode is also known as *the Stranski-Krastanov (SK) mode*: The relation of bond strength between like atoms and dislike atoms is more subtle. The bonding environment is changed once the surface atoms are covered and hidden by the first one or two mono-layers such that islands start to form. The intermediate SK mode is not completely understood, but factors such as the film-substrate, lattice mismatch, or the strain energy accumulated in the growing film, may be the cause of such growth [169].

For the three growth modes, similar mechanisms control depositions and agglomeration of the incoming atoms in the initial and stationary growth phases.

The film nucleation depends first and foremost on the nature of the material deposited (metal, insulator ...). Niobium as most metals usually grows in the island mode.

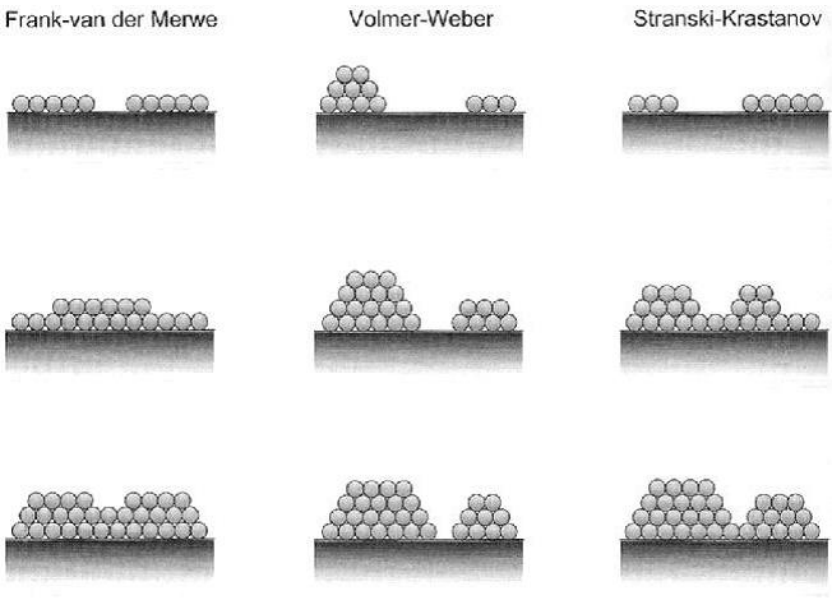

Figure II.1.3: Three modes of thin film nucleation and growth showing 2-D layer by layer growth mode proposed by Frank-van der Merwe, 3-D island growth by Volmer-Weber, and Stranski-Krastanov mixed growth

II.1.2 Coalescence and Early Stages of Growth

The growing islands eventually coalesce and form a contiguous and later continuous film. Three common mechanisms are involved:

- Ostwald ripening: atoms leave small islands more readily than large islands. The more convex the curvature, the higher the activity, more atoms escape.
- Sintering: reduction of surface energy
- Cluster migration: Small clusters (<100 Å across) move randomly. Some are absorbed by larger clusters (increasing radius in height).

Figure II.1.4 represents some STM work for the growth of vanadium (V) on chromium (Cr) [170]. The topography STM maps show V islands deposited on Cr (001) substrates at 525 K with coverages from 0.12 to 1.65 AL (atomic layers). Layer-by-layer growth is observed.

Figure II.1.5 represents the evolution of the lattice parameter of an Nb film on a measured via reflection high energy electron diffraction (RHEED) versus the film thickness as it grows on an Al_2O_3 $(11-\bar{2}0)$ surface. A hexagonal (hcp) Nb surface structure is observed for the first 3 atomic layers followed by a transition structure and then a strained body-centered cubic (bcc) Nb (110) structure to relax the strain due to lattice mismatch and to stabilize the subsequent growth of Nb(110) phase. The lattice parameter relaxes after 3 nm or so. Such initial layers are shown to affect the superconducting properties of the films.

Once the Nb template has been formed, the film grows homo-epitaxially. Stemming from the two possible epitaxial orientations, biaxial anisotropy is observed for thicknesses up to 100 nm while uniaxial anisotropy is observed for thicker films when one crystalline domain grows preferentially (figure II.1.5) [171].

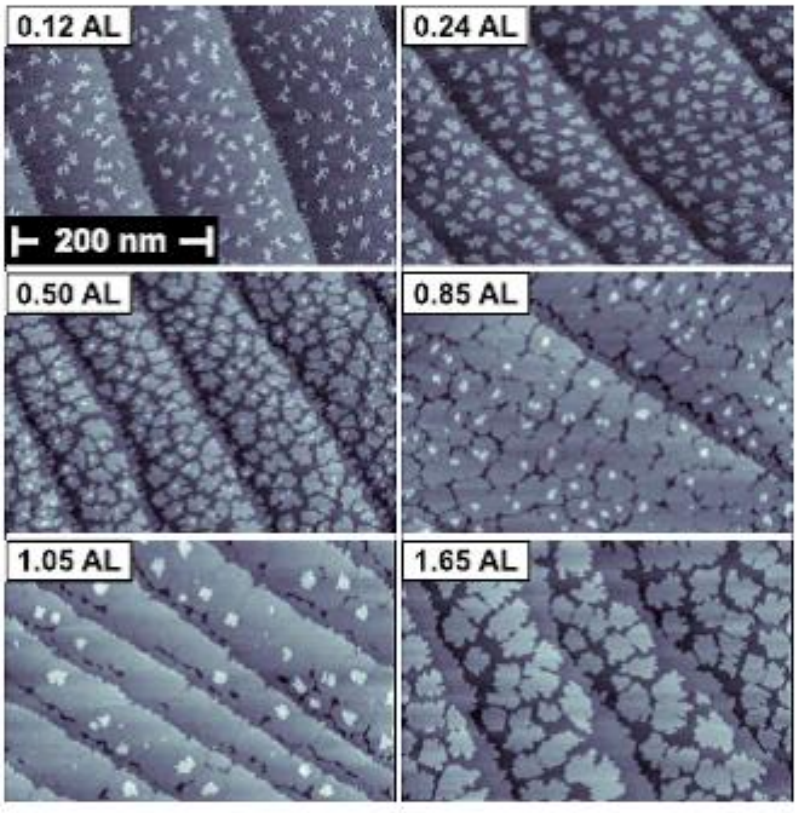

Figure II.1.4: Island growth and coalescence for a V film on Cr (001) observed by STM [170].

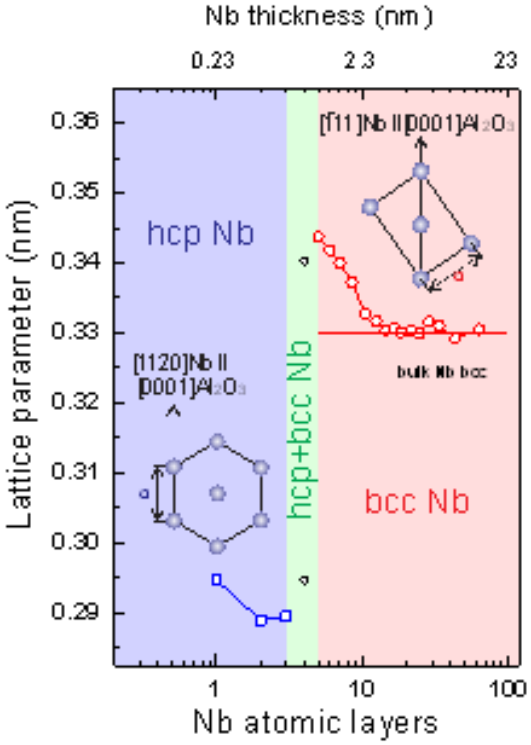

Figure II.1.5: Nb films coated on crystalline Al_2O_3 $(11\bar{2}0)$ [171].

II.1.3 Subsequent Crystal Growth

Further growth depends on bulk diffusion, surface diffusion, desorption, geometry and shadowing (line of sight impingement). It also depends on the substrate temperature and the deposition rate.

The commonly observed fiber structures result from limited mobility and are often oriented towards the source, as in the case of the previously cited CERN films [4]. The resulting films have a lower density and a significant presence of voids.

The grain size of a polycrystalline film is affected by a variety of parameters. Large crystallite sizes are favored by high substrate temperature, high adatom diffusivity during deposition and high annealing, low deposition flux and low impurity content, high film thickness, high energy of bombarding ions/atoms [172].

II.1.4 Recrystallization

Polycrystalline thin films can undergo recrystallization instead of, or in addition to, grain growth. Recrystallization is distinguished from grain growth in that new grains with less defects nucleate and grow at the expense of pre-existing more defective grains [158]. The new grains are separated from the defected region by high-angle grain boundaries (<10-15°). The driving force for recrystallization is the stored energy associated with different types of lattice defects.

II.1.5 Thin Film Formation on the Substrate

In thin film deposition , one is dealing with heterogeneous nucleation. By opposition to homogeneous nucleation (where a solid forms homogeneously from a liquid), in heterogeneous nucleation [156], a new solid phase forms on a pre-existing particle or surface which catalyzes the nucleation event. The nucleation is driven by nucleation centers such as defect, impurities on the substrate surface or simply by the orientation of the underlying substrate.

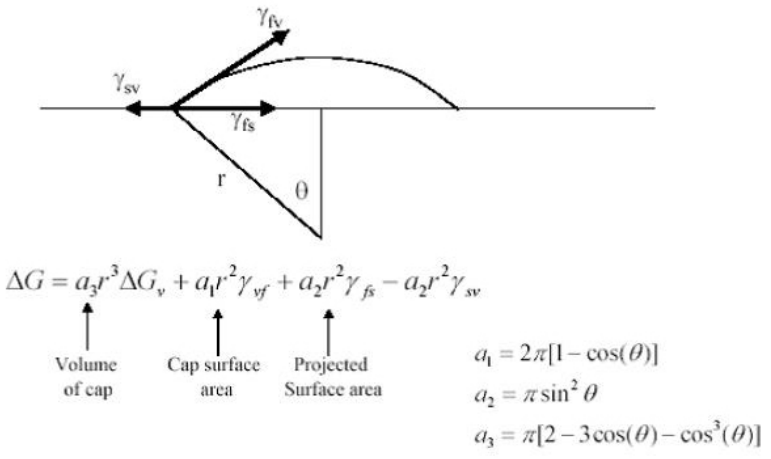

Figure II.1.6: Heterogeneous nucleation versus homogeneous nucleation

The adatoms can diffuse above the substrate surface with a motion determined by its binding energy to the substrate, the temperature of the substrate and the energy of the adatom

[173].

Two common structures are found in Nb film growth for example. The first one is fiber growth with grain competition, often in the case of an amorphous substrate. The second one is hetero-epitaxy where the film growth is driven by the orientation of the underlying crystalline substrate. Hetero-epitaxy is the growth of crystals of a certain material on the crystal face of another. The thin-film will be a single crystal if the substrate happens to be a "perfect" or clean single crystal.

II.1.5.1 Substrate Nature

In this section we will focus on niobium since it was one of the main topics of this work.

Niobium has established hetero-epitaxial relationships for a variety of materials.

Niobium on α-Al_2O_3

The Nb/α-Al_2O_3 system has a unique feature which is a three-dimensional relationship (3D-registry) between metal and substrate: Al_2O_3 [$11\bar{2}0$] ∥ Nb [110] and Al_2O_3 [0001] ∥ Nb [$1\bar{1}1$]. This results from the fact that sapphire, α-Al_2O_3, has an hexagonal structural unit cell with three-fold symmetry about the c-axis , differing from the six-fold symmetry of a pure hcp crystal structure. Figure II.1.7 shows the Nb hetero-epitaxial directions for Nb grown on different planes of sapphire (α-Al_2O_3) as proposed by Wildes et al. [174]. The lattice mismatch (i.e. the difference in the atom arrangement and spacing between the film and substrate materials) with Nb varies from ~1.9% for the a-plane ($11\bar{2}0$) to 12% for the c-plane (0001). Sapphire and Nb have similar thermal expansion coefficients which minimizes strain and stress during film growth generally induced by difference in thermal expansion rate.

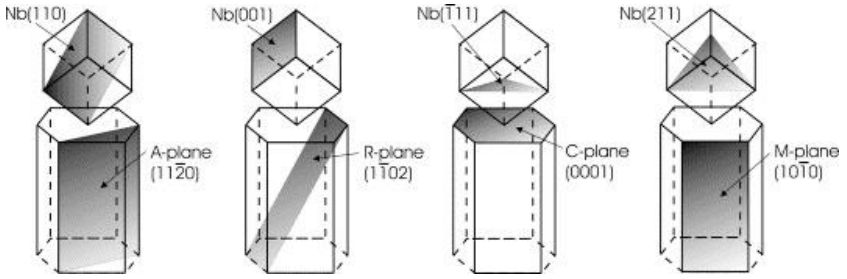

Figure II.1.7: Hetero-epitaxial relationships between Nb and the different sapphire planes (α-Al_2O_3) [from 22]

Most available studies have used have involved a-plane ($11\bar{2}0$) and c-plane (1000) oriented sapphire as substrates. As seen previously in figure II.1.5, RHEED and TEM studies [171] have shown that Nb films grown on sapphire ($11\bar{2}0$) surfaces exhibit an hexagonal structure, more energetically favorable, at thicknesses smaller than a critical value, varying between 5 and 15 Å depending on substrate temperature. A strained bcc Nb (110) then follows and progressively relaxes after a few Nb atomic layers.

Only a few studies have described Nb growth on R-plane oriented ($1\bar{1}20$) sapphire. However, this orientation provides an ideal substrate to promote epitaxy of Nb with (001) orientation. The initial growth stage of niobium films on an atomically flat substrate follows the step-flow model. Niobium adatoms move on the terraces, rearrange themselves along the sapphire step-edges and form patches which eventually percolate, leading to a mosaic polycristal film. When the layer gets thicker, typically over 10 ALs, volume interactions become dominant

with respect to step-edge interaction and force the film to be single-crystalline with a (100) niobium bulk orientation.

Niobium on MgO

MgO has a NaCl structure with a lattice parameter of 4.217 Å. The binary phase diagram of Nb and Mg indicates that they are completely immiscible over the full range of synthesis temperatures [175]. No ternary phase diagram exists for Nb, Mg and O. This implies that no interphase and no intermixing of Nb, Mg and O across the interface occur and thus the interfaces between Nb films and MgO substrates should be chemically abrupt at dimensions of several atomic layers. The lattice mismatch between Nb and MgO is about 10.8% [176, 177]. The epitaxial growth of Nb films on MgO(001) substrates can exhibit one of two distinct crystallographic registries as sketched in figure II.1.8: Nb(110)/MgO(001) with two possible azimuthal crystalline domains corresponding to Nb[110]‖MgO[100] and Nb[110]‖MgO[010] as well as Nb(001)/MgO(001) where Nb[100]‖MgO[100]. The determination of a particular epitaxial Nb registry is highly sensitive to the initial substrate conditions (i.e., miscut, domain distribution, and roughness) as well as the growth conditions.

Table II.1.1: Three-dimensional epitaxy relationship of Nb/MgO(100)

TABLE I. Tabulation of the lattice misfit parameters for the observed orientation (O), $(001)_{Nb}//(001)_{MgO}$ with $[010]_{Nb}//[010]_{MgO}$, a more favored orientation (F), $(101)_{Nb}//(001)_{MgO}$ with $[0\bar{1}1]_{Nb}//[100]_{MgO}$, and a second possible orientation O_p, $(001)_{MgO}$ with $[110]_{Nb}//[010]_{MgO}$.

Orientation	Parallel directions	% misfit
O	$[100]_{Nb}//[100]_{MgO}$	19.4
	$[010]_{Nb}//[010]_{MgO}$	19.4
O_p	$[100]_{Nb}//[010]_{MgO}$	8.0
	$[100]_{Nb}//[110]_{MgO}$	56.5
F	$[0\bar{1}1]_{Nb}//[100]_{MgO}$	8.0
	$[010]_{Nb}//[010]_{MgO}$	19.4

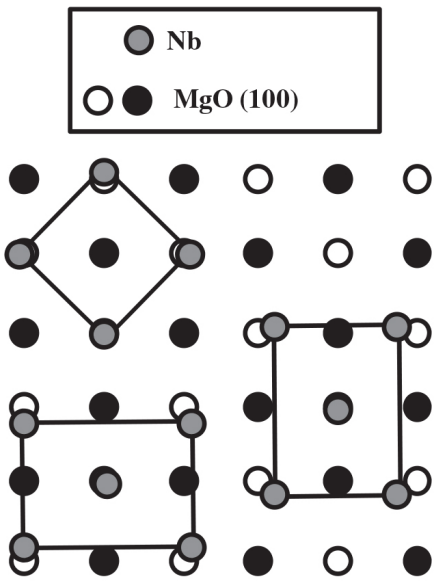

Figure II.1.8: Overlays of relaxed Nb lattices on an MgO(100) surface

Growth domains due to two possible equivalent orthogonal orientations are possible for (011) Nb film grown on MgO (100). Figure II.1.9 presents atomic force microscopy (AFM) scans of magnetron sputtered films on MgO (100) with a thickness of 50 nm and 600 nm [179]. Similar growth variations (at different angles) are observed for ECR films grown on MgO, α-Al_2O_3 and Cu.

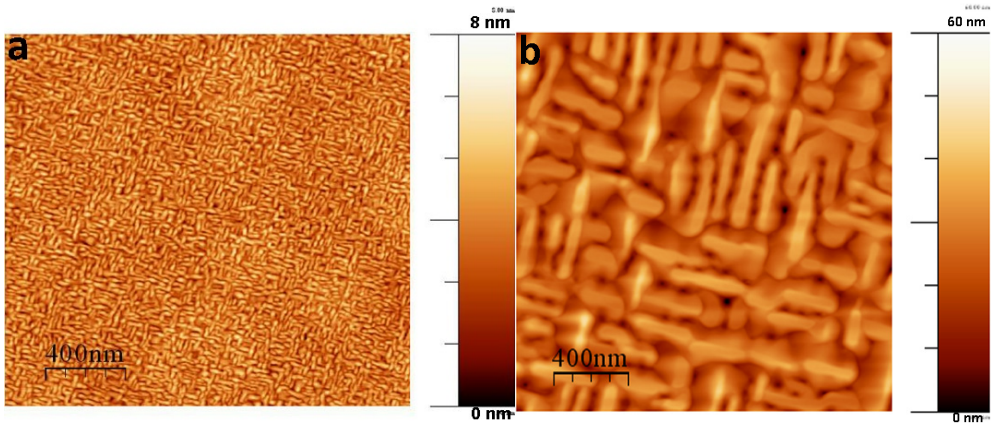

Figure II.1.9: Morphology of Nb (011) grown on MgO (100) for a thickness of 50nm (a) and 600 nm (b) [179].

Niobium on Cu

the Nb/Cu system is of great interest for SRF applications. The lattice mismatch between Nb and Cu is about 10.4%[180].

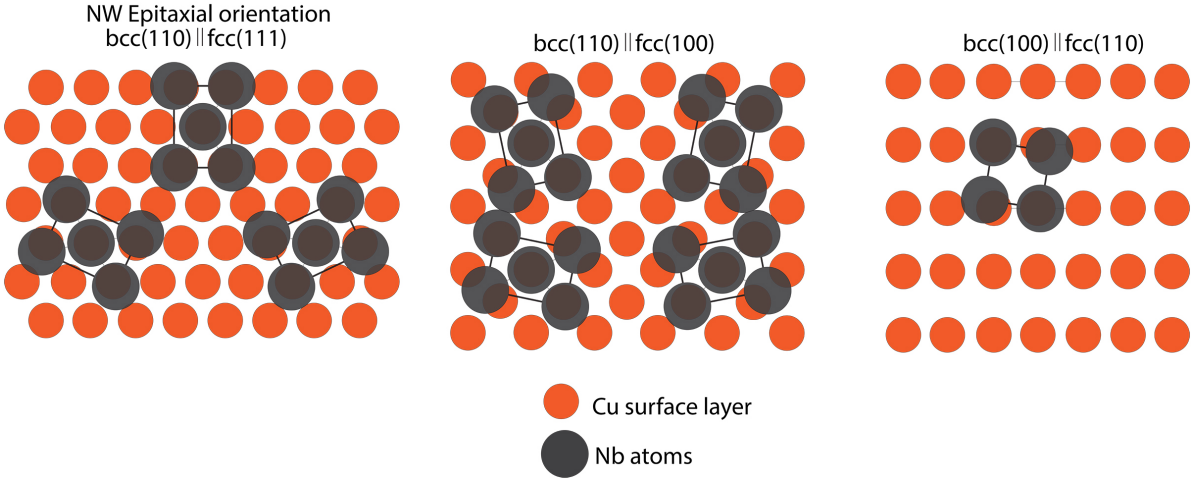

Figure II.1.10: Overlays of relaxed Nb lattices on Cu surfaces

The epitaxial relationships between fcc(111) (Cu) and bcc(110) (Nb) [181, 182, 183, 184, 185] were predicted by theoretical models based on calculations of minimum free energy conditions, including the rigid-lattice approximation, and other sophisticated methods in which elastic interactions between the atoms are considered thus allowing for lattice and misfit strains. In the case of a bcc(110)/fcc (111) interface, two epitaxial orientation relationships are usually possible; either the Nishiyama-Wasserman(NW) or the Kurdjumov-Sachs (KS) orientation [186]. RHEED measurements reported in [180] indicates NW epitaxial relationships: Nb (110)||

Cu (111), Nb[0 0 1]|| Cu [1$\bar{1}$0]. The value of $r = a_{Cu}/a_{Nb} = 0.894$ of the nearest neighbor distance ratio between atoms is in the region for the NW orientation predicted by the theoretical model given by Bauer and Van der Merwe [181]. Van der Merwe et al.[184, 185] predicted a pseudomorphic growth strictly reproducing the underlying crystal structure in the first monolayer of metal on metal growth with atomic radii ratios between 0.894 (Cu/Nb)<r<0.915 (Co/W). This pseudomorphic growth is limited to the first monolayer and is followed by a progressive transformation into the crystal structure observed in thicker films. According to the substrate surface symmetry, three equivalent epitaxial positions of crystal grains rotated by 60° are possible.

For Nb grown on Cu (100), the film is formed by four equivalent domains of crystal grains having the [1$\bar{1}$1] direction parallel to the Cu [011]. This orientation is similar to the KS orientation of the fcc(1 1 1)/bcc(1 1 0) system (fcc[110]||bcc[111]). The two domains have a common [1$\bar{1}$1] crystallographic direction but they differ in the position of the [0 0 1] direction in the plane parallel to the substrate surface (it corresponds to a rotation by 70.5 °around the [1 1 0] axis). The other equivalent pair of domains is rotated by 90 °according to the substrate surface symmetry.

In the growth direction: {111}Cu|| {110}Nb; < 110 >Cu||< 111 >Nb, the lattice mismatch between Cu and Nb is about $\sim$ 10.5%. The early stages of nucleation and growth of Nb islands on Cu (111) under selected growth conditions were investigated in [185b]. After evaporation at RT and annealing at 350 ℃, the Nb atoms rearrange forming a hexagonal lattice during the early stages of growth. This structure strongly differs from the expected tetragonal Nb(110) surface found in bulk and is considerably more compact than the well-known Nb(111) surface. Sub-atomic layer growth of Nb at RT leads to disordered Nb islands with 1 and 2 AL heights, while annealing at 350 ℃leads to the crystallization of the islands following a hexagonal compact surface lattice configuration with lattice parameter a=3.3Å, precluding a pseudomorphic growth with the substrate. Growth of higher Nb coverage above 1AL at 350 ℃reveals a preferential Volmer-Weber growth mode while further annealing at 600 ℃promotes interdiffusion of Nb atoms into the Cu substrate and alloying of the islands. Molecular dynamics simulations validate the growth mode seen in experiments and reveal the onset of interdiffusion and alloying within the islands.

Table II.1.2 shows the different relationships between Nb and sapphire [174], MgO [176] and Cu [180] substrates.

Table II.1.2: Hetero-epitaxial relationships between Nb and various single crystal substrates

Substrate material	**Substrate orientation**	**Nb orientation**
Sapphire	(11$\bar{2}$0)	(110)
	(1$\bar{1}$20)	(100)
	(0001)	(111), (110)
MgO	(100)	(100), (110)
	(110)	(111)
	(111)	(110)
Cu	(100)	(110)
	(110)	(100)
	(111)	(110)

Niobium on native metallic oxides and on ceramics

The presence of an oxide on the surface, common with metallic substrates, inhibits epitaxy. Figure II.1.11 represents two films coated on 1.5 GHz cavities at CERN with the same parameters by cylindrical sputtering [4]. In figure II.1.11a, film was grown on the native copper oxide (CuO). Because the substrate presents an amorphous surface, Nb grows in the fiber growth with preferred orientation along the close-packed plane (110). In figure II.1.11b, the Nb film was grown on a Cu surface free of oxide (obtained by heat treatment at 300 °C prior to coating), one can see that the Nb grains follow the Cu grains. TEM analyses revealed hetero-epitaxy. Films grown on a fresh Cu coated surface under vacuum have the same hetero-epitaxial structure.

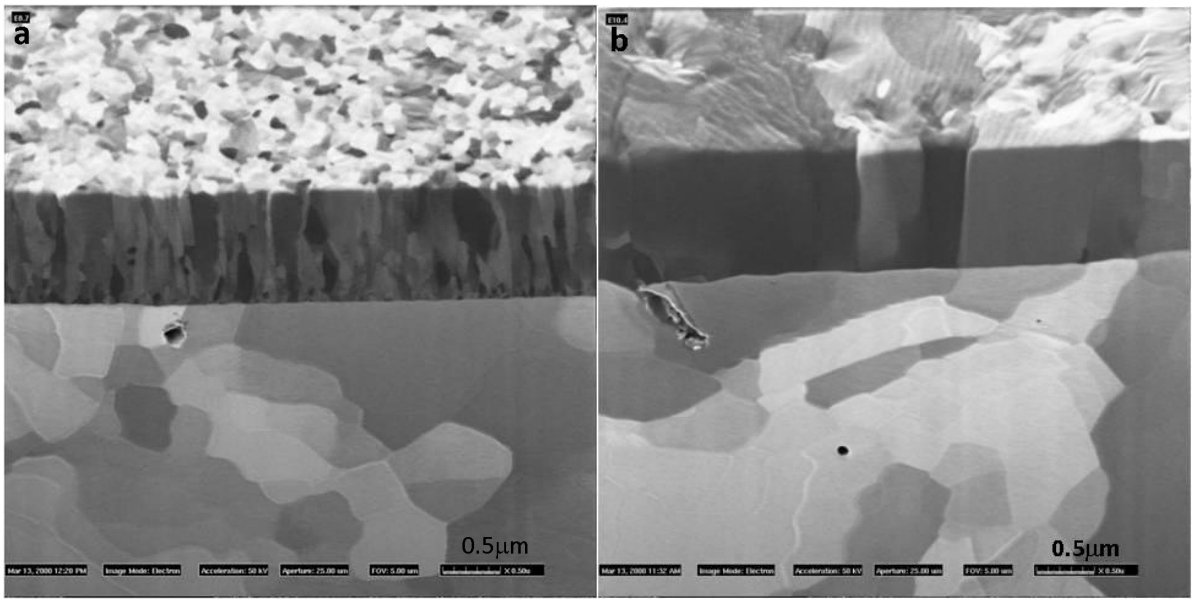

Figure II.1.11: Cross section FIB imaging of CERN magnetron sputtered 1.5GHZ Nb/Cu films coated with Ar on (a) oxidized Cu and (b) non-oxidized [74][courtesy of P. Jacob (EMPA-FEI Company) and CERN]

II.1.5.2 Substrate Quality, Roughness and Cleanliness

The nucleation and growth can be affected by the surface preparation, the miscut as well as the roughness of the substrate. Surface inhomogeneities, impurities adsorbed on the surface can generate for example stacking defaults, screw dislocations...

Whatever the inherent nature of the film, the roughness of the substrate will dictate the minimum roughness of the film. The final roughness depends as well on the coating technique and other refinements.

II.1.5.3 Tailoring the Interface

The interface between substrate and film can be tailored to promote the desired film growth and properties. Oxides on metallic substrate can be removed to promote hetero-epitaxy by substrate heating or surface etching with Ar ions for example. The interface can also be amorphitized to grow a film independently of the substrate (anodization or other modification). A seed layer can be coated at the interface to favor the growth of a particular structure, minimize the density of grain boundaries [179]. The substrate parameters mentioned such as crystallinity, lattice

constant, thermal expansion coefficient, and surface condition (smoothness, purity, surface defects) can bias the crystallinity, orientation, purity and roughness of the resulting film, but they are considered to) be second order parameters in film growth, because they are not subject to active control during deposition.

Ion "massaging" processes are commonly used to alter the nucleation and growth of thin films allowing modifying, controlling the composition, properties of the deposited film and improving surface coverage, adhesion and coating density. Among these processes, *ion stitching* is ion bombardment at energies sufficient to penetrate the interface between a thin coating and the substrate. It is used to enhance adhesion of the material deposited to the substrate by breaking the remaking of inter-atomic bonds (for metallic films on ceramic substrate for example). Another technique is *Ion beam mixing* where coating atoms are transported into the substrate by ballistic processes and by radiation to a depth related to the ion energy.

Chapter II.2

Common PVD Deposition Techniques

This chapter introduces the commonly used techniques for metallic and compound film deposition. There is a wide variety of processes used to deposit a thin film: physical vapor deposition (PVD), chemical vapor deposition (CVD), electro-deposition and plasma spraying. The standard method for the deposition of high-quality superconducting films onto substrates is PVD. The most common techniques of PVD produce thin films by evaporation or sputtering.

Emphasis is given to reactive magnetron sputtering which is used in this work to deposit NbTiN, AlN and SIS structures based on these materials. Structure zone diagrams (SZD) will be introduced as useful tools to predict the resulting structures of a film according to its deposition parameters.

II.2.1 Brief introduction to Plasma Physics for Film Deposition

Plasmas have two important characteristics making them ideal for thin film processes. First, they are sources of chemically active species, radicals and ions that result from the collision of neutral background gases with electrons sufficiently energetic to break their chemical bonds. Substrate surface reactions can thus take place at much lower temperatures than in thermal processes. Second, low-pressure plasmas offer the added advantage of a non-collisional sheath, ensuring that the energy of the ions striking the surface can be accurately controlled within a broad range. Energetic ions play a synergetic role in deposition and etching processes and a determining role in sputtering processes (see below).

II.2.1.1 General description

Irving Langmuir introduced the term *plasma* in 1928 [187] when he investigated oscillations in an ionized gas. He was describing a region containing a balanced number of charges of ions and electrons. Today, a plasma is defined as a gas containing charged and neutral species [188, 189, 190] showing collective behavior. It is often referred to as the "Fourth State of Matter" because of its unique physical properties, distinct from solids, liquids and gases. Examples of plasmas include the sun (and other stars) and the aurora borealis (northern light), making up about 99% of our visible universe [191].

A plasma consists of electrons, positive ions, negative ions, atoms, radicals, molecules and sometimes, in the case of dusty plasmas, atomic clusters with a negative charge. On average plasmas are electrically neutral, since any charge imbalance would create electric fields that would tend to move the charges to eliminate the imbalance. As a result, the combined density of

electrons and negative ions will be equal to that of positively charged ions in any given volume of plasma. This property of plasmas is called quasi-neutrality. A plasma can be created by heating up a gas. At a sufficiently high temperature, the gas molecules will decompose to form freely moving gas atoms. With increasing temperature, these gas atoms will release some of their electrons resulting in free, randomly moving electrons and ions. A plasma is then generated if enough gas atoms are ionized making the collective motion controlled by electromagnetic forces. Even in a weakly ionized plasma (ie only a small fraction of the atoms are ionized) the dynamics of the system is governed by effects caused by a small number of strongly interacting ions and electrons compared to the large number of weakly interacting neutrals.

Plasma science includes a variety of science disciplines ranging from plasma physics to aspects of chemistry, atomic and molecular physics, and material science. Its broad nature also characterizes its plasma physics component, which includes ionized gases that range from weakly ionized to highly ionized, from collisional to collisionless, and from cold to hot. These terms characterize various plasmas ranging from relatively high-pressure gases with a small fraction of the atoms ionized and relatively low charged-particle temperatures (light sources) to very low-density gases with a large fraction of the gas atoms ionized and very high-temperature (fusion plasmas).

Plasmas are used in a number of ways in the field of thin film production and surface modification.

II.2.1.2 Important parameters

Plasmas can be described by several important parameters including [155, 190, 192, 193]:

- The plasma density n_e, which is the concentration of charged species of the same sign.
- The plasma temperature T_e, which is the electron temperature measured in eV.
- The degree of ionization, which is the fraction of the original neutral species (atoms and molecules) that have been ionized. Plasmas with a degree of ionization much less than unity are referred to as weakly ionized plasmas.
- Other plasma parameters, such as the collision frequency, the Debye length and plasma frequency, will be discussed later in the next chapter (II.3.3).

Ionization requires a constant source of energy. The loss of both ions and electrons due to recombination and diffusion and/or convection to the walls must be balanced by the rate of ionization. All technological plasmas are initiated and sustained by electric fields, produced by either direct-current (DC) or alternating-current (AC) power supplies. Typical AC frequencies of excitation are 100 kHz in the low frequency range, 13.56 MHz and its harmonics in the RF range and most commonly 2.45 GHz in the microwave region.

Let's now consider the different plasma regimes. The common way of generating a plasma for thin film deposition is to use two metal electrodes: a cathode, connected to the power source, and an anode (usually the grounded chamber walls) enclosed in an evacuated vacuum chamber. A working gas, such as argon (Ar) is introduced into the chamber. The gas serves as the medium where the electrical discharge is initiated and sustained. The pressure used is around 1 mTorr - 1 Torr (0.13 - 133 Pa). By applying a few hundred volts to the cathode there will be a visible glow between the cathode and the anode, and a plasma is being maintained from this *glow discharge* [To describe the creation mechanism of a plasma from a gas, the analogy to a dielectric breakdown in an insulating solid can be made, where the dielectrics will start conducting current at a critical voltage. In the case of the gas, it starts with a free

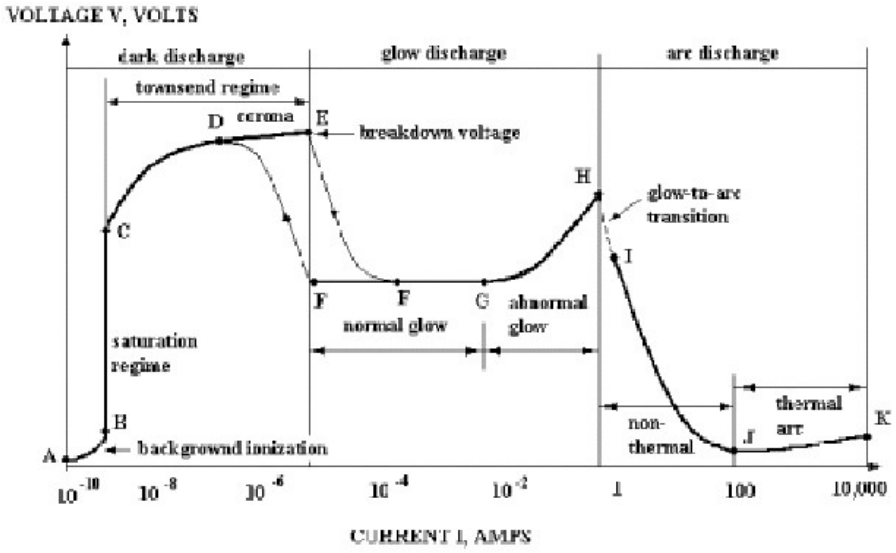

Figure II.2.1: Different plasma discharge regimes. (After Roth [196]).

electron, caused by *e.g.* background radiation or thermal energy, being accelerated towards the anode by an electric field, created by the voltage difference applied between the electrodes. The accelerated electron will gain energy and eventually collide with neutral gas atoms and ionize them. For Ar gas, the following reaction will take place:

$$e^- + Ar \rightarrow 2e^- + Ar^+.$$

The resulting two electrons can now bombard two other neutrals, while the Ar ion will be accelerated and collide with the cathode releasing, among other particles, electrons (often called *secondary electrons*). This regime is called the *Townsend discharge* [155], and very little current is flowing due to the small amount of charge carriers (see Fig. II.2.1). The cascade of ionizing collisions will ultimately result in a large current causing the gas to break down, and eventually the discharge becomes self-sustained, meaning that enough secondary electrons are generated to produce the required amount of ions to regenerate the same number of electrons. The gas begins to glow and there is a sharp voltage drop. This is the *normal glow* regime [155]. With increasing power the current density will eventually be evenly distributed over the entire cathode surface. If the power is further increased, the *abnormal discharge* regime will be reached. Here, the ion bombardment already covers the whole cathode surface and increasing power result in both an increase in voltage as well as in current density. The resulting charge carrier density (plasma density) is found in the range from 10^{15} to 10^{19} m^{-3}. Here is where plasma processing, such as sputtering and etching, takes place [194]. Increasing the current density even further results in thermionic emission of electrons at the cathode. The voltage drops sharply while the current density is very high. This is an *arc discharge* and is the regime used for cathodic arc deposition (see next chapter) [195].

II.2.2 Sputtering

Sputtering is a process in which atoms are ejected from a solid material (sputtering target) by bombarding the target surface with energetic particles, often ions of an ionized inert gas (sputtering gas) [155].

Sputter deposition is a vacuum coating process. A schematic drawing of a typical sputtering setup is presented in Figure II.2.2. The sputtering target, usually solid, serves as the cathode by applying a negative voltage to it while the walls of the chamber serve as the anode. The chamber is evacuated using a vacuum pumping system after which an inert gas such as Ar is introduced to the chamber and the plasma is generated by an electrical discharge of the gas. The distance between cathode and target d and the gas pressure p determine the break-through voltage U_d.

The break-through voltage U_d determines the point from which on the self-sustaining gas glow discharge starts.

The ions from the plasma bombard the target surface and sputter out atoms via momentum transfer [155]. The rate of sputtering is proportional to the current density of inert gas ions bombarding the target surface [197]. The sputtered atoms traverse through the plasma and reach the substrate where they may condense and form films as seen in chapter II.1. The energy of the sputtered atoms have an energy range of a few eV up to tens of eV, described by the so-called *Thomson energy distribution*. The number of sputtered atoms per incident ion, known as the *sputtering yield*, depends on the target material, surface binding energy of the target atoms, the incident ions kinetic energy, the bombarding particle mass and angle of incidence [198].

The emission of secondary electron from the target is important to sustain the discharge as described in section II.2.1.2 (Glow discharge). The number of emitted electrons per incident ion (known as *secondary electron yield* or *secondary electron emission coefficient*) also determines the discharge voltage [199].

Compared to thermal methods such as evaporation, sputtering has many advantages:

- A greater number of materials such as alloys and compounds can be sputtered.
- A higher packing density of the film can be achieved.
- A better adhesion between film and substrate can be achieved, if the film stress is low.
- Control of film composition and grain structure is more easily accomplished by sputtering.
- Better step coverage, because the material beam is non-directional.

On the other hand, sputtering involves many process parameters. Also, some materials have a very low sputtering rate. To obtain a film with desired properties a large number of variables must be investigated and controlled. This is particularly critical for very thin films (< 20 nm).

II.2.3 Magnetron Sputtering

To enhance the sputtering yield at the cathode, a magnetic field configured parallel to the target surface can constrain the motion of secondary electrons ejected by the bombarding ions to a close vicinity of the target surface. An array of permanent magnets, creating a magnetic field of the order of a few 100 G, is placed behind the sputtering source. The magnets are placed in such a way that one pole is positioned at the central axis of the target, and the second pole is placed in a ring around the outer edge of the target. This kind of sputtering is called magnetron sputtering and a schematic representation is given in figure II.2.2. In this configuration, the electrons generate a much higher ionization probability and the plasma ignition then takes place at lower gas pressures compared to conventional sputtering. Another advantage of magnetron sputtering is the higher density of ionized argon atoms which result in

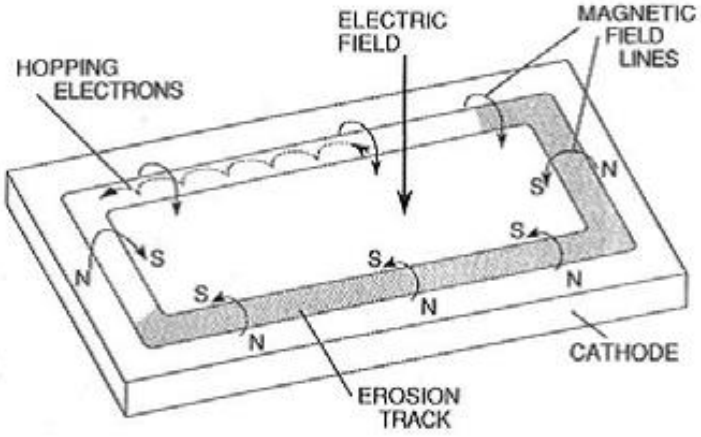

Figure II.2.2: The principle of a magnetron. From M. Ohring [155]

a higher deposition rate at lower pressures. Also less secondary electrons reach the substrate and therefore the substrate is less heated compared to conventional sputtering.

This configuration creates crossed E and B fields, where electrons drift perpendicular to both E and B according to $v_H = E/B$. If the magnets are arranged in such a way that they create closed drift region, electrons are trapped, and relies on collisions to escape. By trapping the electrons in this way, the probability for ionization is increased by orders of magnitudes. Ions are also subjected to the same force, but due to their larger mass, their trajectory radius (Larmor radius, see II.3) often exceeds the dimensions of the plasma. Although in general, one can say that the ions are not directly confined, they are so indirectly by trapping the electrons, to keep the quasi-neutrality of the plasma. The trapping of electrons and ions creates a dense plasma, which in turn leads to an increased ion bombardment of the target, giving higher sputtering rates and, therefore, higher deposition rates at the substrate. The electron confinement also allows for a magnetron to be operated at much lower voltages compared to basic sputtering ($\tilde{}$ 500 V instead of 2-3 kV) and be used at lower pressures (typically in the mTorr region). This is an advantage since less material is lost to the chamber wall and back to the target through scattering in the discharge gas. The shape of the magnetic field efficiently erodes the target where the magnetic field lines are parallel to the target surface; a so-called race-track is created.

The magnetic field configuration of magnetrons can be divided in two different categories: intermediate (balanced), and unbalanced (type I and II) [200].

Balanced magnetron

The inner and outer magnets have the same strength which confines the electrons close to the target surface. This means that the plasma does not reach to the substrate and results in low ion bombardment of the substrate (ion current density < 1 mAcm^{-2}) during film growth, thereby leading to low mobility of the depositing atoms on the substrate.

Unbalanced magnetron

If the inner magnet has a stronger pole than the outer magnet, the magnetic field configuration is unbalanced (type I unbalanced magnetron). In the type II configuration, the inner pole is weaker than the outer pole; the magnetic field lines open up and extend towards the substrate. The electrons follow the field lines and, therefore, the plasma is also extended to the substrate. Ion bombardment (ion current density = 2 - 10 mAcm^{-2}) during growth can ben-

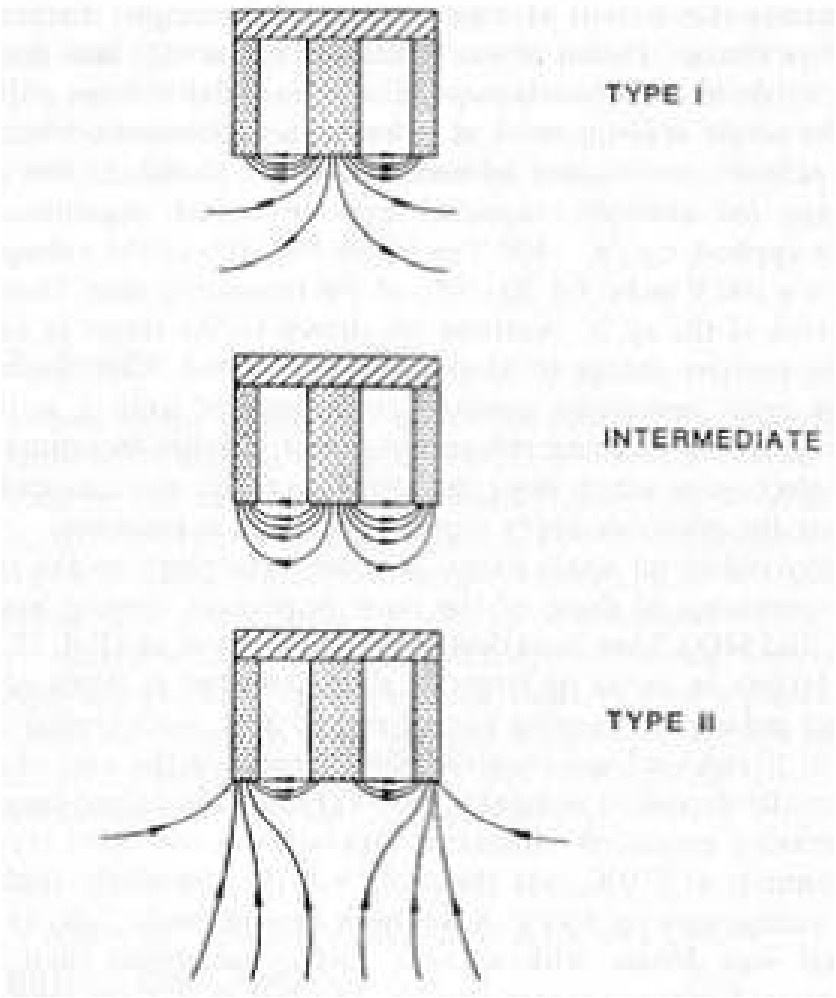

Figure II.2.3: The different magnetic field configurations for magnetron sputtering

eficially influence the film properties, such as increase coatings density and improve adhesion to the substrate.

The differences in design between the different categories are only slight. However, the difference in performance regarding film growth between the different types can be significant. During film growth it is often desired to have an effective ion bombardment of the film. This can be achieved by applying a bias onto the substrate. In most cases it is preferred to have a high ion current containing low energy ions, rather than high energy, since this can generate stress and defects in the film [201]. It is therefore desired to design the magnetic field in such a way that it allows for some of the plasma to escape from the close vicinity of the cathode, and reach the substrate. This is the reason for the different magnetron designs. A schematic of the different designs are illustrated in figure II.2.3.

II.2.3.1 Magnetron sputtering mode of operations

There are variants or modes of operation of magnetron sputtering depending on how the power is applied. Among these, one of the techniques used in this thesis is direct current magnetron. Direct current magnetron sputtering (dc-MS) is successfully used to grow conducting thin films at high deposition rates whereas it can also be scaled for making large scale deposition of thin films. This makes dc-MS an industrially attractive deposition technique. In dc-MS,

a constant power is applied to the target which is limited by the thermal load on the target. This power limitation (maximum power densities of a few tens of Wcm^{-2}) does not allow to generate high plasma densities and the resulting ion fraction of the sputtered material is quite low (only a few percent for metals) [202]. The majority of the flux thus consists of neutral depositing species with energy of few eV. Overall, this results in the energy of the sputtered species limiting the energy input into the substrate. It is possible to improve the film quality by applying a negative potential to the substrate, increasing the substrate temperature and using an unbalanced magnetron (type II). This will provide

Magnetron sputtering deposition parameters affecting the film evolution

The resulting film properties are typically highly dependent on the preparation parameters due to the non-equilibrium nature of the sputter-deposition process. The main process parameters are: substrate temperature, substrate bias voltage, sputter gas pressure, deposition rate and background pressure.

As seen in the previous chapter, the substrate temperature is a critical parameter in controlling the relative importance of the various processes, since the substrate temperature affects diffusion and thereby the atomic mobility [158]. For example, if the grain boundary mobility is low, the initial grain sizes are small and tend only to change through coarsening at the surface of the growing film. In addition, the strain energy may easily increase due to the incorporation of defects in the crystal lattice, since the atomic mobility is insufficient for diffusion to low-energy sites.

The substrate bias voltage is as well important in controlling the effective adatom mobility [155]. If substrate bias voltage is applied, more energetic ions bombard the growing film and transfer energy to the film surface, thus increasing the adatom mobility. However, if the ion energy is sufficiently high, ions may be implanted or induce defects in the crystal lattice.

As a consequence, compressive stresses may arise in the film due to *atomic peening* effects [203]. The sputter gas pressure also affects the energy (and direction) of the arriving adatoms due to collisions between the sputtered atoms and the gas atoms [155]. In magnetron sputtering, the effects of increased bias voltage are approximately equivalent to a lower sputtering gas pressure.

The rate at which clusters nucleate and the characteristic adatom diffusion time are both affected by the deposition rate [158]. For instance, if the deposition rate is relatively high, the time during which the adatoms are free to diffuse to low-energy sites before being buried by newly arriving adatoms is short resulting possibly in a very porous film. On the other hand, if the deposition rate is low, the impurity content (depending on the background pressure) may increase due to a larger relative flux of background gas particles.

II.2.4 Reactive Sputtering

Reactive sputtering is a method to deposit compound films of the target material by adding a reactive gas to the conventional magnetron sputtering process to form, depending on the reactive gas, oxides, nitrides, carbides and other compounds.

The reactions can take place at the target, in the gas phase and on the substrate. Target reactions result in actually sputtering a compound target. These usually have a lower sputter yield (which is the number of sputtered particles of the target per primary ion) than elements and result in a reduction in deposition rate [203].

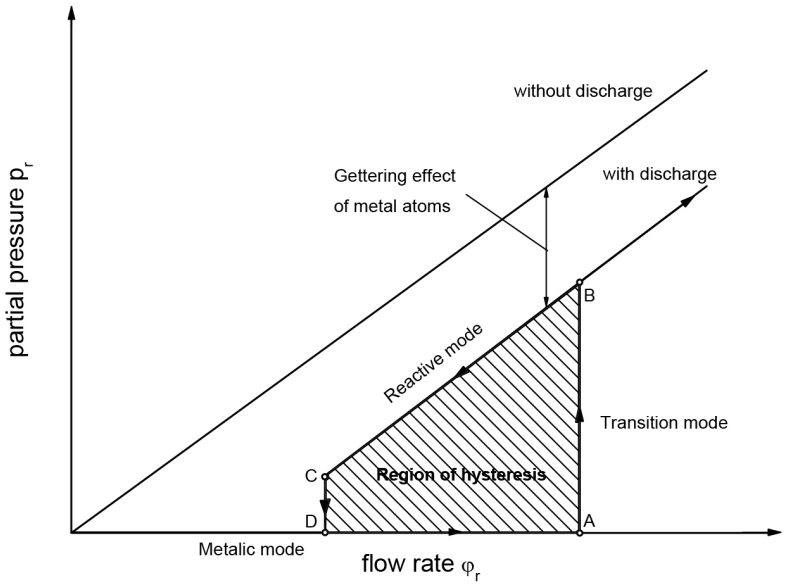

Figure II.2.4: Hysteresis loop of the flow rate ϕ_r and the partial pressure p of the reactive gas occurring in a reactive sputtering process (from [205]).

Attempts to sputter from targets of stoichiometric superconducting compounds produce degraded superconducting properties of thin film. This is due to the presence of oxides within the grain boundaries inside the target material [204].

Reactive sputtering is the favorable method for the deposition of thin NbN and NbTiN layers for different scientific and industrial applications (phonon-cooled HEBs, Terra Herz (THz) mixers, hard coatings for tooling). One basic problem of the reactive sputtering process is to determine the essential process parameters to control the superconducting film growth and quality.

The most important process parameter in the preparation of thin films by reactive sputtering is controlling the partial pressure of the reactive gas.

The partial pressure of the reactive gas is a function of the reactive gas flow rate in a glow discharge process. A hysteresis loop occurs, which is unwanted for the deposition of a superconducting film with a desired crystal structure and the required stoichiometry [205]. The sputtering of the target surface and the deposition of the reactive product on the target surface determine the hysteresis loop. An idealized reactive sputtering hysteresis loop for the partial pressure p and the flow rate ϕ_r of the reactive gas is shown in figure II.2.4.

The graph clearly shows the dynamics taking place in a reactive sputtering process. For a low flow rate of the reactive gas, its partial pressure remains zero. This is caused by pumping the reactive gas with the vacuum pump and the reaction of reactive gas on surfaces within the deposition chamber. This phenomenon is called gettering. This part of the sputtering process is called the *metallic mode*, because only the metallic target material is sputtered.

The *metallic mode* is characterized by a high deposition rate and metal sputtering occurs. The deposited film is a metal film doped with atoms form the reactive gas - in the case of nitrides the film is called "under-nitrogenized". The discharge voltage and current barely differ from the values for sputtering in a pure working gas atmosphere [206].

Beyond point A, indicated in figure II.2.4, the gettering process is saturated and the limited pumping capacity leads to an increase of the partial pressure of the reactive gas and a decrease

in deposition rate. The target and the deposition chamber walls are coated with a layer of the reactive compound. Because of the presence of the compound layer on the target surface, the target is called "poisoned". When the target becomes poisoned, the sputtering rate drops rapidly because the compound will have a lower sputtering yield than the purely metallic surface [207]. When the target is poisoned, several instabilities can occur like arcing, because an increasein secondary electron emission from the compound surface takes place, especially when sputtering nitrides [208]. Due to the lower sputtering rate, less reactive gas is consumed, and its partial pressure jumps to a much higher level, which differs from the partial pressure without discharge.

Increasing the flow rate ϕ_r further causes a higher partial pressure, but the difference in pressure with and without discharge will remain constant. This pressure difference corresponds to the amount of reactive gas included into the deposited film, which is now a stoichiometric compound. Therefore this mode is called *reactive or compound mode*. In *the reactive mode*, the sputtering rate is very low because of the lower sputter yield of the compound and the higher secondary electron emission of the compounds [206]. By decreasing the flow rate below point B the system remains in the reactive mode and returns into the metallic mode for flow rates below a certain value (point C).

The optimal value of the reactive gas flow rate ϕ_r is located within a narrow range around point A/B. Then it is possible to deposit a compound film with good stoichiometry at a comparable rate to that of the metallic film [209].

II.2.5 Structure Zone Diagrams (SZM)

As mentioned previously, a variety of possible deposition conditions can be chosen, which result in films with different microstructures.

In order to provide an illustration of the relationship between the microstructure of vacuum-deposited coatings and the most prominent deposition parameters, growth models, called structure zone models (SZM), have been developed. The basis of the structure zone models is to represent the growth process as proceeding in three general steps:

- Transport of atoms to the growing surface, where shadowing [Shadowing arises from the geometric constraint imposed by roughness of the growing film and the line-of-sight impingement of arriving atoms] may affect the structure formation
- The adsorption and diffusion on the surface
- Bulk diffusion.

In the case of sputter deposition, the transport step is controlled by parameters such as the apparatus geometry and the working gas pressure, while the diffusion steps are controlled largely by the substrate temperature, but may also be significantly influenced by bombardment of energetic species. The activation energies for surface, grain boundary, and bulk/lattice diffusion are typically in the ratio 1:2:4 [210], implying that, at lower temperatures, surface and grain boundary diffusion rates can be orders of magnitude larger than bulk diffusion rates.

The first structure zone model was proposed by Movchan and Demschishin in 1969 [211]. They concluded that the observed microstructures of thick evaporated metal and oxide films could be systematically categorized into three zones , namely Zone 1, 2 and 3, according to their homologous temperatures $T/T_m$where T is the substrate temperature and Tm is the coating material melting point.

A similar zone model was introduced by Thornton [212, 213, 214] for thick sputtered films. Besides the homologous temperature, the effect of sputter gas pressure was also taken into account [Actually it is the product of the gas pressure and the target-substrate distance, *pd*, that is the relevant parameter [215], but when the distance is kept fixed the pressure can be regarded as the key parameter. The product *pd* relates to the degree of "thermalization" of the sputtered and reflected species]. The gas pressure affects the film microstructure primarily due to the fact that the mean free path of the sputtered atoms is inversely proportional to the gas pressure. Increasing the pressure reduces the energy of the bombarding species, which lowers adatom mobilities. Furthermore, the gas scattering also increases the oblique component of the deposition flux, whereby self-shadowing decreases the density at the grain boundaries. The Thornton structure zone diagram is shown in figure II.2.5. The inclusion of gas pressure as an additionalparameter introduces a transition zone, zone T, between zone 1 and 2.

During deposition, the surface diffusion, the bulk diffusion, and the adsorption scale directly with the melting temperature of the deposit (metal). This can result in 4 different film structures:

Zone 1 corresponds to low deposition temperatures ($T/T_m \lessapprox 0.3$). The structure exhibits amorphous or fine grained polycrystalline films, with a high dislocation density. The internal structure of the crystals is poorly defined. The absence or insufficiency of surface diffusion to overcome the effects of atomic shadowing (i.e. a "frozen in" structure) at low Ts yields heavily voided columnar (or fiber) structures and results in porous and rough films.

Zone T is the transition zone between zones 1 and 2 [216] observed when the gas pressure is decreased. The decrease of the gas pressure results in an increase in the energetic bombardment of the films. In this zone, the morphologyis characterized by columnar grains with dense grain boundariesand a high dislocation density. At low pressure, zone T is promoted withrespect to zone 1, since the enhanced energy of the impinging species enhancesthe surface mobility, causing the structure to become denser.

Zone 2 ($0.3 \lessapprox T/T_m \lessapprox 0.5$) exhibits a dense columnar structure with smoother surfaces as a result of surface diffusion controlled growth. The columnar grains can have highly faceted surfaces due to surface energy anisotropy. The grain size generally increases with increasing Ts. Dislocations are primarily located in the boundary regions. Surface or grain-boundary diffusion seems to be dominating parameters, since the columnar grain size increases with T/T_m, in accordance with activation energies for these mass-transport mechanisms.

Zone 3 ($\frac{T}{T_m} \gtrsim 0.5$) is characterized by bulk diffusion processes such as grain growth and recrystallization. The grain shape may be equi-axed or columnar, and the grain boundaries are dense. Generally, the boundaries between the zones are diffuse and the transition from one zone to another occurs gradually over a relatively wide range in T/Tm.

In order to incorporate the effects of ion bombardment (e.g. bias sputtering) on the structure of thin films, Messier et al. [216] proposed a revision of the zone model (figure II.2.6), replacing the gas pressure by the inverse substrate bias. The application of a negative substrate-bias potential (V_s) enhances the effect of ion bombardment, which is essentially similar to what can also be accomplished by reducing the gas pressure as mentioned previously.

Structure zone models present a semi-quantitative guideline for the expectations for the structural evolution as a function of primary deposition variables for physically deposited films. Although the original sputter zone model was based on metal coatings deposited by magnetron sources, its general features have been found to be rather universal. It is, however, important to note that such models or diagrams are developed for a specific class of materials and are based on assumptions concerning specific processing conditions such as impurity content [217], deposition rate etc. Hence, some variation should be expected regarding for example the

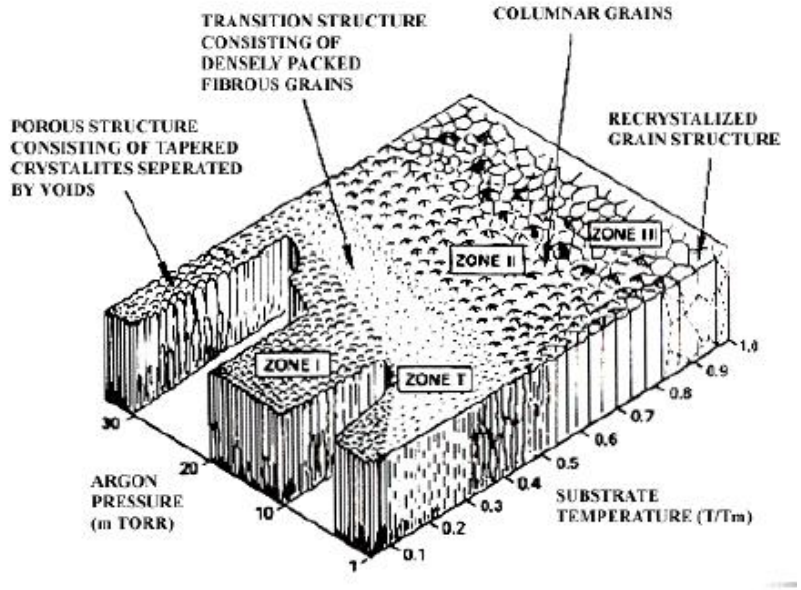

Figure II.2.5: Microstructure zone diagram for metals deposited by magnetron sputtering showing the dependence of coating structure on substrate temperature and argon pressure. From[214].

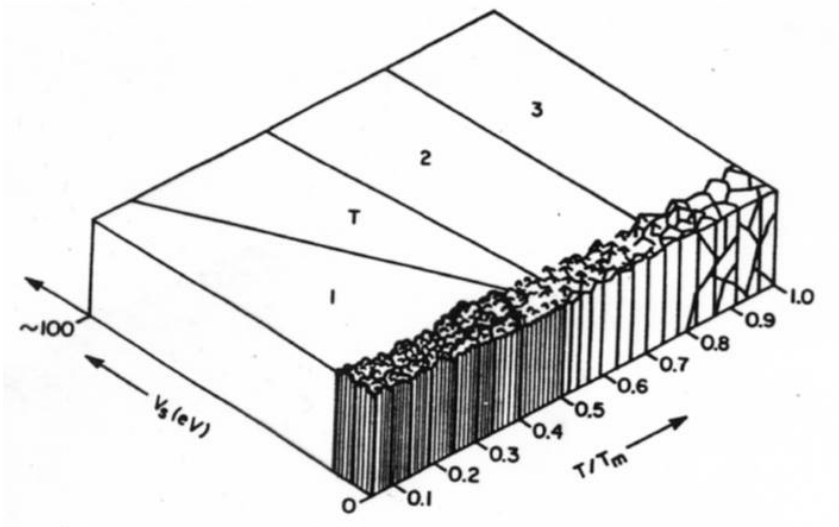

Figure II.2.6: Structure zone model for films showing the effect of both ion bombardment (negative substrate bias voltage Vs) and thermal-induced mobility. From [216].

homologous temperatures associated with the transitions between different structural zones.

The influence of ion bombardment on the film properties of metals can be reconciled with the accepted models of thin-film growth. However, energetic condensing particles or bombardment promote the zone T structure [212, 216]. Evaporated atoms usually have energies in the vicinity of 0.1 eV, while sputtered atoms usually have energies of a few eV. Condensing atoms from these different sources will produce films of different densities.

Chapter II.3

Energetic Condensation

This chapter presents an overview of the processes involved in the growing set of techniques known as IPVD (ionized physical vapor deposition) or energetic condensation. The second part of the chapter cover a brief description of the most common IPVD techniques with emphasis given to the techniques used in the present work.

As mentioned before, control over the deposition process is exercised by only three first-order vapor parameters and one first-order substrate parameter. The vapor parameters are the absolute arrival rates of film atoms, the partial pressures of background gases in the chamber and the energy of the deposition fluxes. The substrate parameter is the substrate temperature.

Without energetic atoms, only the substrate temperature influences the processes of physi- and chemisorption, thermal desorption, nucleation, nuclei dissociation, surface diffusion, and formation of specific nucleation sites. Crystalline defects, grains connectivity and grain size may be improved with a higher substrate temperature which provides higher surface mobility (the important parameter is the "homologous temperature"= $T_{substrate}/T_{melting\_of\_film}$). However practical substrates for SRF cavities such as Cu or Al may not allow heating to high temperatures.

The missing energy may be supplied by ion bombardment. Energetic condensation (implemented in high power impulse magnetron sputtering-HiPIMS [218], cathodic energy deposition - CED^{TM}[219], Vacuum Arc Deposition [220], electron cyclotron resonance- ECR [221]) is a deposition process where a significant fraction of the condensing species have hyper-thermal and low energies (10 eV and greater).

II.3.1 Phenomenology

Energetic condensation is characterized by a number of surface and subsurface processes that are activated or enabled by the energy of the particles arriving at the surface [160, 222] such as desorption of adsorbed molecules, enhanced mobility of surface atoms, and the stopping of arriving ions under the surface.

If the incident ions have enough energy, i.e. between the surface displacement energy and bulk displacement energy, surface diffusion of atoms is promoted but no defects are created in the bulk of the film thus promoting epitaxial growth [223].

When the incident ion energy is increased beyond the bulk displacement energy (usually in 12-40 eV range [224]), the ions can be incorporated into the surface (sub-implantation), the collision cascades under the surface generating defects and intrinsic stress followed by re-

nucleation.

A maximum of intrinsic stress exists for kinetic energies of about 100 eV; the actual value depends on the material and other factors. The existence of such maximum can be explained by insertion of atoms under the surface yet still without significant annealing of the surrounding film [225].

As the energy of these penetrating ions increases, a very short ballistic phase with displacement cascades occur followed by a thermal spike phase (atomic scale heating) with a very high mobility of atoms in the affected volume. The thermal spike can be considered as a transient liquid. As soon as atoms have found their place, i.e. the liquid "freezes", large amplitude thermal vibrations still facilitate diffusion, especially the migration of interstitials inside grains and adatoms on the surface. This favors the annihilation of defects and re-nucleation. When the majority of condensing species are ions, each of the atoms in the growing film is subject to atomic scale heating several times, namely, once when it arrives and again when neighboring atoms arrive.

As the kinetic ion energy is increased, usually by biasing, the sputtering yield from the deposited film is increased and the net film deposition rate is reduced (re-sputtering). Film growth ceases as the average re-sputtering yield approaches unity (between 400 eV and 1400 eV). If the energy is further increased, the surface starts to be etched.

All energy forms brought by particles to the surface will ultimately contribute to broad, non-local heating of the film thus shift the working point of process conditions to higher homologous temperature (T/T_m). This could replace conventional heating and so produce dense films via enhanced surface mobility at generally low bulk temperature. At higher temperature (higher homologous temperature or temperature increase due to the process itself) the grains are enlarged because the increase of ad-atom mobility dominates over the increased ion-bombardment-induced defects and re-nucleation rates [226].

II.3.2 A Structure Zone diagram updated for energetic condensation

The relationship between the coating morphology, the substrate temperature, kinetic energy of the ions and the deposition rate is summarized in the revised structure zone diagram proposed by A. Anders [226](figure II.3.1).

The variation from the Thornton SZD is as follows:

- The linear axis with the homologous temperature T/Tm is replaced by a generalized temperature T*, which includes the homologous temperature plus a temperature shift caused by the potential energy of particles arriving on the surface.
- The linear pressure axis is replaced by with a logarithmic axis for a normalized energy E* describing displacement and heating effects caused by the kinetic energy of bombarding particles.
- The unlabeled z-axis is replaced with a net film thickness t* which will allow us to maintain the familiar qualitative illustration of film structure while indicating thickness reduction by densification and sputtering; it also allows us to include "negative thickness", i.e. ion etching. The axes are comprised of a generalized homologous temperature, the normalized kinetic energy flux, and the net film thickness, which can be negative due to ion etching.

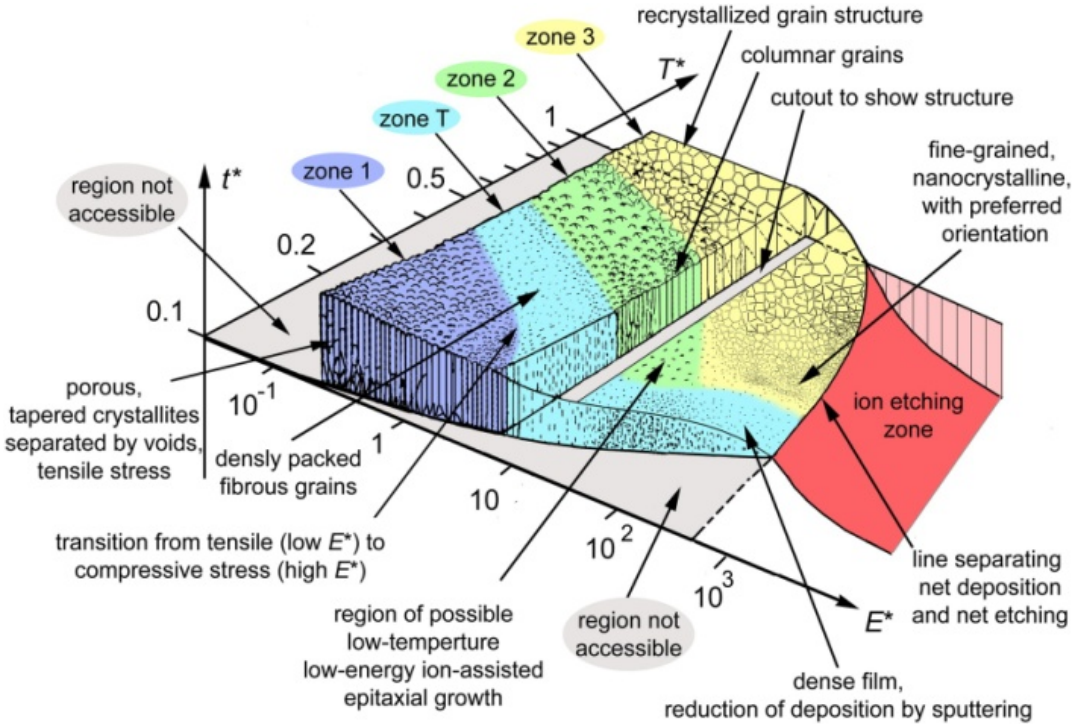

Figure II.3.1: Generalized Structure Zone Diagram [226].

The potential energy includes the heat of sublimation, or cohesive energy, E_c as well as the ionization energy Ei reduced by the work function of the electron needed for neutralization. Thus $E_{pot} = E_c + (E_i - \phi)$. Of course, the ionization term does not apply to atoms but is very significant for multiply charged ions. E_c and E_i are between 1 and 9 eV / atom, and 4 and 10 eV / ion, respectively, for the case of elementary metal films and singly charged ions. φ is about 4 eV for many materials.

A generalized homologous temperature may be defined as $T^* = T/T_m + T_{pot}$ where $T_{pot} = E_{pot}/kN_{moved}$ is the characteristic temperature of a heated region affecting the rearrangement of N_{moved} atoms (k is the Boltzmann constant). Ions arriving at the substrate but not remaining with the growing film can also contribute potential energy. Upon neutralization on the surface they leave behind the ionization energy reduced by the electron work function.

The *kinetic* energy of arriving positive ions is comprised of an initial component from the plasma E_0 plus a change due to acceleration in the sheath, $E_{kin} = E_0 + QeV_{sheath}$where Q is the ion charge state number, e is the elementary charge, and V_{sheath} is the voltage drop between plasma and substrate surface.

II.3.3 Advantages of energetic condensation

The competing processes, mentioned in the previous section, due to the additional energy provided in energetic condensation techniques can induce the following changes to the film growth process (Figure II.3.2):

- residual gases are desorbed from the substrate surface
- chemical bonds may be broken and defects created thus affecting nucleation processes and film adhesion

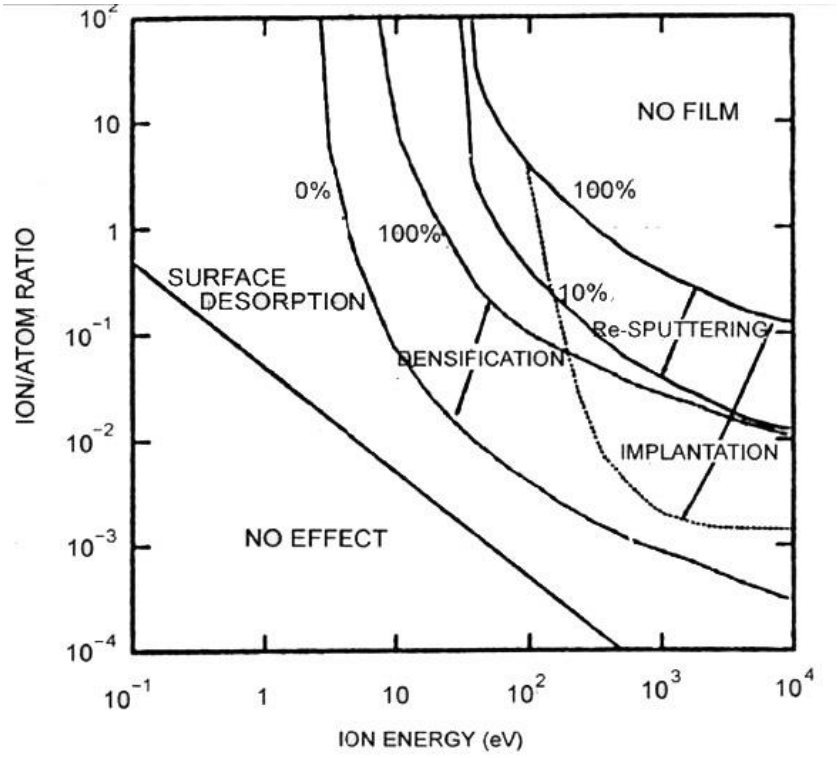

Figure II.3.2: Regions of dominance for various ion-bombardment processes as a function of ion/atom ratio and ion energy [227].

- film morphology changes
- microstructure is transformed
- stress in the film modified

As a result of these fundamental changes, energetic condensation allows added opportunities of controlling some of the film properties. The density of the film may be modified and the crystal orientation may be controlled to give the possibility of low-temperature epitaxy.

II.3.4 Energetic Condensation Techniques: ECR, HiPIMS and Cathodic Arc Deposition

In this work, we have explored the ECR and HiPIMS techniques, with the development at set-up. Cathodic Arc Deposition (CAD) was explored in the framework of a collaboration with Alameda Applied Sciences Corp. (AASC).

II.3.4.1 Electron Cyclotron Resonance (ECR) Plasma Deposition

Electron Cyclotron Resonance is typically used as an ion source for efficient plasma generation, especially to produce high intensity ion beams. It has acquired a unique importance in a wide variety of technical field, such as proton therapy for cancer treatments, advanced semiconductor manufacturing, space industry with electric propulsion devices, particle accelerators for online mass separation and reactive ion charge breeding. It is widely used for film processing, both deposition and etching, as it allows to enhance other deposition technique lacking ion

energy such as molecular beam epitaxy (MBE), chemical vapor deposition (CVD), magnetron sputtering (MS).

Electron Cyclotron Resonance Principle

Electron Cyclotron Resonance is typically used as an ion source for efficient plasma generation, especially to produce high intensity ion beams. It has acquired a unique importance in a wide variety of technical field, such as proton therapy for cancer treatments, advanced semiconductor manufacturing, space industry with electric propulsion devices, particle accelerators for online mass separation and reactive ion charge breeding. It is widely used for film processing, both deposition and etching, as it allows to enhance other deposition technique lacking ion energy such as molecular beam epitaxy (MBE), chemical vapor deposition (CVD), magnetron sputtering (MS).

Motion of a Charged Particle in an Electromagnetic Wave The theoretical study of microwave plasmas is done by solving the equation of motion for an electron in an electromagnetic harmonic field [29, 30, 71]:

$$E\exp(j\omega t), H\exp(j\omega t) \tag{II.3.1}$$

.

It suggests a fluid model of electrons in motion with mean velocity V of the particle and several hypotheses and simplifications:

- The magnetic force of equation (II.3.2) is negligible compared to the electric force.

$$F_M \approx eE \times \frac{V}{c} \tag{II.3.2}$$

.

- No motion of ions, which are heavy compared to the electrons.
- The collision frequency between an electron and heavy particles is given by ν.

The resulting equation of motion is then

$$m_e \frac{dV}{dT} = -eE(t) - m_e V \bullet \nu \tag{II.3.3}$$

.

The first term of the right hand side of the equation (II.3.3) refers to the electric force, and the second term to the friction force. The mean velocity is thus given by

$$V = -\frac{eE}{m_e}\frac{1}{\nu + j\omega} \tag{II.3.4}$$

.

The solution results in several characteristic definitions, such as the root mean square value of electron displacement:

$$r_{rms} = \frac{eE_{rms}}{m_e\omega(\nu^2+\omega^2)^{\frac{1}{2}}} \tag{II.3.5}$$

.

As this value is small compared to the reactor's dimensions, collisions with the walls can be neglected. The electron-plasma angular frequency is given as:

$$\omega_{pe} = (\frac{ne^2}{m_e \epsilon_0})^{\frac{1}{2}} \tag{II.3.6}$$

.

This value depends only on the electron density. It is used to define the plasma density and identification of the different plasma zone types by comparing it with the electromagnetic field frequency [190].

The Debye length is given by

$$\lambda_D = (\frac{k_B T_e}{m_e})^{\frac{1}{2}} \omega_{pe} \approx 743 \sqrt{\frac{T_e}{n_e}\,(cm)} \tag{II.3.7}$$

,

with the electron temperature T_e in volts. The Debye length depends on the electron temperature and density. It represents the length over which a significant variation of charge density can only be observed, and is used as a characteristic dimension of the plasma and the sheath.

For ECR plasmas, the study is very similar, with the exception of two points [188, 189]:

- The collision frequency is much lower due to the very low pressure (in the mTorr range) consequently the MFP is much greater and the electrons reach ionization energy with fewer or no elastic collisions.
- Only the magnetic field linked to the electro-magnetic wave can be neglected. The static magnetic field created by the permanent magnets or the magnetic coils cannot be neglected. It creates the cyclotronic motion of the electrons, which will be discussed in the following section.

The Larmor radius and the Electron Cyclotron Resonance The trajectory of a charged particle in a static magnetic field is determined by the Lorrentz force [192]:

$$F = q(V \times B) \tag{II.3.8}$$

.

Under a constant magnetic field and in the absence of electric force it will follow a helicoidal trajectory with a constant radius. The Larmor radius is the characteristic of this cyclotronic motion which is the gyration of the charged particle in the magnetic field. In ECR, it is specifically used to describe the motion of electrons.

For an electron in a constant magnetic field, the Larmor radius is given by the formula

$$r_L = \frac{\sqrt{2 m_e T}}{eB} = \frac{m_e V_e}{eB} \tag{II.3.9}$$

,

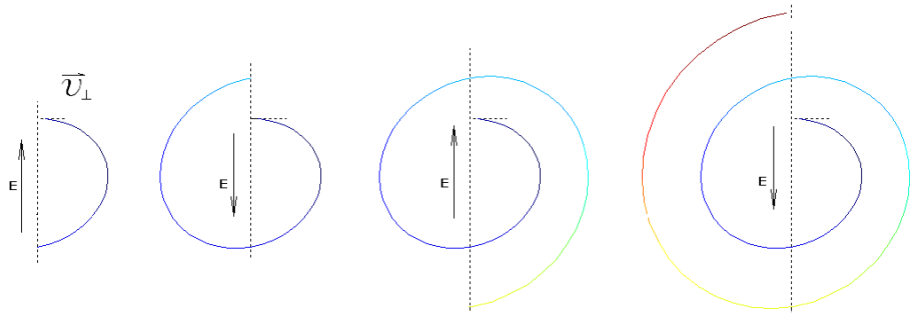

Figure II.3.3: Electron accelerated clockwise by a periodic electric field

where $m_e$is the electron mass, T its kinetic energy, V_e its velocity, -e the charge of the electron and B the magnetic field strength. The subsequent Larmor angular frequency will then be

$$\omega_L = \frac{eB}{m_e} \tag{II.3.10}$$

.

When applying microwaves, the alternating electric field (see previous section) will contribute to this motion. Resonance will exist when the microwave frequency is equal to the Larmor frequency:

$$\omega_{MW} \approx \omega_L \tag{II.3.11}$$

.

This signifies that the motion of the electron in the field created by the magnets is in phase with the electric field generated by the microwaves. In the absence of collisions, the electric field constantly increases the electron velocity, and consequently its kinetic energy beyond the ionization threshold required for ionization and the creation of discharges [228, 229]. The electrons path eventually forms an open helix as illustrated in figures II.3.3 and figure II.3.4. For a standard microwave power supply operating at 2.45 GHz, ECR will occur in the regions where the magnetic field component perpendicular to the plane of oscillation of the electric field vector is equal to 875 Gauss:

$$\frac{eB}{m_e} = 2\pi \times 2.45\ GHz \ \Rightarrow B \approx 0.08753\ Tesla\ \approx 875\ G \tag{II.3.12}$$

.

When the electrons are accelerated to a large enough energy, they will ionize nearby neutral atoms to create a plasma. In practical applications, it is not required to have a uniform magnetic field to create ECR plasma. Most magnetic fields actually have only a limited shell-like ECR region. The RF power absorption mostly happens around the ECR region and keeps the plasma stabilized. The more uniform the magnetic field, the greater is the efficiency of the ECR plasma.

Operating at low pressure is an important condition to sustain the ECR effect. Pressures below 10 mTorr are typically used. Above this pressure, the collision frequency is increased resulting in transition to a collisional microwave plasma [229].

ECR plasmas have distinct features due to the high ionization and gas dissociation levels at low pressures [229].The plasma and deposition process under such conditions depend on

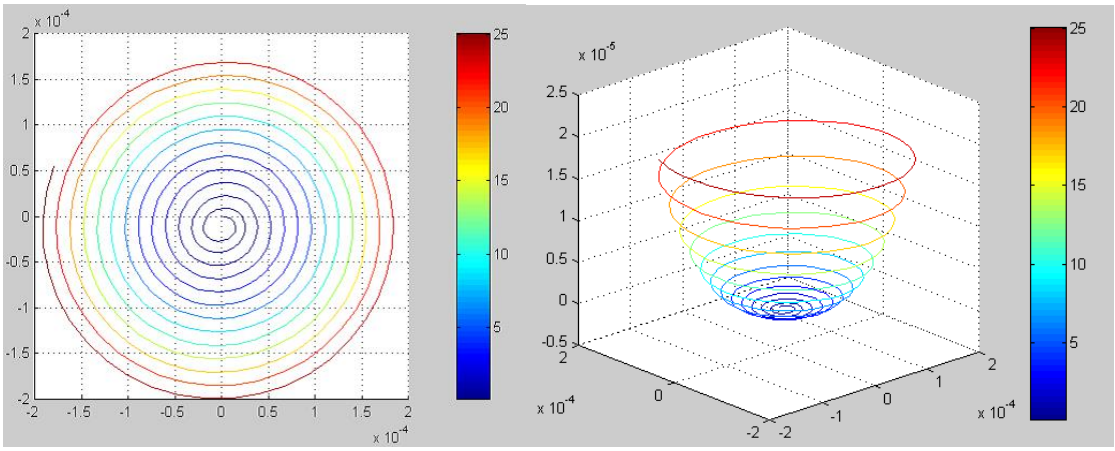

Figure II.3.4: Electron's spiral path in an external magnetic field superimposed with a perpendicular periodic electric field illustrating the ECR effect and the resulting increase in the Larmor radius.

several parameters such as pressure, microwave power, substrate temperature and reactive gas flow if any. The energy and flux of impinging ions depend also on these parameters and can additionally be controlled by biasing the substrate.

Application of the ECR technology to thin films deposition

ECR technology application to thin film deposition has led to the development of different ECR reactor designs [230] including divergent ECR, microwave plasma disk reactors, distributed ECR, integrated ECR and multi-dipolar (or matrix distributed) ECR reactors. Divergent ECR systems are considered to be the most typical ECR reactors. The microwaves, traveling through a rectangular or circular waveguide, are introduced into the vacuum chamber through a dielectric window [230]. One or several magnetic coils wound around the reactor are used to form a magnetic field with a specific strength and profile. The reactor volume may have from one to several ECR regions. The magnetic field profile along the chamber axis can be adjusted in order to localize the ECR region of the plasma where it is necessary [231]. The divergent ECR setup used in this work is similar to the work carried out by Holber [232] and his colleagues from IBM. The basic idea is to use electron cyclotron resonance to create metal ions to do direct film deposition, a process usually called ECR plasma deposition. In Holber's system, Cu was the only material studied, and it worked very well. The ECR plasma deposition is typically a post-ionization process. Neutral or low energy ions are created via alternative techniques such as evaporation, magnetron sputtering, CVD. These species are then ionized by the electrons accelerated to their cyclotron resonance in the ECR chamber. This leads typically to an almost complete ionization [233].

Advantages of ECR deposition

The ECR plasma deposition of Nb has the potential to produce superior quality Nb films as it brings undeniable advantages compared to the deposition via dc-MS, such as:

- Production of singly or quasi-singly charged Nb ions
- Absence of carrier gas leading to freedom from gas inclusions

- Control of the ion energy with applied bias to the substrate
- Quasi conformal deposition

II.3.4.2 Cathodic arc deposition

Cathodic arc deposition is extensively used in industry to deposit extremely hard film of a variety of materials, such as TiN, TiAlN, CrN, ZrN... Its use extends from cutting tools, medical devices, to jewelry. Another wide-spread use is for the production of diamond-like carbon (DLC) films with a high percentage of sp^3 diamond.

The arc evaporation process begins with the striking of a high current, low voltage arc on the surface of a cathode (known as the target) that gives rise to a small (usually a few micrometers wide), highly energetic emitting area known as a cathode spot. The localized temperature at the cathode spot is extremely high (around 15000 °C), which results in a high velocity (10 km/s) jet of vaporized cathode material, leaving a crater on the cathode surface. The cathode spot is only active for a short period of time, then it self-extinguishes and re-ignites in a new area close to the previous crater. As the arc is basically a current carrying conductor it can be influenced by the application of an electromagnetic field, which in practice is used to rapidly move the arc over the entire surface of the target, so that the total surface is eroded over time. This magnetic field can be used to control the motion of the arc. In the case of a cylindrical geometry, the cathode(s) can also be rotated during deposition. By not allowing the cathode spot to remain in one position too long, low melting material targets such as aluminum, can be used and the number of droplets is reduced [234].

The technique provides a high coating rate, and of course the coating flux can be attracted at the desired energy towards the substrate. The arc has an extremely high power density resulting in a high level of ionization (30-100%), multiple charged ions, neutral particles, clusters and macro-particles (droplets). As for ECR deposition techniques, a discharge gas is not needed, contrary to classical sputtering, resulting in no trapped impurities. However, if a reactive gas is introduced during the evaporation process, dissociation, ionization and excitation can occur

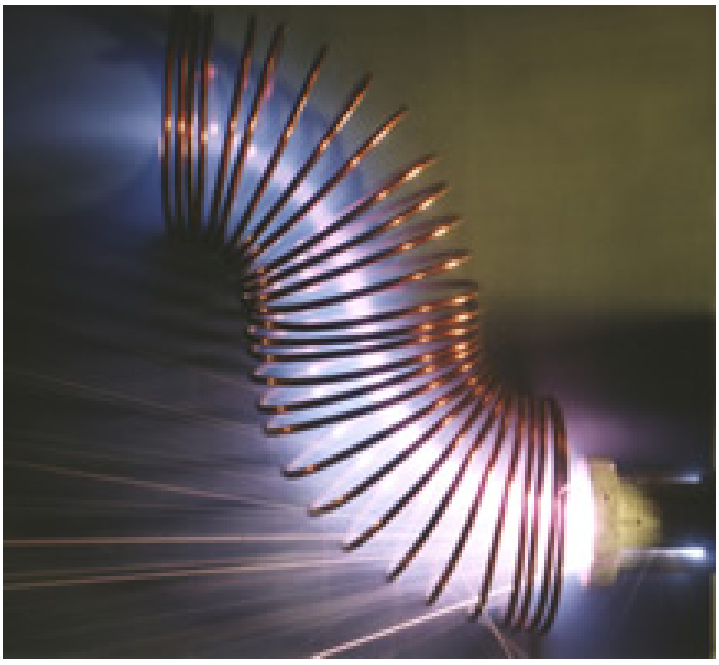

Figure II.3.5: Vacuum arc

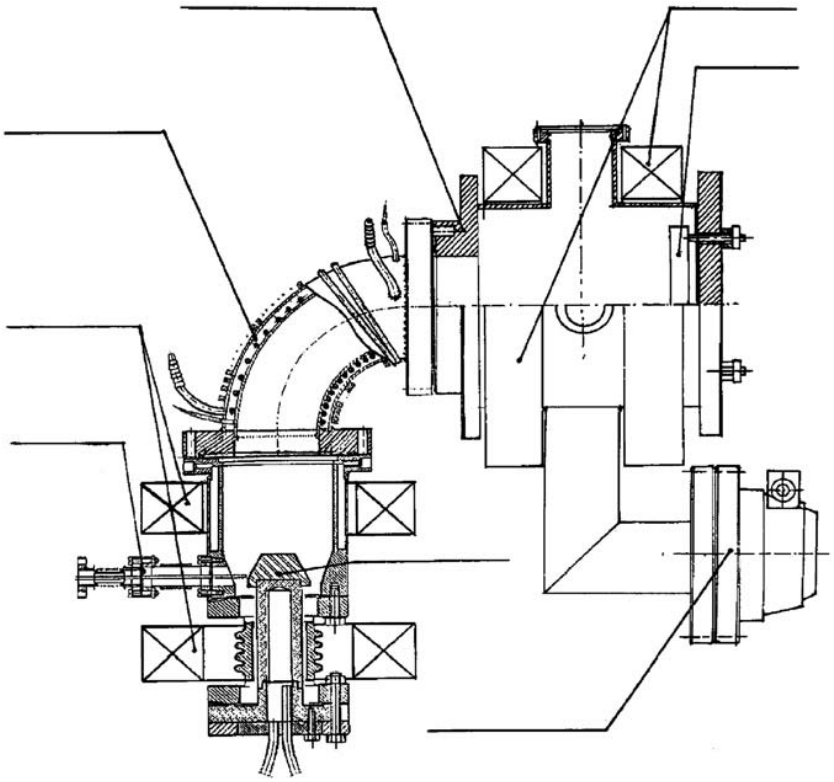

Figure II.3.6: Representation of a typical planar-arc (PA) source with the magnetic filter used for the elimination of micro-droplets emitted from the cathode surface, from [102].

during interaction with the ion flux resulting in the deposition of a compound film.

A strong disadvantage is however the formation of macro-particles because of the explosive nature of the process. If the cathode spot stays at an evaporative point for too long, it can eject a large amount of its material in form of droplets or macro-particles. These macro-particles are detrimental to the performance of the coating as they have a poor adhesion and typically extend through the coating. Magnetic filtering and steering of the ion flux (figure II.3.6) is then needed, in order to remove macro-particles from the flux and to obtain a defect-free coating, adding complexity to the coating system [235, 236].

This technique is currently developed by AASC corp. a collaborator of the thin films research group at Jefferson Lab for Nb thick films and alternative SRF materials.

II.3.4.3 High Power Impulse Magnetron Sputtering (HiPIMS) and its variants

HiPIMS technology is an array of ionized physical vapor deposition techniques. It is a complex variation of conventional sputtering techniques such as dc-MS. It has been of great interest over the last decade, generating extensive developments especially in the field of industrial hard coatings [237]. It relies on 100 μs high voltage pulses of the order of 1 kV compared to the 300 V of the standard dc-MS process. During the pulse, a huge power density is deposited onto the target, of the order of a few kW/cm^2 compared to a few W/cm^2 of the standard DC process, producing a highly dense plasma in which also the target atoms are partially ionized. These can in turn be attracted to the substrate with a suitable bias. A further advantage of the technique lies in the fact that no hardware changes are required compared to a standard dc biased magnetron system, except for the obvious replacement of the power supply.

In the following we will focus on variants of this techniques particularly adapted to the deposition of a refractory metal like niobium and its compounds.

The HiPIMS Discharge

HiPIMS uses very short pulses (Fig. II.3.7) with power densities at the target surface (during the pulse) exceeding the typical dc power density by about two orders of magnitude (of the order of kW/ cm^2). This increases the ionization of the sputtered material creating a metal-based plasma in contrast with a gas plasma for conventional sputtering. Since the duty cycle is small (<10%) the average heating of the target is manageable. The initially high negative bias voltage used, leads to an increased kinetic energy of the charged particles bombarding the film surface, which is known to generate a denser, less columnar structure, where re-nucleation commonly takes place [222]. The energy of the ions produced is in the 20 eV - 100 eV range versus only about 2 - 10 eV in conventional sputtering. Table II.3.1 displays typical parameters for a HiPIMS plasma by comparison to a dc-MS plasma.

Table II.3.1: Plasma parameters for HiPIMS versus dc-MS [238]

Parameter	**HiPIMS**	**dc Sputtering**
Peak Power Density	10^3 Wcm^{-2}	1 Wcm^{-2}
Average Power Density	10^3 Wcm^{-2}	1 Wcm^{-2}
Current Density	1-10^3 Acm^{-2}	0.01-0.1 Acm^{-2}
Discharge Voltage	500-1000 V	500 V
Process Gas Pressure	10^{-3}-10^{-2} Torr	10^{-3}-10^{-2} Torr
Magnetic Field Strength	0.010-0.100 T	0.010-0.100 T
Electron Density	10^{18}-10^{19} m^{-3}	10^{16} m^{-3}
Electron Temperature	1-5 eV	1-7 eV
Degree of Metal Ionisation	30-100 %	<5 %
Ion energy (average for metal ions)	20 eV	5 eV

The HiPIMS plasma breaks down in isolated ionization zones (IZs) [86] that rotate in the

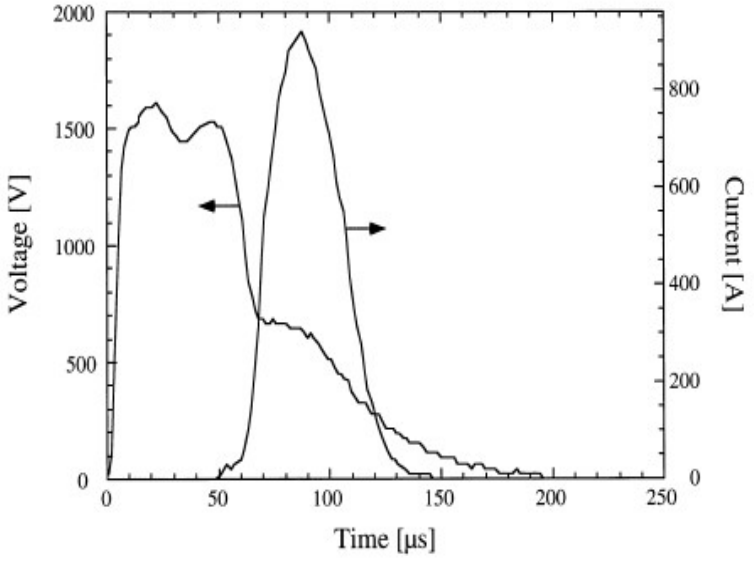

Figure II.3.7: Typical HiPIMS pulse [85]

direction given by the ExB drift, with velocities around 10^4 ms^{-1} and frequencies in the range of about 100 kHz. The positive feedback loop between electron mean free path and ionization leads to "bunching" of plasma ionization zones. These IZs move in ExB direction because ions are "evacuated" from ionization zones by electric field, exposing new neutrals to ionization by drifting electrons. Electrons drift according to the local E and B fields, perpendicular to both, and produce electron jets related to the azimuthal electric field of the plasma zone. From the target point of view, a HiPIMS discharge represents therefore a situation of continuous temporal and spatial change in local sputtering conditions. The physically relevant power density of HIPIMS is much higher than the typically reported average power density. IZs explain how HIPIMS can offer "energetic condensation" in the context of sputtering.

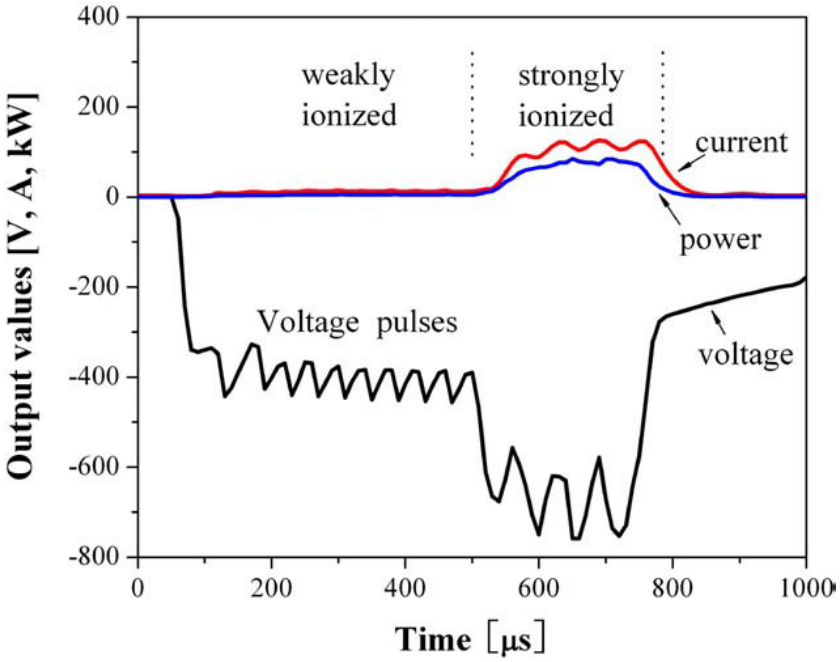

Figure II.3.8: Modulated pulsed power discharge [87].

An alternative approach to HiPIMS, referred to as modulated pulse power (MPP), consists in modulating the pulse such that in the initial stages of the pulse the power level is moderate (typical for dc-MS) followed by a high power pulse. The MPP technique uses longer pulse lengths (up to 3 ms) than classic HiPIMS and utilizes multiple steps and micro pulses in one pulse period. One typical MPP pulse consisting of two stages in one pulse is shown in Fig. II.3.8. The first step is the weakly ionized period, in which low voltage current and power are loaded on the target to ignite the plasma. Then the pulse goes to the strongly ionized period with high voltage, current and power. There can be multiple steps in one MPP pulse to reach the strong ionization period. By varying the pulsing width, frequency, the width and the distance between micro pulses, MPP can generate controllable peak power, a maximum average target power, and a maximum peak current on the target during the strong ionization segment. The micro pulses within the pulse segments offer the flexibility to stabilize the plasma and control the voltage, current and power. A combination of reduced gas rarefaction effects, prevention of sustained self-sputtering, and a relaxation of ion trapping leads to an increase of the deposition rate.

Self-Sputtering

One of the most important and widely recognize effects of reducing power-normalized rate in HiPIMS is due to the fact that a large fraction of sputtered atoms are ionized and some of the newly formed ions return to the target where they contribute to the current, and so the power included in the normalization of rates and cause self-sputtering (figure II.3.9).

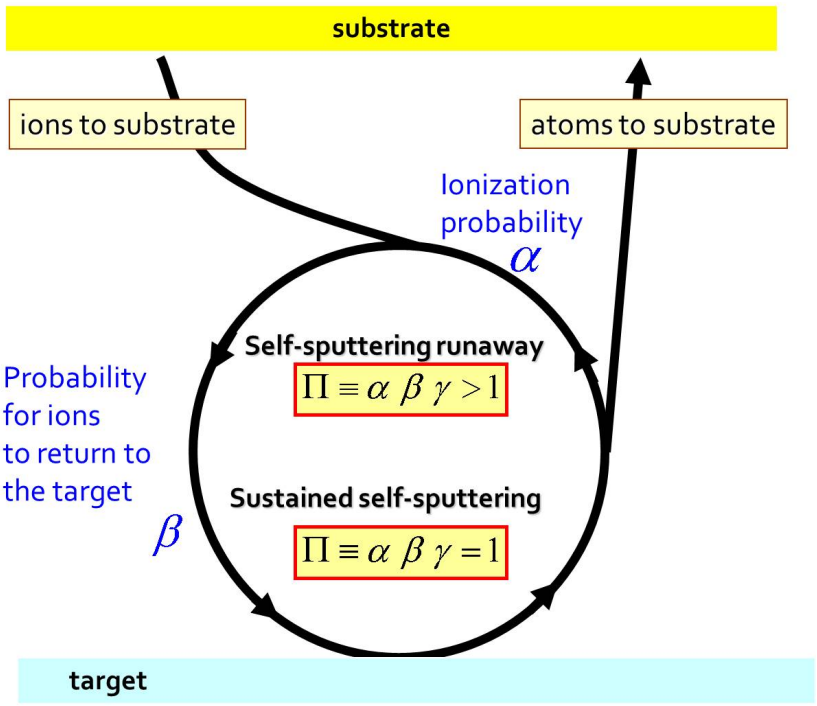

Figure II.3.9: Diagram of self- sputtering in HiPIMS, from [6]

Such *gasless* self-sputtering has been demonstrated for HiPIMS using high sputter yield materials such as copper [110]. The possibility of gasless self-sputtering [109] of Nb, i.e. a HiPIMS mode in which the sputtered atoms satisfy the need for a process gas was explored as mentioned in I.2. Thus no argon (Ar), krypton (Kr) or any other gas is needed, eliminating the issues related to noble gas inclusion.

However, in the case of Nb [111], the sputter yield is not sufficient to produce enough "niobium gas". Rather, noble process gas is always needed to obtain HiPIMS pulses. This leaded into the exploration of the minimum pressure needed to obtain a HiPIMS Nb discharge [112]. It was found that, due to some residual plasma of the previous pulse, the pulse repetition rate is an important parameter that allows pressure reduction while still maintaining a stable and reproducible operation.

Another recent development of the HiPIMS process consists in superimposing a Mid Frequency (MF) discharge in between the HiPIMS pulses to lower the frequency pulses of the HiPIMS pulses. Though they do not depend on MF pulse pattern, the HiPIMS pulses can be spaced as far (or close) in time as desired as long as the MF discharge is present. Conditions are found where the species in the plasma are largely dominated by Nb^+ [113].

Reactive HiPIMS

Reactive HiPIMS differs significantly from reactive dc-MS due to the fact that self-sputtering can quickly become dominant and the sputtering gas (mostly Ar+ and N+) is depleted from

the area in front of the target due to rarefaction. The current wave form for reactive HiPIMS discharges is highly dependent on the pulse repetition frequency unlike in the case of a pure Ar HiPIMS discharge.

NbN, or NbTiN film deposition is relatively straightforward by using the HiPIMS discharge in a reactive gas (N_2) atmosphere. The ion species measured in the studies reported in [112] (figure II.3.10) suggest the formation of dense, textured NbN films.

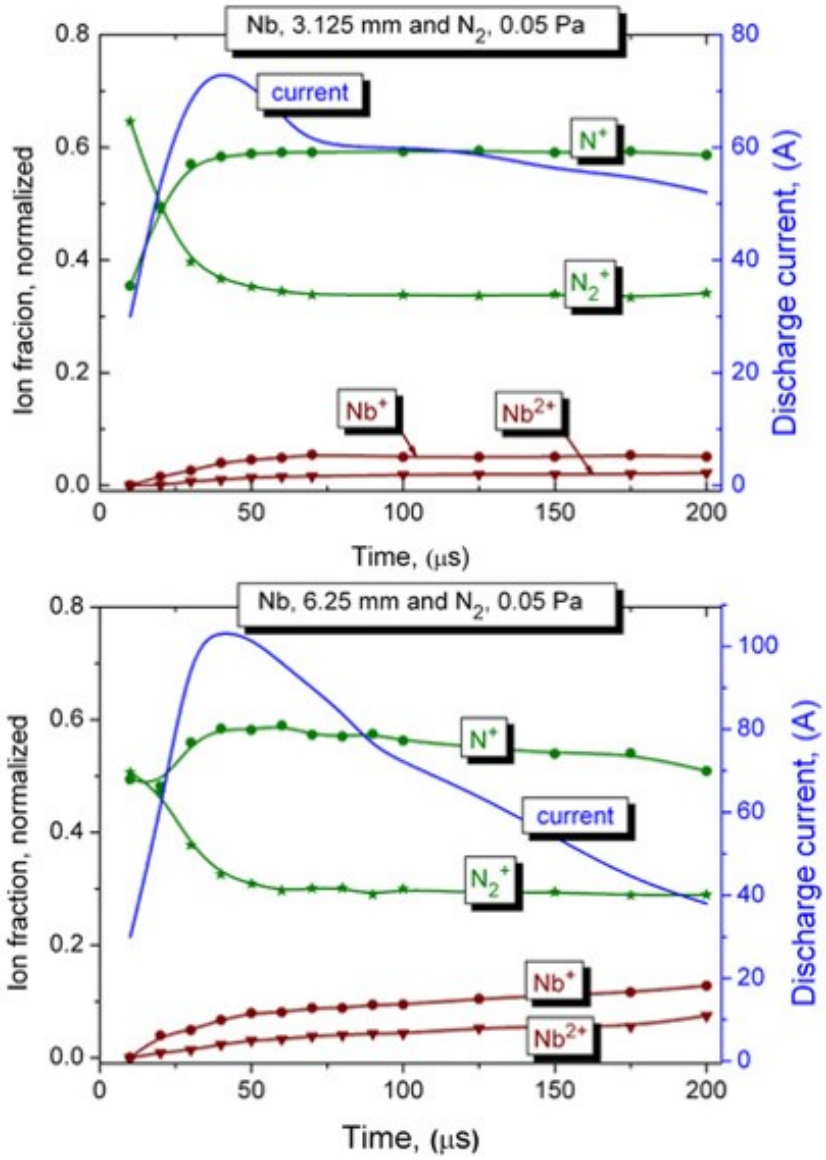

Figure II.3.10: Time-Of-Flight study of Nb HiPIMS with N2 gas [112].

HiPIMS advantages

HiPIMS plasma and the resulting films have been found to display the following characteristics:

- High level of ionization
- High energy ions, tunable with bias voltages
- Possibility to control the film structure

- Phase-tailoring [242] leading to improved performance
- Allows lower temperature process
- Proven improved coverage of complex-shaped surfaces (even for high aspect ratio objects and rough substrate surfaces) [243]
- Enhanced adhesion to substrate
- Film smoothness
- Film densification

Other opportunities in the use of HiPIMS present themselves beyond just the film growth. The substrate can be treated in-situ to clean the surface or remove native oxides, typically with plasma etching (high voltage applied to the substrate) [reference plasma cleaning with HiPIMS], thus generating an optimum surface for film nucleation. By using very high energy incident ions, film forming species can be implanted in the substrate, forming a gradient towards the surface allowing interface engineering for the creation of an adequate template for the SRF film subsequent growth.

Some of the shortcomings of HiPIMS are the reduction of deposition rate and the potential transition to an arc discharge. The deposition rate for the HiPIMS discharge is expected to be in the range 30-80 % compared to a conventional magnetron discharge, with the same average power. The other problem with HiPIMS is the generation of arcs on the cathode surface, especially for target materials with low melting point.

Chapter II.4

Research Approach for the development of bulk-like Nb films and SIS multilayers

This chapter presents both approaches chosen in this experimental work for the development of Nb thick films with bulk-like properties and the development of multilayer SIS structures as a proof of principle for the Gurevich's concept [5] (see chapter I.1).

II.4.1 Nb films

The challenge in developing SRF Nb thin films is to reproduce and go beyond the performance of bulk Nb. While tight correlation with the characterization of real materials has yet to be described, there exists a theoretical framework describing the relevant material parameters of surfaces as they influence SRF properties. Several material factors, highly dependent upon the surface creation conditions, contribute to degraded SRF performance with respect to ideal surfaces. These limiting factors such as intra-granular impurities and lattice defect density, inter-granular impurities and oxidation, surface topography and chemistry, may lead to the reduction of the electron mean free path, thus the reduction of the lower critical field H_{c1}.

Thus, understanding of the film growth dynamics from nucleation to final exposed surface is crucial. The defect density (which determines the electron mean free path) within the RF penetration depth is certainly affected by intra-grain contaminants incorporated during the final stage film growth, but it is also strongly affected by the underlying crystal texture, which is in turn developed from the initial film nucleation process, which necessarily is strongly influenced by the substrate. The development of every stage can be expected to depend strongly on the kinetic energy distribution of the arriving Nb ions. Although the material thickness submitted to the RF field corresponds only to the very top 40 nm of the Nb film, this final surface is dictated from its origin, i.e. the substrate, the interface, and deposition technique (ion energy, substrate temperature...). By opposition to bulk Nb surfaces, the top Nb film surface is anticipated to be the cleanest.

II.4.1.1 Energetic condensation for Nb films

The deposition method chosen to develop engineered Nb films for SRF applications is plasma deposition via electron cyclotron resonance (ECR) as it creates hyperthermal Nb ions in vac-

uum.

The parameter space of the ECR plasma deposition technique is explored to determine the influence of the coating parameters on the structure for Nb films (in relation of the SZD proposed by A. Anders [6]) and their superconducting and RF properties by varying the bias voltage applied to the substrate during deposition and the coating temperature. The film growth mode, epitaxy or fiber growth, is controlled, for metallic substrates by the baking temperature or for insulators by the nature of the substrate (single crystal or ceramic, nanocrystalline or amorphous).

II.4.1.2 Growth in 3 phases

Film growth for SRF applications can be approached in 3 sequential phases. The film nucleation on the substrate can be tailored to enhance film adhesion, minimize intrinsic film stress and favor an optimum structure. One can then grow an appropriate template for subsequent deposition of the final RF surface, and then followed by deposition of the final surface optimized for minimum defect density. One can also seal the final surface (oxide layer, cap layer) to protect the SRF surface from any exterior or post-deposition potential degradation. Following such an approach could be a path towards bulk-like engineered Nb films.

In an effort to tailor the interface, ECR Nb films have been grown on a variety of substrates, insulating and metallic, single crystal, polycrystalline and amorphous.

II.4.2 Development of Multilayer SIS films

The SIS concept [5] proposes to take advantage of high-T_c superconductors without being penalized by their lower H_{c1}. SRF cavities are coated with alternating superconducting and insulating (SIS) layers with a thickness d smaller than the penetration depth λ so the Meissner state can be retained at a magnetic field much higher than the bulk H_{c1}. The thin higher-T_c layers provide magnetic screening of the bulk superconducting cavity delaying vortex penetration. The BCS resistance is also strongly reduced because the envisioned superconducting materials (Nb_3Sn, NbTiN ...) have a larger gap Δ than Nb. With such structures, Q-values at 4.2 K could be increased a couple orders of magnitude above Nb values.

The materials chosen to develop SIS multilayer structures in this work are NbTiN and AlN. Although NbTiN is not necessarily the optimum material for ultimate enhancement of SRF surfaces, its relative ease of fabrication and stability at room temperature make it an adequate superconductor to develop a proof of principle for the SIS concept. AlN is chosen due to its good insulating properties and similar B1 structure. It is also found, in literature, to enhance the superconducting properties of NbN and NbTiN, especially for very thin films.

Particular attention is given to the interface insulator/substrate, superconductor/insulator due to the necessity of these films to be very thin to implement the enhancement proposed by the SIS concept.

As a first approach, SIS structures were developed with reactive dc-MS. The optimization was performed by defining the Target composition, sputtering gas pressure, reactive gas ratio and discharge power.

In view of the potential benefits of energetic condensation, the aim is also to apply it through the HiPIMS process to the development of alternate SRF materials and SIS multilayer structures and further improve the results achieved with dc-MS.

A concept for coating cavities with multilayer structures based on cylindrical HiPIMS is also under development.

Part III

Characterization Methods

As described before, particular material characteristics have been implicated as contributing to degraded SRF performance of candidate thin films. The material and superconducting properties of SRF films, Nb thick films or SIS multilayers, need to be carefully evaluated to determine their influence on the films RF performance. This section gives an overview of the different characterization techniques used for this work.

Chapter III.1

Cryogenics and RF characterization Methods

As seen in Part I, SRF thin films are useful for accelerators at cryogenic temperature (typically 2 K for Nb). It is then important to characterize the superconducting properties film with cryogenic methods and determine their RF performance.

III.1.1 T_c and RRR via the four-point electrical probe method

RF measurements to evaluate the RF surface resistance for coated samples are complex and they need a well calibrated RF and cryogenic systems. Preliminary studies on samples are needed to understand if the modified coating technique is valid and if it introduces significant changes in the film quality [244].

One of the common figure of merit used to define the quality of a material is *Residual Resistivity Ratio (RRR)*. The RRR is an immediate estimate of the film quality: the higher the value, the higher the purity of the material. It is a direct measure of the mean free path and quality of the film that is affected by any present scattering center.

The RRR and the transition temperature T_c of films are measured with the so-called *four-point method*. The film dc electrical resistance, R, is measured at room temperature (R_{300K}) and just above the superconducting state, at 10 K (R_{10K}) for Nb. As long as the sample geometry is homogeneous, the measurement does not depend on its geometry. In case of an inhomogeneous sample, the four leads need to be connected in line to avoid spurious effects [245, 246]. RRR is a dimensionless parameter as the geometric dimensions remain constant with temperature and get eliminated in the ratio.

The low temperature resistance of the sample is fixed at 10 K and the RRR is calculated with the following formula:

$$RRR = \frac{R\ (300K)}{R\ (10K)} \approx \frac{\varrho_{phon}(\ 300K) + \varrho_{res}}{\varrho_{phon}\ (\ 10K) + \varrho_{res}} \tag{III.1.1}$$

$\rho_{phon}(\ (T)$ is the resistivity due to the electrons-phonons collision which decreases with temperature.

ρ_{res} is the residual resistivity and is temperature independent.

The electrical resistivity, ρ, is inversely proportional to the relaxation time, τ, which enters

in the definition of the mean free path l of a conduction electron, l=$v_F\tau$, v_F being the Fermi velocity. The product ρl can be considered constant for a given metal (3.75 ± 0.05 x $10^{-6}\Omega m^2$ for Nb) and can be used to estimate the mean free path from the resistivity.

At 300 K, the net resistivity,$\rho = \rho_{phon}$ (T)+ ρ_{res}, is usually dominated by collisions between the conduction electrons and the lattice phonons. A 10 K, it is dominated by collisions with impurity atoms and lattice imperfections. The value of ρ_{phon} (T) can be assumed to be 1.45± 0.05 x 10^{-7} Ω.m at 300 K and negligible at 10 K. ρ(10K) and the electron mean free path l can then be estimated from the measured RRR.

The transition temperature $T_c$and the transition width ΔT_C are calculated from the resistance curve with the following formulae:

$$T_c = \frac{T_{(90\%)} + T_{(10\%)}}{2} \quad and \quad \Delta T_c = T_{(90\%)} - T_{(10\%)} \tag{III.1.2}$$

where $T_{(90\%)}$ is the temperature corresponding to the 90% of the resistance before the transition and $T_{(10\%)}$ is the temperature corresponding to the 10% of the resistance before the transition. ΔT_c is the error on the critical temperature estimation.

Testardi and Mattheiss studied the relation between RRR and critical temperature for thin niobium films [247]. It is an universal curve independent from the coating technique applied.

From Matthiessen's rule, the niobium resistivity, at low temperature and normal state, is related with RRR and phonon resistivity at 300 K ρ_n:

$$\varrho_n\,(10K) = \frac{\varrho_{ph}}{RRR - 1} \tag{III.1.3}$$

The four-point probe measurement setup used in the present work is shown in figure III.1.1. Four wires (or probes) are attached to a sample surface. A constant current flows the length of the sample through probes labeled 1 and 4 in the figure. This can be done using a current source or a power supply as shown. The sample's resistance to the flow of electrical current causes a potential drop as the current flows along the sample, for example between the two wires (or probes) labeled 2 and 3 in the figure. The resistance of the sample between probes 2 and 3 is the ratio of the voltage drop to the value of the output current of the power supply. A multiplexed system with 4 boards with 8 seats each was used to accommodate the large number of samples.

The sample temperature is carefully controlled and the current intensity is chosen as not to deposit any significant heat in the sample. A Labview program is used to acquire the resistance curve from 300 K to below the transition temperature (typically 5 K). A current of 10 mA is applied to the sample (for ECR samples) and the voltage is measured. The same method is used for the temperature probe, applying a direct current of 10 mA, the resistance is measured and the temperature is obtained from the calibration curve.

Method for RRR measurements for Nb films deposited on metallic substrates

In the case of Nb films deposited on Cu, the signal from the Cu substrate overwhelms the measurement. To get rid of this artifact, the Cu substrate is dissolved in a solution of ammonium persulfate. The Nb film is then stabilized on double-sided kapton tape on glass slides. Although he film is somewhat altered by the process and manipulation, the resulting value measurement constitutes a lower value for RRR. Typically strain induced by the difference in lattice match from the substrate is also released when the substrate is removed.

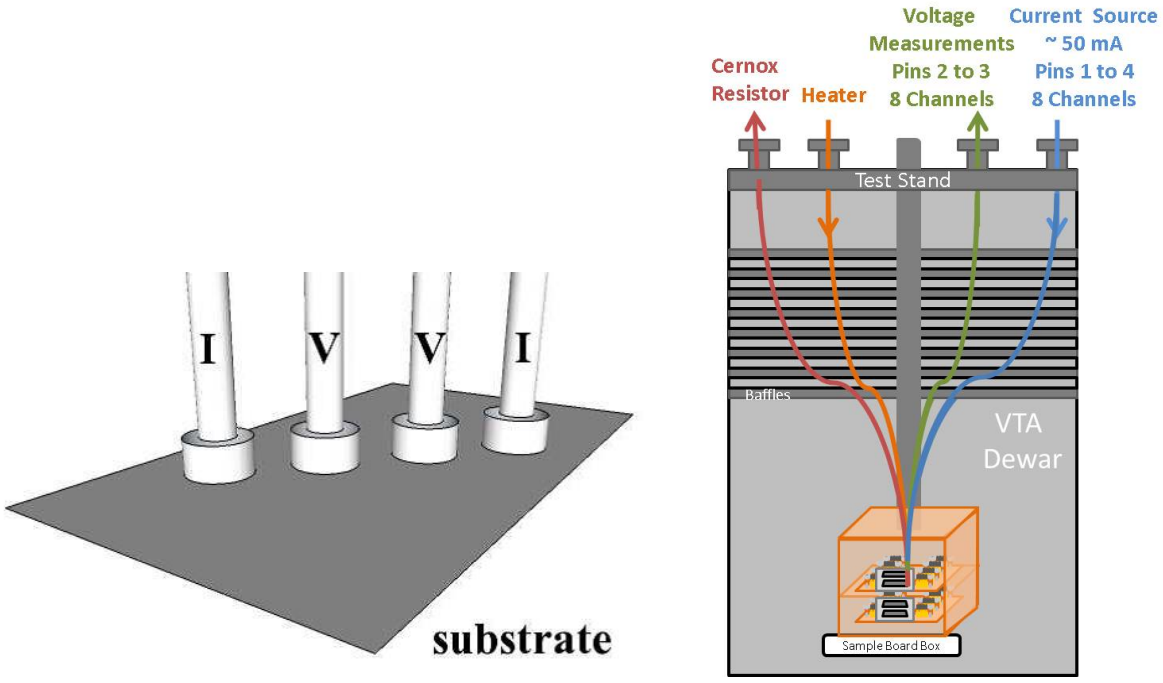

Figure III.1.1: Schematic of a four point probe measurement and test stand setup

III.1.2 SIC measurement: surface resistance and penetration depth

As seen, in chapter I.2, the performance of SRF cavities is qualified by the RF surface resistance at operating temperature, typically bellow 4.2 K, the liquid He temperature. It is then important to qualify the RF performance of thin films to determine their adequacy for SRF applications. Meaningful RF surface resistance measurements on samples are convoluted. There are several setups available in different institutions but they all have their limitations.

Such measurement is performed at JLab with the Surface Impedance Cavity (SIC) [27]. The system consists of a TE_{011}-mode cylindrically symmetric niobium cavity loaded with a sapphire rod in order to keep the frequency of the system relatively low (7.5 GHz) while maintaining the physical dimensions as small as practicable. The sample is presented as a non-contacting end plate of the resonator, separated from the niobium body by a triple choke joint. The sample is separated from the planar end face of the sapphire rod by a 1 mm gap. The flat sample size: 50 mm diameter; active RF area: 20 mm diameter; RF frequency: 7.5 GHz. The sample surface exposed to $> 90\%$ of the peak magnetic field consists of an annular ring of width ~2.8 mm and mean diameter 4.0 mm.

The surface impedance can be measured as a function of temperature and field. The sample is thermally isolated from the rest of the RF structure (maintained < 2 K) and its temperature may be independently regulated at some higher temperature and dissipated heat sensed in a calorimetric fashion. The duty cycle of the pulsed RF source is set to provide a small but accurately measured temperature rise for the field value selected.

The calorimeter sensitivity can be selected by the design of its support structure to operate at low values of field and surface resistance, R_s. In order avoid excessive excursions in temperature at high fields, the RF source may be pulsed and the duty factor accurately measured.

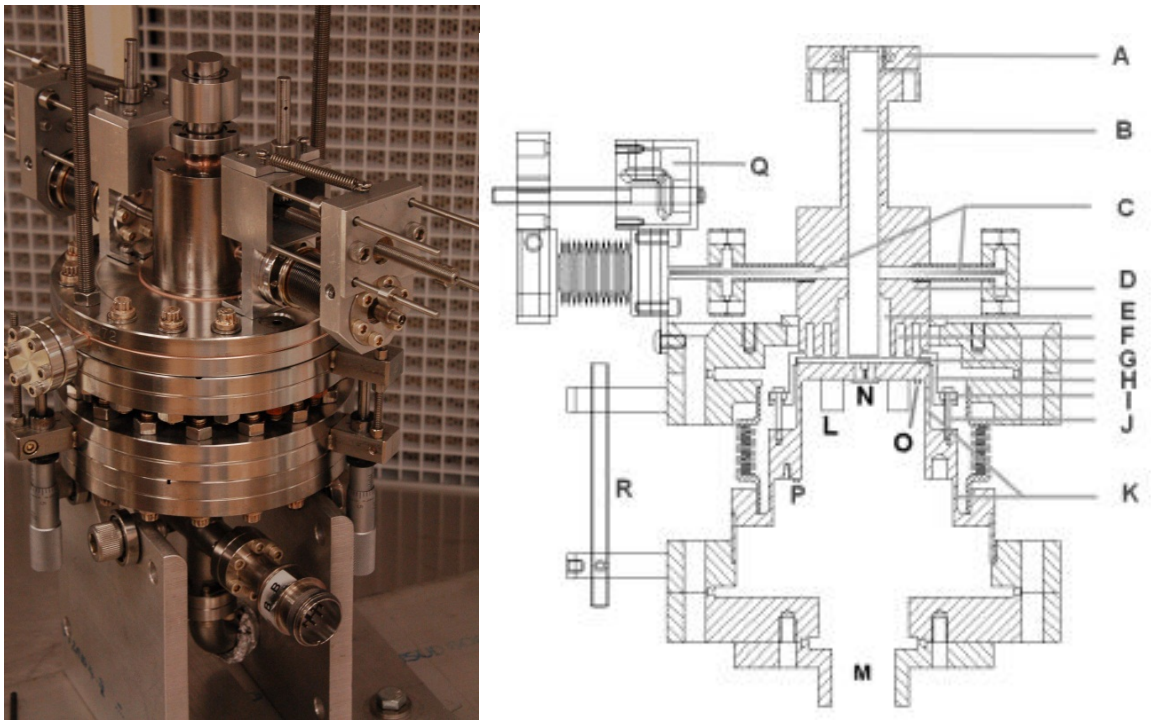

Figure III.1.2: JLab surface impedance characterization (SIC) system and schematic of the SIC TE_{011} cavity, calorimeter, and variable input coupler mechanism

Figure III.1.3: Relative magnetic field distribution on SIC sample. r/(r_0=10mm)

The power dissipated on the sample is given by:

$$P_s = 3.7x10^7 R_s B_{max}^2 watts \tag{III.1.4}$$

,

where R_s is in ohms, and B_{max} is in Tesla.

The system can directly accommodate flat 50 mm (2") diameter thin film samples.

The surface impedance is measured as a function of magnetic field and temperature from 1.9 K to 9.4 K. With the normal state surface impedance at 10 K, one can determine the surface value of the electronic mean free path and surface B_{c1}.

The superconducting penetration depth λ at low field can be measured by carefully tracking the cavity frequency with temperature as the sample temperature is swept slowly back and forth across the transition temperature (SIC sensitivity: 30 Hz/nm) while the rest of the cavity is

held at 2 K. The RRR of the RF surface within the penetration depth measurement can also be determined.

III.1.3 Point contact tunneling for superconducting gap measurement

Measurements of the surface superconducting gap Δ of Nb films were performed at ANL and IIT on a selection of ECR Nb films with the point contact tunneling technique [250, 251].

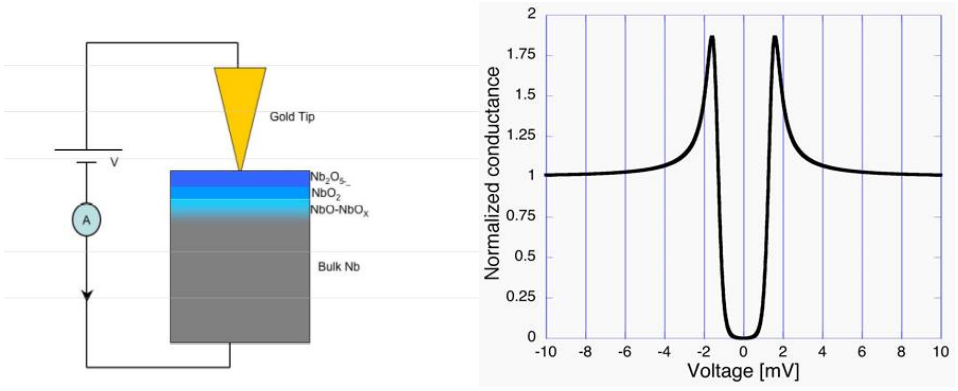

(a) PCTsetup (b) PCTcurve

Figure III.1.4: Point Contact Tunneling setup from [250, 251]. B. Typical dynamic conductance curve for a bulk Nb sample.

Tunnel junctions are formed by using a mechanical contact between the sample and an Au tip attached to a differential micrometer screw (figure III.1.4) fully described in [250]. Figure III.1.4 shows the dynamic conductance curve (dI/dV versus V). Typically, the measurement is conducted by forming a series of independent junctions in as single run by completely retracting the Au tip (~1 mm) and then re-advancing the tip until a tunnel current is observed. These junctions probe different regions over an area estimated to be greater than 10 μm^2.

The data is analyzed using the tunnel current in superconductor-insulator- superconductor (S-I-S) and superconductor-insulator-normal metal (S-I-N) junctions written as

$$I(V) = c\int_{-\infty}^{\infty} |T|^2 \rho_1(E)\,\rho_2(E+eV)\,[f(E) - f(E+eV)]\,dE[250], \tag{III.1.5}$$

Where $\rho_1(E)$ and $\rho_2(E)$ are the quasi-particle DOS in the two electrodes, $c$is a proportionality constant, $f(E)$is the Fermi-Dirac distribution function which describes thermal smearing and $|T|^2$ is the tunneling matrix element [252].

Measurements on bulk Nb [253] give Δ of about 1.55 meV which is in good agreement with previously published experiment [254].

III.1.4 SQUID magnetometry

Another physical figure of importance, especially for the development of superconducting thin films appropriate for SIS structures, is the lower critical field H_{c1}.

H_{c1} measurement were performed at the College William & Mary with a superconducting quantum interference device (SQUID) magnetometer, the Quantum Design Magnetic Property Measurement System (MPMS) [255]. The MPMS measures the magnetic moment of small samples as a function of temperature and applied field using a secondary derivative coil (see figure III.1.5 left), consisting of two outer coils oriented in one direction and two inner coils oriented in the opposite direction. These coils are made of superconducting wires which are connected to a SQUID. The SQUID is a tool that takes advantage of the Josephson effect, first predicted by Brian Josephson in 1962[256] and experimentally observed by Philip Anderson and John Rowell in 1963 [257]. The Josephson effect is observed when two superconductors, separated by an insulating material, are coupled by a super-current tunneling through the separating material. This geometry is called a Josephson junction. SQUIDs have a Josephson junction installed in the current loop that is connected to the detection coil which acts as a current to voltage converter. If the sample size is sufficiently smaller than the detection coil, the output voltage (figure III.1.5 right) can be modeled as the movement of a point-source dipole moving through the coil and using standard fitting algorithms is used to determine the magnetic moment of the sample.

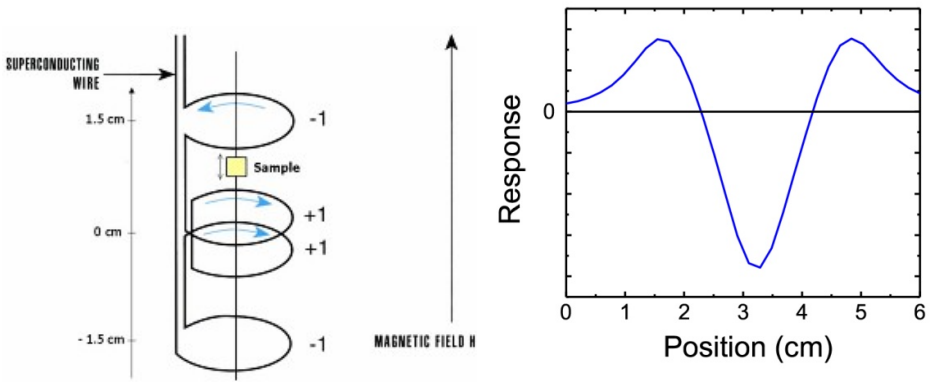

(a) squidpickupcoils (b) SQUIDresponse

Figure III.1.5: (left) The SQUID coil geometry showing the four detection coils, the sample and the direction of the applied field. The directions of the arrows show the opposing directions of the inner and outer coils.

The H_{c1} measurements are done with two different methods which are compared. The first method involves isothermal ramping of the applied field. Once the sample temperature is brought below T_c and fixed, the moment is measured as the applied field increases to achieve a curve similar to the one represented in figure III.1.5. However, if flux pinning occurs, H_{c1} does not occur at the peak moment, but at the first deviation from the Meissner slope. When flux pinning occurs and the magnetization is not reversible, a procedure develop by Böhmer at al. is implemented [258].

This procedure accurately determines $H_{c1}$by measuring trapped magnetic moments that appear after the application and removal of an applied field. The first step is to do a zero field cool (ZFC) down into the superconducting state, where the sample's magnetic moment is measured. An external magnetic field is then applied and removed and the magnetic moment is measured once more. The sample's magnetic moment value before the field application is subtracted from the value after the filed application. The sample is then warmed up into the normal state and the procedure is repeated for different field values. H_{c1} is determined to be the field at which there is a difference in the two magnetic moments, indicating filed penetration.

Any misalignment between the film' surface and the direction of the applied field will lead

to a decreased value for the measured critical field. Thus, even when the samples are aligned as well as experimentally possible, the field measured will represent a lower limit of H_{c1} since the perpendicular component of the applied field would promote earlier vortex penetration.

The magnetic moment of a thin film can be determined by:

$$m = \frac{VH}{4\pi}(cos^2\theta + \frac{1}{1-D}sin^2\theta), \tag{III.1.6}$$

where m is the magnetic moment, v is the sample volume, H is the applied filed, θ is the angle between the sample' surface and the applied field and d is the demagnetization factor. The optimal alignment is achieved when m is minimized by achieving θ=0 (thus 1-D=0). For the measurements presented in this work, the sample position was adjusted to achieve a minimum magnetic moment, thus aligning the sample surface as parallel as possible with the applied magnetic field.

In an SRF elliptical cavity, magnetic fields always travel parallel to their surface and there are no edge effects. However, edge effects can be of concern in SQUID measurements. During SQUID measurements with the field oriented parallel to the surface, the applied magnetic field will also interact with the edges of the sample, causing a perpendicular contribution, and potentially the backside or the interface of the film and its substrate depending on the substrate magnetic behavior.

As mentioned in chapter I.4, Antoine et al. considered the contribution of the samples' edge effects on the overall behavior of the multilayer [151, 152]. In addition to DC SQUID measurements, an AC third harmonic analysis [100, 259, 260] was used to measure the superconducting properties of the samples. Because this measurement technique uses a local probe which is much smaller than the sample, edge effects do not alter the results. The technique probes the sample only on the side of the multilayer replicating an SRF cavity where the niobium will only see a magnetic field attenuated by the SIS coating. The DC and AC measurement results were consistent with each other. This gives us confidence that the DC SQUID measurement can be considered to represent accurately the samples.

Chapter III.2

Methods for Solid State Physics

III.2.1 Microstructure and morphology analyses

The structure of films deposited on substrates may differ significantly from that of the bulk material. It will definitely vary from one substrate type to another.

III.2.1.1 X-ray Diffraction

XRD is a powerful non-destructive method used to measure structural properties, such as residual stress, grain size, epitaxial relations, texture, defect structure, and crystal structure. The X-rays have wavelengths in the order of a few angstroms, the same as typical interatomic distances in crystalline solids. When certain geometric requirements are met, X-rays scattered from a crystalline solid can constructively interfere, producing a diffracted beam. The condition for constructive interference is given by the Bragg's law:

$$n\lambda = 2dsin\theta \tag{III.2.1}$$

,

where n is an integer, λ is the wavelength, d is the interatomic spacing, and θ is the diffraction angle. The diffracted beam intensity will depend on several factors such as the chemical composition of the film and the local arrangement of the atoms. Detailed descriptions of the technique are found in reference [261, 263, 262]. It should be noted that (III.2.1) is only valid for $\lambda \leq$ 2d, thus requiring the short wavelengths found in X-rays in order to probe the lattice spacing.

The x-rays are scattered by the electrons and the resulting angular dependent intensity distribution is measured with a detector. Using an x-ray wavelength in the order of the atomic distances within the sample structure ($\sim$ 1) results in extended interference patterns. As the probability of the scattering process is quite low, x-rays penetrate deep enough into the sample (up to several hundred nanometers) to give detailed information about the internal structure. The scattered intensity can be mapped in angular space or reciprocal space (often also referred to as K-space or Q-space). Thus, it is not possible to take a direct image of the real space sample structure with this method.

Combining the information from the reflectivity and the Bragg range provides a comprehensive insight into the sample architecture and film quality including information about the film thickness, the interface roughness, the electron density, the crystal structure, the lattice pa-

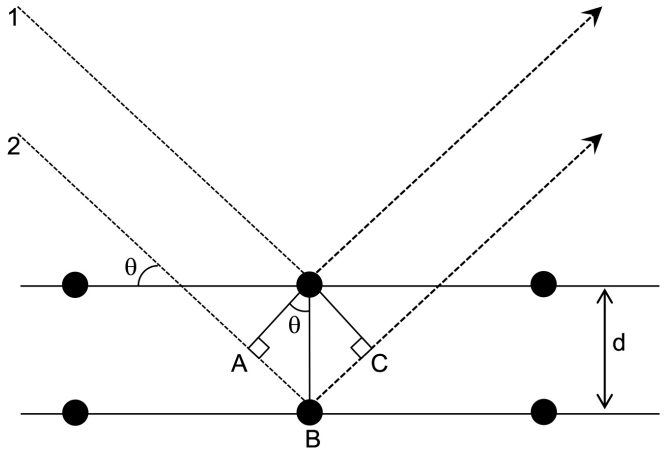

Figure III.2.1: Constructive interference of two X-rays with atomic planes

rameters (including strain), the surface miscut, the crystal mosaicity and the coherence length of the individual layers.

The XRD peaks are obtained due to constructive interference of a monochromatic beam scattered from lattice planes at specific angles (see figure III.2.1). Therefore, the x-ray diffraction pattern is representative of the crystal structure of given sample. XRD can also provide information of preferred orientation (texture), average grain size, residual stress, and crystal defects. Three types of XRD configurations (conventional, glancing incident and rocking) were recorded to study the films generated for this work.

The crystal structure of the films was characterized by monochromatic Cu-Kα radiation (1.5418 Å) on a Philips X-ray diffractometer Pan-analytical operated at 45 kV and 30 mA.

Conventional Bragg-Brentano Configuration

A typical XRD scan, Bragg-Brentano or θ - 2θ, measures the intensity of diffracted x-rays and a function of 2θ. A peak in intensity around a given angle indicates that there are atoms arranged in a periodicity that can be calculated using (III.2.1). In this arrangement, the incident and detection angles relative to substrate plane were equal during all the measurements. In this arrangement, the only information related to the planes parallel to the substrate surface is obtained. Data taken from conventional XRD scans can also be used to determine the size of the crystallites in the films.

Considering a single crystal film that is free of defects, grain boundary, or any other scattering centers, reflections from the planes would approach delta function. In a crystal that contains scattering centers, the reflection that occurs would be broadened over a range of angles. In polycrystalline materials, the presence of crystallites and grain boundaries reduce the periodicity of the crystal lattice thus broadening the reflection peak. The Scherrer method uses an analysis of x-ray data from a θ - 2θ scan to calculate the average crystallite size in a polycrystalline material [265]. For a polycrystalline thin film, the crystallite size is given as:

$$D = \frac{K\lambda}{\Delta_{2\theta}\cos(\theta)} \tag{III.2.2}$$

λ is the x-ray wavelength (0.15418 nm) for Cu $K\alpha$; 2θ is the location of the peak cor-

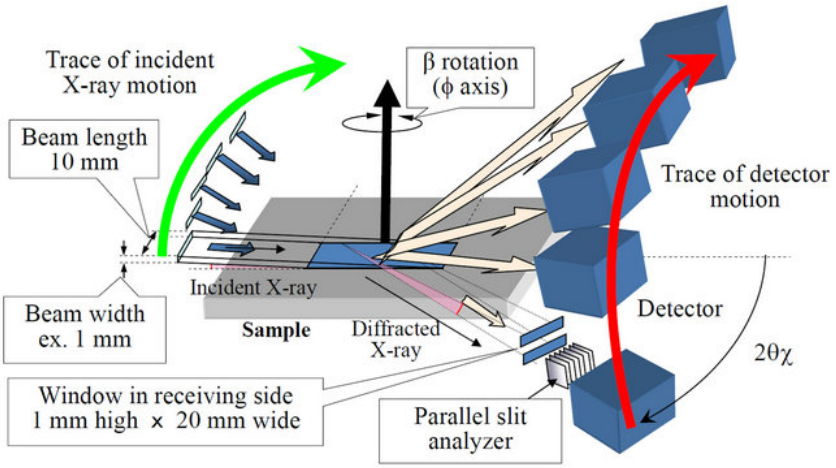

Figure III.2.2: Schematic of conventional and rocking XRD configuration-X-ray diffraction in (a) conventional configuration θ- 2θ with the incident angle being the same as Bragg angle, (b) and (c): change of the incident angle for a fixed Bragg angle to obtain rocking curve.

responding to the (002) orientation. $\Delta_{2\theta}$ is the full with at half maximum (FWHM) of the peak and K is the appropriate shape factor (0.94 for cubic crystals) [266, 267]. Ultimately, the Sherrer equation gives a lower limit of the grain size sine other factors such as strain or instrumental effects can result in further peak broadening. Because the X-rays are probing the entire sample and sampling multiple grains, the calculated grain size represents an average of all grains within the probed region.

Rocking Curve

Pole figure or rocking curve measurements (ω-scan) are an efficient way to reveal the polycrystalline structural character in a material.

In real crystals, all of the atoms will not perfectly arranged in a lattice. Instead, there will be small regions or grains in which the atoms are arranged on a lattice. There can be a small misalignment between individual rains leading to what is called a mosaic structure. The degree of mosaicity in a crystal can be determined using a rocking curve. In this XRD configuration, the detector is fixed at diffraction angle of interest and the sample is rocked through an angular range, bringing the plane of interest in and out of the Bragg condition. The width of the measured peak measured at its half-maximum (FWHM) contains information of the amount by which the measured plane is off the surface normal and is often referred to as degree of orientation or texturing of the specimen. A schematic of conventional and rocking XRD configuration is shown in Figure III.2.2.

Glancing-Incident X-Ray Diffraction (GIXRD)

Glancing incident angle XRD is used to study the diffraction pattern of films deposited on various substrates with suppressed peaks interfering from the substrate. In this configuration, the incident angle θ is fixed at grazing angles of 1 to 10° and the diffraction profile is recorded by detector scan only.

Since the penetration depth of the x-ray in this configuration is lower, the substrate effect is reduced and only the surface layers of the film are measured. The GIXRD method can also be used to measure the residual stress inside the film. Diffraction patterns obtained in

conventional arrangement contain information averaged over a larger fraction of the sample. Whereas, analysis of diffraction patterns acquired at gradually increasing incident angles allow quantitative residual stress in the films.

The crystal structure and texture were investigated via X-ray diffraction (XRD) $\theta/2\theta$ and pole figure scans with a four-circle PANalytical X'Pert PRO-MRD diffractometer. The diffractometer scanned over a 2θ range from 30° to 120° at step size 0.02°. The slit aperture of the X-ray source is 10×17mm. The scan has a divergence slit of 0.5°, a receiving slit of 0.1° and use a line focus Mirror primary optics with Cu $K\alpha$ source. The source with wavelength λ_{Cu}=1.54 Å was operated at 45 kV and 40 mA. XRD Pole Figures in Stereographic Projection format were used to investigate the "texture" (grains distribution in-plane) [261].

III.2.1.2 Electron Backscatter Diffraction (EBSD)

Electron backscattered diffraction (EBSD), also known as backscattered Kikuchi diffraction (BKD) is a micro-structural crystallographic technique used to examine the crystallographic orientation of many materials, which can be used to elucidate texture or preferred orientation of any crystalline or polycrystalline materials [268]. EBSD can be used to index and identify the seven crystal systems, and as such it is applied to crystal orientation mapping, defect studies, phase identification, grain boundary and morphology studies, regional heterogeneity investigations, material discrimination, microstrain mapping, and using complimentary techniques, physico-chemical identification. Traditionally these types of studies have been carried out using x-ray diffraction (XRD), neutron diffraction and/or electron diffraction in a TEM.

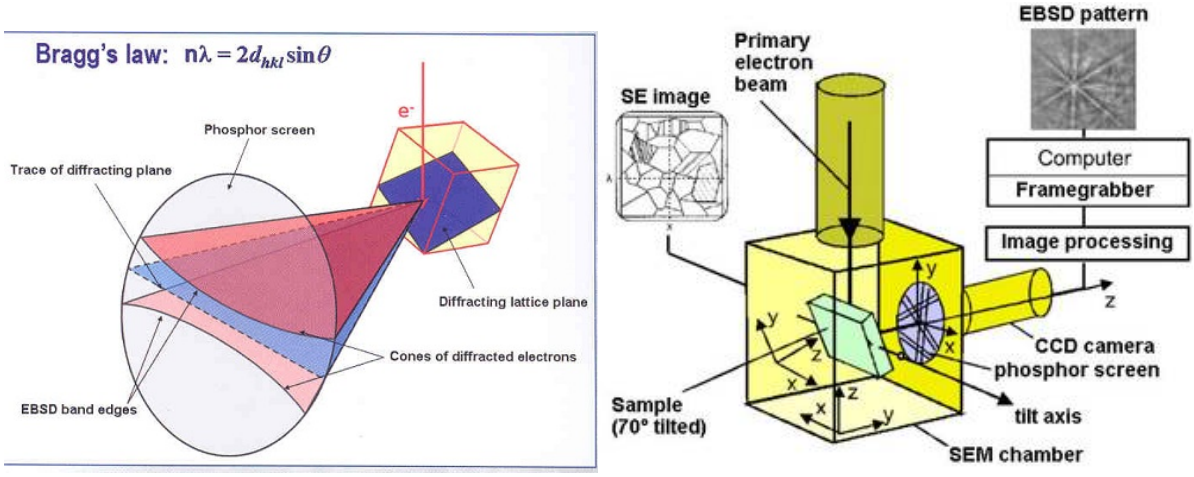

(a) EBSD01 (b) EBSD2

Figure III.2.3: EBSD principle and setup

Experimentally EBSD is usually conducted using a Scanning Electron Microscope (SEM) equipped with a backscatter diffraction camera. The diffraction camera consists of a phosphor screen - which is inserted into the specimen chamber of the SEM at an angle greater than or equal to 90° to the pole piece - and a CCD camera on the end of a light pipe to register the image on the phosphor screen. A flat/polished crystalline specimen is placed into the normal position in the specimen chamber, but is highly tilted (~70° from horizontal) towards the diffraction camera. When the electrons impinge on the specimen they interact with the atomic lattice planes of the crystalline structures. Bragg diffraction occurs in three dimensions from these planes either side of the diverging beam, giving rise to two cones of radiation, the so-called Kossel cones. Those diffraction cones intersect with a phosphor screen placed in front

of the specimen (imaging plane). Since Bragg angles are rather small for energetic electrons (about 0.5°), the section of a pair of Kossel cones with the flat phosphor screen forms a pair of virtually parallel straight

Kikuchi lines (called a Kikuchi pattern). The angular distance between a pair of Kossel cones is twice the Bragg angle. So, the width of the bands corresponds to twice the Bragg angle. The center line corresponds to the intersection line between the lattice plane and the phosphor screen. Hence, the angle between center lines corresponds to the angle between crystallographic planes. Since the Kossel cones are rigidly fixed in orientation to their lattice planes, Kikuchi patterns exactly follow any rotation of the crystal lattice and contain complete information on the orientation of the diffracting crystal. They can be indexed individually by the Miller indices of the diffracting plane which formed it. The bands formed can also be analyzed to show the deformation present within the material: pattern blurring gives an indication of the plastic strain (as dislocations present within the interaction volume deform the crystal and alter the diffraction conditions) within the crystal and small shifts/rotations of the pattern (compared to a perfect crystal at this orientation) indicate lattice rotation and elastic strain.

The typical scattering area is $\sim$ 10 nm x 1 nm and probing depth is $\sim$ 20-100 nm.

Often, the first step in the EBSD process after pattern collection is indexing. This allows for identification of the orientation at the single volume of the sample from where the pattern was collected. With EBSD software, pattern bands are detected via a mathematical routine called the Hough transform, in which every pixel denotes a unique line in the EBSD pattern. As angles between bands represent angles between lattice planes, when the position / angles between three bands are known an orientation solution can be determined.

A further function of EBSD is mapping of information collected from a prescribed grid of points on the sample. A sample area is designated and collection parameters selected. The system then automatically rasters the electron beam accordingly, and at each point the indexed orientation information is stored into a dataset. From this dataset numerous maps, charts and plots can be generated. Some of these include grain orientation maps, grain boundary maps, image quality maps, grain size charts, misorientation charts and texture plots.

Additionally, all Kikuchi raw bmp images acquired and used for indexing and imaging, can also be recorded for future cross-reference. These raw bmp images can be then re-indexed off line to verify previous calibration and indexing results.

When simultaneous EDS/EBSD collection can be achieved, the capabilities of both techniques can be enhanced. To accomplish integrated mapping, analysis area is scanned and at each point Hough peaks and EDS region-of-interest counts are stored. Positions of phases are determined in X-ray maps and measured EDS intensities are given in charts for each element. For each phase the chemical intensity ranges are set to select the grains. All patterns are then re-indexed off-line. The recorded chemistry determines which phase / crystal structure file is used for indexing of each point. Each pattern is indexed by only one phase and maps displaying clearly distinguished phases are generated.

An impressive aspect of the SEM/EBSD/EDS combination is that, at the nanometer scale, the sample's geometrical features (surveyed via secondary electron imaging), crystal structure (via Kikuchi pattern indexing), and chemical composition (via EDS - see section below) could all be revealed in-situ by one instrument. Most critically, the probing depth of EBSD (on the scale of tens of nanometers) is relevant to the functional layer of SRF particles accelerators, whose typical London penetration depth is $\sim$ 30 nm. Thus, the crystal structure of a material investigated by EBSD is directly relevant to the material's SRF performance.

The measurements performed on the films in this present work were performed at JLab and

at NASA Langley on, respectively, an AMRAY 1830 equipped with EDAX EDS and EBSD detectors and associated TSL OIM data acquisition software package and on a .... equipped with the same type of detectors and software packages.

In this study, the grayscale of all the IPFs is rendered by the *Confidence Index* (C.I). Dark and gray pixels are the points of low confidence indexes (CI < 0.05). Although there is no quantified relationship between crystalline order and CI, qualitatively, lower CI suggests lower crystallinity. The black or deep gray areas in an IPF color map might be the zones where either the grain size is <50 nm or the grains might be entirely amorphous. The Kikuchi-diffraction patterns from these low CI zones were observed to be very faint or could not be indexed by the OIM^{TM} software.

In order to discriminate within a plane family (because all orientations within a pane family are rendered in the same color), the OIM^{TM} software can plot the raw data in a view of pole figure to visualize the texture. Compared to the XRD's probing depth of 1-2 microns, EBSD probes only the top most surface ($\sim$ 50 nm). Pole figures generated by both EBSD and XRD are complementary tools to reveal the reciprocal lattice (structural properties) of materials.

III.2.1.3 Scanning electron microscopy (SEM)

SEM is a versatile and widely used tool as it allows high magnification observation of samples with great resolution and easy sample preparation. Combined with energy dispersive X-ray spectroscopy (EDS), it is capable of fast elemental analysis at high resolution. A monochromatic electron beam is focused onto a fine probe which is scanned over a rectangular area of the sample. As the electrons collide with the surface, a number of interactions occur resulting in the emission of electrons and photons from the surface. The intensity of the secondary electrons is point-to-point mapped onto a screen. The electron beam in the cathode ray tube illuminating the screen is synchronized with the electron beam scanning the sample. High-resolution images of the morphology or topography of a specimen at very high magnifications can be obtained. Compositional analysis of a material may also be obtained by monitoring secondary X-rays produced by the electron-specimen interaction. Thus detailed maps of elemental distribution can be produced from multiphase materials. Characterization of fine particulate matter in terms of size, shape, and distribution as well as statistical analyses of these parameters, may be performed.

The Hitachi S-4700 cold field emission Scanning Electron Microscope (FE-SEM) with EDAX EDS attachment, located at the College of William & Mary. This SEM permits ultra high resolution imaging of thin films, semiconductor, and bulk material surfaces. The S-4700 is configured to detect secondary and back- scattered electrons as well as characteristic X-rays. As mentioned before, in the framework of EBSD analyses, the SEM instruments at JLab and NASA Langley were used.

III.2.1.4 Focused Ion Beam

Focused Ion Beam (FIB) systems [270] utilize a finely focused beam of gallium ions (Ga^+) operating at low beam currents for imaging and at high beam currents for site-specific milling.

Cross-section TEM samples preparation by using a Focused Ion Beam (FIB) as become a common preparation technique as it involves less preparation process steps than the standard technique (see bellow) and seems to introduce less artefacts. By controlling the location, beam size and current density of the ion beam, material can be selectively removed from sub-micron areas. Thus a finished electron transparent portion of the sample (usually 5 μm x 20 μm) is

obtained by FIB micro-milling and then placed by a micro-manipulator on a sample holder to be inserted into the TEM microscope: this procedure at present represents the one site-specific and artefact-less outstanding TEM sample preparation techniques.

Most state of the art systems also contains in-situ scanning electron microscopy (SEM) capabilities for real time imaging of the ion milling site. The capability of high-resolution imaging using both secondary electron and secondary ion signals has made the FIB microscope a unique imaging tool. Stress-free cross sectioning using the primary gallium ion beam provides valuable microstructure information beneath the specimen surface. The samples used for TEM cross-section in this dissertation were ion milled and imaged in a FEI Titan FIB at the Facility (AIF) of North Carolina State University (NCSU).

Additionally, FIB imaging can provide useful qualitative information. One example of FIB applications has been presented in chapter II.1 with figure II.1.11. It reveals the difference in structure of "standard" polycrystalline Nb films grown on oxidized copper surface and epitaxially grown ones deposited on oxide-free copper [74].

III.2.1.5 Transmission electron microscopy (TEM)

This is a powerful tool with an optimal image resolution of ~1 Å for an accelerating voltage of 200 kV. Materials for TEM must be specially prepared to thicknesses that allow electrons to transmit through the sample. This is a time consuming task, especially for cross-sectional images. TEM images provide information on the sample microstructure and exhibit contrasts caused by defects and grain boundaries, for example. They are especially useful for the study of interfaces between films and substrates. There are two mechanisms responsible for the contrasts observed in a TEM image, a diffraction contrast used for the formation of bright field and dark field images, which reveal areas that are diffracting the electron beam differently due to changes in orientation or presence of crystallographic defects, and a phase contrast that uses the phase difference of the transmitted electrons to form the image [271].

The TEM cross section sample preparation were prepared by FIB ion milling as described in section III.2.1.4 or by the standard cross-section TEM sample preparation involving mechanical polishing and ion milling.

The whole process includes:

1. Sample cutting by low speed Diamond Saw or Tuned Piezo Cutting Tool. 2. Sample binding for cross-section TEM sample. 3. Mechanical pre-thinning by disc grinder down to 70-100 μm 4. Further thinning the specimen by Dimple Grinder 5. Ion milling by Precision Ion Polishing System (PIPS) at low angle (2-4°). The area useful for TEM observation should be thinner than 100 nm.

III.2.1.6 Scanning transmission electron microscopy (STEM) coupled with electron energy Loss spectroscopy (EELS)

A scanning transmission electron microscope (STEM) is a type of transmission electron microscope (TEM). It is distinguished from conventional transmission electron microscopes (CTEM) by focusing the electron beam into a narrow spot which is scanned over the sample in a raster.

By using a STEM and a high-angle detector, it is possible to form atomic resolution images where the contrast is directly related to the atomic number (z-contrast image). The directly interpretable z-contrast image makes STEM imaging with a high-angle detector appealing. This is in contrast to the conventional high resolution electron microscopy technique, which

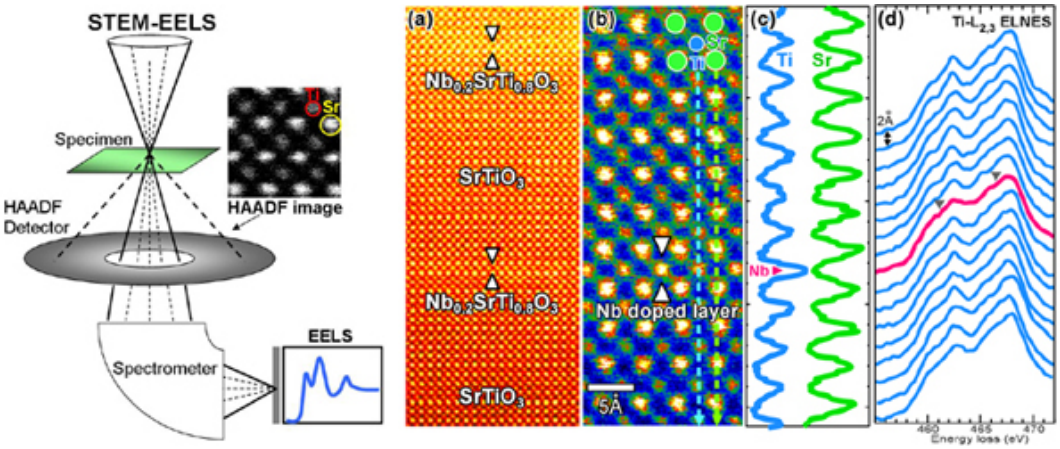

Figure III.2.4: Schematics of STEM system and EELS

uses phase-contrast, and therefore produces results which need interpretation by simulation [272]

The rastering of the beam across the sample makes this instrument suitable for analysis techniques such as mapping by energy dispersive X-ray (EDS) spectroscopy, electron energy loss spectroscopy (EELS) and annular dark-field imaging (ADF). These signals can be obtained simultaneously, allowing direct correlation of image and quantitative data.

Electron energy loss spectroscopy

In electron energy loss spectroscopy (EELS) a material is exposed to a beam of electrons with a known, narrow range of kinetic energies. Some of the electrons will undergo inelastic scattering, which means that they lose energy and have their paths slightly and randomly deflected. The amount of energy loss can be measured via an electron spectrometer and interpreted in terms of what caused the energy loss. Inelastic interactions include phonon excitations, inter and intra-band transitions, plasmon excitations, inner-shell ionizations, and Cherenkov radiation. The inner-shell ionizations are particularly useful for detecting the elemental components of a material [273]

The HR-TEM and STEM observations presented in this dissertation were performed on several systems:

- HR-TEM JEOL 2100F equipped with a Gatan SC1000 ORIUS CCD camera (11 megapixel) and an Oxford INCAx-sight EDS detector at Old Dominion University, on JLab campus.
- HR-TEM JEOL 2000FX equipped with a 4PI EDS system at the Analytical Instrumentation Facility (AIF) of North Carolina State University (NCSU) .
- At the University of Illinois- Chicago, on a JEM-ARM200CF equipped with Gatan Enna 1000 EELS system.
- At AIF-NCSU, on an aberration corrected FEI Titan G2 80-300 kV STEM with a XFEG Shottky electron gun and is equipped with a 4 quadrant EDS detector (Chemi/STEM), an HAADF detector (Z contrast) and a Gatan EELS system.

III.2.2 Chemical composition

As it was mentioned in chapter I.3, impurities embedded in SRF films can be detrimental to their SRF performance. It is then important to determine the composition of these films compare to what is commonly observed in bulk Nb SRF surfaces.

III.2.2.1 EDS

Energy desorption spectroscopy (EDS) is a rapid diagnosis for elemental composition that can be implemented in an SEM or a TEM [274].

EDS analyses on the films created in this work were performed with EDAX EDS attachments on the AMRAY 1830 at JLab and on the FEG-SEM at the College William & Mary.

III.2.2.2 SIMS

The goal of this technique is to analyze the chemical composition of the samples. It is a destructive diagnostic which gives the profiles of the different species studied as a function of depth. A simplified representation of the equipment can be seen on figure III.2.5. The sample is placed in a very low pressure chamber ($<10^{-9}$ Torr obtained by a cryogenic pump) and sputtered by an oblique beam of energetic primary ions (accelerations in the range 0.5 - 15 keV). The diameter of the primary ion beam is typically of a few microns and it is scanned to sputter a crater of 100 μm x 100 μm to 200 μm x 200 μm in our measurements. The ejected atoms or groups of atoms have a certain probability to be ionized, positively or negatively, depending on their electronic affinity and of the surrounding matrix. These secondary ions will be accelerated in the electric field present in the analysis chamber between the sample and the extraction electrode and will be counted by an electron multiplier or a Faraday cup of a mass spectrometer [275].

To detect negative (respectively positive) secondary ions, positive cesium Cs^+ (respectively positive oxygen O^{2+}) ions are used as primary ions. In order not to charge the analyzed sample, it should preferably be conductive.

The raw outcome of the measurement is a signal in counts per second as a function of the sputtering time. The sample is taken out and the depth of the crater is measured by a profilometer. The sputtering time can then be converted into the depth, assuming a constant sputtering rate.

The SIMS analyses presented in this dissertation were performed at North Carolina State University (NCSU, NC, USA) on a CAMECA IMS-6F.

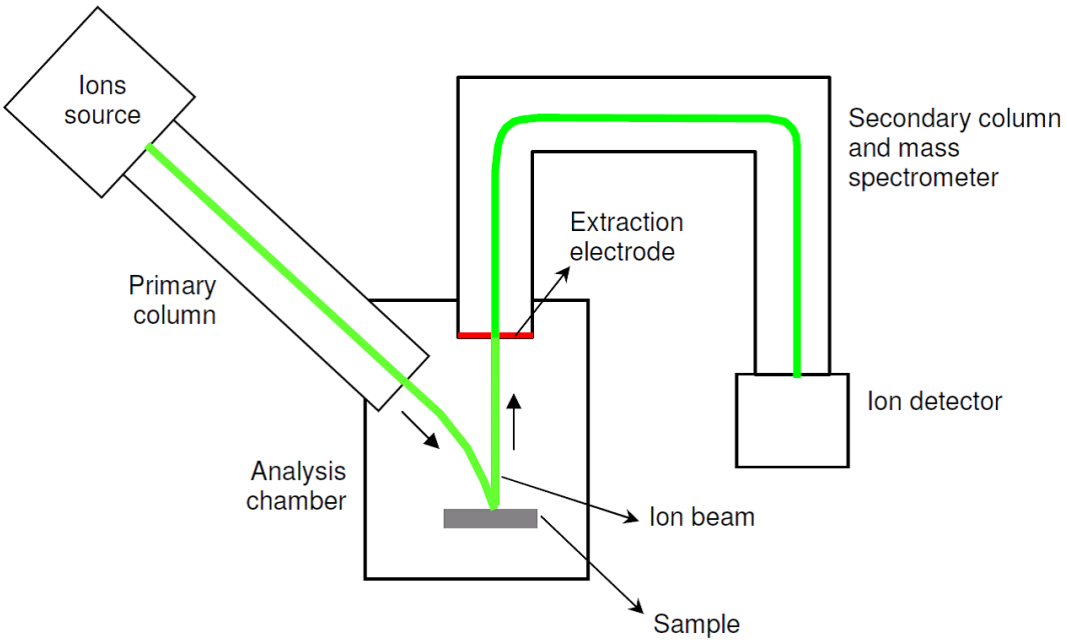

Figure III.2.5: Schematic representing the different parts of a SIMS system

III.2.3 Thickness and Morphology

III.2.3.1 Profilometry

Thickness measurements in this work have been performed by stylus profilometry on a Dektak 3 ST Surface Profiler in the ARC surface laboratory of William & Mary on JLab campus.

III.2.3.2 Atomic force microscopy (AFM)

Atomic force microscopy is one of many scanning probe microscopy techniques and is used to characterize the surface topography of samples. The working principle is that a sharp tip is scanned across the surface in a raster pattern while the vertical position of the tip is monitored as the tip follows the surface profile to build up a height map of the surface as shown in figure III.2.6. The tip is located at the end of a thin cantilever mounted on a piezoelectric scanner able to scan the tip laterally and vertically. When the tip is brought to a close proximity (a few Å) of a sample's surface, repulsive Van der Waals forces between the atoms of the tip and those of the sample cause the cantilever to deflect. The magnitude of the deflection depends on the distance between the tip and the sample. Normally the lateral AFM resolution of an AFM is about 1 nm. However, with a highly sharp tip and a flat sample, even atomic resolution could be obtained [276].

Atomic force microscopy has three main modes of operation contact mode, tapping mode and non-contact mode. In contact mode the tip is put into contact with the surface and dragged across the surface while the deflection of the cantilever is monitored and kept constant. Contact mode AFM can result in damage of the tip and/or the surface resulting in erroneous measurements of the surface topography. Tapping mode AFM, also known as intermittent contact mode AFM, is gentler on the tip and sample than the contact mode. Here the cantilever is made to oscillate at or near its resonance frequency with constant amplitude. Height information is gained using the oscillation amplitude as a regulation parameter. The tip is lowered towards the surface until the oscillation amplitude decreases because the tip

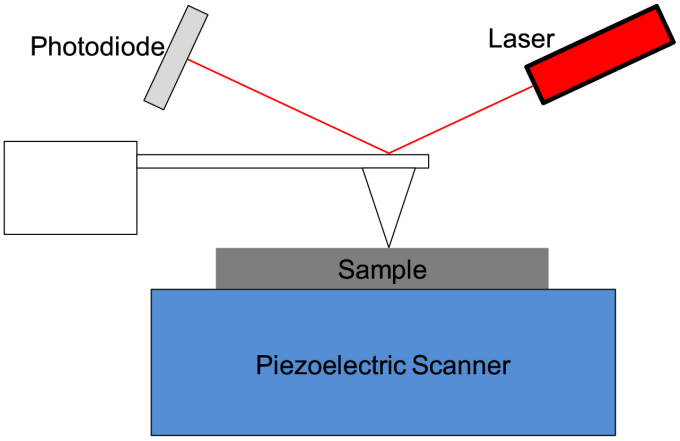

Figure III.2.6: Diagram of an AFM setup

comes into contact with the surface, the height of the cantilever above the surface is then kept constant by the regulation as the tip is scanned across the surface. Non-contact AFM also utilizes an oscillating cantilever and amplitude regulation, here however the tip oscillates close to but not touching the surface. At these distances the tip interacts with the sample through attractive Van der Waals-forces causing amplitude shifts when cantilever height above the surface changes. In contact mode and tapping mode the tip penetrates the thin liquid layer present on surfaces exposed to atmosphere allowing for higher resolution imaging of surfaces than non-contact mode under ambient conditions. Tip effects need to be taken into account when interpreting AFM micrographs as they can result in image artifacts. Some examples are imaging sharp features using a tip with a radius larger than the feature radius, which results in an image of the tip rather than the feature, or that tips with more than one peak results in repetition of features.

Atomic force microscopy has been used for surface imaging and characterization of the surface morphology and surface roughness for the films in this work. The instrument used, a Digital Instruments Scanning Probe Microscope (SPM), is hosted by the College William & Mary surface characterization laboratory on JLab campus. The software enables useful topographic analysis such as the root mean square (RMS) and the average (Ra) roughness. The RMS roughness value is determined by creating a histogram of the height values in an image, fitting a Gaussian curve to the histogram, and using the standard deviation of this Gaussian as the RMS roughness. Additional frequency domain information can be obtained using fast Fourier transforms (FFT). Further analysis such as wavelength selection can be determined using power spectral density (PSD) on FFT images. This process is illustrated in figure III.2.7.

Recently, PSD analysis methods have been specifically developed to provide useful insight on how the various processes commonly applied to SRF cavity surfaces alter their morphology [277, 278, 279].

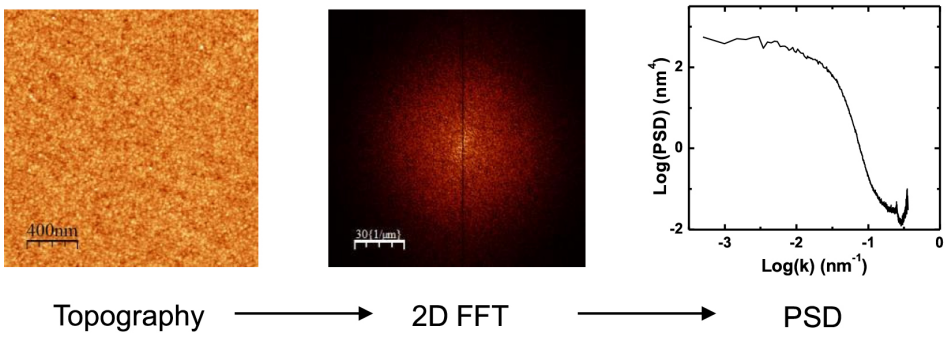

Figure III.2.7: Starting from a topographic AFM image, a two dimensional FFT is calculated. From this 2D FFT, the PSD is calculated as a function of spatial frequency, k.

III.2.4 Ellipsometry for Dielectric characterization

Ellipsometry is a common optical technique for measuring thin films and bulk materials. It relies on the polarization changes caused by reflection or transmission from a material structure to deduce the material's properties, like thickness and optical constants [280].

Ellipsometry is a non-destructive, light optical analysis technique that requires neither sample preparation nor special measurement environment. It measures a change in polarization as light reflects or transmits from a material structure. The polarization change is characteristic of the surface structure of the sample and is represented as an amplitude ratio, Ψ, and the phase difference, Δ. The measured response depends on optical properties and thickness of individual materials. Thus, ellipsometry is primarily used to determine film thickness and optical constants. However, it is also applied to characterize composition, crystallinity, roughness, doping concentration, and other material properties associated with a change in optical response.

Schematic setup of an ellipsometry experiment Electromagnetic radiation is emitted by a light source and linearly polarized by a polarizer. It can pass through an optional compensator (retarder, quarter wave plate) and falls onto the sample. After reflection the radiation passes a compensator (optional) and a second polarizer, which is called an analyzer, and falls into the detector. Instead of the compensators, some ellipsometers use a phase-modulator in the path of the incident light beam. Ellipsometry is a specular optical technique (the angle of incidence equals the angle of reflection). The incident and the reflected beam span the plane of incidence. Light which is polarized parallel to this plane is named p-polarized (p-polarised).

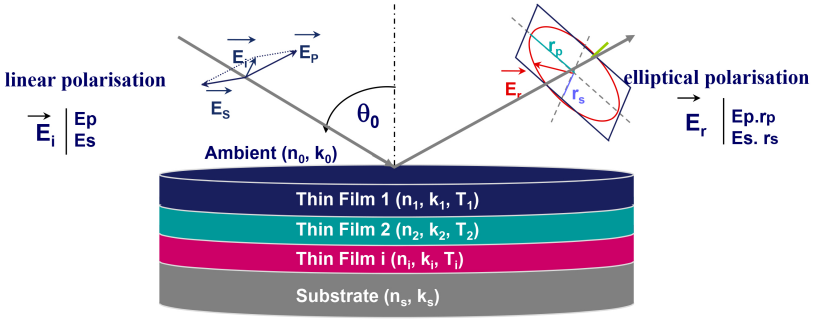

Figure III.2.8: Spectroscopic ellipsometry principle

A polarization direction perpendicular is called s-polarized (s-polarised), accordingly. The "s" is contributed from the German "senkrecht" (perpendicular).

Data acquisition Ellipsometry measures the complex reflectance ratio, ρ, of a system, which may be parametrized by the amplitude component *Psi* and the phase difference *Delta*. The polarization state of the light incident upon the sample may be decomposed into an s and a p component (the s component is oscillating perpendicular to the plane of incidence and parallel to the sample surface, and the p component is oscillating parallel to the plane of incidence). The amplitudes of the s and p components, after reflection and normalized to their initial value, are denoted by r_s and r_p, respectively. The angle of incidence is chosen close to the Brewster angle of the sample to ensure a maximal difference in r_p and r_s. Ellipsometry measures the complex reflectance ratio, ρ (a complex quantity), which is the ratio of r_p over r_s:

$$\rho = \frac{r_p}{r_s} = \tan\Psi e^{i\Delta} \tag{III.2.3}$$

Thus, $tan(\Psi)$ is the amplitude ratio upon reflection, and Δ is the phase shift (difference). (Note that the right hand side of the equation is simply another way to represent a complex number.) Since ellipsometry is measuring the ratio (or difference) of two values (rather than the absolute value of either), it is very robust, accurate, and reproducible. For instance, it is relatively insensitive to scatter and fluctuations, and requires no standard sample or reference beam.

Data analysis Ellipsometry is an indirect method, i.e. in general the measured Ψ and Δ cannot be converted directly into the optical constants of the sample. A model analysis must be performed. Direct inversion of Ψ and Δ is only possible in very simple cases of isotropic, homogeneous and infinitely thick films. In all other cases, a layer model must be established, which considers the optical constants (refractive index or dielectric function tensor) and thickness parameters of all individual layers of the sample including the correct layer sequence. Using an iterative procedure (least-squares minimization) unknown optical constants and/or thickness parameters are varied, and Ψ and Δ values are calculated using the Fresnel equations. The calculated Ψ and Δ values which match the experimental data best provide the optical constants and thickness parameters of the sample.

The more common procedure used to deduce material properties from ellipsometry measurements follows the flow chart in Figure III.2.9. Regression analysis is required because an exact equation cannot be written. Often the answer is over-determined with hundreds of experimental data points for a few unknowns. Regression analysis allows all of the measured data to be included when determining the solution.

Data analysis proceeds as follows: After a sample is measured, a model is constructed to describe the sample. The model is used to calculate the predicted response from Fresnel's equations which describe each material with thickness and optical constants. If these values are not known, an estimate is given for the purpose of the preliminary calculation. The calculated values are compared to experimental data. Any unknown material properties can then be varied to improve the match between experiment and calculation. The number of unknown properties should not exceed the amount of information contained in the experimental data. For example, a single-wavelength ellipsometer produces two data points (Ψ,Δ) which allows a maximum of two material properties to be determined. Finding the best match between the model and the experiment is typically achieved through regression. An estimator, like the Mean Squared Error (MSE), is used to quantify the difference between curves. The unknown parameters are allowed to vary until the minimum MSE is reached.

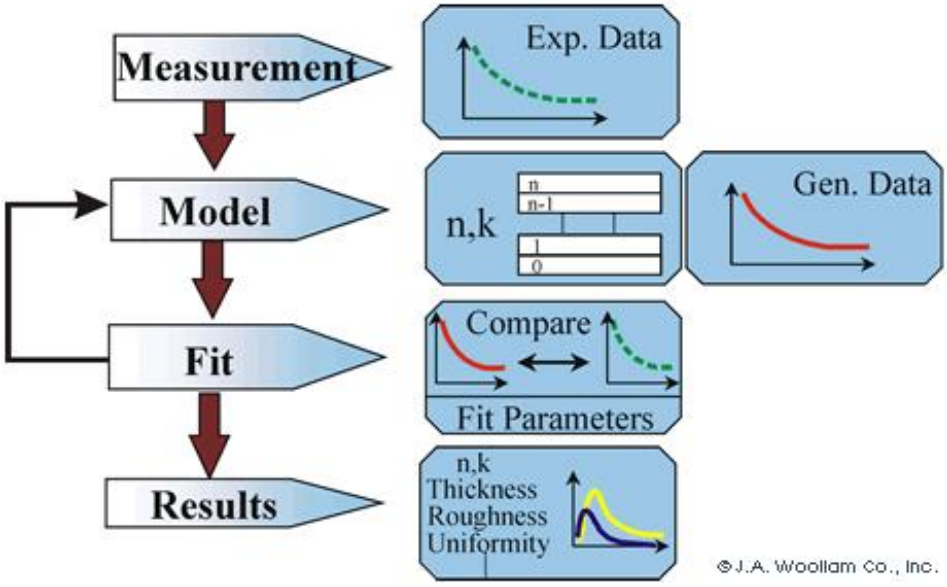

Figure III.2.9: Flowchart for ellipsometry annalysis

Optical constants measurements The optical constants define how light interacts with a material. The complex refractive index is a representation of the optical constants of a material, it is represented by

$$\tilde{n} = n + ik. \tag{III.2.4}$$

The real part or index of refraction, n, defines the phase velocity of light in material:

$$v = \frac{c}{n}, \tag{III.2.5}$$

where v is the speed of light in the material and c is the speed of light in vacuum. The imaginary part or extinction coefficient, k, determines how fast the amplitude of the wave decreases. The extinction coefficient is directly related to the absorption of a material and is related to the absorption coefficient by:

$$\alpha = \frac{4\pi k}{\lambda}, \tag{III.2.6}$$

where α is the absorption coefficient and λ is the wavelength of light.

Thickness measurements are not independent of the optical constants. The film thickness affects the path length of light traveling through the film, but the index determines the light waves' velocity and refracted angle. Thus, both contribute to the delay between surface reflection and light traveling through the film. Both n and k must be known or determined along with the thickness to get the correct results from an optical measurement.

The optical constants for a material will vary for different wavelengths and must be described at all wavelengths probed with the ellipsometer. A table of optical constants can be used to predict the material's response at each wavelength. However, it is not very convenient to adjust unknown optical constants on a wavelength-by-wavelength basis. It is more advantageous to use all wavelengths simultaneously. A dispersion relationship often solves this problem, by describing the optical constant shape versus wavelength. The adjustable parameters of the dispersion relationship allow the overall optical constant shape to match the experimental results. Compared to fitting individual n, k values at every wavelength, this greatly reduces the number of unknown "free" parameters.

For transparent materials, the index is often described using the Cauchy or Sellmeier relationship. The Cauchy relationship is typically given as:

$$n(\lambda) = A + fracB\lambda^2 + fracC\lambda^4 \tag{III.2.7}$$

where the three terms are adjusted to match the refractive index for the material. The Cauchy is not constrained by KK consistency and can produce unphysical dispersion. The Sellmeier relationship enforces Kramers-Kronig (KK) consistency, which ensures that the optical dispersion retains a realistic shape. The Sellmeier relationship can be written as:

$$\varepsilon_1 = fracA\lambda^2{\lambda_0}^2 \tag{III.2.8}$$

Absorbing materials will often have a transparent wavelength region that can be modeled with the Cauchy or Sellmeier. However, the absorbing region must account for both real and imaginary optical constants. Many dispersion relationships use oscillator theory to describe absorption for various materials. These include the Lorentz, Harmonic, and Gaussian oscillators. They all share similar attributes, where the absorption features are described with an Amplitude, Broadening, and Center Energy (related to frequency of light). Kramers-Kronig consistency is used to calculate the shape of the real component after the imaginary behavior is described by the oscillator. An offset to the real component is added to account for extra absorption outside the measured spectral region. The Lorentz oscillator can be written as:

$$\tilde{\varepsilon} = \varepsilon_{1,offset} + \frac{AE_c}{E_c^2 - E^2 - iBE} \tag{III.2.9}$$

where the parameters for Amplitude (A), Broadening (B), Center Energy (Ec), and offset (e1, off set) are also shown in Figure 13 for a typical Lorentz oscillator. The energy, E, is related to the frequency of a wave, n:

$$E = h\nu \cong \frac{1240}{\lambda_{nm}} \tag{III.2.10}$$

where h is Planck's constant and the wavelength, λ, is given in nanometers. More advanced dispersion models, like the Tauc-Lorentz and Cody-Lorentz, will include terms to describe the bandgap energy.

The ellipsometer used to characterize the AlN films in this work is a M44 Variable Angle Spectroscopic Ellipsometer (VASE) located at Norfolk State University.

Part IV

Energetic condensation of Nb Films

This section is dedicated to the development of *bulk-like* Nb films engineered via energetic condensation. The challenge in developing SRF thin films, made of niobium or alternative materials, is to reproduce and go beyond the performance of bulk Nb. While tight correlation with the characterization of real materials has yet to be described, there exists a theoretical framework describing the relevant material parameters of surfaces as they influence SRF properties. Several material factors, highly dependent upon the surface creation conditions, contribute to degraded SRF performance with respect to ideal surfaces. These limiting factors such as intra-granular impurities and lattice defect density, inter-granular impurities and oxidation, surface topography and chemistry, may lead to the reduction of the electron mean free path, thus the reduction of the lower critical field H_{c1}.

Thus, understanding of the film growth dynamics from nucleation to final exposed surface is crucial. The defect density (which determines the electron mean free path) within the RF penetration depth is certainly affected by intragrain contaminants incorporated during the final stage film growth, but it is also strongly affected by the underlying crystal texture, which is in turn developed from the initial film nucleation process, which necessarily is strongly influenced by the substrate. The development of every stage can be expected to depend strongly on the kinetic energy distribution of the impinging ions. Although the thickness corresponds to the very top 40 nm of the Nb film, this final surface is dictated from its origin, i.e. the substrate, the interface, and deposition technique (ion energy, substrate temperature ...).

The growth of Nb films has been studied by exploring the parameter space of the ECR plasma technique and the use of a selection of substrates of various natures form an ideal surface to surfaces that can be implemented in an SRF cavity.

Chapter IV.1

Experimental Deposition Setup

In chapter I.3, we have discussed the Nb/Cu technology has successfully been demonstrated as a contender to bulk Nb technology. However, so far the SRF cavities based on Nb/cu have displayed rapid degradation of their RF performance with increasing accelerating gradients. It is believed that these limitations are inherent to the coating technique commonly used. Magnetron sputtering is a coating method with some limitations when applied to cylindrical applications and when the coating temperature is limited. To overcome this, energetic condensation via ECR is chosen in this work for the development of high quality Nb films.

IV.1.1 Deposition setup for ECR deposition

IV.1.1.1 ECR sample deposition system

An electron cyclotron resonance (ECR) plasma metal ion source is the ideal tool for direct niobium thin film deposition with the flexibility to adjust the niobium ion deposition energy [281]. Ultra-high vacuum and freedom from macro-particles are added advantages for this ion source. The main advantages are the production of a high flux of singly charged ions with controllable kinetic energy and the absence of macro-particle production.

To generate niobium metal ions inside a vacuum, a thermionic electron gun is used to create a dense neutral niobium flux, and an ECR chamber is used to convert the passing neutral niobium vapors to niobium plasma as shown in the illustration below. The ECR chamber is made of a copper cylinder that is inserted into the two slightly separated copper coils. The ECR chamber, copper coils and the electron gun sit in the vacuum chamber. When the cylinder is connected to the RF source, an electric field is established perpendicular to the magnetic field created by the copper coils. The niobium plasma is created when the electrons resonate with the RF field. The niobium plasma has a static potential of 64V. Energetic niobium ions are extracted to a biased substrate. Deposition energy is simply controlled by the substrate bias voltage.

The ECR chamber is housed in a dumbbell style vacuum chamber with a 24" wheeler flange sealed with a viton gasket. The pumping system consists of a cryopump CTI Cryo-Torr 8 (4000l/s) and an oil roughing pump (combined with a sieve trap to avoid roughing oil back-streaming in the vacuum chamber). A 10" manual VAT Gate valve separates the main chamber and the cryopump.

An SRS RGA -100 is mounted on one of the chamber port behind a $2^{3/4}$" VAT gate valve. The RGA is run on Faraday mode during plasma deposition. The vacuum is monitored by

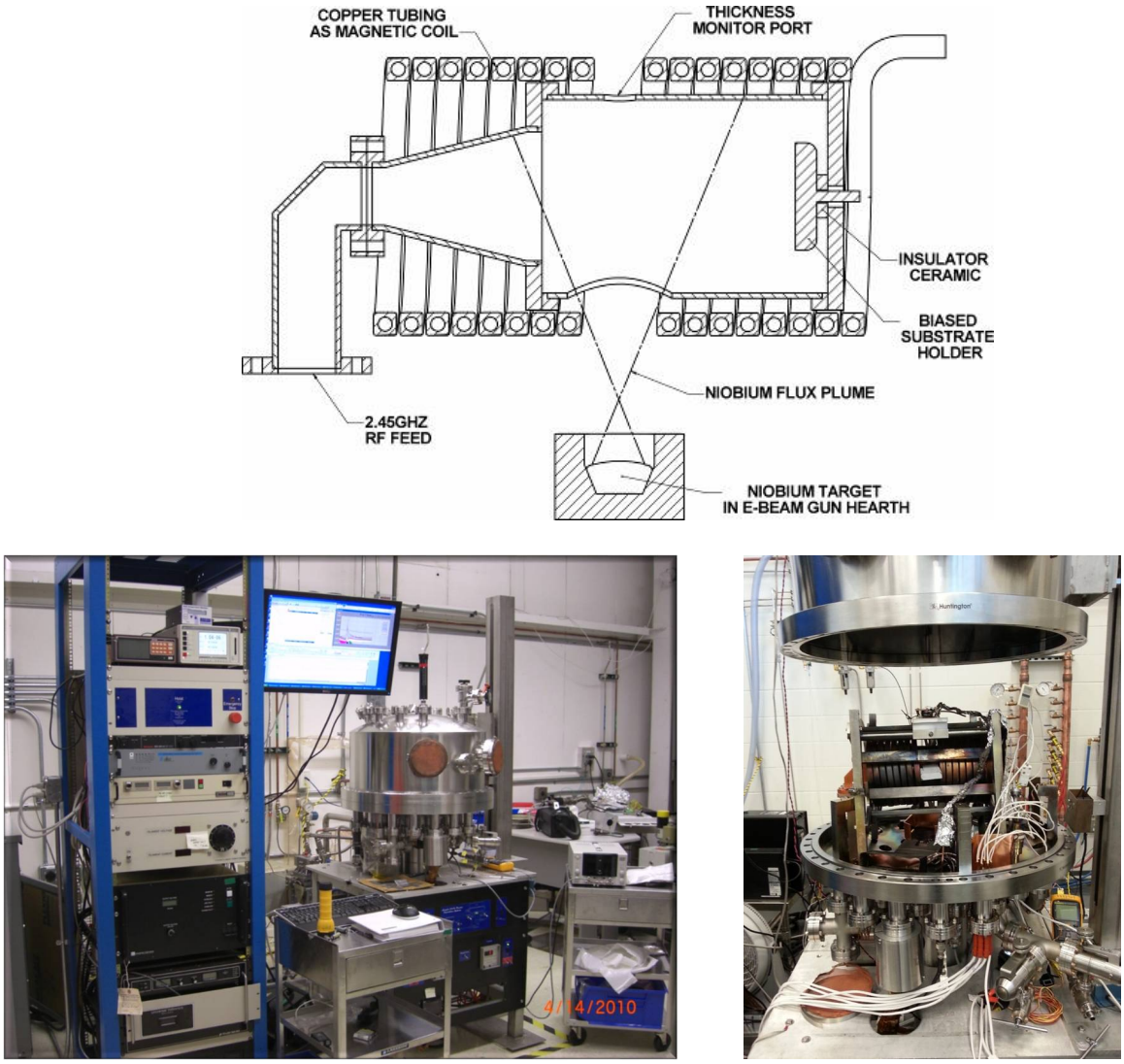

Figure IV.1.1: The ECR deposition system and inside the vacuum chamber

a Varian UHV-24 hot cathode ion gauge controlled by an SRS IGC-100 controller. A water-cooled thickness monitor is mounted above the ECR chamber and monitors the neutral Nb flux emitted from the e-beam gun.

A water-cooled 14kW Thermionics E-beam gun with a 40 cc crucible provides the neutral vapor of Nb. Although it is common to use a crucible (typically graphite) liner with e-beam guns, no liner is used in this system to avoid any carbon contamination of the films produced. At 10kW of e-beam power, the evaporation rate for niobium can be as high as 150 Å/s at a 12-inch distance. The Nb target is made of RRR Nb disks and replenished, for each deposition run, with RRR Nb pellets. Both targets and pellets are chemically etched by buffer chemical etching (BCP, a mixture of HNO_3, HF and H_3PO_4) and then vacuum fired before being used in the deposition system.

The e-beam gun high voltage supply is a 15 kV Universal Voltronics supply (BRC-15-1111R-STD-J37). A Cu shield is strongly clamped to the e-beam gun (to benefit from its water cooling) and to avoid system damage from any back-scattered electron beam. Since Nb is a high-Z material, when one applies a 10 kV electron beam to the Nb target, a back-scattered beam of about 2.2 keV is emitted towards the back of the system.

The electric field is supplied via a rectangular waveguide by a 2.45 GHz Richardson Electronics microwave generator (MH2.0W-S) which can provide 1.5 kW of total microwave power. A simple ceramic window is installed to transfer the RF power inside the vacuum chamber to the ECR chamber through a 90-degree waveguide. A taper couples the TE_{10} mode in the rectangular waveguide to the TE_{11} circular mode. The size of the circular waveguide is carefully adjusted so that the large area of RF electrical field is right in the path of the neutral niobium flux. The forward and reflected powers are measured through a circulator by 2 USB Agilent U2000 Power sensors. The magnetic field is established with 2 slightly separated coils powered by a 2kA Sorensen DCR 4-800T and a PowerTen P66C-52000 current supplies in parallel. The substrate holder is mounted at the end of the ECR chamber, out of the line of sight of the Nb flux, so that the substrate can only collect ionized niobium.

The ECR conditions are established with a coil current of 1730 A (3V) and roughly 350W of forwarded RF power. The power needed to produce enough Nb vapor to sustain the plasma is in the range of 10kW. The base pressure of the ECR before coating with the samples a temperature is in the range of $2x10^{-8}$ Torr. Before deposition, the Nb target is conditioned a low filament emission current (<200 mA). The samples are baked at temperature for 24 hours before coating.

IV.1.1.2 Sample holders

Two sample holders have been used for this work. Before and during deposition, the substrate heating temperature can be regulated from room temperature to 700 °C.

Multi-bias holder

A multi-bias sample holder made of OFHC CU was built in order to perform simultaneous deposition at various bias voltages. It has 8 bias seats insulated from the heater holder and holding flange. On each seat, a selection of substrates can be mounted as shown on figure IV.1.2.

The heater is a 50 mm (2") Momentive^{TM} pyrolitic boron nitride (BN) resistive heater (resistance 19 Ω) controlled by a Watlow DCA SCR and a Fuji Electrics PXG-9 temperature controller and embedded in the sample holder. The temperature is controlled by an ARI Industries thermocouple placed just underneath the sample holder surface, electrically insulated from the sample holder.

The dc bias voltage is provided through a 5 kV feed-through by a chain of diodes powered by an Advanced Energy MDX-1K DC power supply (1000 V). The bias for each seat can be chosen from 0 to -360 V by increments of -30 V.

Single-bias holder

To enable the coating of larger sample sizes (Ø 50 mm/2") required for RF measurements, a single bias holder (see figure IV.1.2, right) is used.

This holder is also made of OFHC Cu with an embedded coiled heater. The heater is a resistive heater (resistance 35 Ω) and a thermocouple mounted just underneath the holder surface, both from ARI Industries^{TM}. Both the heater and thermocouple are insulated in a 316LN stainless steel sheath filled with MgO.

The DC bias voltage is provided through a 500 V feed-through powered by a 2 kV Spellman SL600 power supply.

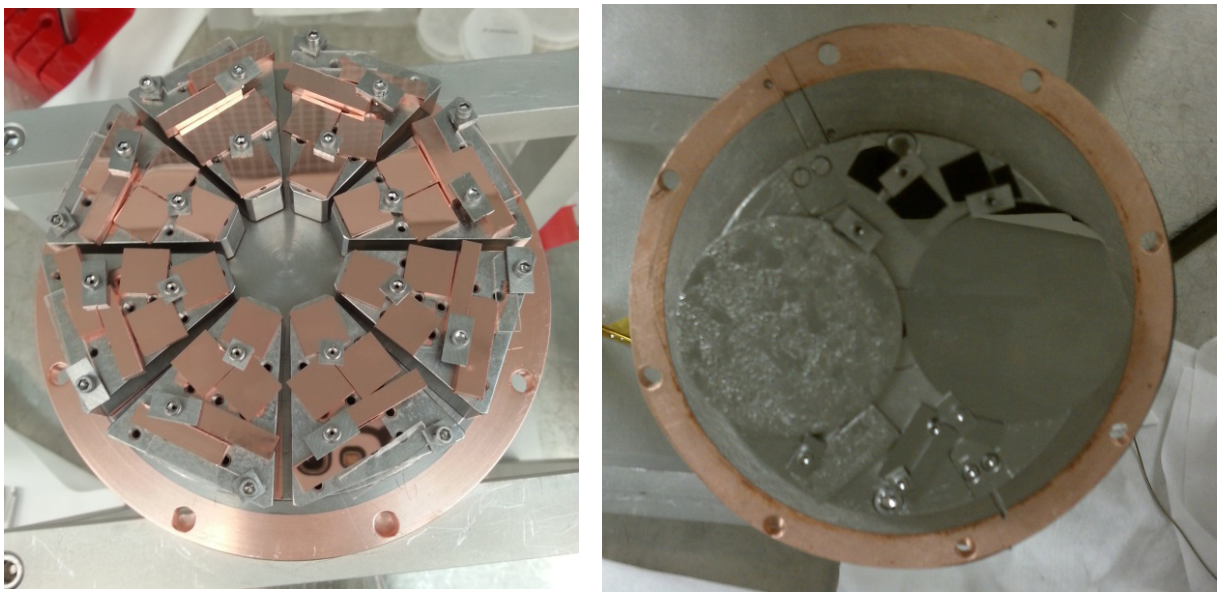

Figure IV.1.2: sample holders for in-situ multi-bias coating loaded with Cu and $(11\bar{2}0)$ α-Al_2O_3 samples prior coating (left) and single bias coating loaded with two 5 cm (2") Ø Cu and $(11\bar{2}0)$ substrates and a selection of small witness samples, after coating.

IV.1.2 Substrates

IV.1.2.1 substrate choice

ECR Nb films are grown on two categories of substrates, insulating and metallic. Although insulating substrates may not be practical as such, they offer valuable insight on the growth modes of Nb thin films on "ideal surfaces" with minimum lattice mismatch and very low roughness (crystalline substrates such as α-Al_2O_3 $(11\bar{2}0)$ or on amorphous substrates with increased roughness and no long-range order (Al_2O_3 ceramic or fused silica). For example, a-plane sapphire is suitable as a substrate is due to the low lattice mismatch (~1.9-12%) and comparable rates of thermal expansion. This makes it a suitable proving ground for niobium thin film studies. The second category of substrates is metallic, Cu, substrates, single crystals, large grain and fine grain OFHC (oxide-free copper). Such studies open the door to subsequent opportunities to tailor the film nucleation by engineering its interface with a practical substrate.

IV.1.2.2 Substrate Surface Preparation

As seen in chapter II.1, in many cases, thin films replicate the substrate morphology and impurities residing at the interface can detrimentally influence the properties of a film. It is then crucial to carefully prepare the substrate surface before deposition. This section presents the procedures used for the different types of substrates used in this work.

Metallic substrates

Cu substrates, for samples or cavities, need a particular attention to surface treatment. It has been shown previously that a reduction in roughness allows for a consistent reduction in film defect density and an improvement in SRF cavity performance [4, 93]. The typical Cu surface

Table IV.1.1: Substrates used for ECR Nb coating

Substrates used for *hetero-epitaxy* studies			Substrates used for *fiber growth* studies		
	Ra [nm]			Ra [nm]	
Cu Large grain	<10	OFHC Cu (Hitachi), heated in-situ above 360 °C	Cu Large grain	<10	OFHC Cu (Hitachi), baking < 200 °C
Cu fine grain	<10	OFHC Cu (Hitachi), heated in-situ above 360 °C	Cu fine grain	<10	OFHC Cu (Hitachi), baking < 200 °C
Cu (100)	3	±2° MTI corp.	Al_2O_3 ceramic	10	MTI corp.
Cu (110)	3	±2° MTI corp.	Fused silica	0.5	MTI corp.
Cu (111)	3	±2° MTI corp.			
α-Al_2O_3 $(11\bar{2}0)$	0.5	±0.5°, Insaco			
α-Al_2O_3 $(11\bar{2}0)$	0.	±0.5°, MTI corp.			
α-Al_2O_3 (0001)	0.5	±0.5°, Insaco			
MgO (100)	0.1	±0.5°, MTI corp.			
MgO (110)	0.1	±0.5°, MTI corp.			
MgO (111)	0,15	±0.5°, MTI corp.			

preparation implemented at CERN for the 1.5 GHz cavities mentioned in chapter I.3 consists in the following sequence of processes:

- Stripping from the previous coating
- 5 hours of electropolishing
- 10 minutes of chemical etching with SUBU (sulfamic acid (H_3NO_3S, 5 g/l), hydrogen peroxide (H_2O_2, 5% vol), n-butanol (5% vol) and ammonium citrate (1g/l))
- 10 minutes of passivation with sulfamic acid
- High Pressure Water Rinsing (HPWR) for 1 hour at 100 bar

The Cu substrates used for the present work, were prepared with the following sequence of process steps aiming at reproducing what the process for a cavity would be:

- Mechanical polishing to a mirror finish
- Light electropolishing
- Heat treatment (for large grain Cu only)
- Light electropolishing
- Sulfamic acid rinse
- De-ionized water rinse
- Methanol bath rinse
- N_2 drying

Mechanical polishing In order to minimize the roughness of fine and large grains samples, polycrystalline cu substrates are mechanically polished with a Buehler EcoMet - Automet polisher with a succession of grits and suspended solutions from 125 μm to 50 nm. The final roughness is about 10 nm RMS. The single crystal substrates are polished by the manufacturer to an average RMS roughness of 5 nm.

Heat treatment To produce large grain Cu samples, OFHC Cu pieces are heat treated up to 1035 °C for 30 minutes in a vacuum furnace after mechanical polishing and a light electropolishing. This process produces Cu samples with mm-size crystallites and releases any intrinsic strain from the Cu sheet fabrication and the mechanical polishing processes.

Electropolishing The Cu samples are electropolished in a 55% phosphoric acid (H_3PO_4) and 45% n-butanol electrolyte with a 50 mA/cm^2 current density. The surface is then passivated in a sulfamic acid solution (20g/l) for 10 minutes and rinsed in DI water. The samples are then rinsed in a methanol bath and finally dried with an anti-static N_2 gun.

The role of electropolishing is here only to remove embedded residues from mechanical polishing or impurities on the substrate surface after heat treatment. So the process is typically very short, just long enough to remove a couple of microns, so as not to lose the benefit from mechanical polishing. The electropolishing process used here seems adequate for sample studies but presents latitude for improvement. It would need development to be optimized for application to SRF cavities.

Figure IV.1.3 and figure IV.1.4 show the EBSD IPF color maps and corresponding AFM scans for the process steps mentioned above. Although mechanical polishing provides smooth mirror surfaces, the mechanical damage induced by the process destroys the structure of the surface. Due to the absence of long range crystallinity, no Kikuchi (k-) patterns can be resolved with EBSD. Thus electropolishing is a necessary step before deposition. Heat treatment at 1000 °C fully recrystallizes the Cu surface releasing any strain due to the metal sheet fabrication and grows crystallites to mm-sizes. However, it also increases considerably the roughness due to Ostwald ripening [282]. After heat treatment, another electropolishing step is required to recover the smoothness but also to rid the surface of contamination , such as alumina and W particulates, originating from the furnace.

IV.1.2.3 Insulator substrates

The insulating substrates, single crystal or ceramic, are prepared following UHV practices. They are cleaned in a flammable-rated ultrasonic bath with subsequent acetone, iso-propyl and methanol baths and finally dried with an anti-static N_2 gun before being mounted on the sample holder.

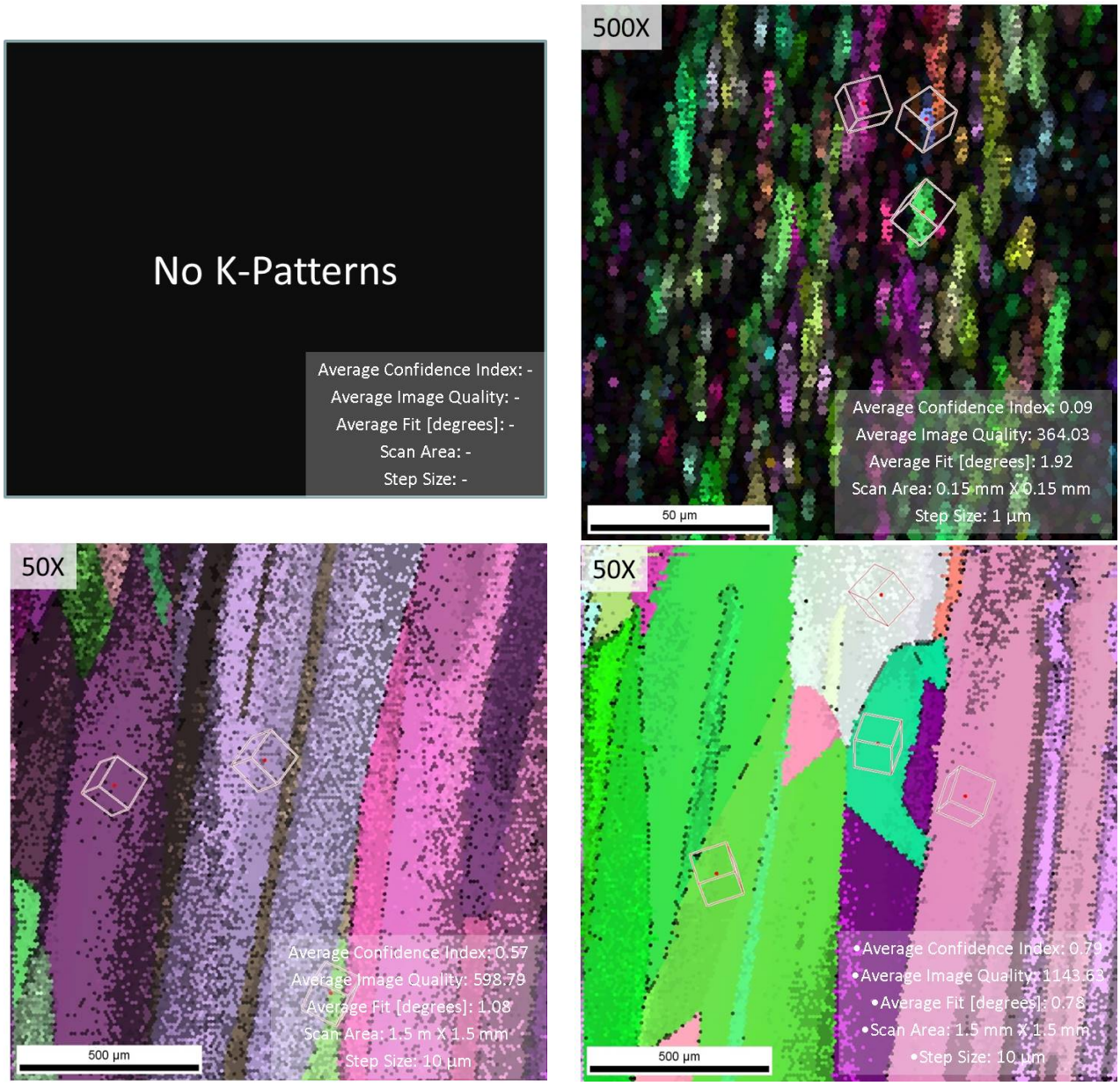

Figure IV.1.3: EBSD IPF color maps for a Cu substrate after each process step: (a) mechanical polishing, (b) electropolishing, (c) heat treatment and (d) electropolishing following heat treatment.

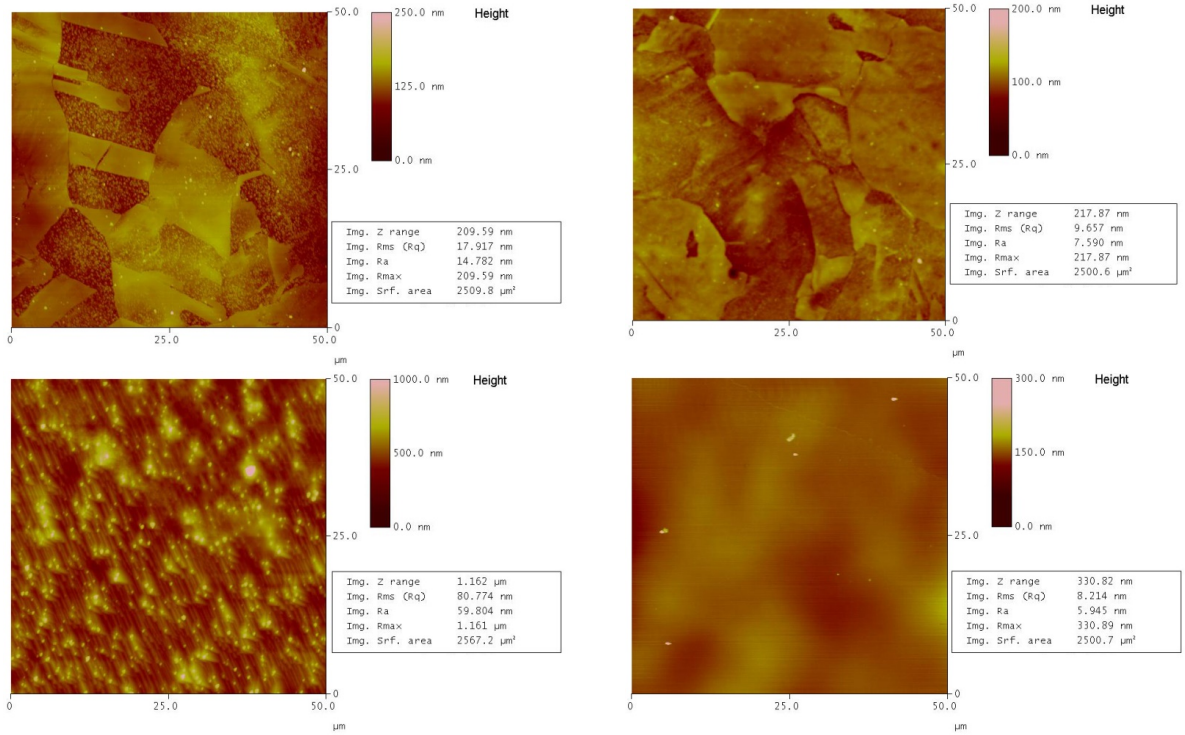

Figure IV.1.4: AFM 50 μm x 50 μm scans for a Cu sample after each process step, corresponding to Figure IV.1.3

Chapter IV.2

Influence of the deposition parameters on ECR Nb film properties

IV.2.1 Nb films on insulating substrates

IV.2.1.1 Nb films on α-Al_2O_3 single crystals and Al_2O_3ceramic

Single crystal sapphire has an *hexagonal* crystal structure, α-Al_2O_3. Figure IV.2.1 shows the Nb hetero-epitaxial directions for Nb grown on different planes of sapphire (Al_2O_3) as proposed by Wildes et al. [174].

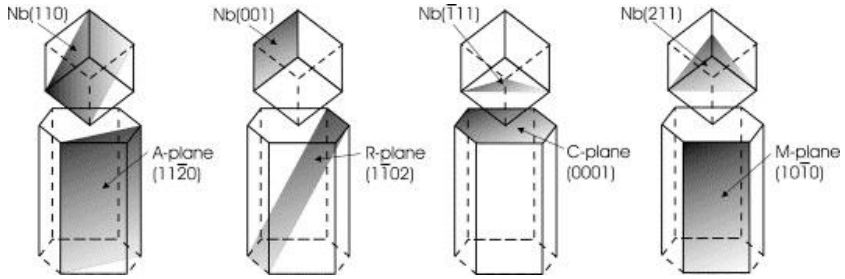

Figure IV.2.1: Hetero-epitaxial relationships between Nb and the different sapphire planes (Al_2O_3) [174]

Lattice mismatch (i.e. the difference in the atom arrangement and spacing between the film and substrate materials) and difference in thermal expansion rate induce strain and stress during film growth. For α-Al_2O_3, the lattice mismatch varies from ~1.9 % for the a-plane Al_2O_3 (11$\bar{2}$0) to 12% for the c-plane Al_2O_3 (0001). The low lattice mismatch (~1.9-12%) and comparable rates of thermal expansion makes this material a suitable proving ground for niobium thin film studies.

Structure analysis

The crystallographic quality of the substrate is of primary importance. Figure IV.2.2 represents the Inverse Pole Figure (IPF) orientation map (with the associated color-mapped IPF for reference) for two Nb films grown simultaneously on single crystal sapphire (11$\bar{2}$0) and on ceramic alumina (quasi-amorphous). These substrates with the same material contribution but different crystallographic structure induced the growth of drastically different film structures.

In the case of single crystal Al_2O_3 $(11\bar{2}0)$, the substrate drives the growth of the Nb film resulting in an hetero-epitaxial Nb single crystal. In the case of Al_2O_3 ceramic, the interface is amorphous as revealed in the FIB-cut TEM cross-section in figure IV.2.3. The resulting Nb film is polycrystalline with fiber structure as revealed by the associated pole figure. It exhibits then equi-axial grains with sizes ranging from 100 nm to 1 μm. By contrast, the film grown on Al_2O_3 $(11\bar{2}0)$ exhibits a continuous crystalline interface (figure IV.2.4). RHEED analyses done by our collaborators at the College William & Mary show that the Nb film grown on Al_2O_3 $(11\bar{2}0)$ actually nucleates with an hcp structure and transitions, across roughly 2-3 nm, to a strained and then relaxed (with subsequent growth) cubic bcc structure [283].

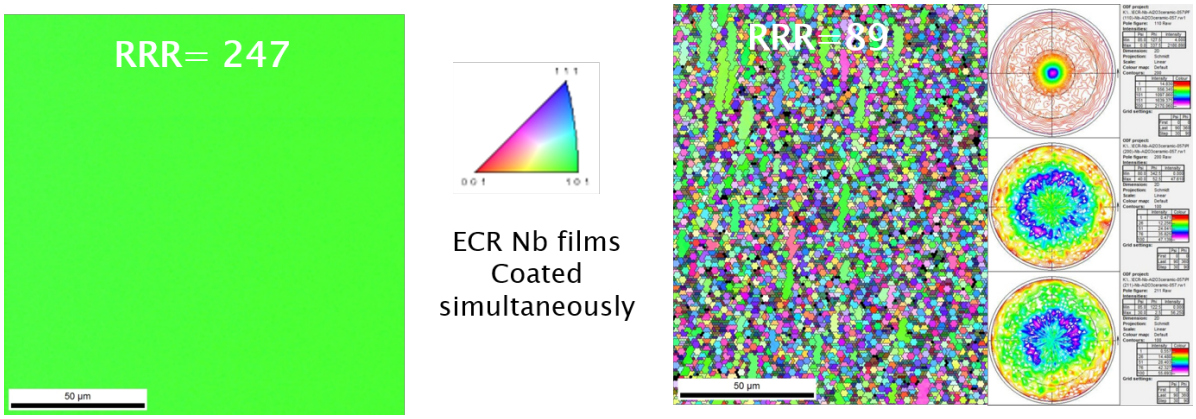

Figure IV.2.2: EBSD IPF color maps (top) for ECR Nb films coated simultaneously at -120 V bias and 360 °C on sapphire (a) and alumina ceramic (b).

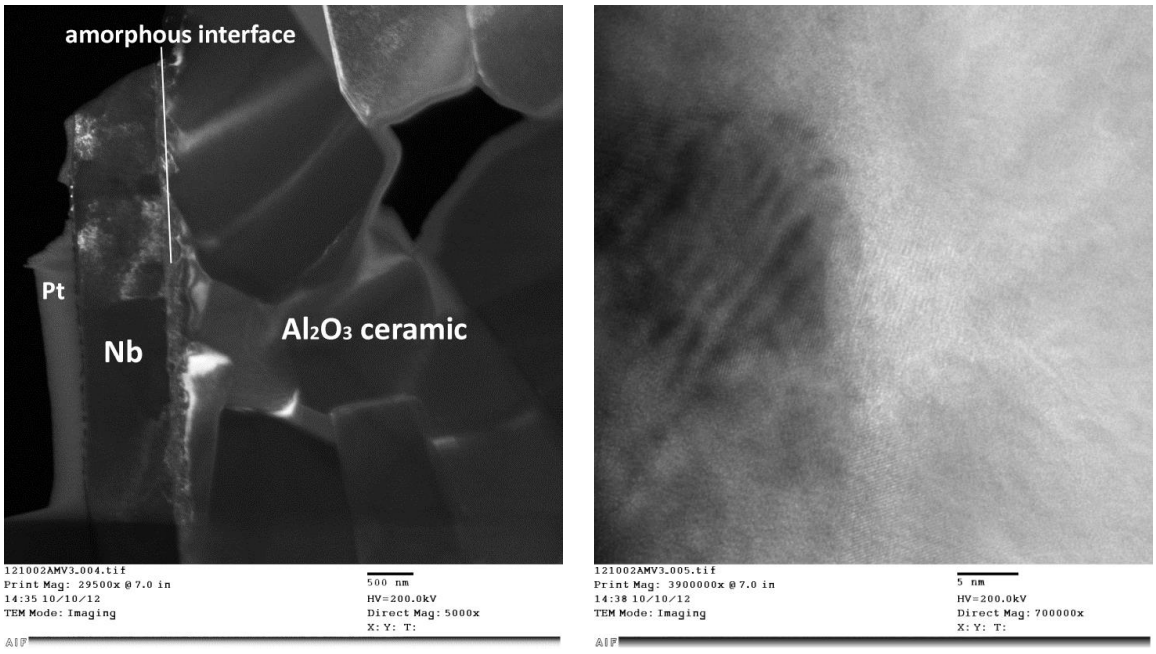

Figure IV.2.3: FIB-cut TEM cross section of the alumina ceramic film from figure IV.2.2 displaying the fiber nature of the film. The high resolution micrograph on the right reveals the amorphous nature of the interface.

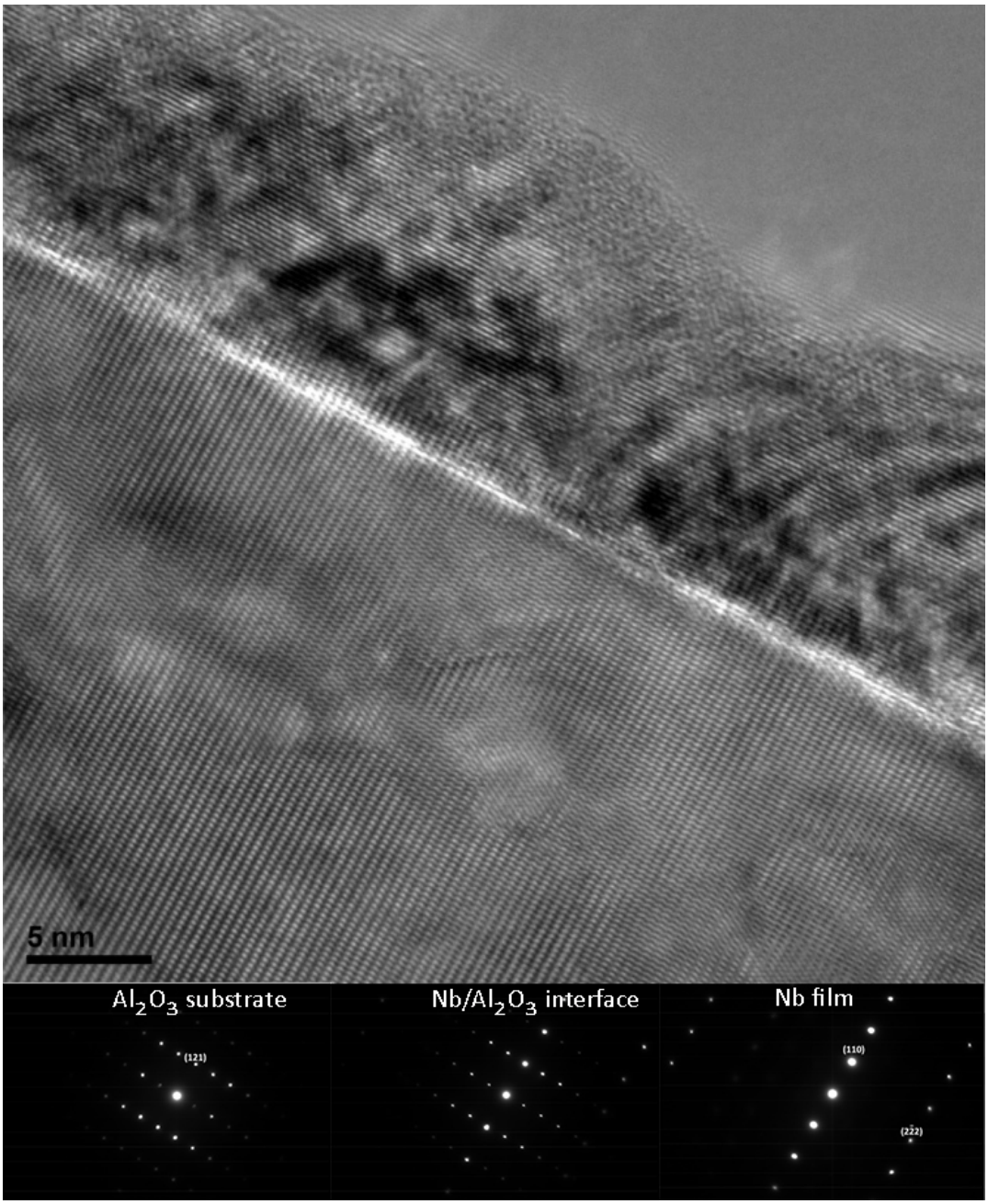

Figure IV.2.4: TEM micrograph of an Nb film grown on Al_2O_3 $(11\bar{2}0)$. The associated diffraction patterns are from left to right for the sapphire substrate, the film-substrate interface and the Nb film.

The topography of the film follows closely the topography of the substrates. Figure IV.2.5 below presents the topographic scans obtained by atomic force microscopy (AFM) for the films represented above. The film average roughness R_a is 3.9 nm and 21 nm for sapphire and alumina ceramic respectively. The respective substrate average roughness is typically 0.5 nm and 10 nm for Al_2O_3 $(11\bar{2}0)$ and Al_2O_3 ceramic.

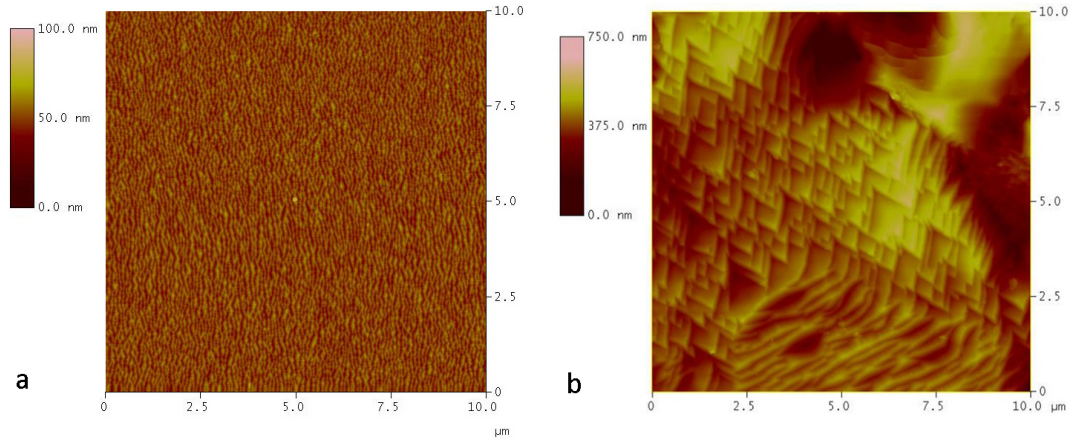

Figure IV.2.5: AFM 10 μm x 10 μm scans for Nb films coated on (a) single crystal Al_2O_3 $(11\bar{2}0)$ and (b) Al_2O_3 ceramic.

The orientation of the films can be tuned as a function of deposition rate, incident ion energy and substrate temperature during coating [221, 284]. Our experiments discovered that the single-crystal-like Nb on Al_2O_3 (0001) films have different epitaxial relationships, depending on bias. For example, for films deposited at 360 °C, above an incident ion energy of 154 eV (-90 V bias), the Nb film orientation switches from (111) to (110) on (0001) Al_2O_3 (Fig. IV.2.6). This was previously observed for MBE (molecular beam epitaxy) Nb films coated at 900 °C and 1100 °C [285].

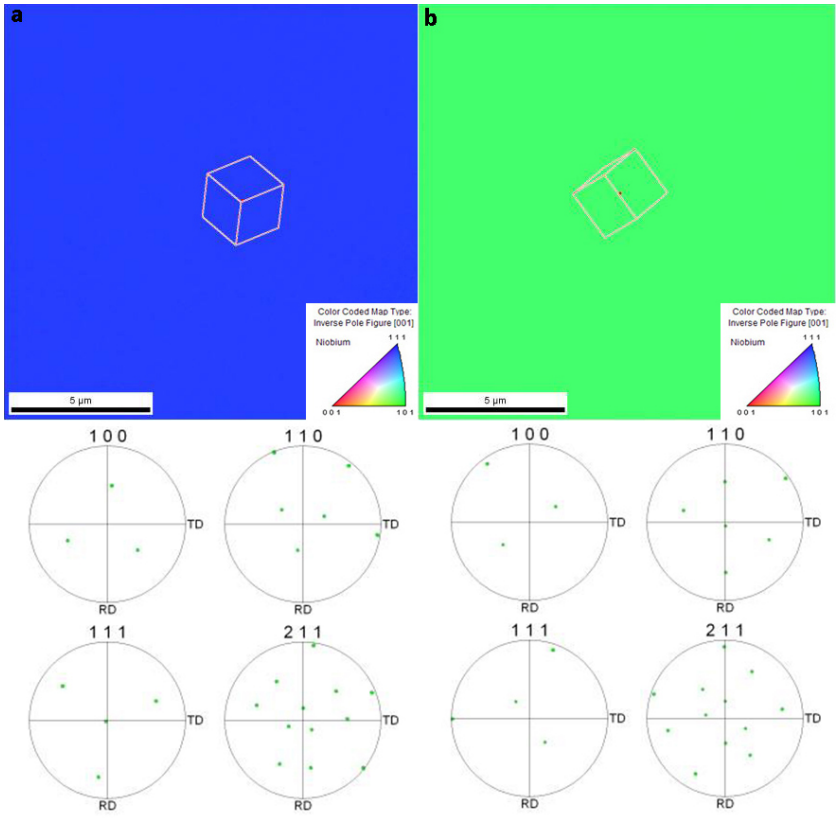

Figure IV.2.6: EBSD survey of two Nb/ Al_2O_3 (0001) samples coated at 360 °C/360 °C with respective ion energy of (a) 64 eV and (b) 214 eV.

Effect of thermal conditions and film thickness

Once the Nb template has been formed, the film grows homo-epitaxially. Stemming from the two possible epitaxial orientations on Al_2O_3 $(11\bar{2}0)$ single crystal, biaxial anisotropy is observed for thicknesses up to a few 100 seconds of nm while uniaxial anisotropy is observed for thicker films where one crystalline domain grows preferentially. On figure IV.2.7, the film on the left is only 230 nm thick where the film on the far right is 2 μm thick.

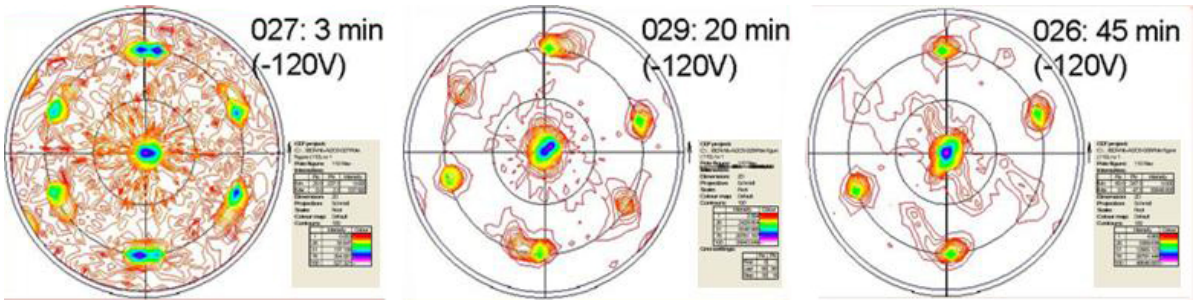

Figure IV.2.7: Structure evolution of Nb films deposited on Al_2O_3 $(11\bar{2}0)$ as a function of thickness represented by XRD pole figures, [110] axis.

Thermal energy is necessary during deposition. For films on insulators, the higher the substrate temperature during coating, typically the higher the quality of the film. The next section will show that Nb films grown on substrates which have been pre-treated in situ at high temperature are typically of higher quality (better crystallinity, higher RRR) due to impurities desorption and defect annihilation with recrystallization

Tunable RRR towards Tunable RF Performance

As mentioned before, one useful tool to assess the quality of a film is the residual resistivity ratio (RRR). It is a direct measure of the mean free path and quality of the film that is affected by any present scattering center. Unprecedented RRR values, although they may not be required for SRF thin films, have been measured on a variety of substrates.

With the variation of the incident ion energy, the substrate nature, preparation and temperature (figure IV.2.8 and table IV.2.1), the Nb films' RRR can be tailored from low values (~7) to high RRR values (500).

Table IV.2.1: RRR for Nb grown on $(11\bar{2}0)$ sapphire (bias voltage= -120V, 184 eV) versus bake and coating temperatures

Bake Temperature[°C]	**Coating Temperature [°C]**	**Bias[-V]**	**RRR**
360	360	120	180
360	500	120	189
500	360	120	348
700	360	120	348
500	500	120	488

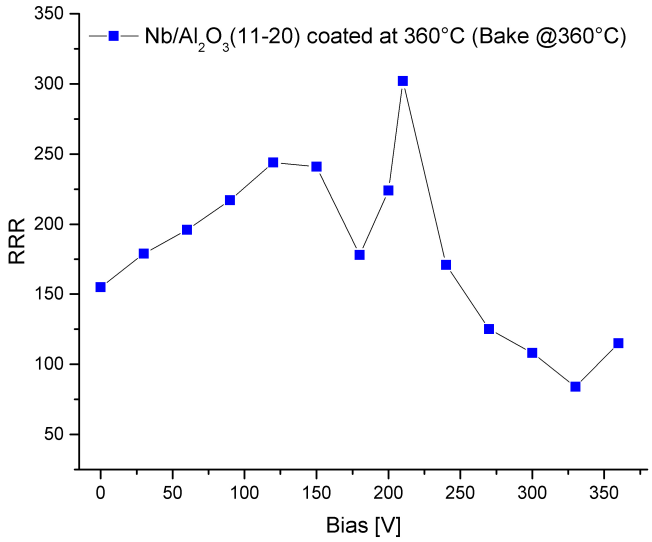

Figure IV.2.8: RRR of ECR Nb films grown on $(11\bar{2}0)$ Al_2O_3 samples baked and coated at 360 °C as a function of bias voltage.

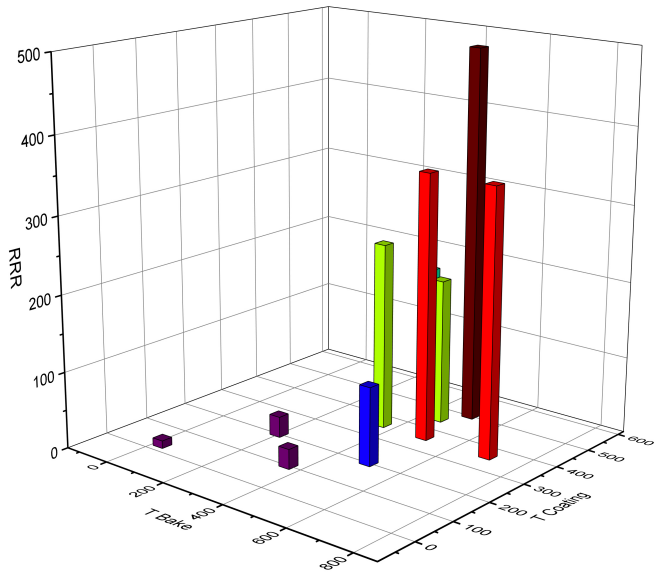

Figure IV.2.9: Variation of RRR as a function of bake-out and coating temperatures for an ion incident energy of 184 eV

Impurities

Hydrogen is often identified as a potential source for RF losses in SRF cavities. As seen in chapter I.2, Heat treatment processes to outgas hydrogen concentrations from bulk Nb are part of SRF cavities preparation standard procedures. In the ECR coating system, potential sources are the residual hydrogen in the chamber and hydrogen trapped in the e-beam gun Nb target. SIMS depth profiles were therefore performed on ECR Nb films using O_2^+ and Cs^+ primary ion beams. The typical experimental parameters for O_2^+ primary beam were 5.5 keV

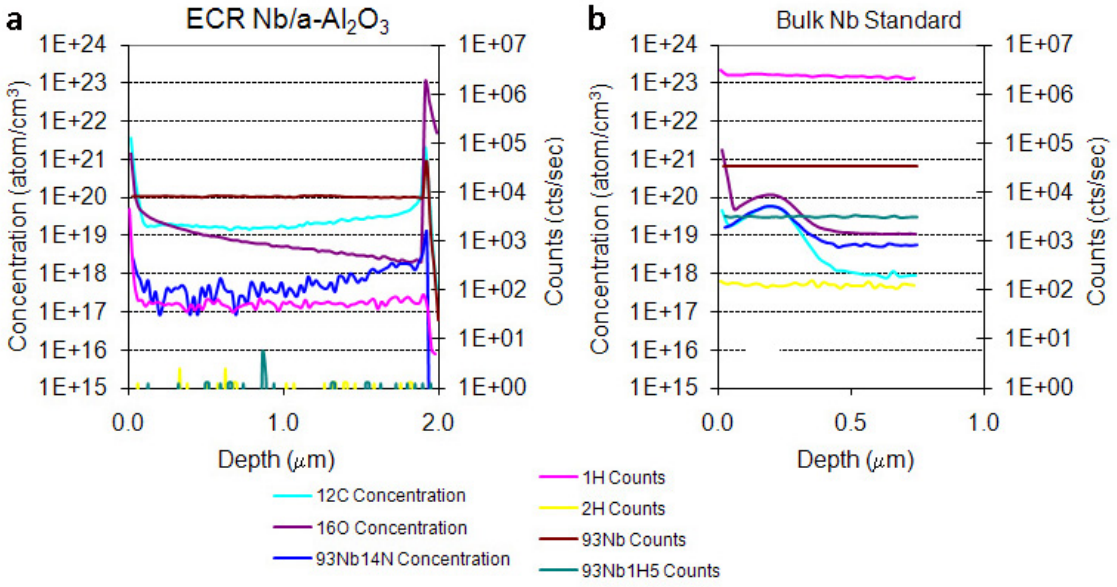

Figure IV.2.10: SIMS depth profile for a Nb film deposited on Al_2O_3 $(11\bar{2}0)$ compared to SIMS standard for bulk Nb.

impact energy, 200 nA into 220 μm x 220 μm raster with detected area of 60 μm diameter and for Cs^+ 14.5 keV impact energy, 20 nA into 110 μm x 110 μm raster with detected area of 30 μm diameter. Analyses for H, C, O, N were made under conditions optimized to reduce background contributions: samples pumped for extended period, use of liquid nitrogen cryopanel, and analysis chamber pressure at about $2x10^{-10}$ Torr. Typical SIMS Cs^+ beam depth profiles for a Nb film deposited on $(11\bar{2}0)$ Al_2O_3 is displayed in figure IV.2.10 along with a SIMS standard measurement on a bulk Nb reference sample. Even though H and D are extremely mobile in Nb, it is possible to compare the levels between the Nb layers and the bulk Nb sample. H had been shown to be at high levels that could be reduced with certain heat treatments in an earlier study of bulk Nb [287] and was of particular interest in this measurement. The hydrogen content of ECR Nb films is found to be four orders of magnitude lower than for the standard bulk Nb material. The H levels in the film are significantly lower than that obtained for any of the bulk Nb samples measured to date, even those that have had substantial additional heat treatments [288, 289]. For C, N, and O, the results for the Nb films showed more C, less N and similar O levels compared with the implanted large grain Nb sample. The Nb film shows a decrease of O with depth that has not been observed for the bulk Nb samples. The secondary ion yield for N^- is too low to measure, therefore the molecular ion NbN^- was used to monitor this element. Similar results were achieved for Nb films deposited on MgO (100) substrates.

Impurities on the substrate surface will drift into the film and up to the surface, often revealed by blemishes on the film surface after coating and affecting the final properties of the film. For example two ECR films grown on two MgO (100) substrates side by side varied in RRR from 348 to 156. SIMS measurement conducted in a similar manner revealed that the H signal was two orders of magnitude higher for the film with the lower RRR.

Energy dependence of RRR

Figure IV.2.11 below presents the RRR values for films coated at 360 °C with various bias voltages on both single crystal sapphire $(11\bar{2}0)$ and alumina ceramic. The influence of ion energy on the film quality appears less significant for the ceramic substrate than in the case of

the crystalline substrate due to the contribution of the increased roughness and high disorder of the substrate surface.

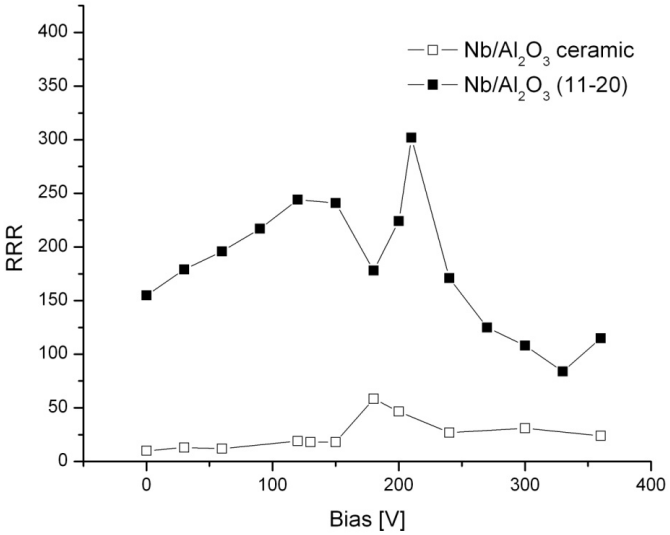

Figure IV.2.11: RRR for Nb films coated on Al_2O_3 $(11\bar{2}0)$ single crystal and Al_2O_3ceramic substrates at 360 ° C

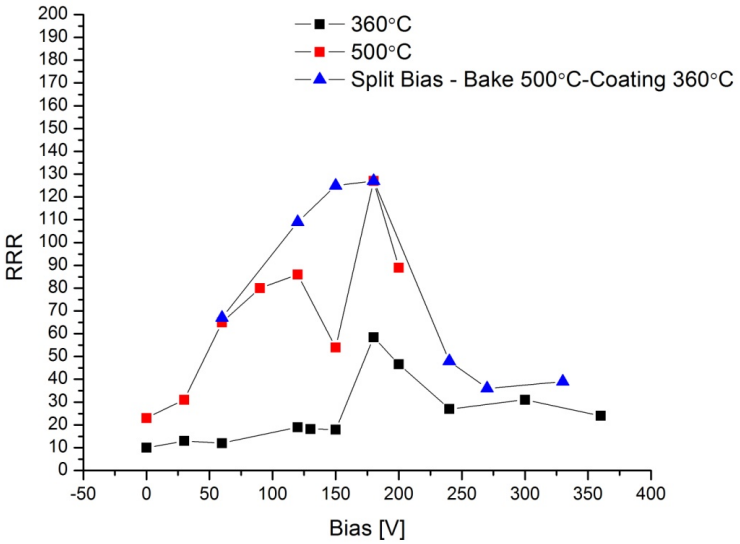

Figure IV.2.12: RRR versus bias voltage for Nb films on Al_2O_3ceramic substrates coated at constant ion energy for different temperatures (black and red) and nucleated at different energies with a subsequent growth at 64 eV (blue)

Figure IV.2.12 displays the RRR versus applied bias voltage for Nb films deposited simultaneously on alumina ceramic. Three series of films are represented. The first two series were continuously deposited with applied bias respectively at 360 ° C and 500 ° C. The series grown with the higher substrate temperature leads to higher RRR value. This suggests that the added thermal energy provides better mobility of the deposited Nb atoms allowing them

to arrange themselves in position minimizing the energy of the system. The third series have been deposited with dual energy, i.e. a bias was applied during nucleation and early growth. The bias voltage was then turned off to allow subsequent growth at 64 eV. The resulting RRR are equivalent or higher than for the film coated continuously at higher energy and higher temperature. This gives indications that once an adequate template on the substrate has been created, higher film quality can be achieved with subsequent growth at energies that promote epitaxy and fewer defects [160, 6]. This is observed for almost all the substrate natures.

In order to determine the evolution of RRR as a function of the substrate orientation Nb (100), (110) and (111) films were coated simultaneously on single crystal sapphire substrates of $(1\bar{1}20)$, $(11\bar{2}0)$, (0001) orientations as well as on alumina ceramic (polycrystalline fiber growth) after heat treatment for 24 hours at 500 °C to anneal and desorb species from the substrate surface. The film nucleation and early growth occurred at 360 °C with various ion energies. Subsequent growth was then performed at 360 °C for 25 minutes with 64 eV ion energy. A second 64 eV coating step of 30 minutes was done the next day after 12 hours interruption with the samples remaining at 360 °C. Nb (100) grows on $(1\bar{1}20)$ Al_2O_3 and displays systematically higher RRR values than Nb (110) and Nb (111) films. The increase of RRR above 150V bias observed for Nb films deposited on (0001) marks the transition in Nb structure from (111) to (110).

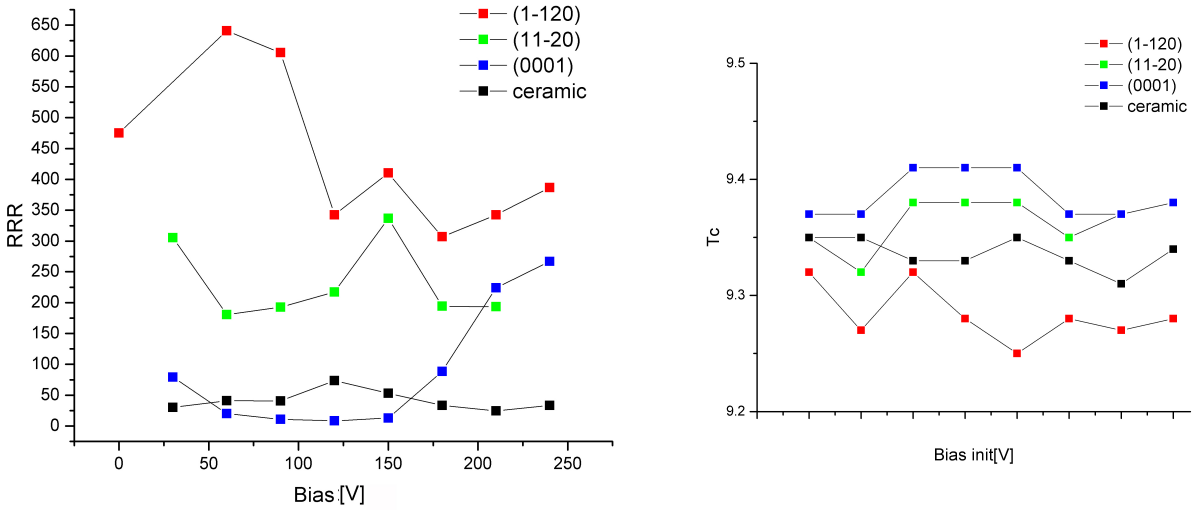

Figure IV.2.13: RRR and T_c versus bias for Nb films deposited on sapphire and alumina substrates

Surface resistance for Nb/ $Al_2O_3(11\bar{2}0)$

ECR Nb films were also deposited on 50 mm single crystal sapphire, $Al_2O_3(11\bar{2}0)$ with a 0.5° miscut for RF measurement in the 7.5 GHz sapphire-loaded TE_{011} cavity. Figure IV.2.14 plots the surface resistance as a function of temperature for two ECR Nb films compared to a large grain bulk Nb sample. As for the RRR results discussed above, on can note that the film grown with high ion energy for nucleation and then low energy for the subsequent growth at 360 °C as a very similar behavior to the film grown with constant energy (-120 V bias) at higher temperature (500 °C). This suggests again that the coating parameters can be tuned to perform the Nb film deposition in more favorable conditions, i.e. lower temperature, while maintaining the final RF performance.

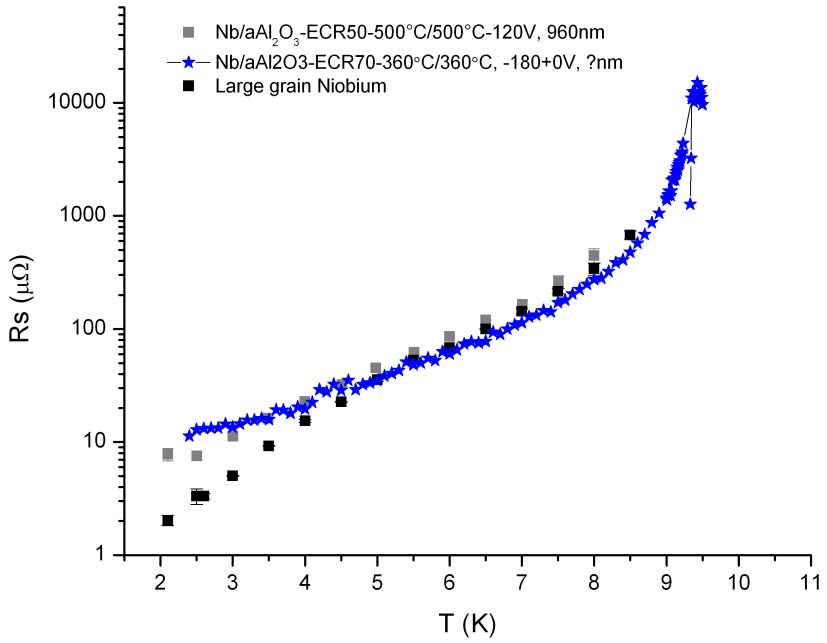

Figure IV.2.14: Surface resistance versus temperature of ECR Nb films deposited on single crystal Al_2O_3 $(11\bar{2}0)$

IV.2.1.2 Nb on MgO substrates

MgO (100), (110) and (111) single crystals were also used as substrates. Similar results were achieved for all orientations within the variations due to epitaxial relationships and lattice mismatch. The results on MgO (100) are reported below. According to Hutchinson *et al* [176, 178, 290], epitaxial growth of Nb on MgO (100) has three possible orientations: O, O_p, and F. The strict relationships are presented by Miller indexes and illustrated in figure IV.2.15.

TABLE I. Tabulation of the lattice misfit parameters for the observed orientation (O), $(001)_{Nb}//(001)_{MgO}$ with $[010]_{Nb}//[010]_{MgO}$, a more favored orientation (F), $(101)_{Nb}//(001)_{MgO}$ with $[0\bar{1}1]_{Nb}//[100]_{MgO}$, and a second possible orientation O_p, $(001)_{MgO}$ with $[110]_{Nb}//[010]_{MgO}$.

Orientation	Parallel directions	% misfit
O	$[100]_{Nb}//[100]_{MgO}$ $[010]_{Nb}//[010]_{MgO}$	19.4 19.4
O_p	$[100]_{Nb}//[010]_{MgO}$ $[100]_{Nb}//[110]_{MgO}$	8.0 56.5
F	$[0\bar{1}1]_{Nb}//[100]_{MgO}$ $[010]_{Nb}//[010]_{MgO}$	8.0 19.4

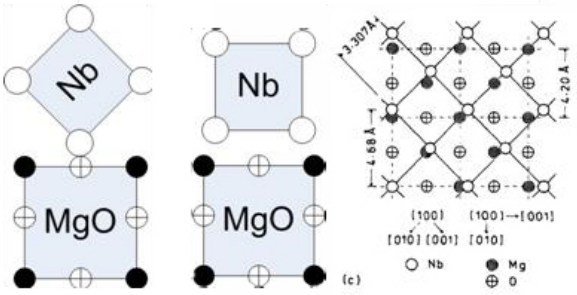

Figure IV.2.15: Three-dimensional epitaxy relationship of Nb/MgO (100), as proposed by Hutchinson *et al.* [290]

In this study, only the F-type orientation has been observed. At high bias voltage (-120V ~ -200V), Nb {110} films exhibit single crystal behavior.

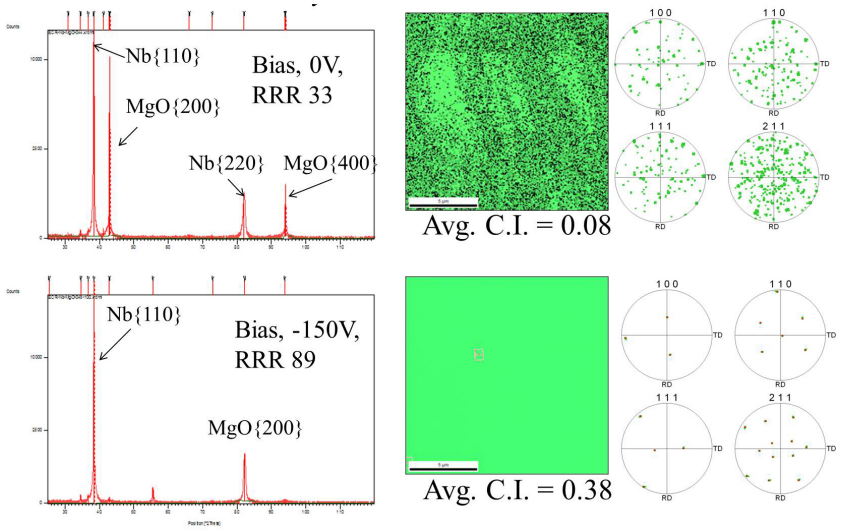

Figure IV.2.16: XRD and EBSD IPF Maps for Nb deposited on MgO(100)

The TEM cross-section for a typical ECR Nb (110)/MgO (100) is reported in figure IV.2.17. The detail of the interface and the associated selected area diffraction (SAD) patterns show that, in this case also, the films exhibit the single-crystal-like structure and the interface between film and substrate is continuously crystalline and has a well-defined orientation relationship.

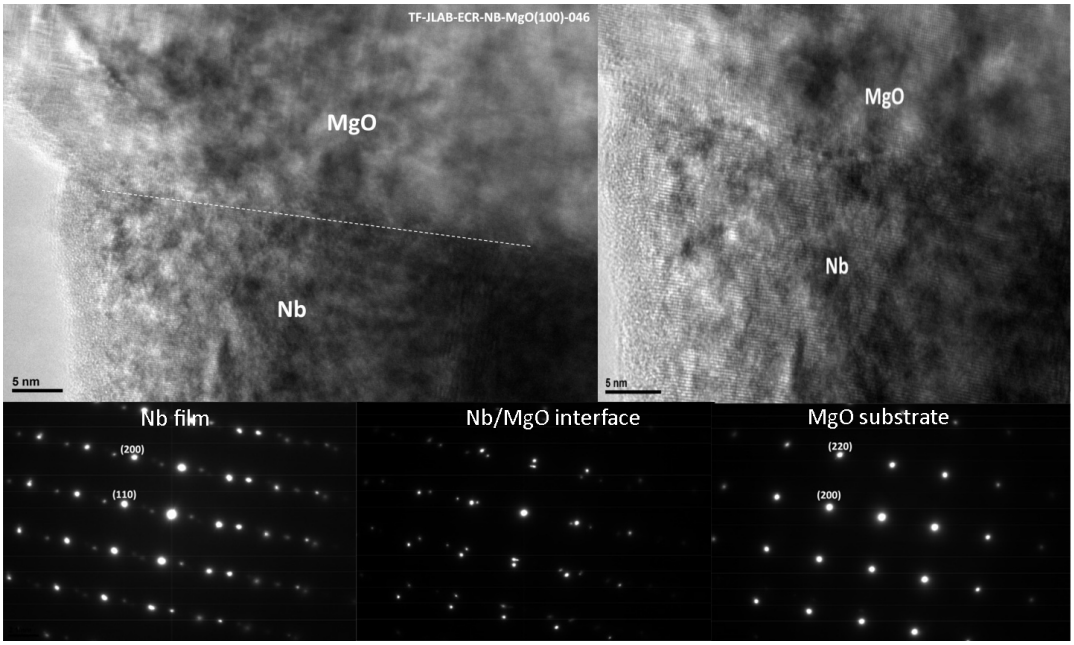

Figure IV.2.17: TEM micrograph of an Nb film and its interface with the MgO (100) substrate. The associated selected area diffraction (SAD) patterns are for, from left to right, the Nb film, the Nb/MgO interface and the MgO substrate.

At constant coating temperature, the quality of the Nb films grown on MgO (100) increases with the incident ion energy. The orientation of ECR Nb films on MgO (100) is (110). Some collaborators have observed the O relationship Nb (100) on MgO (100) [105] in certain conditions by vacuum arc deposition and fast magnetron sputtering, exhibiting very high RRR, but

this has never been observed with ECR films.

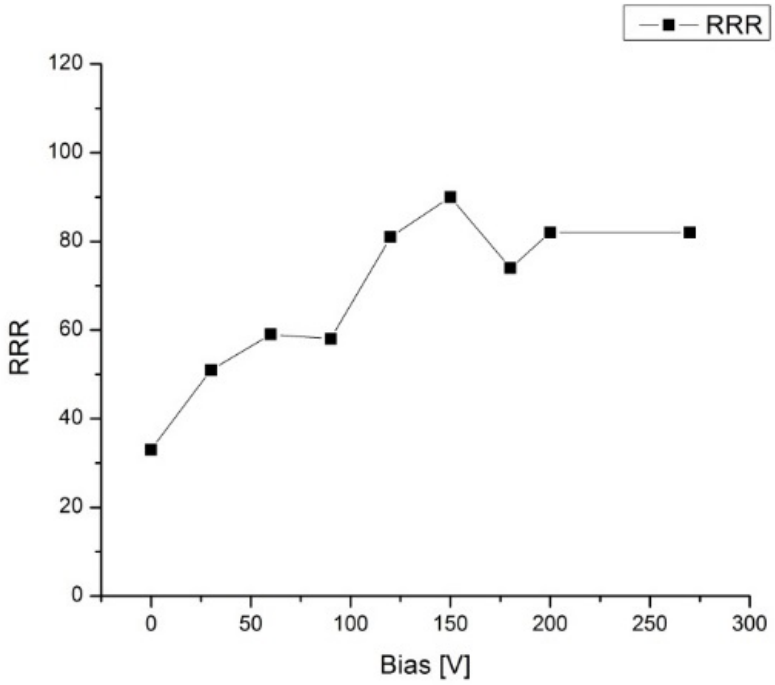

Figure IV.2.18: Variation of RRR as a function of bias voltage for films coated at 360 °C on MgO (100).

IV.2.1.3 Nb on amorphous substrate: fused silica

Single crystal substrates such as α-Al_2O_3 or MgO drive the growth of Nb film hetero-epitaxially across most of the range of temperatures and ion energy. It is useful to investigate the growth of Nb in conditions where it is not driven by the crystalline orientation of the substrate. At this effect, films have also been grown on fused silica as it is a fully amorphous material but it retains minimum roughness. Figure IV.2.19 represents the EBSD survey (top) and 10 μm x 10 μm AFM scan (bottom) of Nb on fused silica films coated at -120 bias and 360 °C after a bake-out at 360 °C. R_a for this film is 4.9 nm.

RRR values versus deposition bias voltage for ECR Nb films grown on fused silica (the substrate bake-out and coating are 360 °C) are reported in figure IV.2.20. The variation as a function of applied bias voltage is much more modest in this case, most likely due to density of grain boundaries. It is worth noting that, even for this type of columnar fibrous films, the RRR is higher than 20 over a large range of ion energy.

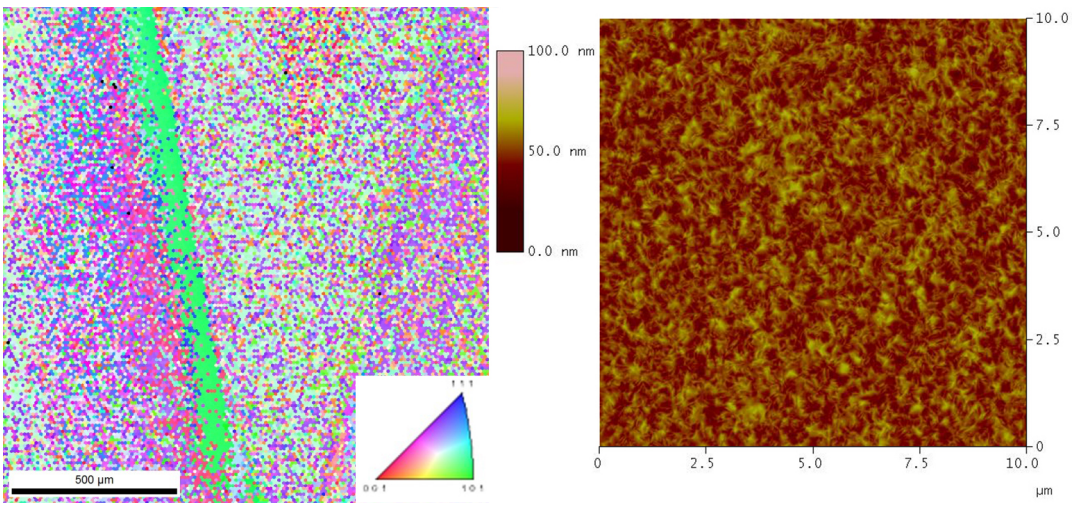

Figure IV.2.19: EBSD map (left) and AFM 10 μm x 10 μm scan (right) of an ECR Nb film deposited on fused silica with a -120 V bias at 360 °C.

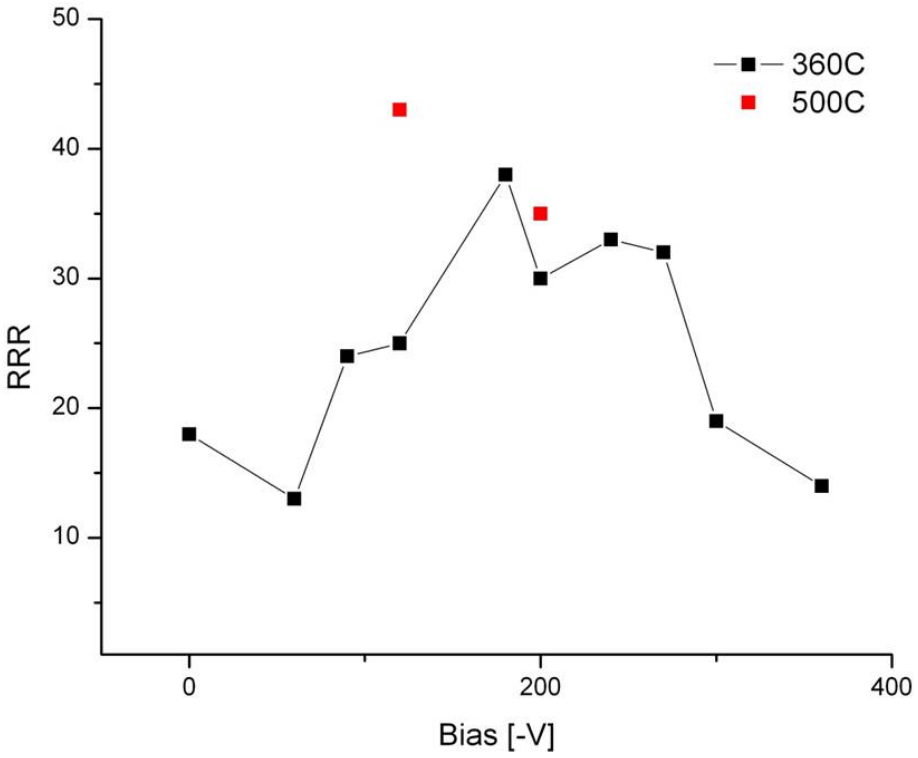

Figure IV.2.20: RRR versus bias voltage for Nb films coated on fused silica at 360 ° C

IV.2.2 Nb films on metallic substrates

Adequate substrates for SRF cavities need to be easily formable and have good thermal conductivity to quickly remove any heat generated by potential defects on the surface. Metals such as Cu or Al present themselves as good canditates. As seen in chapter I.3, Nb/Cu technology has already demonstrated to be a route worth pursuing for SRF cavities. Although Al is a material of great interest as a substrate for SRF cavities due to its low cost, thermal conductivity and castability which could potentially allow to completely separate x from the final SRF surface, this study only considered the growth on Nb on Cu.

Structure analysis as a function of substrates and thermal conditions

As in the case of crystalline insulating substrates, with higher energy and/or temperature as provided in deposition by electron cyclotron resonance, Nb adatoms have enough energy to diffuse on the surface and hetero-epitaxy is favored on crystalline Cu substrates. Fig. IV.2.21 represents EBSD maps for Nb films grown simultaneously on various Cu substrates at 360 °C and with a bias of -150V (214 eV). Heat treating the substrates prior to coating at 360 °C allows the complete dissolution of the native Cu oxide layer into the bulk without suffering from roughening due to Ostwald ripening occurring for Cu at temperatures higher than 400 °C [291]. ECR Nb films (figure IV.2.21 a, b, c) grow on single crystal Cu (100), (110) and (111) respecting the hetero-epitaxial relationships for Nb and Cu [180]. On polycrystalline Cu substrates (figure IV.2.21 d, e), the Nb films replicate the grain size of the underlying substrates. The RRR values for these given films are reported in table IV.2.2

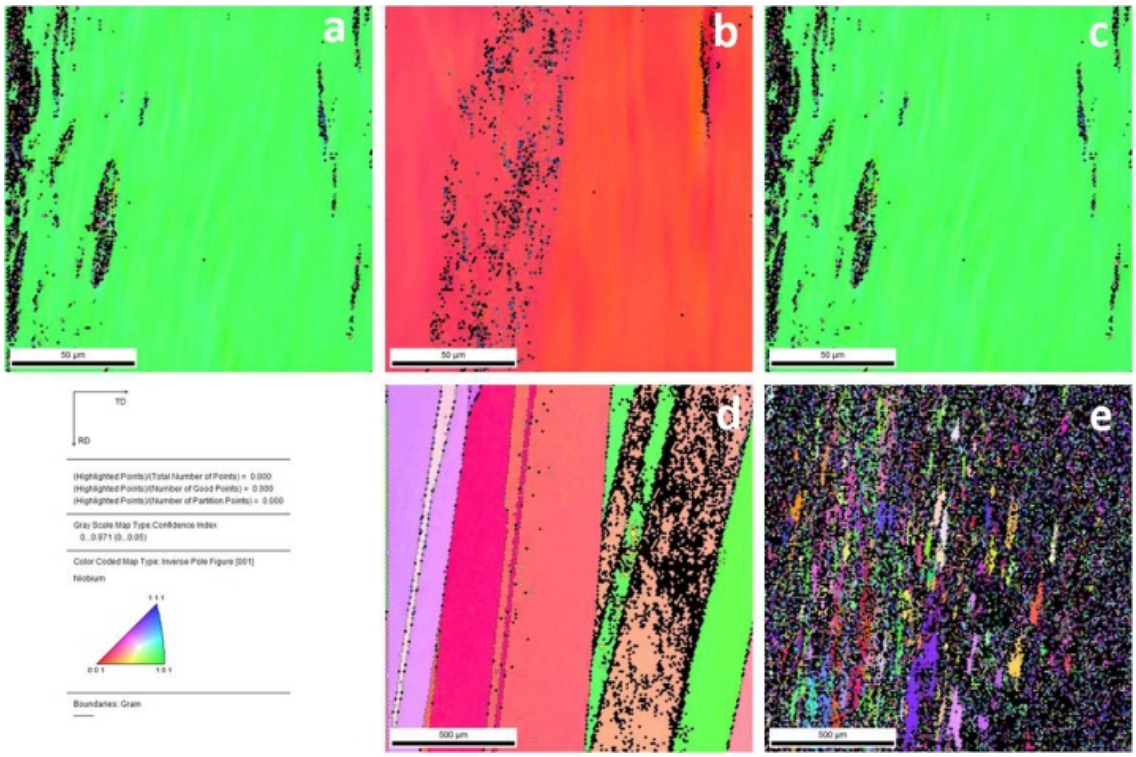

Figure IV.2.21: EBSD maps of Nb films grown on Cu (a, b, c) single crystal (100), (110), (111), polycrystalline (c) large grains and (d) fine grains simultaneously.

HR-TEM cross-sections of Nb films grown hetero-epitaxially on polycrystalline Cu substrates show sharp interfaces between the Nb film and Cu substrate. The film presented in

Table IV.2.2: RRR for ECR Nb films from figure IV.2.21 (ion energy =-214 eV, 360 °C, 360 °C) versus Cu substrate nature.

Cu Substrate	**RRR**
(100)	89
(110)	77
(111)	249
Polycrystalline large grains	170
Polycrystalline fine grains	82

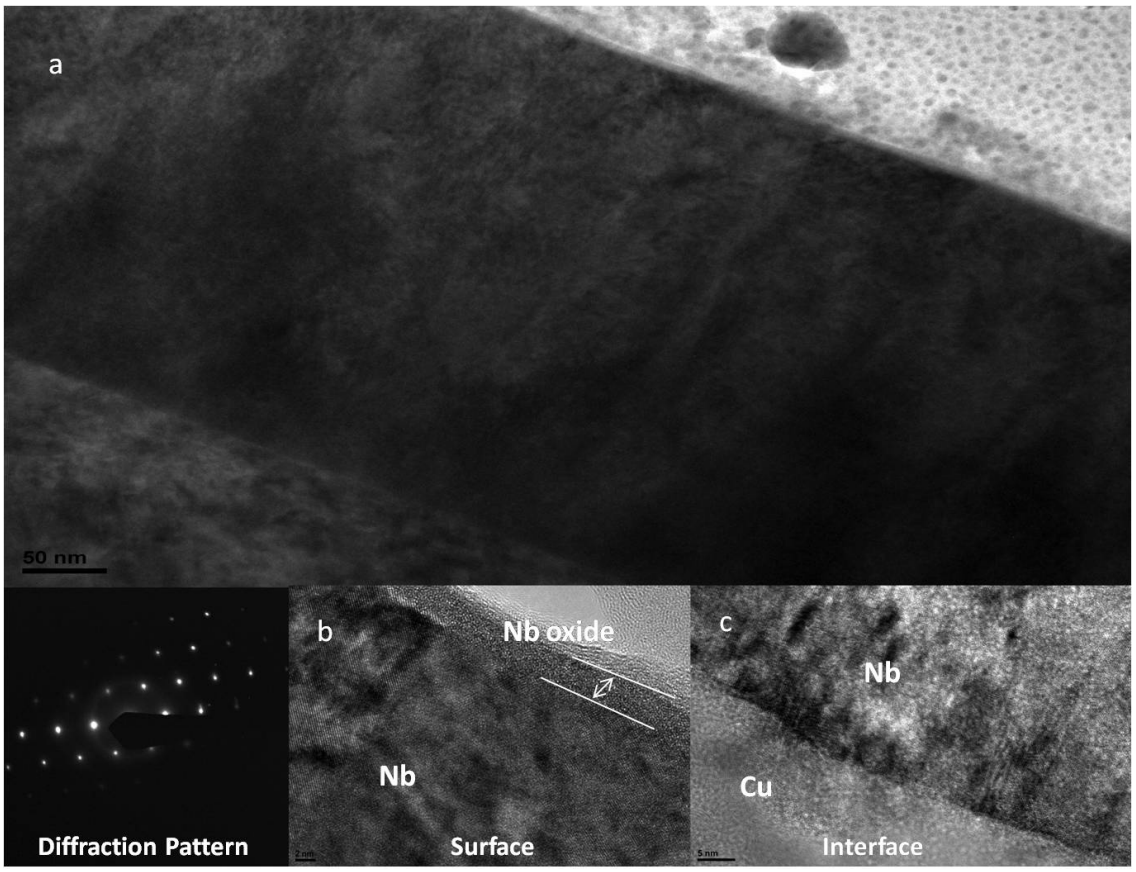

Figure IV.2.22: TEM cross-section of Nb film grown on polycrystalline Cu with details of the surface oxide and the interface with the substrate.

figure IV.2.22 was deposited at 184 eV and 360 °C. Although the film is very thin, only 250 nm thick, the RRR measured was 120. As a comparison, the reported RRR for 1.5 μm magnetron sputtered films in the framework of the 1.5 GHZ Nb/Cu studies at CERN, was 40. Thus the ECR Nb film show enhanced film qualities compare to films deposited with conventional techniques.

The figure IV.2.23 represents EBSD maps for ECR films coated at 360 °C for bias voltages of -120 V and 0 V corresponding to incident ion energies of 184 eV and 64 eV. For higher ion energy, the film grows in the ab-normal mode [172] (a) and the grain size is considerably enlarged.

The presence of an oxide on the surface, common with metallic substrates, inhibits epitaxy and leads to fiber growth. Figure IV.2.24 displays the EBSD IPF maps and STEM micrographs

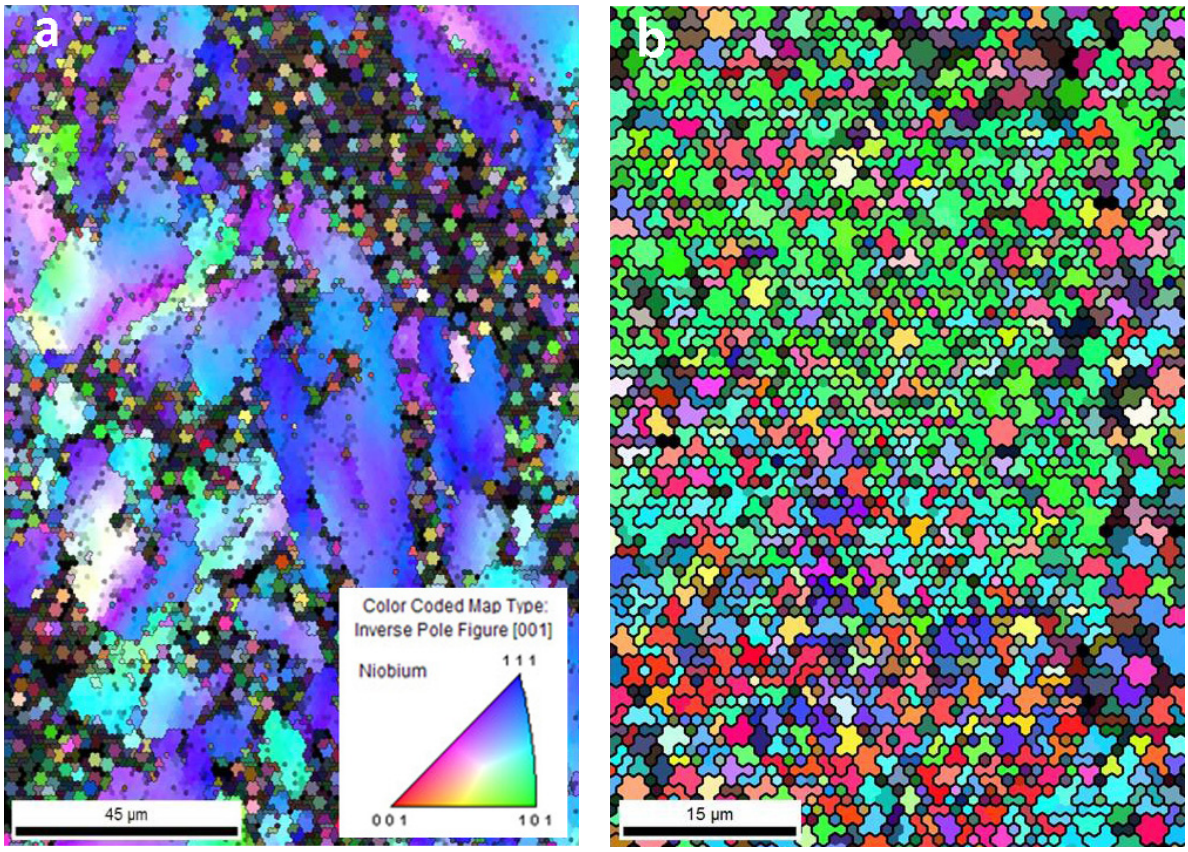

Figure IV.2.23: EBSD maps of Nb films grown on heat treated Cu with a bias voltage of (a) -120 V and (b) 0 V.

for films nucleated at 184 eV (-120 V) on polycrystalline Cu (left, substrate heat treated to 500 °C prior coating) and on the native amorphous Cu oxide (right, substrate heat treated to 200 °C). One should note the difference in scale (3 mm versus 3 μm) for the EBSD maps. The film grown on a crystalline interface shows hetero-epitaxy with a grain structure duplicating the substrate structure. The interface is continuously crystalline . The film grown on Cu oxide exhibit a grain size of the order of 1 μm or less with a preferential (110) orientation.

It is found that thermal energy is necessary during deposition. However for Nb on Cu, dependent of ion energy, there is a thermal threshold. Nb delaminates when coated at high energies and high substrate temperatures. With a substrate at 500 °C, delamination occurs for ion energies higher than 90 eV. At 360 °C, ion energies up to 360 eV form films without delamination. This shows how the intrinsic stress threshold evolves with incident ion energy and substrate temperature.

IV.2.2.1 Influence of substrate quality

Any defect (scratch, pin-hole) is duplicated and enhanced in the film as it grows. Figure IV.2.25c shows transmission electron (TEM) micrographs from a focused ion beam (FIB) cut sample of an ECR Nb film grown on polycrystalline Cu. The presence of a void in the Cu substrate near the surface induced surface defects which resulted in ab-normal growth revealed by the presence of columnar grains in between very large grains on each side.

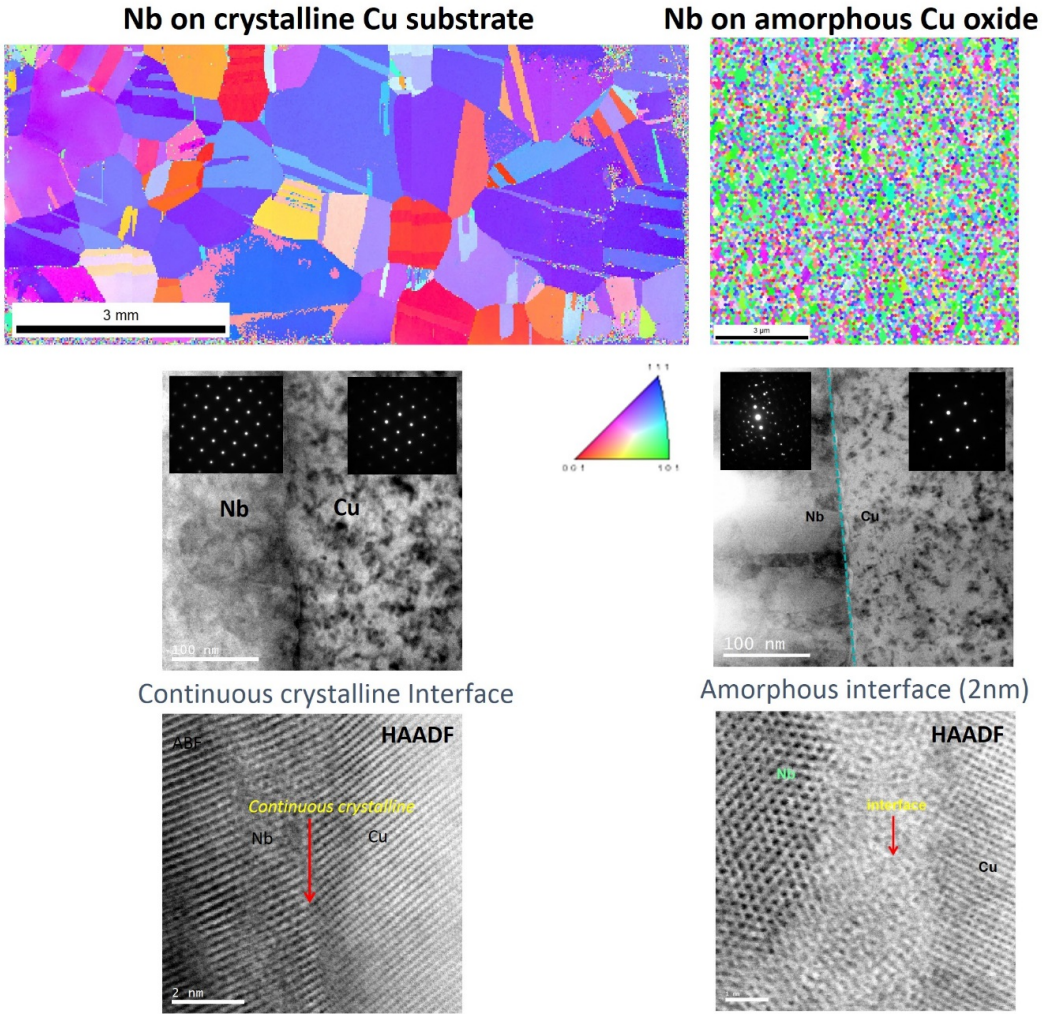

Figure IV.2.24: Structure and interface comparison for Nb films grown on a crystalline Cu surface and on an amorphous Cu oxide surface.

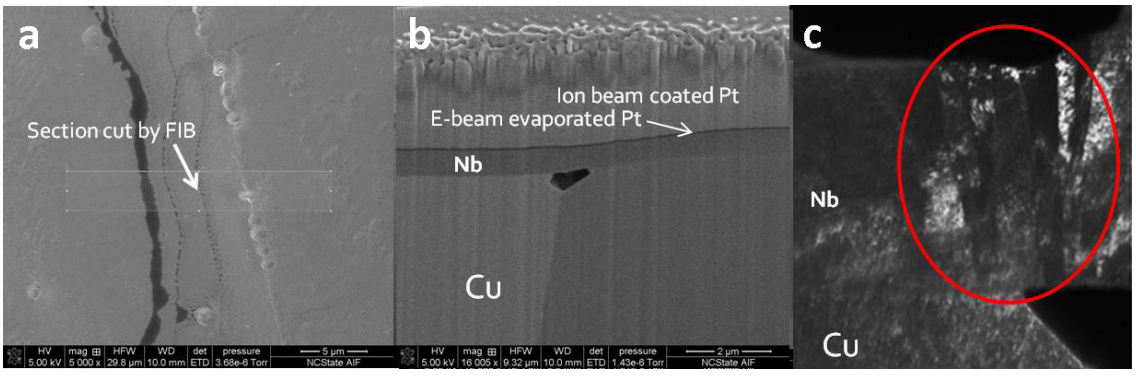

Figure IV.2.25: (a), SEM micrograph of an ECR Nb/Cu film at the location of FIB cut (b) FIB cross section revealing a void in the Cu substrate near the surface, (c) TEM cross section in dark field revealing the resulting ab-normal growth in the Nb film.

IV.2.2.2 Energy dependence of RRR

Figure IV.2.26 gives the variation of RRR as a function of incident ion energy for films deposited on the 3 different single crystal Cu planes as well as on polycrystalline large and fine grains cu substrates. Even though, the quality of the film is highly dependent on the vacuum conditions, substrate stress, cleanliness, one can distinguish a trend of increased quality and RRR value for increasing energy up to a an optimum for the different orientations of Cu. This is also observed for polycrystalline fine grain Cu substrates. The RRR of Nb (100) films on Cu (110) are almost systematically higher than for Nb (110) and (111). As it was reported in section IV.2.1, the same phenomenon also occurs for Nb (100) films deposited on Al_2O_3 $(1\bar{1}20)$.

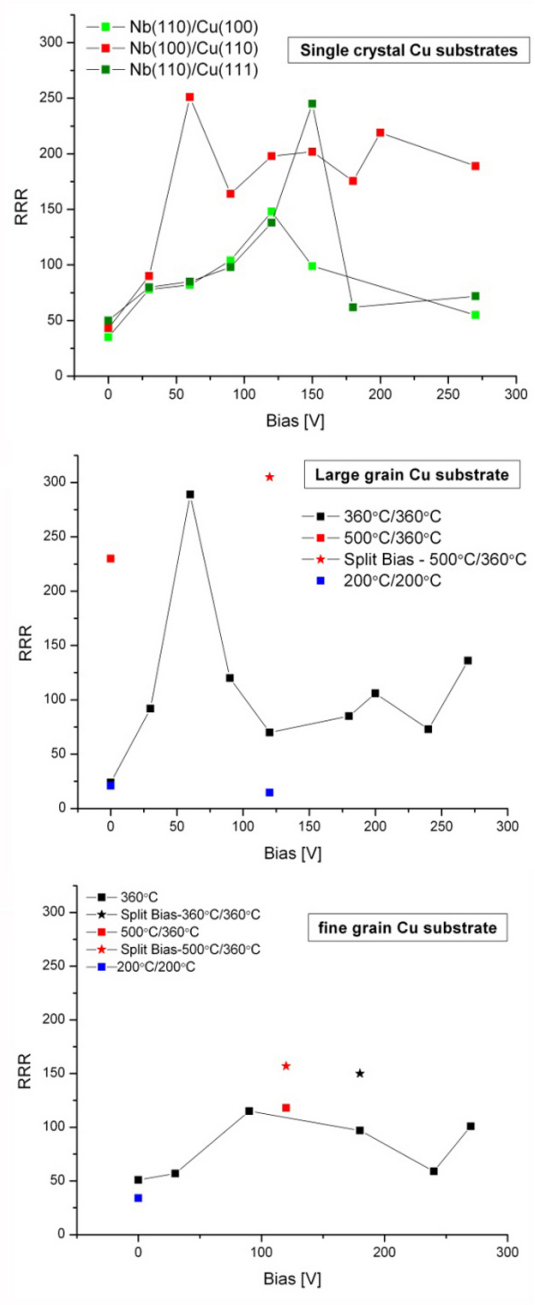

Figure IV.2.26: Variation of RRR as a function of bias voltage for Cu single crystal and polycrystalline substrates

IV.2.2.3 DOS gap analysis

As seen in chapter I.1, viable SRF material for Gap measurement were performed on a series of Nb on Cu films by Point Contact Tunneling (PCT) spectroscopy [250] on ECR Nb films deposited on large grain Cu substrates at different temperatures. Hetero-epitaxial films have a superconducting gap similar to bulk Nb (Δ=1.61-1.56 meV, figure IV.2.27) where fiber films grown on the native Cu oxide have a superconducting gap of 1.3 meV.

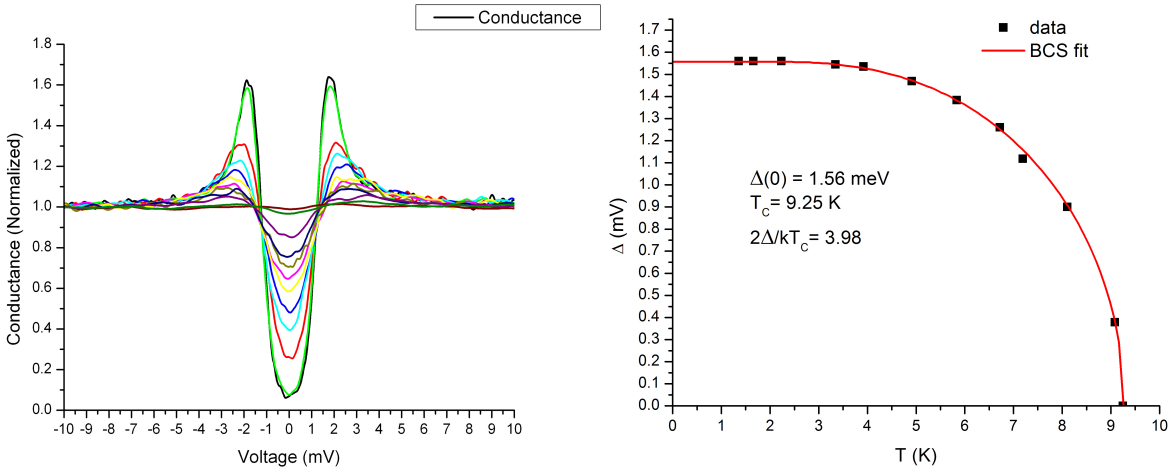

Figure IV.2.27: Superconducting gap measurement for a hetero-epitaxial polycrystalline Nb/Cu film (RRR=289)

Figure IV.2.28 shows the PCT gap measurement results for a film grown continuously with an ion energy of 184 eV and for a film grown at 184 eV for the nucleation and coalescence phases followed by subsequent growth at 64 eV in two steps (i.e. the growth of the film was interrupted for a few hours at temperature). It is interesting to note that for the thicker film grown with dual energy and in two steps, two gap values are measured: one similar to the other hetero-epitaxial films and the other one similar to fiber films. The TEM cross-section observations of such film did not reveal any notifiable change in structure or any interface within the film thickness. The change in gap could be due to the residual vacuum species, such as O and H, absorption after the first part of the film growth.

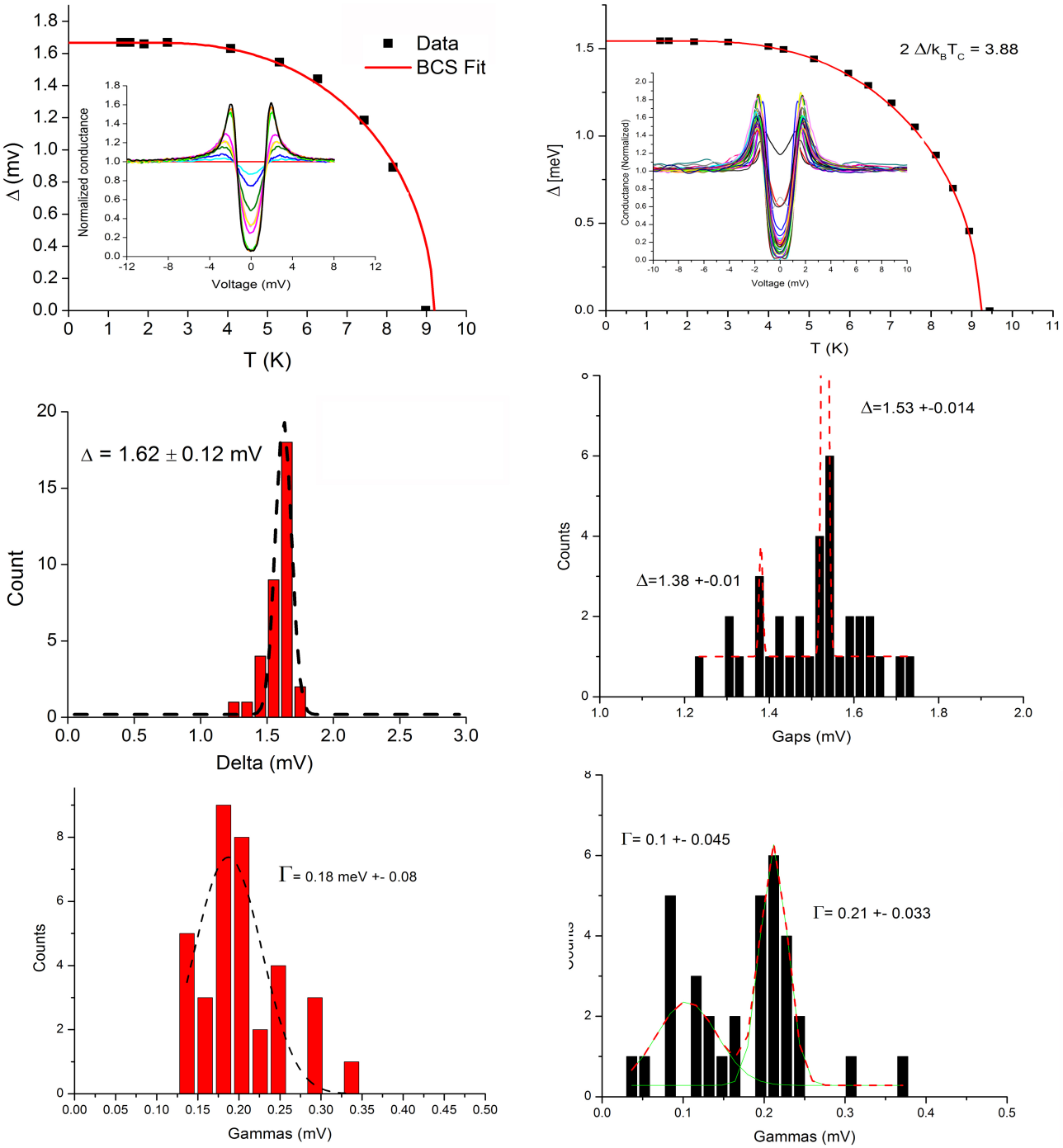

Figure IV.2.28: Superconducting gap measurement for hetero-epitaxial polycrystalline Nb/Cu films coated at 184 eV for the entire film growth (RRR=182) (left) and for the nucleation and coalescence phase followed by subsequent growth at 64 eV (RRR=305) (right).

IV.2.2.4 Surface resistance at 7.5 GHz

A series of 50 mm disk samples dedicated to RF measurements have also been produced to be investigated with the 7.5 GHz TE_{011} sapphire loaded cavity (SIC) setup. Even though, the RF measurements need to be refined, some trend seems to emerge.

Effect of deposition ion energy

Figure IV.2.29 displays the surface resistance (R_s) versus temperature for films coated with ion energies from 64 eV (no bias) to 264 eV (-200 V bias) revealing a trend of the surface resistance decreasing with increasing ion energy. One can note that for the highest incident ion energy (264 eV), although below 4 K, the residual resistance is still higher than for bulk Nb, above 4 K the measured resistance is similar to bulk Nb.

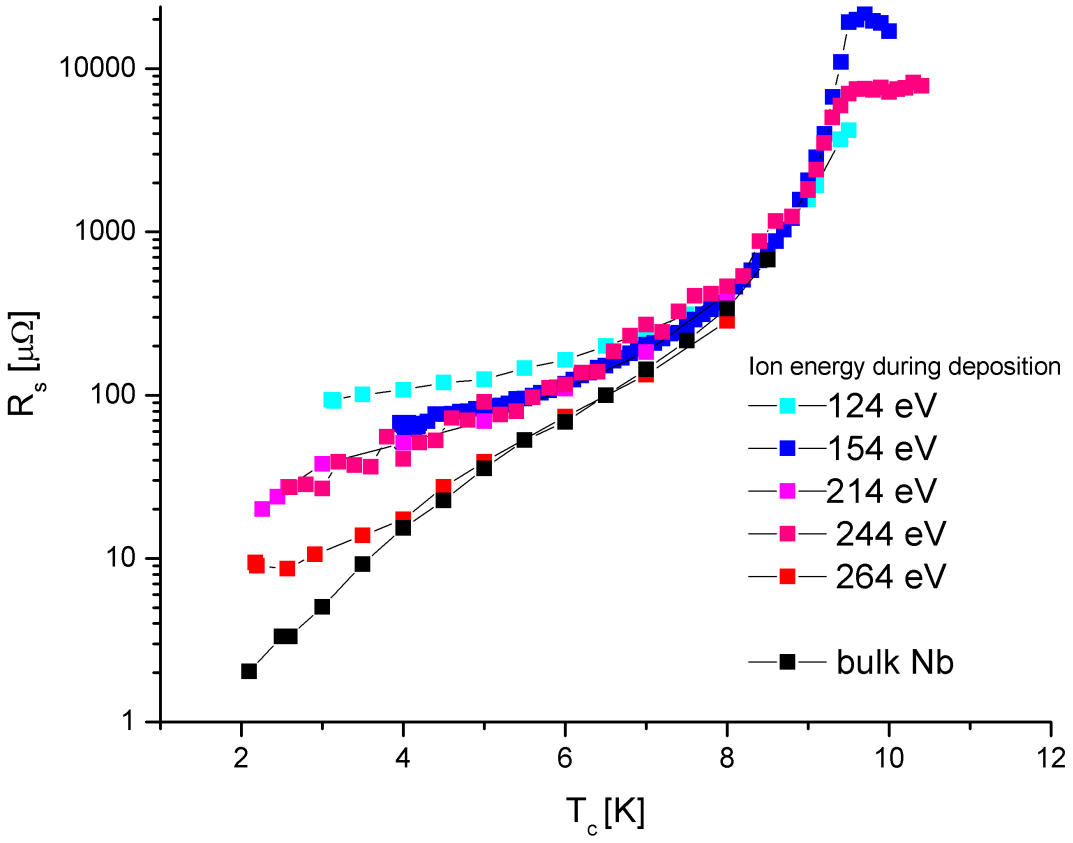

Figure IV.2.29: Surface resistance measurements for a series of ECR Nb films coated on Cu at 360 ° C and at various bias voltages.

Nucleating the film with high energy ions initially and then lowering the ion energy for the subsequent film growth by opposition to keeping the ion energy constantly high over the whole film growth seems also to have some effect on the RF performance. Figures IV.2.30 display R_s curves as a function of temperature for films deposited with a constant ion energy of 184 eV (-120 V bias), 244 eV (-180 V bias) and 124 eV (-60 V). The second set of curves (stars) represents the surface resistance for films deposited at high energy for the initial nucleation and coalescence and then switched down to 64 eV (no bias applied) for subsequent film growth. One can notice a surface resistance decrease for the films coated with dual ion energy by comparison with films grown at constant high ion energy. Once an appropriate template has been deposited, a lower ion energy favors a film growth with less defects.

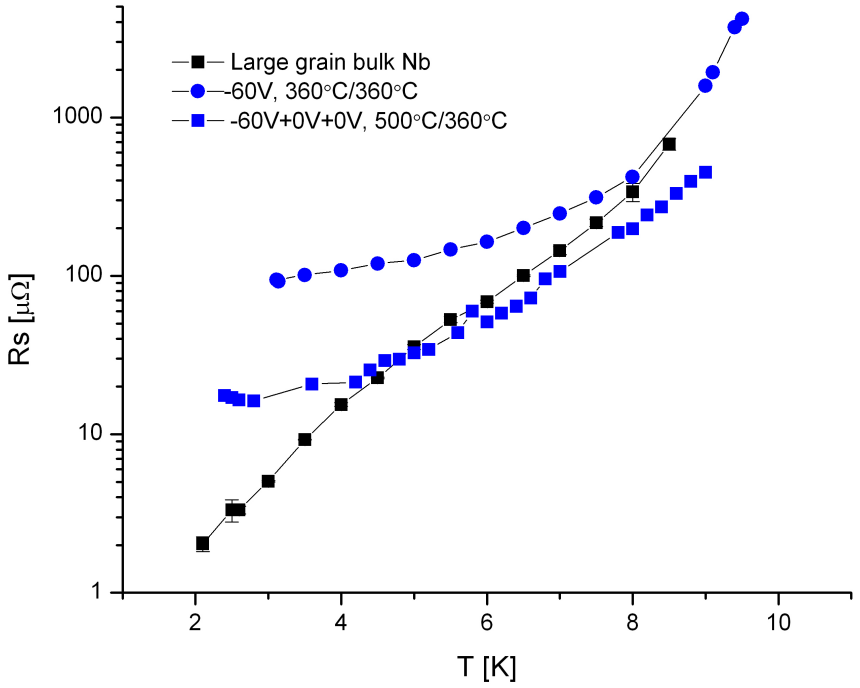

(a) Ion energy : 124 eV

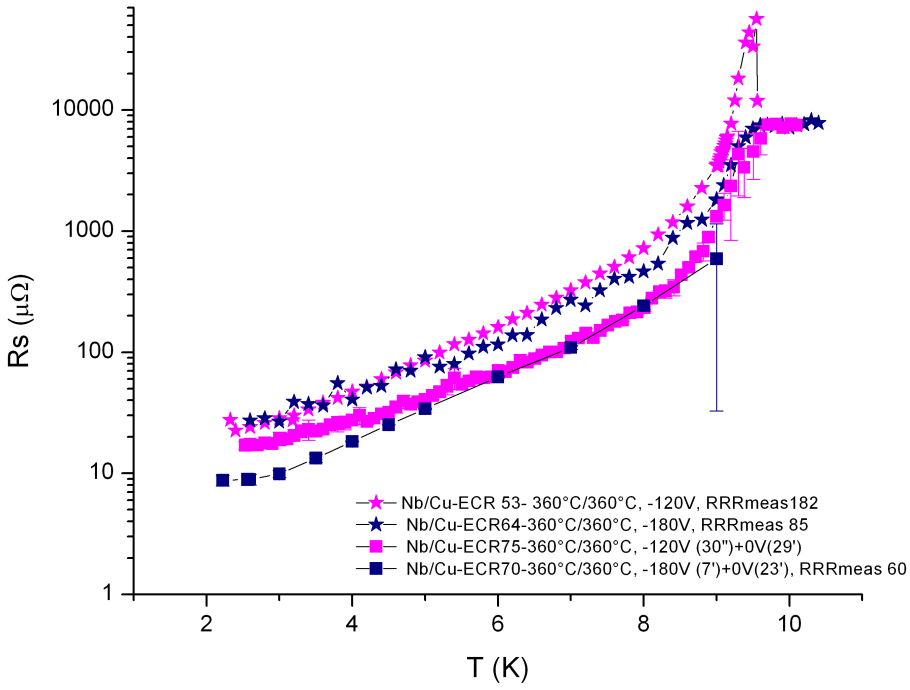

(b) Ion energy : 184 and 244 eV

Figure IV.2.30: Surface resistance measurements for ECR Nb films coated with constant or dual ion energy during film growth.

Influence of grain boundaries on *Rs*

Grain boundaries have often been in the past designated culprate contributors to RF losses in SRF cavities, in particular for Nb/Cu cavities. Figure IV.2.31 shows the Rs curves for two ECR Nb films deposited simultaneously on Al2O3 (1120) and on heat treated large grain OFHC Cu substrates. The resulting films are respectively (110) single crystal and polycrystalline. One can notice that the RF behavior of these too films are almost identical. This suggests that the presence of grain boundaries if dense is not necessarily detrimental to RF performance.

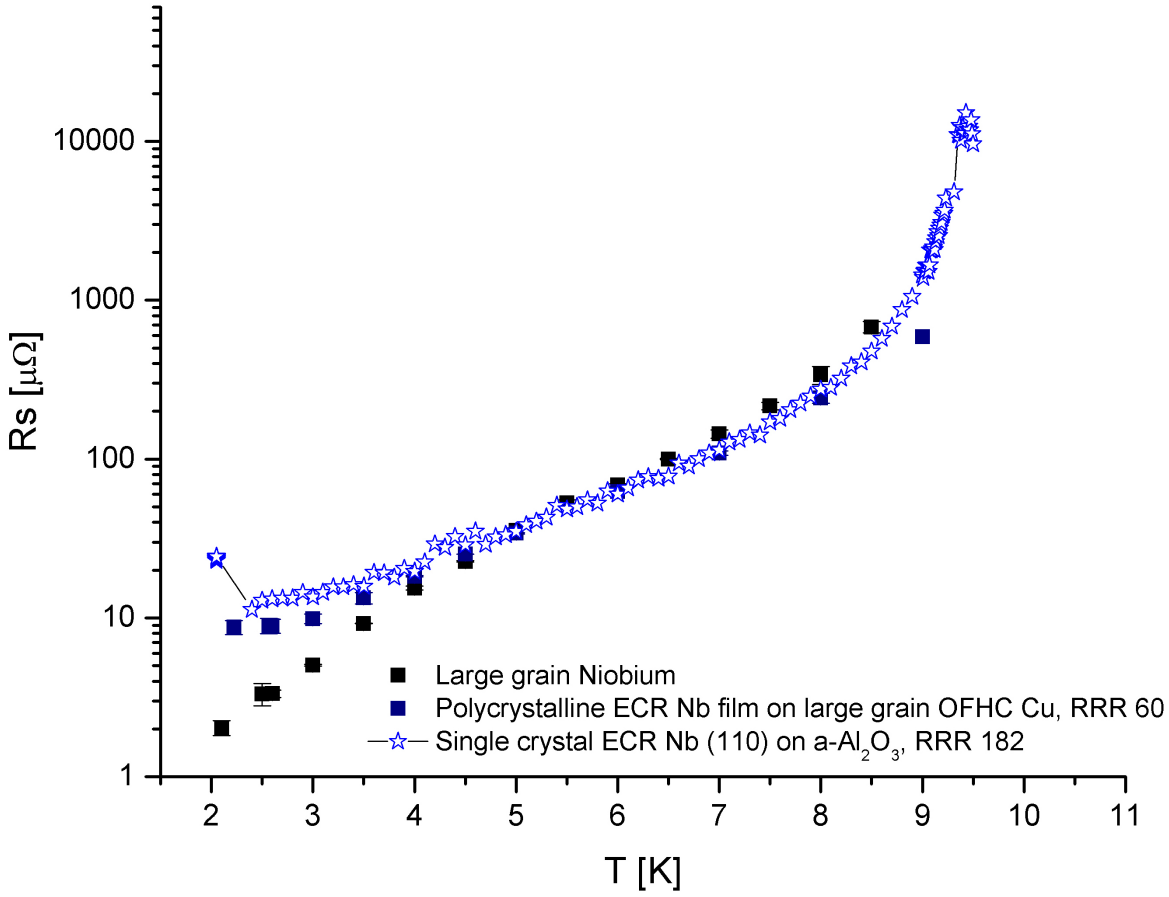

Figure IV.2.31: Surface resistance of single crystal versus large grain Nb films coated simultaneously,bake and coating at 360 °C

IV.2.2.5 Conformality of the ECR deposition process

Nb films coated on SRF cavities coated with cylindrical magnetron sputtering have issues of shadowing and porosity due to adatom incidence angle being smaller than normal incidence away from the equator. Half-cells have been coated in the ECR chamber to test the conformality of the ECR technique at 184 eV and 360 °C. Here, no particular precaution was taken to optimize the surface on the half-cell. The surface was just roughly mechanically polish prior deposition. Figure IV.2.32 shows the SEM cross-section of the equator and iris locations. The Nb film looks uniform and conformal over the whole cell surface with a thickness variation from 4 μm at the equator to 6 μm at the iris. Although the film is quite thick and the substrate roughness is high, no delamination has been observed.

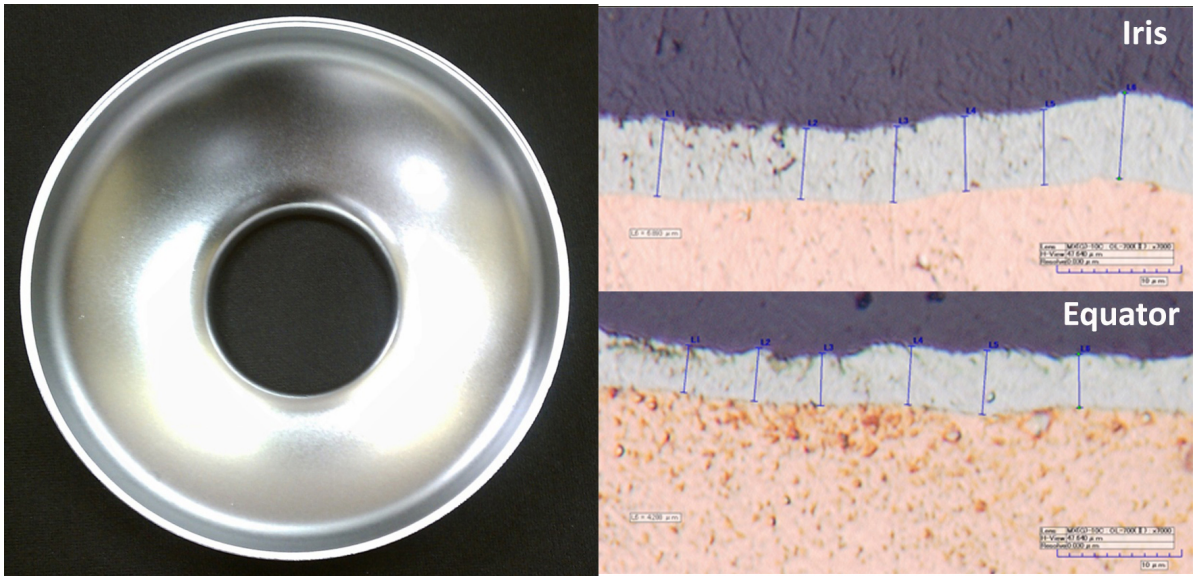

Figure IV.2.32: Cu half-cell coated in the ECR chamber (top) and cross-section of the film at the iris (center) and the equator (bottom)

Chapter IV.3

Summary

Results of this study are helpful to understand the growth of Nb under different conditions and contribute to the determination of the optimum coating parameters for SRF surfaces based on thick Nb films. Much more work is needed to optimize the film growth for ultimate RF performance, but insight has been gained. The influence of the ion energy and temperature on the structure of the film has been studied exploring the different regions of the Modified Structure Zone Diagram proposed by Anders [6] both on "ideal" and practical surfaces, such as Cu, for SRF cavities.

Single-crystal-like Nb films have been produced by ECR plasma deposition on a variety of crystalline substrates, metallic and insulators. The films' growth mechanism is hetero-epitaxy. The orientations of the thin films depend strongly on the substrate crystal planes, as well as on the bias voltage i.e. the kinetic energy of the incident Nb^+ ions. This study reveals such epitaxial relationship as: Nb{100}||Al_2O_3{$(1\bar{1}20)$}, Nb{110}||Al_2O_3{$(11\bar{2}0)$}, Nb{111}||Al_2O_3{0001} and Nb{110}||MgO(100), Nb{110}||Cu {100}, Nb{100}||Cu {110}, Nb{110}||Cu {111}. The minimum substrate heating temperature (about 360^0C) to promote epitaxy via ECR coating is moderate, roughly $0.23\,T_{m,Nb}$. The growth of Nb films on polycrystalline and amorphous surfaces was also studied, revealing that, by tuning the ion energy and substrate temperature, the structure of the film itself can be tuned. We have demonstrated that energetic condensation via ECR allows the Nb film to develop properties that, in a thermal environment, would require substrate temperatures that approach melting, i.e. a so-called homologous temperature of near unity. Good quality films can be produced at substrate temperatures practical for SRF applications.

In the past, arguments that Nb films have an inherent limitation due to their low RRR have been put forward. In this work, it was demonstrated that ECR Nb films RRR values can be tuned from single digits to bulk-like values. Unprecedented RRR values(table IV.3.1) have been measured on Nb films on a variety of substrates. The superconducting gap measurements demonstrated that the ECR films gap is very similar to bulk Nb.

The RF performance of Nb films deposited on Cu and Al_2O_3 $(11\bar{2}0)$ was measured in a sapphire loaded TE_{011} cavity at 7.5 GHz. Although the interpretation of the RF results is hindered by the limitation of the RF experimental system, some trends emerge. It was shown that grain boundaries in high quality Nb films are not necessarily detrimental to RF performance. Films deposited on re-crystallized polycrystalline Cu substrates have RRR values as high as a single crystal-like Nb film and can have a similar RF behavior. We also learned that treating the film growth in phases, nucleation/early growth and subsequent growth, can be beneficial to lower the surface resistance of the Nb film. x

Table IV.3.1: Some of the higher RRR values measured recently for ECR Nb films

	Substrate	RRR max
Single crystal	MgO(100)	196
	MgO (110)	424
	MgO (111)	197
	Al_2O_3 $(11\bar{2}0)$	488
	Al_2O_3 (0001)	247
	Al_2O_3 (1-120)	640
	Cu (100)	181
	Cu (110)	275
	Cu (111)	245
Polycrystalline	Cu fine grains	193
	Cu large grains	305
Amorphous	Al_2O_3 ceramic	135
	AlN ceramic	110
	Fused Silica	84

Part V

SIS Multilayer Structures

As seen in Part I, for the past four decades, bulk niobium has been the material of choice for SRF cavities applications. RF cavity performance is now approaching the theoretical limit for bulk niobium. For further improvement of RF cavity performance for future accelerator projects, Superconductor-Insulator-Superconductor (SIS) multilayer structures (as recently proposed by Alex Gurevich) [5] present the theoretical prospect to reach RF performance beyond bulk Nb, using thinly layered higher-T_c superconductors with enhanced H_{c1}. This section presents the development of NbTiN and AlN based multilayer SIS structures. First, the choice of materials for this study will be explained and an introduction of the experimental setup is given. The results on the characteristics of NbTiN and insulator films deposited via reactive magnetron sputtering (dc-MS) are then presented. Preliminary results on NbTiN deposition with High Power Impulse Magnetron Sputtering (HiPIMS) and the first RF measurements on NbTiN-based multilayer structures are then discussed.

Chapter V.1

Experiment

V.1.1 CANDIDATE MATERIALS

V.1.1.1 Superconductor: NbTiN

Although A15 compounds such as Nb_3Sn have a higher T_c, the Nb B1-compounds are less sensitive to radiation damage and crystalline disorder.

B1-compounds have a NaCl structure (figure V.1.1) where metallic atoms A form a face-centered cubic (fcc) lattice and non-metallic atoms B occupy all the octahedral interstices. These compounds are characterized by the fact that they always have a certain amount of vacancies, usually distributed randomly throughout the lattice [117]. The superconducting properties of B1-compounds are very sensitive to deviation from stoichiometric composition. Among these compounds, NbN and NbTiN have the highest critical temperature.

The binary NbN has a cubic NaCl-type phase (δ-phase) with a bulk critical temperature up to 17.3 K [292, 293]. However, at temperatures below 1300 °C, the δ-phase exists over a narrow range of nitrogen concentrations. Outside this range, the tetragonal γ-Nb_4N_3 and hexagonal, non-superconducting ρ-NbN phases may also form [118, 119], resulting in films with lower critical temperatures [294, 295, 296]. The Nb-N phase diagram is reproduced in figure V.1.2 from [297].

T_c is very sensitive to the nitrogen (N) stoichiometry and NbN suffers from a high resistivity due to the presence of both metallic and gaseous vacancies randomly distributed in both sub-lattices, in amount of 1.3% respectively. The equi-atomic composition is $Nb_{0.987}N_{0.987}$ [28]].

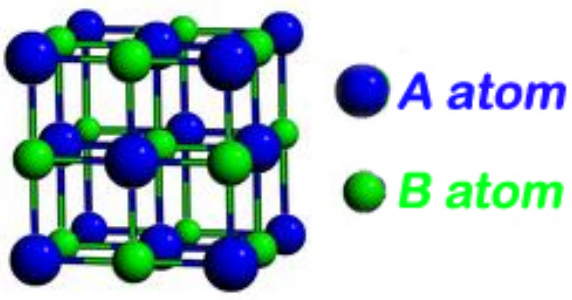

Figure V.1.1: NaCl-type structure NbTiN is based on

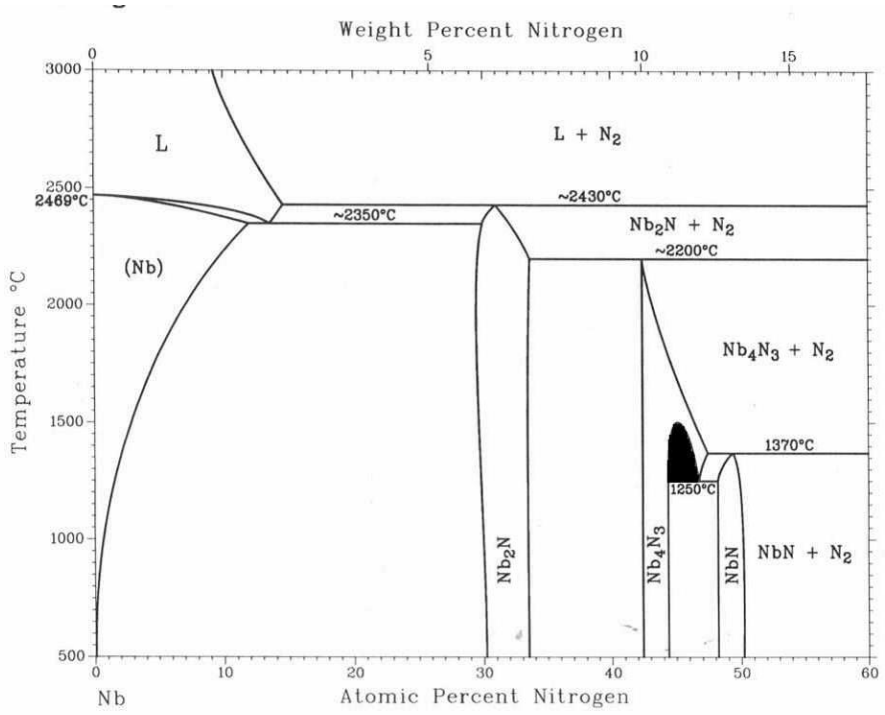

Figure V.1.2: NbN phase diagram

The Nb-N binary phase diagram, reproduced from [297]. According to Zhitomirsky et al., the δ-phase is formed in the black shaded region [296]. However, this seems topologically impossible in a binary phase diagram [298]. A more likely interpretation is that δ-NbN is formed in the region between approximately 48 and 50 atomic percent of nitrogen. While this is a narrow range of compositions, δ-NbN is not evidently unstable at low temperature.

The ternary NbTiN is about as widely used as NbN for technical applications with a T_c for the δ-phase up to 18.3 K. However, the exact nature of its crystal structure is not well described in literature. The most explicit statement about the crystal structure of NbTiN seems to be that it has a cubic, NaCl type, crystal structure, in which Nb and Ti form a substitutional solution with random occupation of the metal sub-lattice sites, while N atoms occupy the non-metal sub-lattice [299, 300, 301, 301]. The NaCl structure is maintained over a range of stoichiometries $Nb_{1-x}Ti_xN$ [127, 302, 303].

Although NbTiN is about as widely used as NbN for technical applications, the phase diagram of the Nb-Ti-N system is almost entirely unmapped. Several sources give isothermal or isobaric sections of the phase diagram, as in figure V.1.3, but only at temperatures above 1200 °C [295, 301, 125] for reactive diffusion of N in Nb-ti alloys. Phase equilibrium data is not available at lower temperatures, likely because of the material's refractory nature.

Recent works tend to focus on the fabrication process optimization relative to the resulting critical temperature without any crystallographic analysis or attempt to establish whether the resultant phases are in equilibrium.

By contrast to NbN, the cubic δ-phase of TiN is quite stable, existing over a wide range of temperatures and nitrogen concentrations but with a low critical temperature, about 5 K and lattice parameter of 4.24 Å [125]. The Ti-N phase diagram is shown in Figure V.1.4 It seems that adding titanium to the Nb-N system beneficially stabilizes the NaCl crystal structure at lower temperatures while retaining a high superconducting critical temperature [295, 125]. Ti is a good nitrogen getter, so the higher the Ti composition, the lower the number of vacancies.

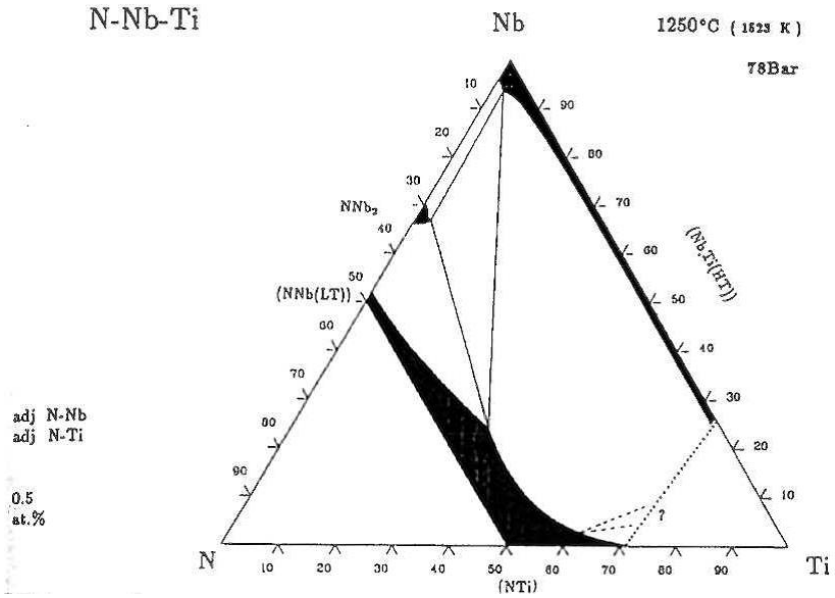

Figure V.1.3: Phase diagram for NbTiN at 1300 °C and 78 bars from [125].

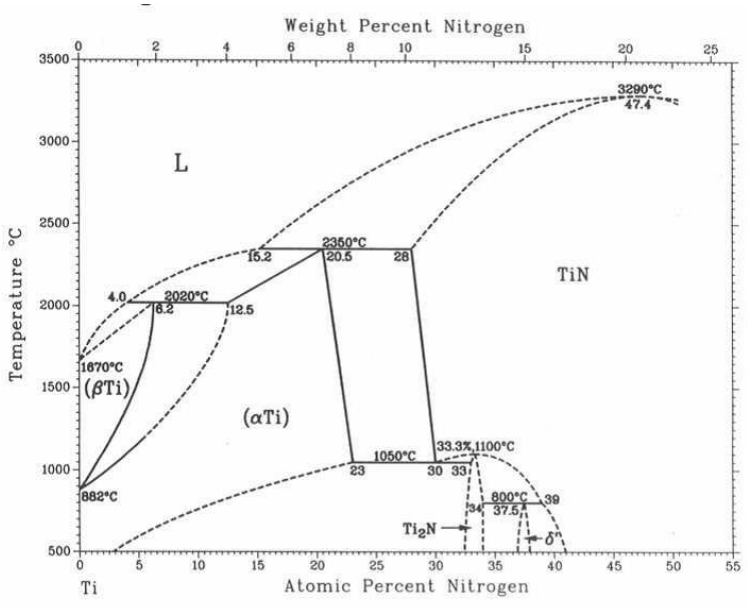

Figure V.1.4: Ti-N phase diagram

Thus, NbTiN presents all the advantages of NbN and exhibits increased metallic electrical conduction properties with higher titanium (Ti) percentage. T_c is slightly higher for NbTiN but as for NbN, N stoichiometry is critical to obtaining the right superconducting phase.

V.1.1.2 Insulator: AlN

Aluminum nitride (AlN) is a dielectric material that can be grown with a wurtzite (hexagonal close-packed, a=3.11 Å, c=4.98 Å) or metastable sphalerite (B1 cubic, a= 4.08 Å) structure (Figure V.1.5). AlN is extensively used for its dielectric and piezoelectric properties for multilayer terra-hertz (THz) mixers and surface acoustic wave sensors. It has some excellent properties such as chemical stability, high thermal conductivity, electrical isolation, a wide band gap (see table V.1.1). Its thermal conductivity (3.19W/cm^2 at 300 K) is comparable to

Cu (4.01W/cm^2).

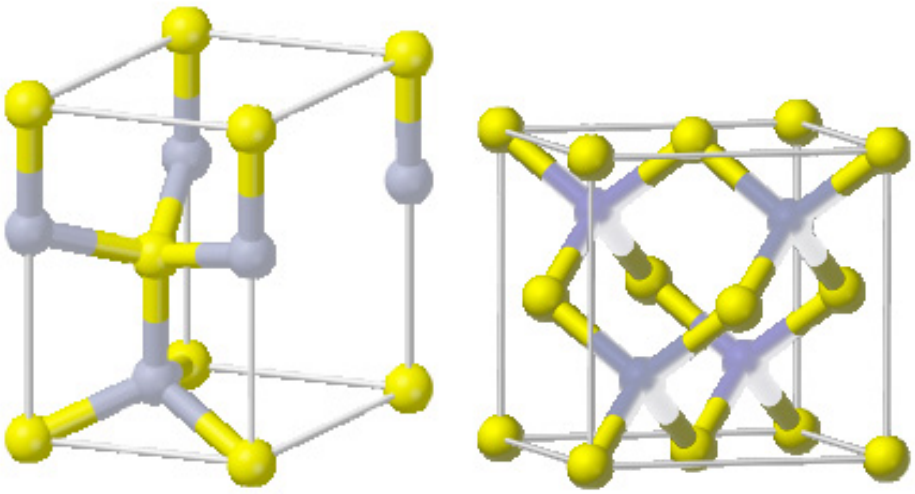

(a) (b)

Figure V.1.5: Wurtzite (a) and sphalerite (b) structures.

Besides its good dielectric properties, the interest AlN presents in this study is that it has been found, in literature, to enhance the properties (T_c) of NbN and NbTiN, in particular for very thin films [304].

Table V.1.1: Properties of AlN

Band gap	6.2 eV
Density	3.3 g/cm^3
Theoretical thermal conductivity	320 W/mK
Thermal expansion coefficient	4.6e^{-6}/ °C
Relative dielectric constant ϵ_r	8.5
Critical field strength E_c	6-15 MV/cm
Refractive index n	2.15
Thermal conductivity	2.0 W/cmK
Melting point	>2000 °C
Lattice constant a	3.112 Å
Lattice constant c	4.982 Å

V.1.2 EXPERIMENTAL METHOD

V.1.2.1 Deposition system

This study uses an ultra-high vacuum (UHV) multi-technique deposition system dedicated to multilayer depositions [305]. The vacuum deposition system consists of a chamber (roughly 470l) in two sections, the top and bottom chambers sealed with a 26-inch Wheeler flange with a Viton gasket. The top chamber lifts up with a mechanical hoist.

The pumping system consists in a cc Iwata scroll pump as a roughing pump combined to a CTI Cryo-Torr 10 cryopump (3000 l/s for air) separated from the main chamber with a 14" VAT UHV throttle valve. Once the chamber is roughed down to approximately 30 mTorr with the scroll pump, the main gate valve is opened to the cryopump. A UV-B lamp system is used to desorb contaminants from the chamber walls, mainly water. The chamber pressure drops to 10^{-7} Torr in a few minutes and reaches the 10^{-9}Torr range after about 4 hours of pumping. An ion gauge monitors the chamber pressure during this stage. The base pressure of the system with the sample holders at temperature is in the low 10^{-9}-high 10^{-10} Torr range.

A residual gas analyzer (RGA) in an appendix chamber monitors the residual species in the chamber and is used for helium leak checking through a 6" VAT UHV gate valve. During deposition, the RGA operates in differential pumping mode (with a Varian 81 M turbo molecular pump (TMP) coupled with an IDP3 scroll pump) and monitors the sputtering gases used for the process and residual gases through a by-pass conductance. A process gauge monitors the sputtering gases pressure during the deposition. The partial pressure of N_2 versus Ar is regulated via actuation of variable leak valves, monitoring the ratio of the N_2 and Ar signals on the RGA. This method allows regulation of partial nitrogen pressure to within roughly 5 %.

The UHV deposition system is equipped with 3 water cooled AJA UHV 320 magnetron guns which can sustain 700 W of DC power or 500 W of RF power. The magnet array is separated from the water cooling.

The magnetrons are powered by 10 kW ENI DC-10 or a 5 kW ENI DC pulse plasma generators for reactive dc-MS. To operate the magnetrons in HiPIMS mode, a 20 kW Huettinger TruePlasma Highpulse 4006 (2 kV, 3 kA)is used. The supply consists of a DC power and pulsing units combined with matching and cable length compensation (CLC) units for load and arc management.

Two sample holders, made of OFHC Cu and 316LN stainless steel, are available on the main chamber to allow the simultaneous deposition of witness samples to probe the quality and properties of the individual layers and allow the variation of deposition parameters during the same deposition run. Both sample stages can be heated up to 800 °C with an embedded coiled heater (from ARI Industries, resistance 35Ω) and are equipped with rotatable shutters to allow the deposition in the same run of multiple sets of samples with different parameters, ensuring directly comparable environmental conditions.

Figure V.1.6: The UHV deposition system (top) , setup inside the chamber(bottom left) and sample holder (bottom right)

V.1.2.2 Substrates

Substrate choice

Two types of substrates are chosen for the deposition of SIS related films. Insulating substrates such as MgO (100) and $(11\bar{2}0)$ Al_2O_3 are used because of their minimum roughness and their structural similarity with MgO and AlN. MgO, like NbTiN and AlN, has a NaCl structure and is adequate as an "ideal case" substrate to optimize the deposited films properties. AlN ceramic is chosen to study the influence of a rough and disordered surface as a worst case scenario in terms of superconductor-insulator interface.

The metallic substrates are chosen to be representative of the surface of SRF cavities. They are bulk Nb and thick Nb films deposited on Cu via ECR (see part IV).

Substrate preparation

As for the ECR deposition process (see chapter IV.1), the insulating substrates are cleaned according to UHV practices.

The bulk Nb substrates are mechanically polished with a similar procedure as for the Cu substrates used for the ECR Nb deposition. They are then electropolished in an HF - H_2SO_4 electrolyte. The electropolishing process is much slower for Nb than for Cu. It takes about 4 hours to remove a couple of microns.

The ECR Nb/Cu films used for this study have been previously RF measured in the SIC TE_{011} cavity. The protocol for this measurement calls for the use of a cryogenic Apiezon grease and a stainless steel ring fixture to insure good thermal contact of the sample during the measurement. This leaves residues all over the back of the sample that need to be mechanically wiped from the sample. The sample is then cleaned with methanol in an ultrasonic secondary bath. The stainless steel fixture leaves a ring imprint at the periphery of the sample. However it is outside the field sensitive region for RF measurement and is covered during deposition. It bears no consequence on the performance of the final SIS structure.

Chapter V.2

NbTiN and AlN Films

Before the Gurevich' SIS concept can be implemented successfully, it is necessary to understand how the thin film microstructure and surface morphology affect the superconducting performance of the films use to shield the underlying Nb surface from flux penetration. As seen in chapter I.4,

V.2.1 NbTiN films

V.2.1.1 NbTiN deposited with DC magnetron sputtering

As a first approach, NbTiN samples have been deposited as standalone layers on "ideal" substrates, such as MgO (100) to promote epitaxial growth. Substrates with hexagonal structures such as Al_2O_3 $(11\bar{2}0)$ and wurtzite (w-)AlN/ Al_2O_3 $(11\bar{2}0)$ are also used as, ultimately, NbTiN films will be grown on AlN to build SIS structures, in the context of this work. The substrates were annealed for 24 hours at 600 °C before deposition to desorb impurities from the surface. The base pressure of the system before deposition and with the samples at temperature is in the range of $8x10^{-9}$Torr (10^{-6}Pa).

Deposition parameters

As a first step, NbTiN films were grown with NbTi composite targets of different Nb/Ti weight ratios: 55%/45%, 70%/30% and 80%/20%. The produced NbTiN films started exhibiting the γ-phase and the δ-phase with a $Nb_{80wt.\%}/Ti_{20wt.\%}$ target with 99.995% purity. The total sputtering pressure was fixed at 2 mTorr (0.27 Pa) and the ratio of N_2/Ar was varied from 5% to 25% to optimize the stoichiometry and T_C.

Table 1: Coating parameters for NbTiN films

	NbTiN
N_2/Ar	0.23
Total Pressure [Torr]	$2x10^{-3}$
Target power density [W/cm^2]	15
Target size [mm]	50
Substrate-target distance [mm]	70
Deposition rate [nm/min]	18

Influence of the substrate nature

The substrate dependence of the crystallographic structures of NbTiN films was investigated by XRD analysis. The films deposited on crystalline substrate exhibit relatively good structure. figure V.2.1 shows the θ-2θ scans for, from top to bottom, NbTiN films coated simultaneously on w-AlN (0001)/$Al_2O_3(11\bar{2}0)$, MgO (100) and $Al_2O_3(11\bar{2}0)$ substrates. The NbTiN film grown on MgO shows clear (200) and (400) peaks, indicating epitaxial growth on the MgO (100) substrate, with a lattice parameter of 4.36 Å.

The film grown on sapphire exhibits epitaxial growth with NbTiN (111) and (222) reflections. For the film grown on an epitaxial AlN layer on sapphire, the θ-2θ scan reveals the expected w-AlN (0001) reflection along with NbTiN (222) and (400).

Table V.2.1 reports the critical temperature and transition width for the films represented in figure V.2.1 and a similar series with a thickness of 175 nm. For this series, as the best transition temperatures are achieved for MgO (100) which has a NaCl structure similar to the film.

Table V.2.1: Transition temperatures and width for 175 and 90 nm thick NbTiN films on different substrates.

	175 nm		90 nm	
	T_c[K]	ΔT_c[K]	T_c[K]	ΔT_c[K]
AlN(0001)/Al_2O_3 $(11\bar{2}0)$	14.69	0.23	14.19	0.09
AlN ceramic	13.97	0.87	12.91	0.26
MgO (100)	16.14	0.48	16.1	0.65
Al_2O_3 $(11\bar{2}0)$	15.33	0.45	15.43	0.45

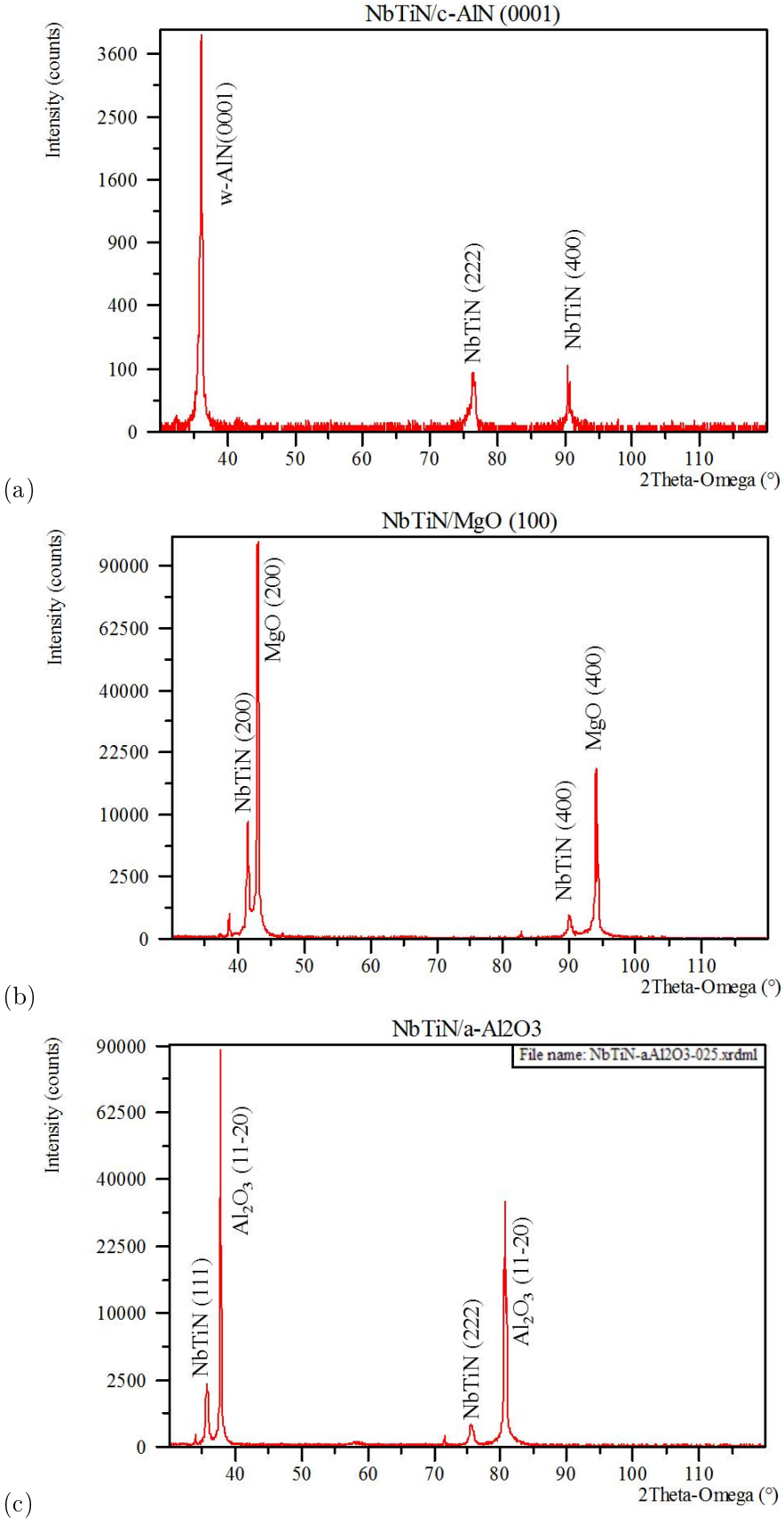

Figure V.2.1: XRD Bragg-Brentano (θ-2θ) spectra for 90 nm thick NbTiN coated simultaneously on (a) w-AlN (0001)/$Al_2O_3(11\bar{2}0)$, (b) MgO (100) and (c) $Al_2O_3(11\bar{2}0)$.

Transition temperature versus thickness

In the SIS structure concept, the superconducting films need to have a thickness smaller than the material's penetration depth, 300 nm in the case of NbTiN. It is then important to investigate how the thickness affects the properties of the film. Good quality films with a structure corresponding to the δ-phase are produced with various thicknesses as reported in figure V.2.2 and table V.2.2 for films deposited on MgO (100). The scatter of the results is due to the variation of film stoichiometry thus quality of the films according to their location on the sample holder during deposition. Bulk-like T_c values are obtained for NbTiN films with a thickness superior to 1 micron.

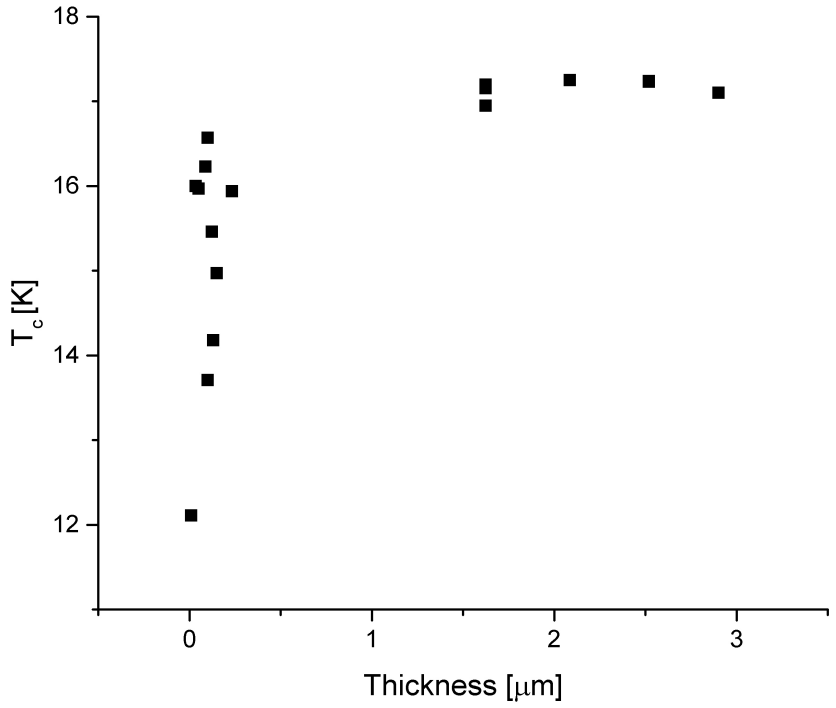

Figure V.2.2: Transition temperatures as a function of thickness for NbTiN films grown on MgO (100).

Table V.2.2 gives the transition temperature and width along with the lattice parameter and RRR for a selection of films grown on MgO (100) at various thicknesses. The RRR values are all above 1 which suggests that a lack of detectable voids and defects between grains and that the electron transport is not dominated by a granular structure in the films .

Table V.2.2: Transition temperatures as a function of thickness for NbTiN films grown on MgO (100)

Thickness [nm]	T_c[K]	ΔT_c[K]	a_0 [Å]	RRR
10	12.11	0.91	4.3487	1
50	15.97	0.16	4.3644	1.14
100	16.57	0.21	4.3657	1.26
1625	17.2	0.06	4.3618	1.13
2500	17.26	0.03	4.3547	1.2

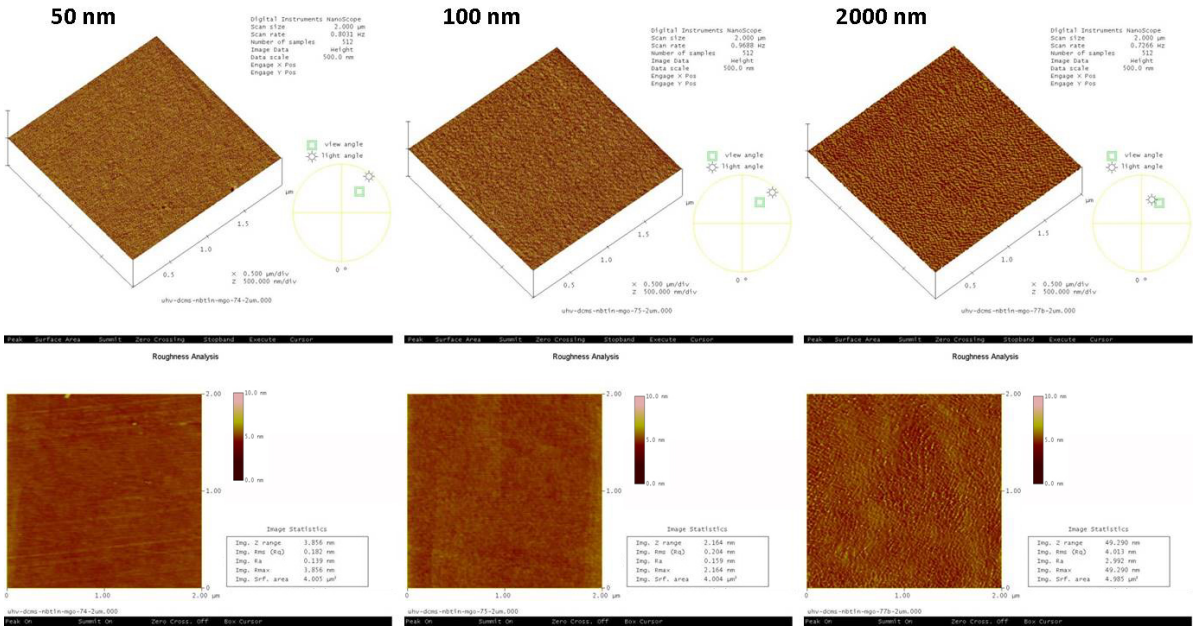

Figure V.2.3: AFM scans for NbTiN films deposited various thicknesses, 50 nm, 100 nm, 2 μm

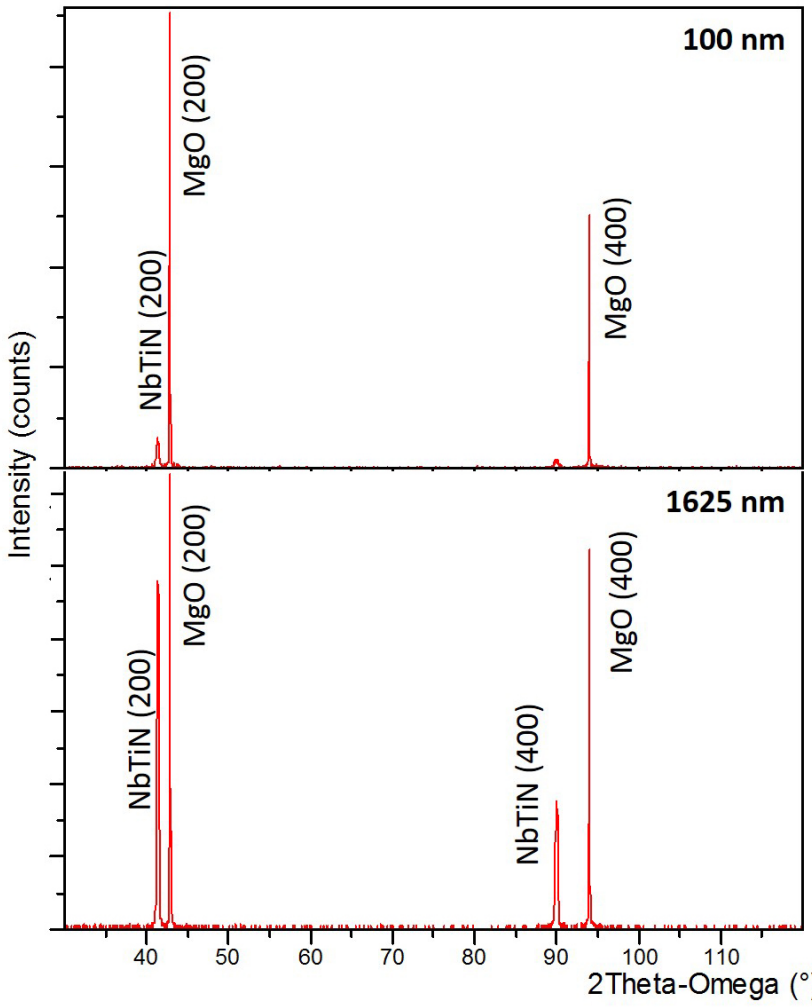

Figure V.2.4: XRD Bragg-Brentano (θ-2θ) spectra for NbTiN coated on MgO (100) with a thickness of (top) 100 nm and (bottom) 1.625 μm.

H_{c1} measurements

H_{c1} measurements by SQUID magnetometry as described in chapter III.1 were performed on a series of films deposited in-situ with different thicknesses. These H_{c1} values are reported in figure V.2.5. Due to the current configuration of the system, these samples displayed inhomogeneous properties as their stoichiometry varied according to their position on the sample holder. Only a couple of samples with a T_c corresponding to the δ-phase demonstrated a modest field enhancement. Figure V.2.6 shows the moment and trapped field as a function of applied field for these two films.

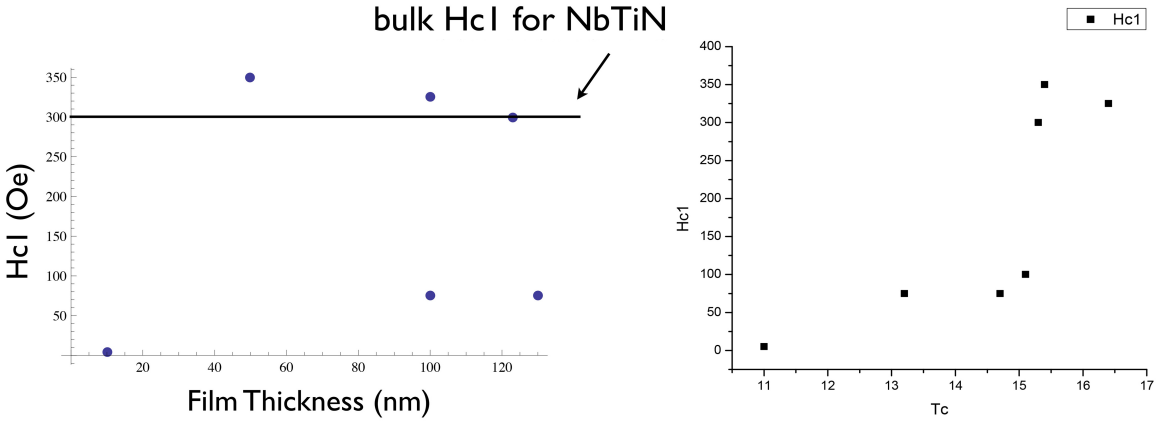

Figure V.2.5: H_{c1} measured by SQUID magnetometry as a function of thickness (left) and T_c (right)

In order to produce well defined thickness series of sample for H_{c1} measurement, the configuration of the system has to be modified so each magnetron can be positioned at the optimum location , but this will be addressed later.

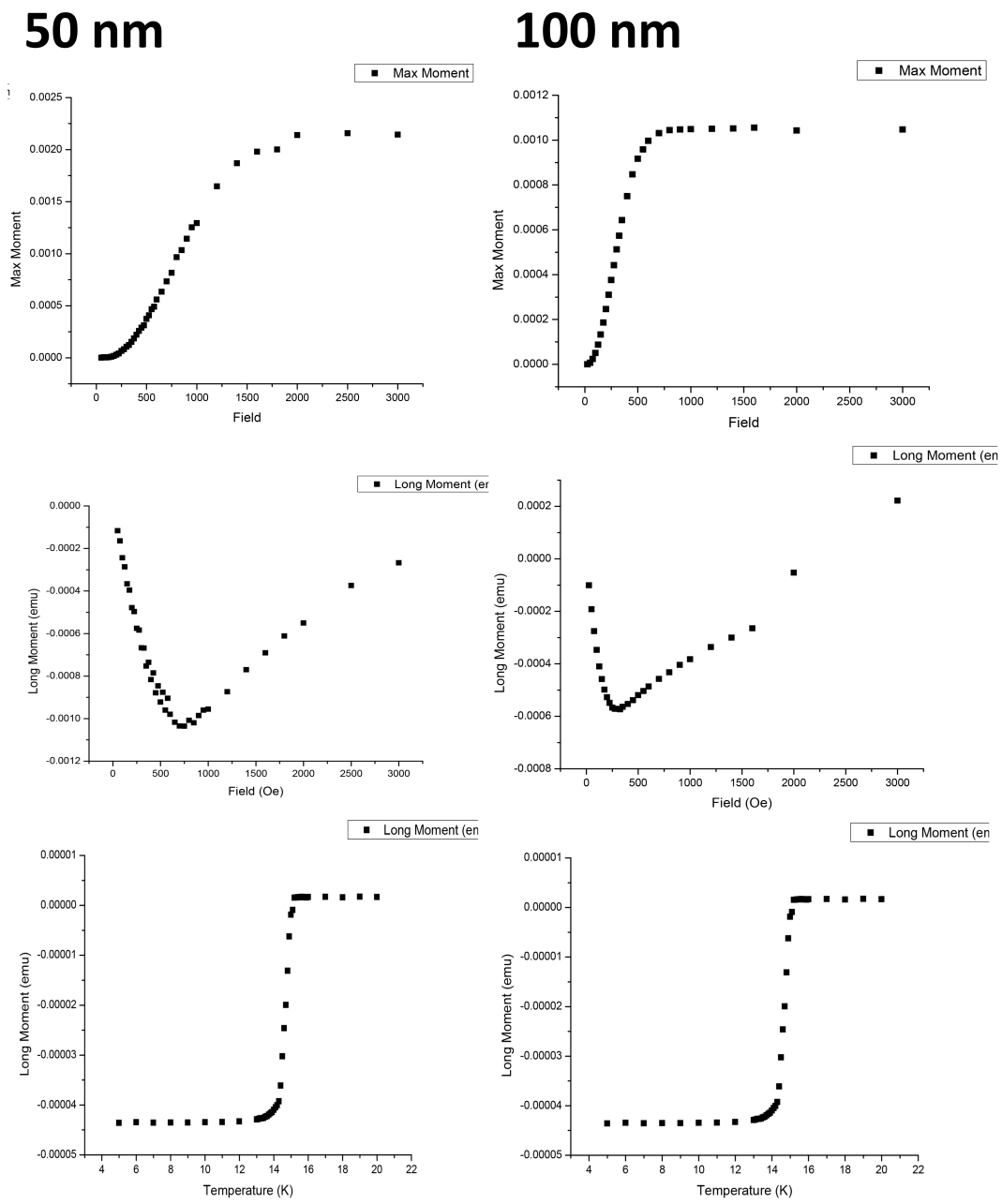

Figure V.2.6: SQUID measurements for two NbTiN/MgO samples of respective thickness of 50 nm (left) and 100 nm (right).

Surface resistance measurements for a thick NbTiN

A 2μm NbTiN thick film was coated on a 50 mm MgO (100) substrate. The film has a bulk-like T_c of 17 K. Both XRD and EBSD show that it is a NbTiN (100) single crystal. As it has been predicted and observed in the past [130], the surface resistance of thick NbTiN is much higher than for Nb as shown in figure . This is due to its higher normal resistivity.

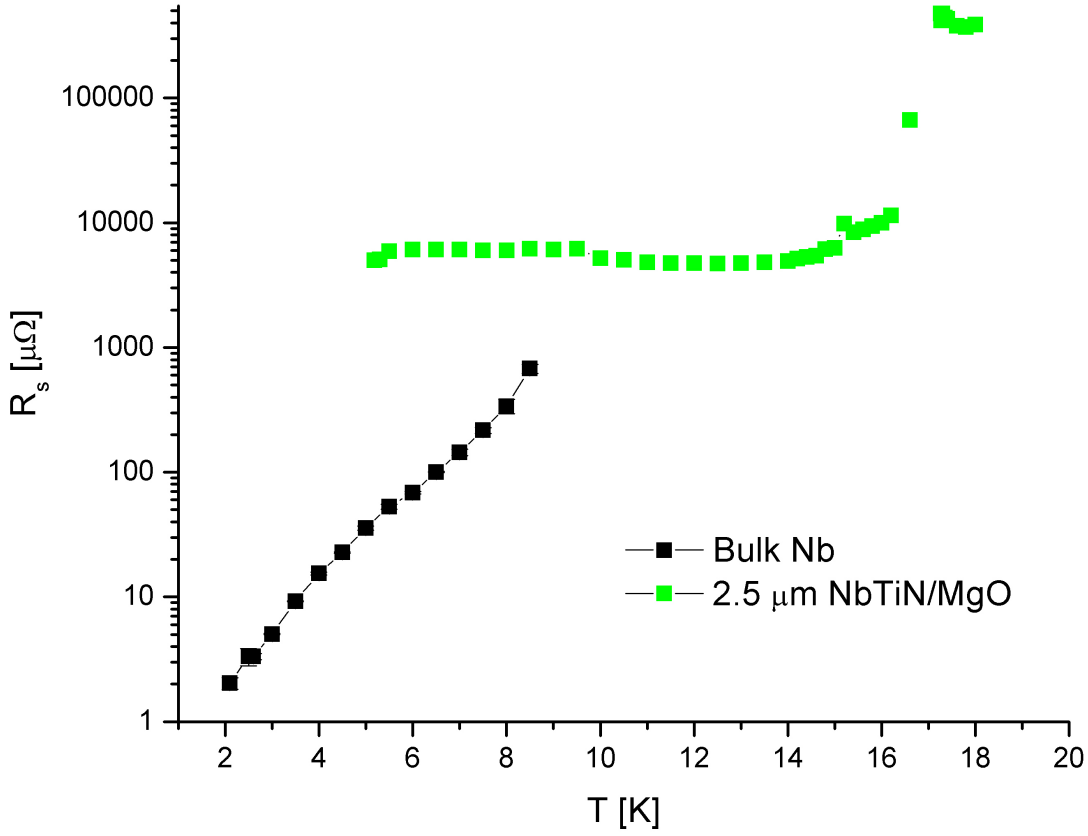

Figure V.2.7: Surface resistance versus temperature for a 2.5 micron thick NbTiN film

Secondary Electron Yield of NbTiN

As seen in chapter I.2, multipacting can be present in certain cavity geometries. To verify that NbTiN deposited on an SRF cavity would not present added risk for multipacting, secondary electron yield (SEY) measurements were carried out at CERN on a NbTiN layer and are represented on figure V.2.8. Measurements were done at room temperature on 3 locations on the sample as received (labeled NbTiN). The maximum SEY was 2.2±0.1 which is comparable to electropolished bulk Nb. A similar set of measurements (labeled NbTiN sputtered) was repeated after sputtering away about 2 to 3 nm of material (until the carbon peak vanished on the XPS spectrometer). The SEY decreased then down to 1.15. In the case of an SRF cavity in operation bellow 4.2 K, water and other species would be adsorbed on the surface and contribute to the SEY. On the other hand, the application of RF power would contribute to the desorption of such adsorbed species. Thus the multipacting situation will be somewhere in between these two points for a cavity coated with a NbTiN SIS structure.

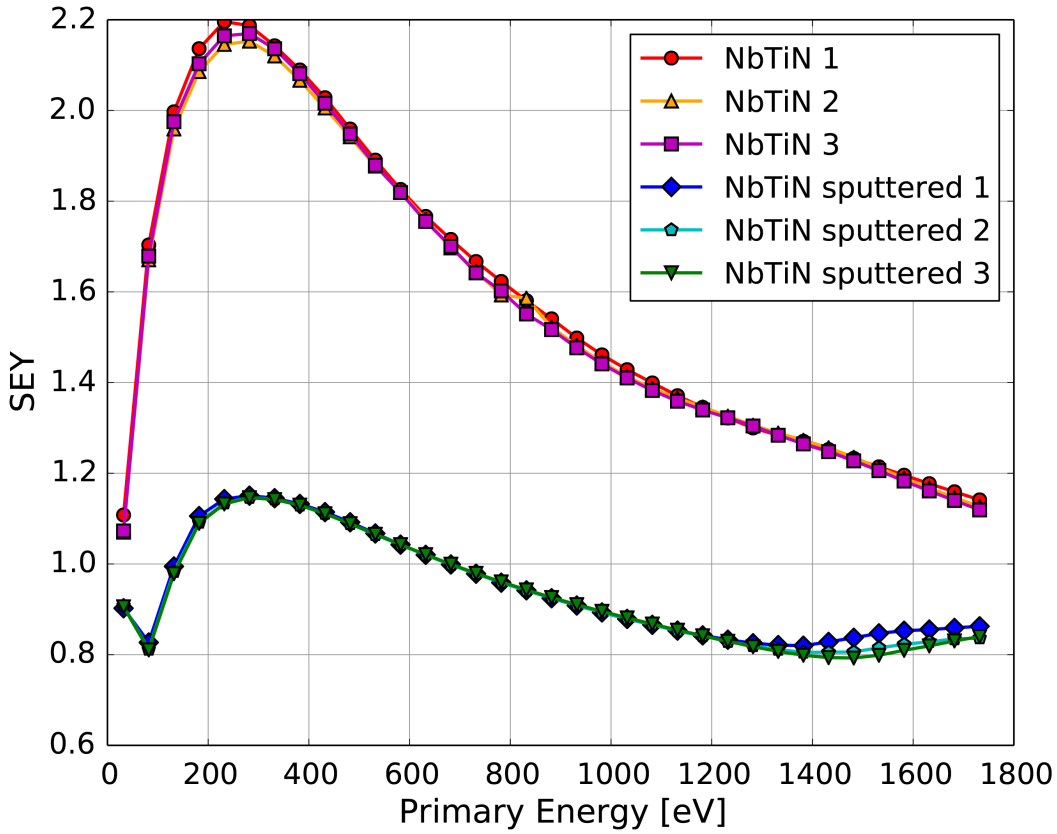

Figure V.2.8: SEY measurements performed on a NbTiN film

V.2.1.2 Preliminary studies of NbTiN deposited with HiPIMS

As mentioned earlier, energetic condensation, as for Nb films, could benefit the NbTiN layers. As it has been demonstrated by A. Ehiasarian and [307], as for elemental films, HiPIMS can produce denser and enhanced NbN films. We then propose implement energetic condensation for NbTiN films with this technique.

Discharge parameters

Preliminary tests were also conducted to deposit NbTiN with HiPIMS. With the 50 mm AJA magnetrons available in the system, the average power is limited to below 700 W DC and 500 W RF. These magnetrons also have an intrinsic operating pressure that is higher than 1.5 mTorr (0.2 Pa). Therefore for these tests, the total pressure of sputtering gas was maintained between 1.6 mTorr (0.21 Pa) and 2 mTorr (0.26 Pa). These tests were conducted with and without the HiPIMS supply matching unit connected. Without the matching unit, the discharge is very unstable with a large number of arcs and the total sputtering gas pressure has to be increased above 5 mTorr (0.66 Pa). No bias voltage was applied to the substrates. Table V.2.3 gives the coating parameters for the films deposited with HiPIMS.

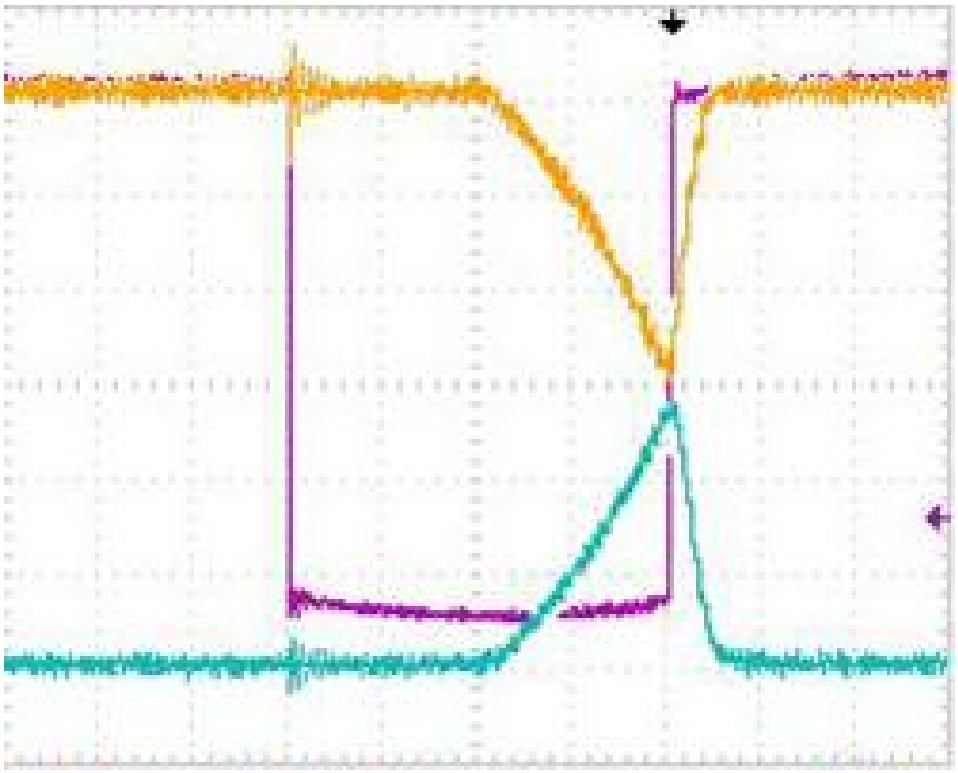

Figure V.2.9: Oscilloscope trace for a HiPIMS pulse in reactive mode (580V, 140A peak current, 100 μs, 200Hz

Table V.2.3: Thickness as a function of HiPIMS deposition parameters (with the matching unit)

Thickness [nm]	Average Power [W]	Peak current [A]	Pulse width [μm]	Repetition rate [Hz]	Coating time [min]
30	100	115	100	100	120
250	400	140	100	200	120
230	400	100	150	200	30
118	400	150	100	200	30
252	400	150	100	200	60
218	400	150	100	200	120

HiPIMS NbTiN film analysis

Θ-2θ scans of the first films produced by HiPIMS reveal that only the films produced with an average power of 400 W and repetition rate of 200 Hz have the δ-phase (Figure V.2.10. The measured T_c is 16.6 K for a 250 nm thick film.

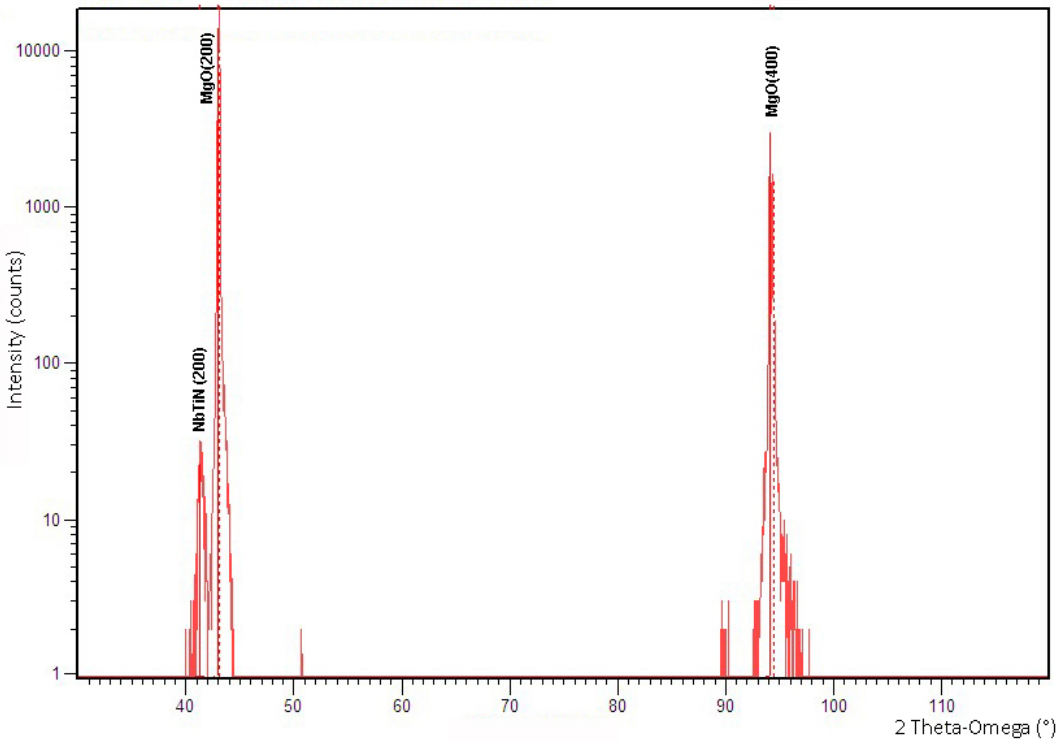

Figure V.2.10: Θ-2θ scan for HiPIMS NbTiN film coated at 450°C

V.2.2 AlN films deposited with DC-MS

So far, AlN deposition was only investigated with dc-MS.

V.2.2.1 Deposition parameters

Reactive sputtering of an elemental Al (99.999%) target was carried out with different N_2/Ar ratios and power values. The MgO (100) substrates were heated to 600 °C for 24 hours. They were maintained at the same temperature during coating and for 4 hours after, for annealing. The AlN layers became fully transparent for N_2/Ar ratios of about 33%. The corresponding deposition conditions are reported in table V.2.4.

Table V.2.4: Coating parameters for AlN

	AlN
N_2/Ar	0.33
Total Pressure [Torr]	$2x10^{-3}$
Target power density [W/cm^2]	5
Substrate-target ratio [cm]	
Deposition rate [nm/min]	15

V.2.2.2 Structural Measurements

The films were examined by θ-2θ x-ray diffraction with Cu $K\alpha$ radiation. Figure V.2.11 (top) shows a θ-2θ scan of an AlN film of about 10 nm in thickness. The scan shows the expected MgO

(200) and (400). The only reflections observed for AlN are at 38.54 ° and 82.70 °, corresponding to B1-AlN (111) and (222) respectively. The lattice parameter a_0 is 4.04 Å. However if the coating temperature is lowered to 450 °C, only hexagonal peaks are encountered for AlN in the grazing angle XRD measurement as presented in figure V.2.11 (bottom). The AlN films are reported [308] to typically nucleate in the cubic phase on substrates such as MgO but with subsequent growth the structure switches to hcp at low temperature. The energy needed to stabilize the cubic phase could be provided with biased HiPIMS deposition.

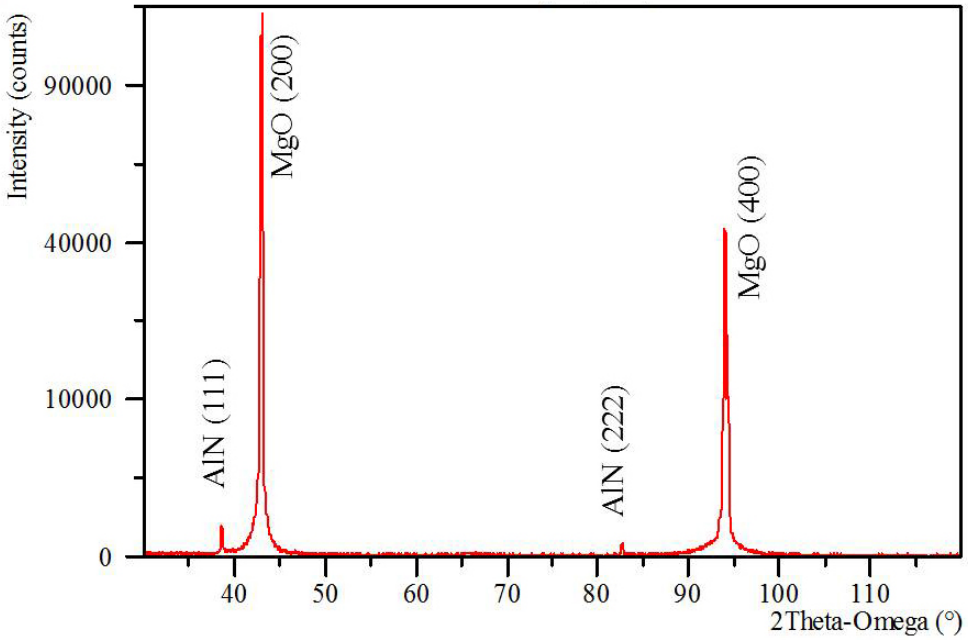

(a) XRD-AlN-MgO-600C

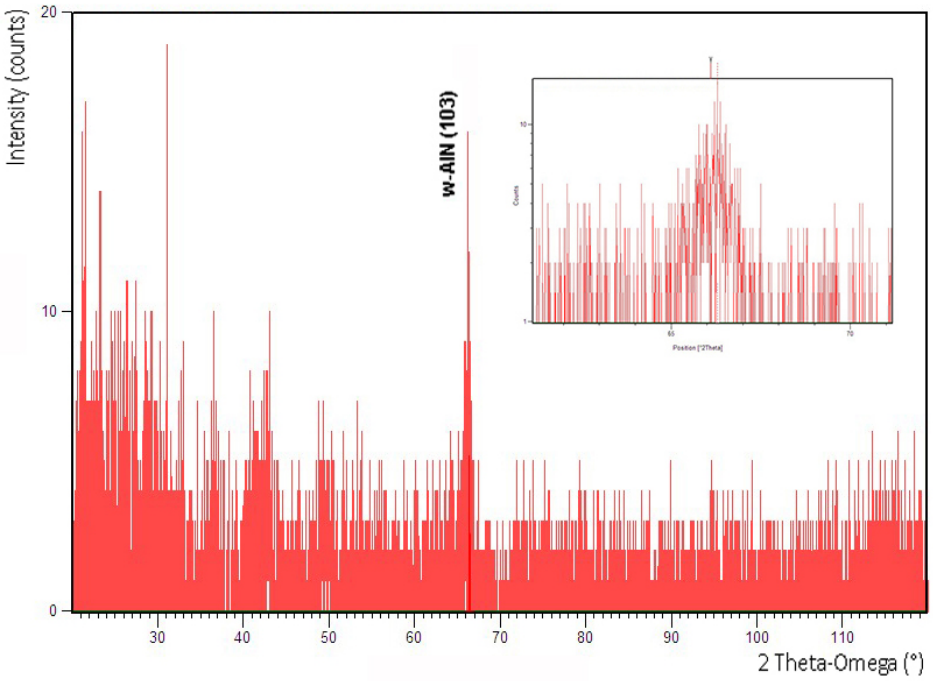

(b) XRD-AlN-MgO-450C

Figure V.2.11: XRD Bragg-Brentano spectrum for AlN coated on MgO (100) at 600 °C (top) and 450 °C (bottom, grazing angle)

V.2.2.3 Ellipsometry measurement

A couple of AlN films deposited at 450 °C on MgO (100) were measured by ellipsometry. The fitting of the data uses a Cauchy layer model with Urbach absorption to model the optical constants of the AlN, along with bulk MgO optical constants, and a roughness layer with 50 % void fraction with ambient. The thickness and roughness of the AlN layers were taken from XRR measurements (respectively 30.409 nm and 28.817 nm in thickness and 0.618 nm and 0.449 nm in average roughness).

The refractive index measured for these films are in the reasonable range of 1.98 - 2.15, corresponding to those of polycrystalline AlN films previously reported [306].

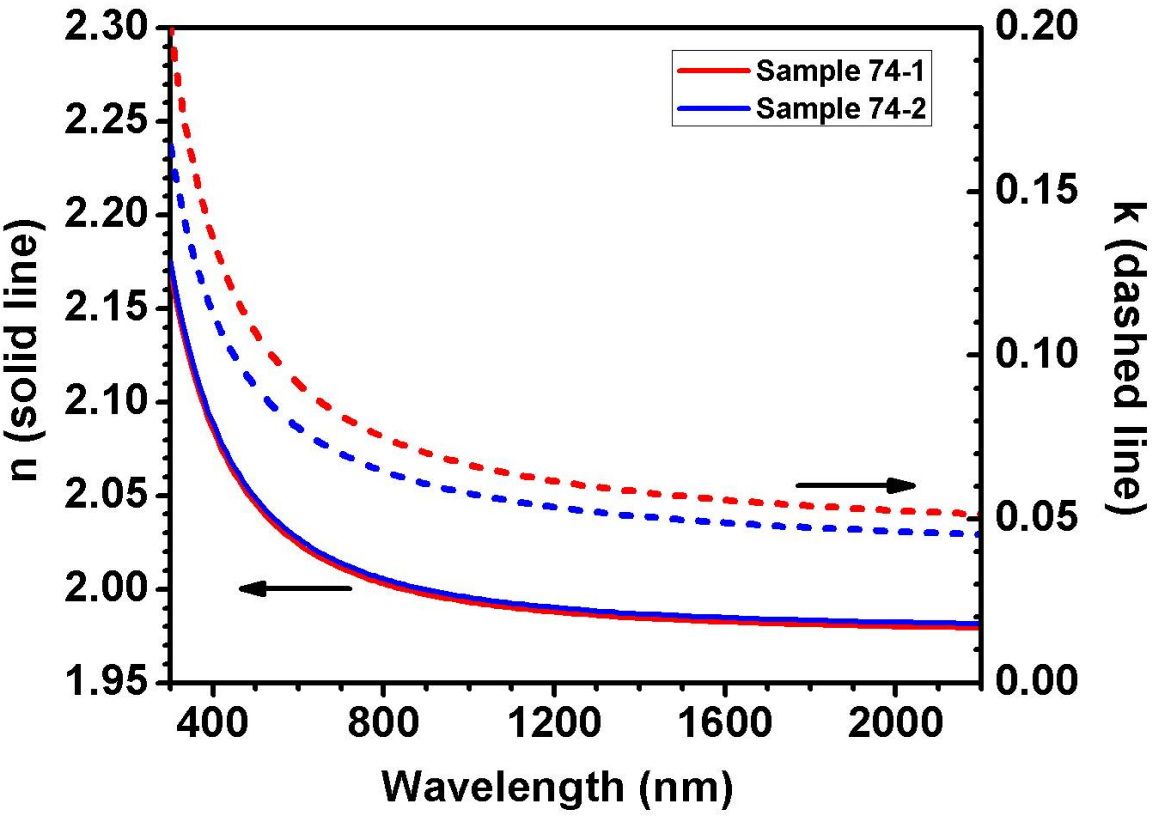

Figure V.2.12: Ellipsometry measurement of two AlN films deposited on MgO (100) at 450 °C

Chapter V.3

SIS Multilayers based on NbTiN

In order to study the properties of the films in a realistic SIS configuration and test their ability to shield an SRF surface , series of SI (superconductor-insulator) layers were deposited on surfaces representative of SRF cavities, i.e. bulk Nb and ECR Nb/Cu thick films. In order to easily determine the T_c of these structures, witness samples were also deposited on MgO and on AlN ceramics. The properties of the NbTiN films are found to be highly dependent on teir substrate. It is therefore important to consider the effect of a realistic interface between superconductor and insulator layers in SIS structures.

V.3.1 Characterization of NbTiN/AlN structures

NbTiN based SI structures were deposited with a 20 nm AlN layer on MgO (100) and AlN ceramic. The AlN ceramic substrates present a polycrystalline wurtzite structure. An example of the θ-2θ XRD scan for such structures on each of these substrates is given in figure V.3.1.

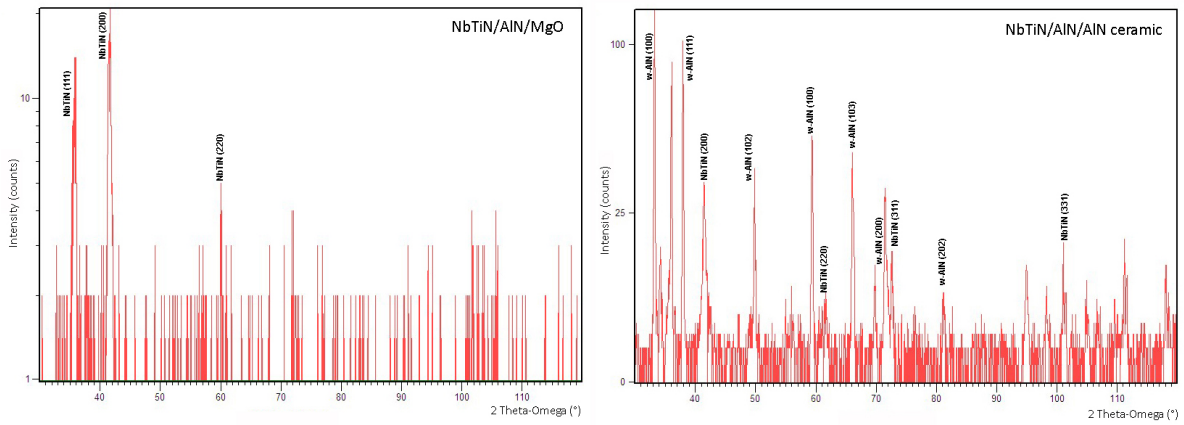

Figure V.3.1: θ-2θ XRD scans for NbTiN/AlN structures on MgO (left) and AlN ceramic (right)

Although the polycrystalline AlN substrate has a much higher roughness than MgO (100), average roughness 10 nm versus 0.1 nm (see figure V.3.2), it seems to present a better template for AlN growth. If one can deposit a high quality AlN interlayer, the average roughness to some extent does not seem to inhibit T_c, as seen in figure V.3.3. However, the influence of the surface roughness on H_{c1} in a parallel field configuration should be investigated as it could induce perpendicular contribution to H_{c1}.

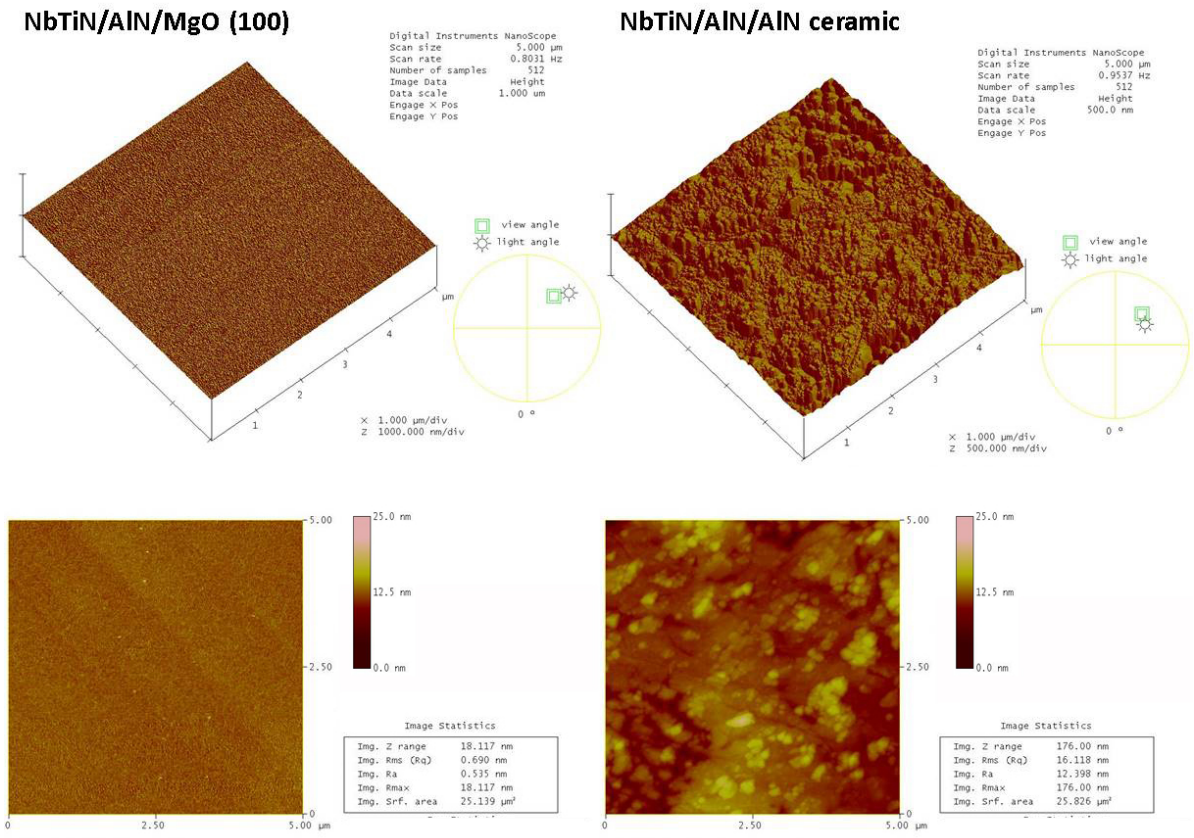

Figure V.3.2: AFM scans for the NbTiN/AlN structures deposited on MgO (100) and AlN ceramic

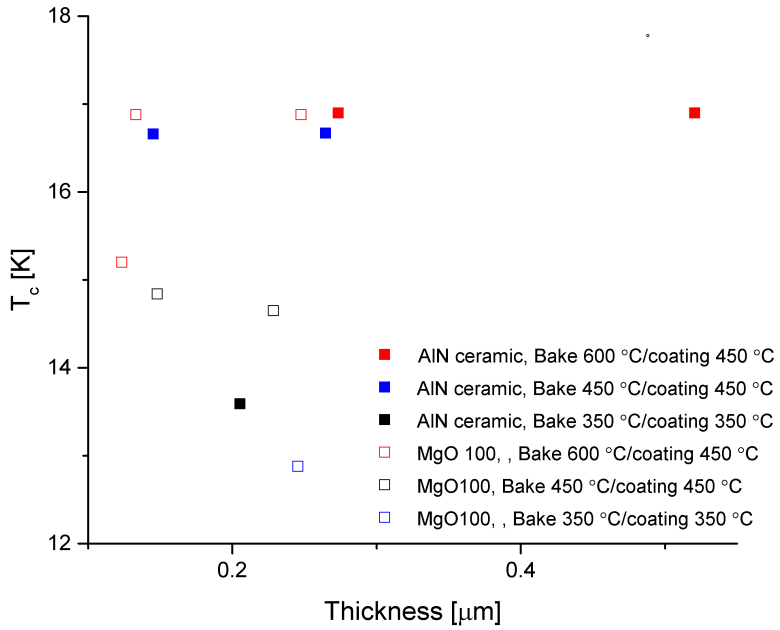

Figure V.3.3: Variation of T_c as a function of thickness for NbTiN/AlN structures on MgO (100) and AlN ceramic for different coating and baking temperatures.

V.3.2 Interface analysis

SIS structures based on NbTiN and AlN have been coated at 600 ° C, 450 °C and 350 °C on bulk Nb and ECR Nb films (Nb/a-Al_2O_3 and Nb/Cu) after a 24 hour bake-out at 600 or 450 °C. The samples were then annealed post-deposition at coating temperature for 4 hours.

Figure V.3.4 shows the TEM cross-section of a NbTiN/AlN/Nb structure coated at 600 ° C. One can observe a smearing of the AlN into Nb and NbTiN. There is some inter-diffusion of Al into Nb and NbTiN similar to what has been reported by Yoshimmori in [308]. The close-up on the right of Figure V.3.4a, shows the NbTiN film is polycrystalline but the AlN layer is amorphous.

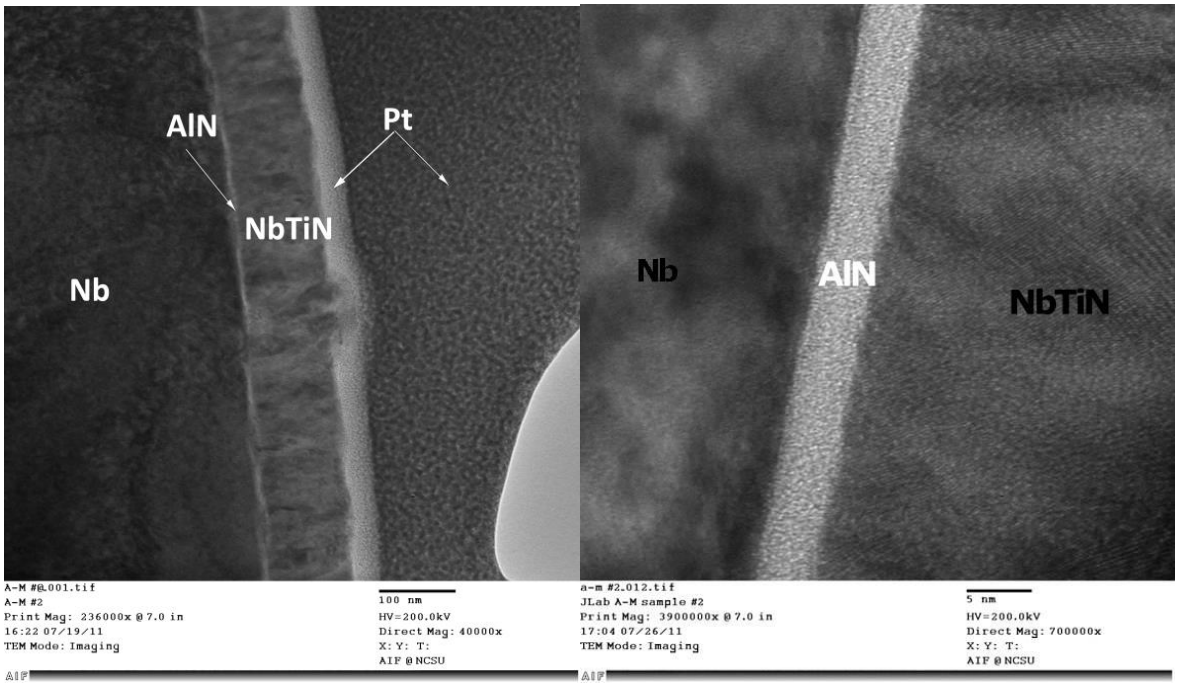

Figure V.3.4: TEM image of a FIB cut NbTiN/AlN/Nb/Cu structure.

Following this observation, the coating temperature was reduced to 450 ° C, allowing film growth without inter-diffusion of Al for the AlN film and with minimum effect on T_c for NbTiN. Figure V.3.5 shows the TEM cross-section which reveals polycrystalline NbTiN and AlN layers of a thickness of 250 nm and 15 nm respectively and with relatively sharp interfaces. The structure was examined by θ-2θ x-ray diffraction with Cu $K\alpha$ radiation. The scan shows reflections for Nb (100) and (200), AlN (111) and NbTiN (111). The lattice parameters $a_0$are respectively3.301 Å, 4.041 Å and 4.330 Å for Nb, AlN and NbTiN.

Closer observation of a similar structure, with 150 nm NbTiN and 15 nm AlN layers, in the STEM with associated EDS mapping, represented in figures V.3.6 and V.3.7, still reveals some inter-diffusion layer of about 2 nm on both sides of the AlN layer. The bulk Nb interface shows also so residual smearing from mechanical polishing.

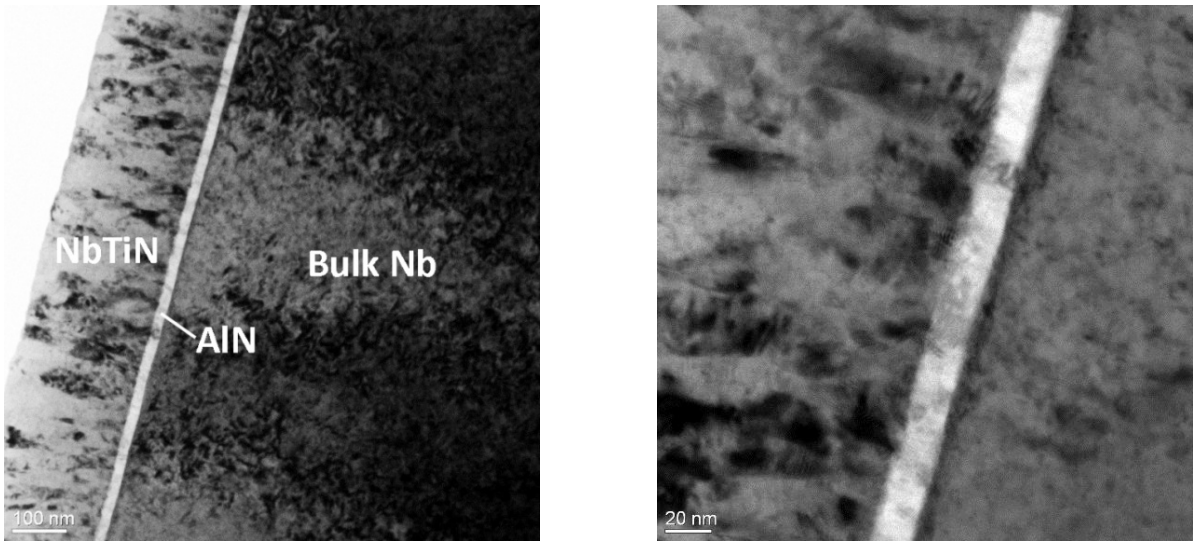

Figure V.3.5: TEM image of a FIB cut NbTiN/AlN/bulk Nb structure.

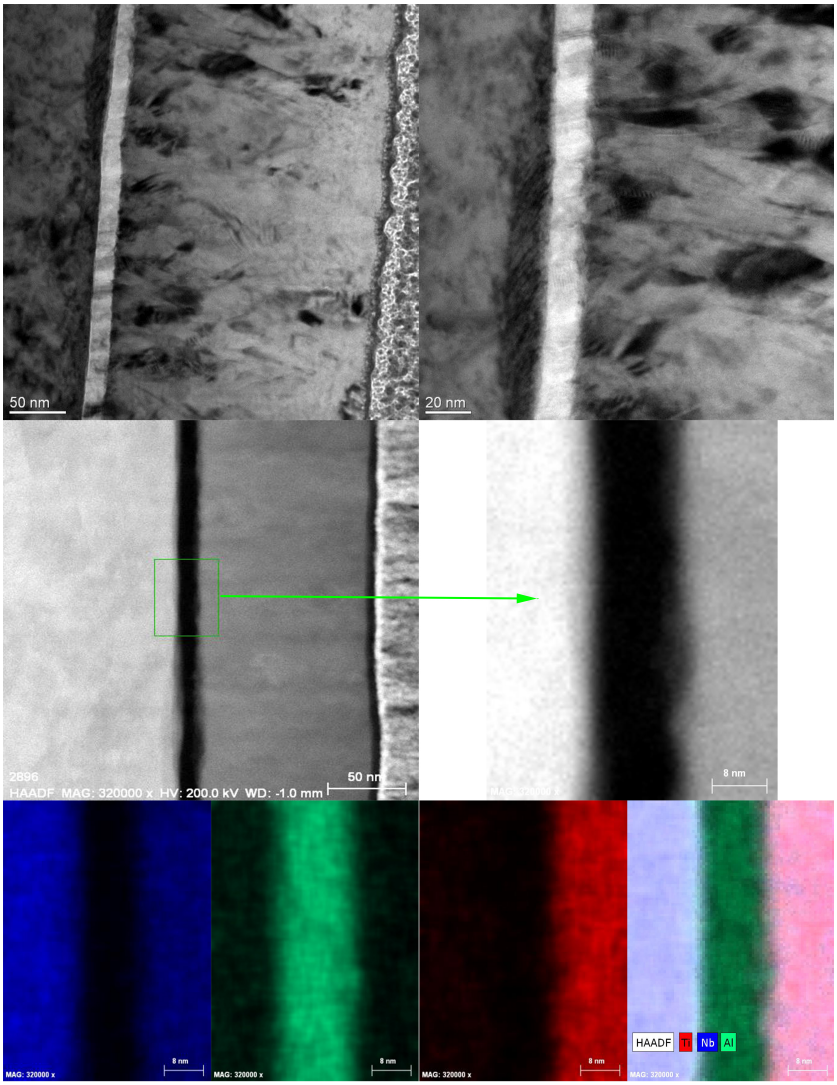

Figure V.3.6: STEM imaging for NbTiN/AlN/Nb with the HAADF and associated EDS maps for Nb, Al and Ti.

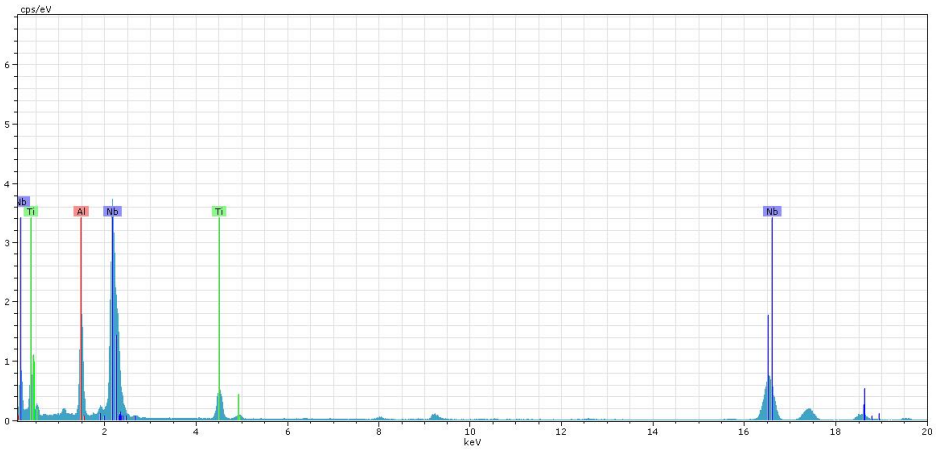

Figure V.3.7: EDS map corresponding to the HAADF from figure V.3.6

V.3.3 Evaluation of SIS RF performance

As the RF performance is the best measure to probe the quality of SRF surfaces for cavity applications, a few SIS layers were also prepared on 50 mm (2“) Nb surfaces, both bulk and thick ECR films.

V.3.3.1 NbTiN/AlN/ECR Nb thick films

The films used here as substrates were coated ex-situ in the ECR chamber on a Al_2O_3 $(11\bar{2}0)$ and large grain Cu substrates. Both films were RF measured after the ECR coating and presented a similar RF behavior (see figure V.3.8).

The first multilayer structure was deposited at 450 °C after heat-treatment at 600 °C on the ECR Nb/Al_2O_3 $(11\bar{2}0)$. The NbTiN and AlN layers are respectively 150 nm and 20 nm thick. The R_s measurement as a function of temperature is shown in figure V.3.8 along with the measurement performed on the standalone ECR Nb film before the SIS deposition as reference. It shows a suppressed T_c of about 8.5 K for the Nb film where it was previously measured at 9.3 K. This is due to oxygen diffusion into the thin film resulting from the oxide layer reduction during the 600 °C bake-out before deposition. The NbTiN layer shows a transition at about 14.7 K.

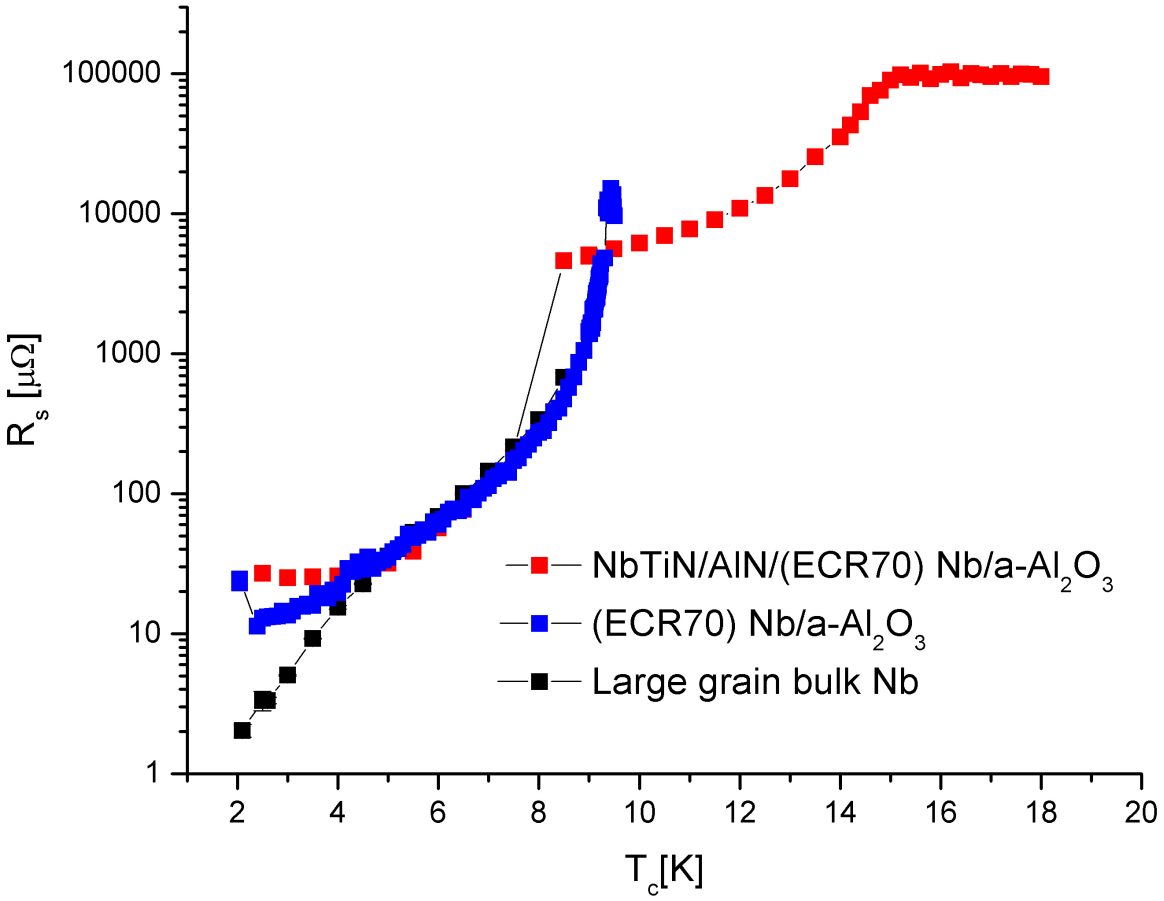

Figure V.3.8: Surface resistance as a function of temperature for a NbTiN/AlN structure coated at 450 °C on ECR Nb / (11$\bar{2}$0) Al_2O_3 film after a bake-out at 600 °C. The NbTiN layer is 150 nm thick with a T_c of 14.7 K. The previous $R_s$measurement on the stand alone ECR Nb / (11$\bar{2}$0) Al_2O_3 film and a large grain bulk Nb film are also plotted for reference.

The second multilayer structure was then deposited at 450 °C after heat-treatment at 450 °C on the ECR Nb/large grain Cu in order to limit the degradation of the thick Nb film due to oxide diffusion. The NbTiN and AlN layers are respectively 148 nm and 20 nm thick. As shown on figure V.3.9, the RF measurement reveals two transitions at about 9.2 K for bulk Nb as expected and at 16 K for the NbTiN layer. There was no T_c degradation of the film with the 450 °C heat-treatment prior deposition. The surface resistance for the SIS coated Nb film is higher than the resistance of the standalone film below 4.2 K. However, above 4.2 K, the BCS resistance is clearly lower for the SIS coated Nb/Cu film compared to the standalone film.

In a practical application to SRF cavities, to avoid the diffusion of oxygen into the Nb material during bake-out, one can also remove the Nb oxide layer by in-situ plasma etching. If dealing with thick Nb/Cu surfaces, a better solution would be to coat both the Nb film and SIS structure in-situ, provided that the deposition techniques for optimum RF performance for these two types of SRF films can be implemented in the same deposition system. This option will be explored in the near future with the implementation of HiPIMS for Nb films (refer to chapter VI.2).

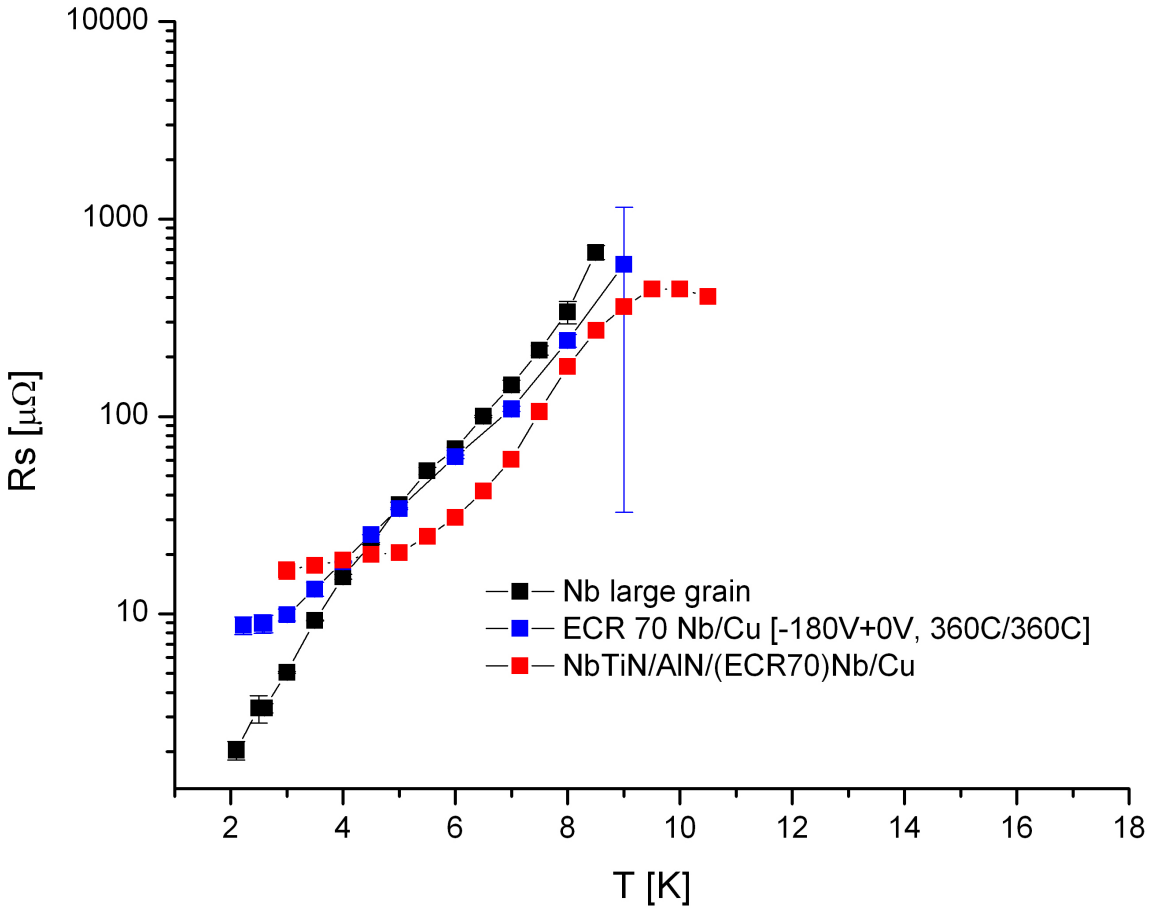

Figure V.3.9: Surface resistance as a function of temperature for a NbTiN/AlN structure coated at 450 ° C on a ECR Nb/Cu film after a bake-out at 450 ° C. The previous R_s measurement on the stand alone ECR Nb/Cu film and a large grain bulk Nb film are also plotted.The NbTiN layer is 148 nm with a T_c of 16 K.

V.3.3.2 NbTiN/AlN on bulk Nb substrate

A NbTiN/AlN structure was also coated on bulk Nb at 450 ° C after a heat treatment at 600 ° C. This structure corresponds to the TEM cross-section in figure V.3.10. The NbTiN and AlN layers are respectively 230 nm and 20 nm thick. In this case the high temperature heat treatment is not necessarily detrimental for bulk Nb as oxygen can diffuse far away from RF penetration depth. Cooling and RF setup issues during the measurement prevented the full measurement of the surface resistance. However the loaded quality factor was measured and is represented in Figure V.3.10. It reveals two transitions at about 9.2 K for bulk Nb as expected and at 16 K for the NbTiN layer. One can also see here a clear improvement in RF losses of the Nb surfaces coated with NbTiN/AlN structures compared to bulk Nb.

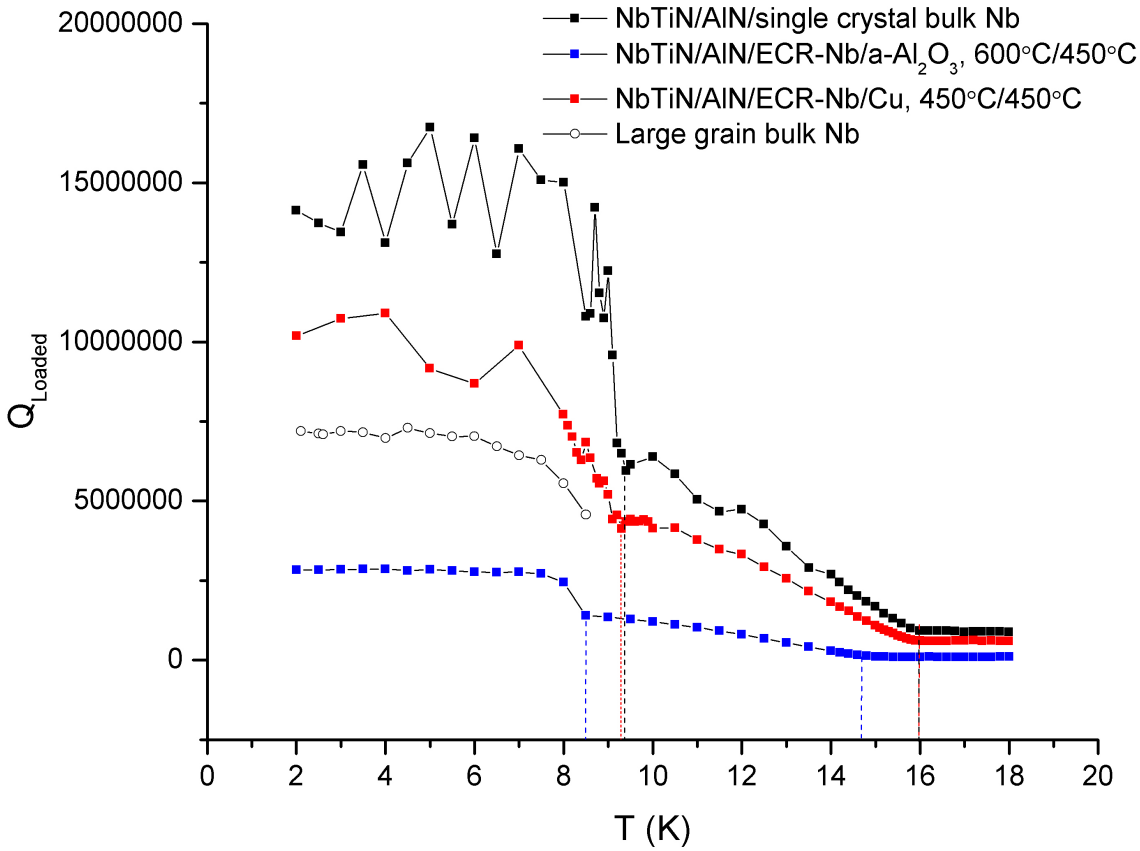

Figure V.3.10: Quality factor as a function of temperature for the NbTiN/AlN/Nb (bulk and films) structures measured in the SIC setup and compared to large grain bulk Nb.

V.3.3.3 Modification of the UHV system for effective multilayer deposition

In order to deposit in-situ multilayers with the current system configuration, the magnetrons position relative to the substrate is not optimum leading to the inhomogeneity across the sample holder in sample quality. To solve this issue, a rotating central stage has been designed and is currently being implemented. It will allow the deposition of each layer in optimal position for the magnetron relative to the substrate to avoid the variation in film quality observed so far.

Two sample holders are fixed on a rotating and differentially pumped 10" conflat flange system (Thermionics RN 800). This system also supports all the feed-throughs for the heaters, thermocouples, bias leads, and thickness monitors.

Each sample holders is constituted of 2 parts: the support and heater fixture and the sample holding plate. The sample holding plate is detachable from the support for ease of sample exchange while the support with all the wiring connections stays in place in the system. It is composed of a fixture plate and of bias seats, electrically insulated from the rest of the holder. There are two types of bias seats, one for bias studies in the development of NbTiN and AlN layers with HiPIMS, the other one for in-situ multiple thickness deposition at constant bias. Each sample holders is equipped with a Momentive 3" or 2" pyrolitic BN heater and a thermocouple electrically insulated. A thickness monitor is mounted at the top of the sample holder. Translational shutters are mounted in front of the holders for variable thickness

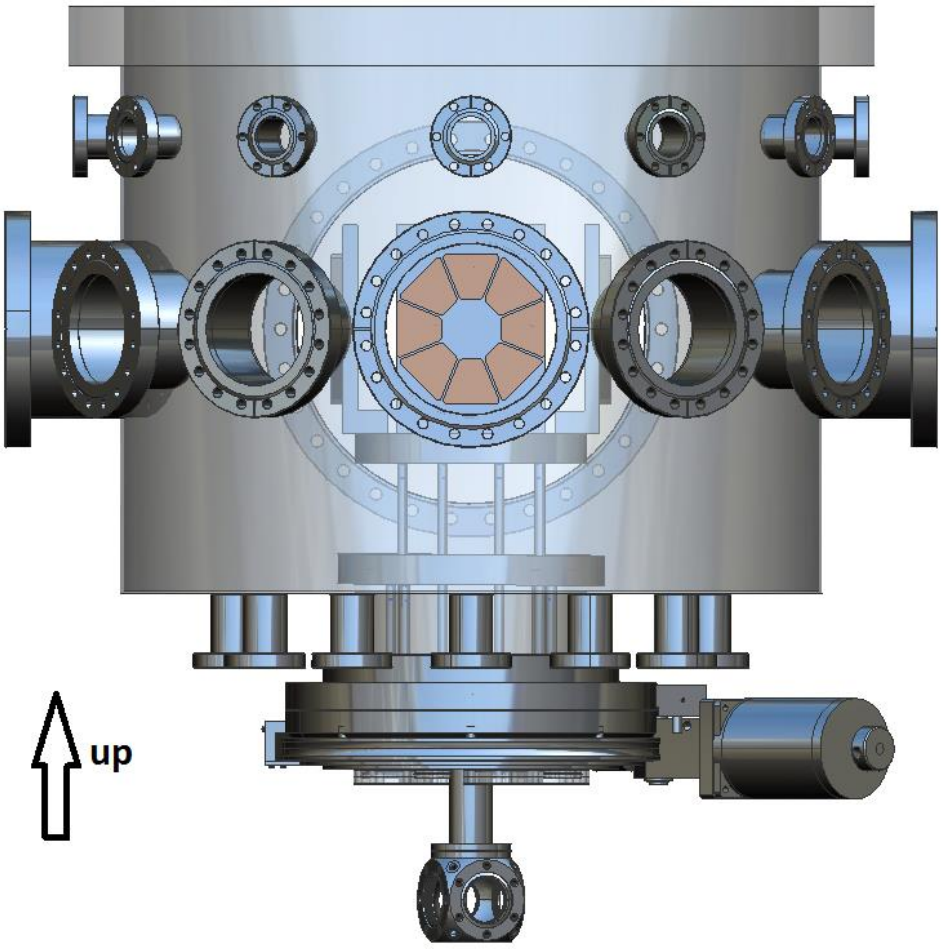

Figure V.3.11: Representation of a new UHV central stage

deposition within a run and to shield the substrates during target conditioning.

An additional 4.5" Eterna DC power 3 kW magnetron is also added to the system to fully exploit the HiPIMS power opportunities. To allow in-situ plasma cleaning or etching of the substrate prior coating, a 20 kW Mantis ion source, housed in a retractable bellow, will also be installed.

Chapter V.4

Summary

In this section, it has been demonstrated that good quality NbTiN and AlN films can be deposited by dc-MS Bulk, i.e. thicker than 1 micron, NbTiN films are readily produced with a T_c of 17.25 K, close to the bulk value. AlN dielectric films of various thicknesses are produced with good dielectric properties. Modest H_{c1} enhancement has been observed by SQUID magnetometry for some NbTiN films. Further studies of the H_{c1} enhancement of thin NbTiN layers are necessary both on MgO substrates and on thin AlN layer deposited on MgO and for both deposition techniques, dc-MS and HiPIMS. Relatively good quality SI NbTiN/AlN layers have been produced on samples with a T_c for the NbTiN layers between 16.6 and 16.9 K. It has been shown that, if the dielectric can be grown as an adequate template for the superconducting NbTiN film growth and the growth temperature is high enough to provide enough adatom mobility, the substrate macro-roughness is not necessarily detrimental to the T_c of the superconducting film. Further improvement of the interfaces is however needed. HiPIMS deposition may be useful in improving the structure of both NbTiN and AlN.

The RF characterization of NbTiN/AlN structures coated on Nb surfaces show indications that SIS coated Nb surfaces, both bulk and thick film, have a promise to delay flux penetration and lower RF losses for SRF cavities. Much is still needed to be to develop a practical application for SRF cavities. In particular, a systematic study of the effect of the NbTiN film thickness in the S-I-S structure over the RF performance enhancement is crucial.

To pursue the development of NbTiN/AlN structures where both types of layer are coated in optimum conditions, some modifications of the deposition system need to be implemented. At this effect, a central stage has been designed and built and will be installed in the very near future.

Part VI

Conclusions and Future Work

This section gives a summary of the work presented in this dissertation and describes briefly future work and directions for further development of thin film structures for SRF applications for both avenues, engineered bulk-like Nb films and SIS multilayers. Much work has yet to be done to produce high performing SRF cavities based on Nb films and SIS multilayer structures.

Chapter VI.1

Conclusions

The main purpose of the present work has been to develop experiments to engineer Nb films with bulk-like properties and to evaluate the potential of multilayer SIS thin film structures for SRF applications.

Both hetero-epitaxial and fiber growth modes of Nb have been studied under different conditions with the objective to contribute to the determination of optimum coating parameters for SRF surfaces based on thick Nb films. Much more work is still needed to fully optimize the film growth for ultimate RF performance, but some insight has been gained. The influence of the ion energy and temperature on the structure of the film has been studied exploring the different regions of the Modified Structure Zone Diagram proposed by Anders [15] both on "ideal" and practical surfaces, such as Cu, for SRF cavities. Both

Single-crystal-like Nb films have been produced by ECR plasma deposition on a variety of crystalline substrates, metallic and insulators. The orientations of the thin films depend strongly on the substrate crystal planes, as well as on the bias voltage i.e. the kinetic energy of the incident Nb^+ ions. The minimum substrate heating temperature (about 360 ^{0}C) to promote epitaxy via ECR coating is moderate, roughly $0.23\,T_{m,Nb}$. The growth of Nb films on polycrystalline and amorphous surfaces was also studied, revealing that, by tuning the ion energy and substrate temperature, the structure of the film itself can be tuned. It was also shown that the content of harmful impurities such as hydrogen is orders of magnitude lower for ECR Nb films than for state of the art bulk Nb surfaces. Good quality films can be produced at substrate temperatures practical for SRF applications.

The past arguments that Nb films have an inherent limitation due to their low RRR are here refuted. It was demonstrated that ECR Nb films RRR values can be tuned from single digits to bulk-like values. Unprecedented RRR values(table IV.3.1) have been measured on Nb films on a variety of substrates. The superconducting gap measurements demonstrated that the ECR films gap is very similar to bulk Nb.

The evaluation of the RF performance of ECR Nb films is ongoing. The RF performance of some of the Nb films deposited on Cu and Al_2O_3 $(11\bar{2}0)$ was measured. Although the interpretation of the RF results is hindered by the limitation of the system used, some trends emerge. It was also shown that grain boundaries in high quality Nb films are not necessarily detrimental to RF performance. Films deposited on re-crystallized polycrystalline Cu substrates have RRR values as high as a single crystal like Nb film deposited on "ideal" sapphire substrate and can have a similar RF behavior. RF measurements also show that treating the film growth in phases, nucleation/early growth and subsequent growth, can be beneficial to lower the surface resistance of the Nb film.

The development of SIS multilayer film structures following the Gurevich's concept has been studied with NbTiN and AlN as respectively the highest Tc superconductor and insulator. It has been demonstrated that good quality standalone NbTiN and AlN films can be deposited by dc-MS. Bulk, i.e. thicker than 1 micron, NbTiN films are readily produced with a T_c of 17.25 K, close to the bulk value. AlN dielectric films of various thicknesses are produced with good dielectric properties. The first depositions of NbTiN films with energetic condensation via HiPIMS have been performed with reasonable results. Modest H_{c1} enhancement has been observed by SQUID magnetometry for some NbTiN films. Further studies of the H_{c1} enhancement of thin NbTiN layers are necessary both on MgO substrates and on thin AlN layer deposited on MgO and for both deposition techniques, dc-MS and HiPIMS. Relatively good quality SIS NbTiN/AlN layers have been produced on samples with a T_c for the NbTiN layers between 16.6 and 16.9 K. It has been shown that, if the dielectric can be grown as an adequate template for the superconducting NbTiN film growth and the growth temperature is high enough to provide enough adatom mobility, the substrate macro-roughness is not necessarily detrimental to the T_c of the superconducting film. Further improvement of the interfaces is however needed. HiPIMS deposition may be useful in improving the structure and properties of both NbTiN and AlN at the small thicknesses required for the Gurevich's concept.

The RF characterization of NbTiN/AlN structures coated on Nb surfaces show some indications that SIS coated Nb surfaces, both bulk and thick film, have a promise to delay flux penetration and lower RF losses for SRF cavities. Much work is however still needed to develop a practical application for SRF cavities. To pursue the development of NbTiN/AlN structures where both types of layer are coated in optimum conditions, some modifications of the deposition system need to be implemented. At this effect, a central stage has been designed, built and installed.

Chapter VI.2

Future Work

VI.2.1 Interface engineering for optimum Nb film deposition on Cu and Al

As seen in this work, the interface of a film with its substrate is at the origin of the quality of the final deposited film and in many circumstances drives the growth. Further tailoring of the Nb film and substrate interface would be beneficial to achieve a full control of the subsequent film growth.

To allow a better control of the cleanliness of the interface between the film and the substrate, a common technique is to apply an in-situ Ar plasma or glow discharge to the samples prior deposition. Preliminary tests were performed with the multi-bias samples at various bias voltages in an Ar atmosphere at 5.10^{-5} Torr (limited by the configuration of the system) with the main gate valve throttled to its half position. However, contamination due to the etching, along with the substrates, of the fixation hardware hindered the results. A thin contamination layer was found at the interface of the film and for some of the films, *percolated* to the film's top surface. EDS examination of the samples showed Fe, O contamination of the film and EBSD showed a break in epitaxy on single crystal substrates, which had never been observed before for ECR Nb films. Despite such a contamination of the interface, the Nb films RRR were surprisingly high, ranging from 96 up to 307 for films deposited on $(11\bar{2}0)$ Al_2O_3 and from 18 to 147 on polycrystalline Cu. In order to perform this study effectively, the system needs some modifications, such as adding a process gauge, modifying the sample holder so the fixation hardware is hidden from the plasma. The use of a higher Ar pressure for a proper glow discharge and less energetic ions should be explored. One can also use higher energy ($\sim 1000eV$) Ar or Nb ion to modify the substrate surface structure (amorphitization) and create a controlled inter-layer (ion stitching or inter-mixing).

Further exploration of the film growth with dual ion energy and pulsed bias voltage and the evaluation of other substrates, such as Al, suitable for SRF applications should be pursued. So far, the ion energy during growth was varied only between nucleation and subsequent growth. However, the energy could also be alternated all along the growth of the film by using a pulsed bias, thus juggling the creation and annihilation of defects during film growth. Another step in engineering SRF Nb films is to explore further the ion energy influence for coating the final SRF surface (top 40 nm). One can imagine to add a coating step at higher ion energy for the very top film thickness corresponding to the penetration depth.

Another material of interest as a Nb film cavity substrate is aluminum (Al). This castable material could allow to decouple the SRF surface from the supporting structures, opening doors

for SRF cavities and other component fabrication in fully integrated system. The potential of this substrate material should also be explored.

VI.2.2 Cavity deposition of high quality Nb films

VI.2.2.1 Beyond accelerator applications - ENS Fabry-Perrot mirrors

SRF cavities have applications beyond particle accelerators. Photons trapped in a n SRF cavity constitute an ideal system to realize some experiments in quantum physics. The interaction of these trapped photons with Rydberg atoms crossing the cavity illustrates fundamental aspects of measurement theory. The experiments performed with this *photon box* at Ecole Normale Supérieure (ENS) belong to the domain of quantum optics called *cavity quantum electrodynamics* (CQED). Experiments with circular Rydberg atoms and Fabry-Pérot resonators have led to fundamental tests of quantum theory and various demonstrations of quantum information procedures. The open geometry of the cavity is essential to allow a perturbation-free propagation of long-lived atomic coherences through the mode. A few years ago, sputtered Nb/Cu technology was applied to these Fabry-Perot resonators to improve the residence time and quality factor.

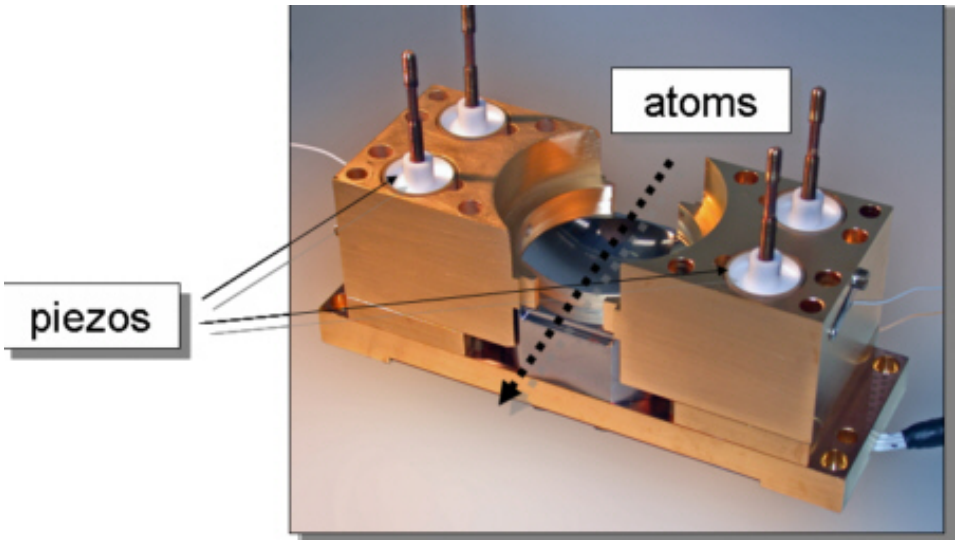

Figure VI.2.1: Photograph of the cavity assembly with the top mirror removed. The atomic beam path is visualized by the arrow. The four posts are used to mount the upper mirror. The piezoelectric actuators, centered by the white Teflon cylinders, surround the posts [309].

The copper mirrors are diamond-machined with a 10 nm residual roughness and an overall 300 nm surface accuracy over the whole 50 mm diameter. The surface is toroidal, with two different radii of curvature (39.4 and 40.6 mm) in two orthogonal planes. This geometry lifts by 1.2 MHz the degeneracy between the two TEM_{900} modes with orthogonal linear polarizations in order to ensure efficient coupling of the atoms to a single mode only.

After machining of a gross shape, the mirrrors are annealed to 400 °C in vacuum and cooled down to liquid nitrogen to remove stresses. The final surface is then machined and measured by optical interferometry. The thickness of the mirrors (30 mm) avoids surface deformation, the back of the mirrors is polished to a 1 μm accuracy and rests on a polished holder. Although it is convenient to use coupling holes (irises) pierced at the mirror apexes to couple microwave in and out of the mode , these irises strongly affect the mirror surface quality at the critical apex

point. Thus this cavity was designed without couping holes. Microwave is fed in the mode through the residual diffraction losses. A 12 um Nb layer is deposited on the carefully cleaned mirror surfaces by magnetron sputtering. The mirrors are then mounted in the evacuated cryogenic apparatus. Such Nb/Cu resonators allowed to increase the atom residence time and achieve cavity quality factor Q of 4.210^{10} with a finesse of 4.610^{9}, the highest ever achieved in any frequency domain for this geometry. In the framework of these experiments, there is continuous interest in increasing further the quality factor of these resonators.

Therefore some plane and torroidal mirrors have been coated via ECR and will be soon tested in the QED setup at the Laboratoire Kassler-Brossel, College de France, in the group of Serge Haroche and Michel Brune.

VI.2.2.2 Nb/Cu cavity deposition with ECR enhanced magnetron sputtering

A way to relatively easily apply ECR plasma deposition to SRF cylindrical cavities is to replace the e-beam gun by a cylindrical magnetron as Nb source. One can imagine using a cylindrical magnetron with a similar geometry as the CERN sputtering system for Nb/Cu cavities (Figure VI.2.2).

If a cylindrical cathode is used, a transverse magnetic field is applied along the axis of the cylinder. Typical cylindrical magnetron configurations are post magnetrons or hollow cathode. In the post magnetron case, the cylinder is the cathode and the outer cylinder is the anode (substrate), while in the hollow cathode case it is the reverse. In both cases, cathode wings (mirrors) are necessary to achieve plasma confinement. With such a system, low-pressure discharges with high deposition rate and good uniformity of axial distribution were demonstrated for metallic tube coatings by Yonesu et al.[311]. Other studies show an enhancement of the deposition rate by the applied microwave power in an ECR-MS with a cylindrical target [312, 313].

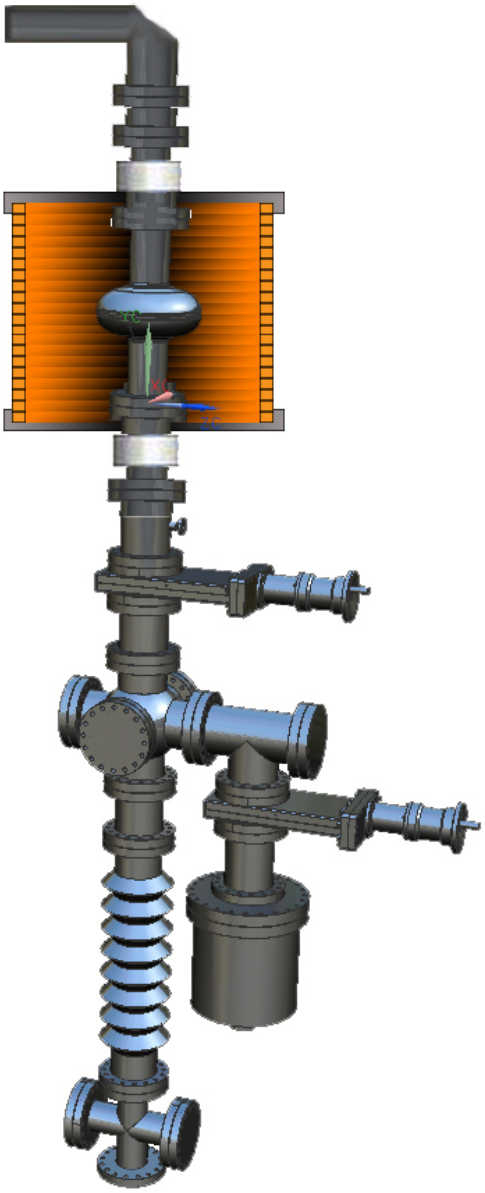

Figure VI.2.2: Envisioned ECR-MS setup for Nb thin films cavities

VI.2.3 Towards multilayer SIS structure deposition on SRF cavities

The development with HiPIMS for NbTiN and AlN based SIS structures is far from being complete. It will be pursued along with the studies of the H_{c1} enhancement for both dc-MS and HiPIMS thin NbTiN with the deposition of controlled thickness series for single and multilayers with the new central stage in the UHV system. In the context of exploring the

benefit of SIS structures also for Nb/Cu films, the HiPIMS parameter space needs to be mapped in the UHV system to reproduce the results achieved with the ECR plasma deposition.

Although planar samples can be tested in various RF testing setups available in different institutions (sapphire loaded TE_{011} at JLab and at Cornell University, Mushroom TE_{013} cavity at SLAC, Dielectric resonator at MIT, quadrupole resonators at CERN and FZB (Germany) , these measurements have their own inherent limitations often inhibiting the clear interpretation of the results. A clean measurement would, of course, be provided by SRF cavities coated with SIS structures as no issue with edge effects is present in this configuration.

At this effect, a multi-layer cavity deposition setup is being designed as an attachment of the UHV system to provide a proof of principle of the SIS concept on elliptical cavities while building on existing infrastructure. Coat SIS multilayer structures on bulk Nb and on Cu (includes in-situ coating of Nb layer) cavities. Figure VI.2.3 gives a representation of the envisioned setup.

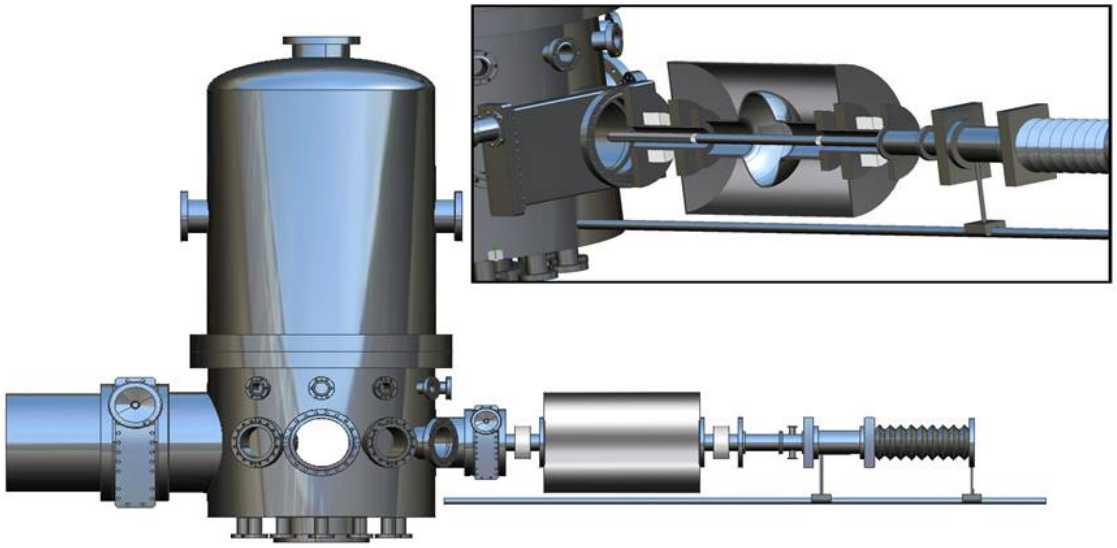

Figure VI.2.3: Concept for a single cell deposition setup as an attachment to the UHV deposition system. Inset shows a cross-section of the setup.

The cylindrical magnetron is movable in a sectioned cathode with Nb, NbTi and Al cathode sections, electrically isolated from each other. The cathode is housed in a welded bellow on tracks. Each section of the cathode can be introduced in the cavity with a stepper motor for sequential coating of Nb, NbTiN and AlN. The cavity is electrically insulated from the system to allow direct biasing. This method could equally be applied to bulk Nb and Nb/Cu cavities (in-situ coated thick Nb film).

VI.2.4 Multilayer SIS structures based on other materials

NbTiN is not necessarily the ultimate candidate material for SIS structures. Thus, exploring the deposition of other alternative materials with energetic condensation via HiPIMS is definitely of interest.

Recently, MgB_2 based SIS layers have demonstrated enhanced RF performance [24]. To this day, the best MgB_2 films have been produced by chemical or hybrid chemical-physical

deposition techniques at high coating temperatures. Energetic condensation could be applied to this compound using potentially a lower coating temperature.

One can also imagine to explore the use of long-range ordered superconductor in SIS structures with *Hybrid energetic condensation* of Nb_3Sn (lower coating temperature). Since Nb and Sn sputtering yields and melting temperatures are drastically different, energetic condensation could be used to create hyperthermal Nb ions and sputtered or evaporated Sn. This would lead to the potential of lowering the temperature needed to produce the adequate A15 phase. As seen in chapter I.4., the temperature needed to produce the LRO A15 phase for Nb_3Sn is above 900 °C, which limits the use of Nb_3Sn based SIS structures to bulk Nb cavities. Arguments exist that Nb_3Sn films could be beneficial to the SRF field only as thick films [314, 315, 316]. Both uses could be explored.

Bibliography

[1] Benvenuti, C. et al., IEEE: New York, NY, USA, 1991; pp 1023-5

[2] Benvenuti, C.; Circelli, N.; Hauer, M., Applied Physics Letters 1984, 45 (5), 583-4.

[3] S. Calatroni, Physica C 2006, 441(1-2), 95-101.

[4] C. Benvenuti et al., Physica C 2001, 351 (4), 421-8.

[5] A. Gurevich, Appl. Phys. Lett. 88, 012511 (2006).

[6] A. Anders, Thin Solid Films 518(2010) 4087.

[7] M. Tinkham, Introduction to Superconductivity, 2nd ed. (Dover Publications, Inc., Mineola, NY, USA, 1996.

[8] A. Leggett, Quantum Liquids: Bose condensation and Cooper pairing in condensed-matter systems (Oxford University Press, Oxford, England, 2006).

[9] A. Abrikosov, L. Gorkov, and I. Dzyaloshinski, in Methods of Quantum Field Theory in Statistical Physics, 2nd ed., edited by R. A. Silverman (Prentice-Hall, Inc., Edgewood Cliffs, NJ, USA, 1963).

[10] H. Kamerlingh Onnes, Konink. Akad. Wetensch. 14 (1911) 113-115.

[11] H. Kamerlingh Onnes, Electrician 67 (1911) 657-658.

[12] W. Meissner, R. Ochsenfeld, Naturwissenshaften 21 (1933) 787.

[13] A. Rose-Innes, E. Rhoderick, Introduction to supercondcutivity, Pergemon Press, Glasgow, Scotland, 1975.

[14] Gorter, C. J., Casimir, H. The thermodynamics of the superconducting state Z. tech. Phys, 1934, 15, 539-42.

[15] J. Bardeen, L. Cooper, J. Schrieffer, Phys. Rev. 108 (1957) 1175.

[16] A. Pippard, Proc. Roy. Soc. (London) A203 (1953) 98.

[17] J. Wildram, Adv. Phys 13 (1064) 1.

[18] S. Nam, Phys. Rev. 156 (1967) 487.

[19] D. Mattis, J. Bardeen, Phys. Rev. 111 (1958) 412.

[20] P. Miller, Phys. Rev. 118 (1960) 928.

[21] H. Padamsee, J. Knoblock, T. Hays, RF Superconductivity for Accelerators, Wiley and Sons, New York, 1998.

[22] J. Matricon, D. Saint-James, Phys. Letters 24 A (1967) 241-242

[23] T. Yogi, G. Dick, and J. Mercereau, "Critical rf magnetic fields for some type-I and type-II superconductors". Physical Review Letters, 1977.**39**(13): p. 826-829

[24] B. P. Xiao, C. E. Reece, and M. J. Kelley, Superconducting surface impedance under radiofrequency field, *Physica C: Superconductivity***490**, 26 (2013), http://www.sciencedirect.com/science/article/pii/S0921453413001718

[25] B. P. Xiao and C. E. Reece, A New First-Principles Calculation of Field-Dependent RF Surface Impedance of BCS Superconductor, Proc. SRF 2013 Conf, Paris, France (2013), pp. MOIOC02.

[26] C. E. Reece and B. P. Xiao, A Parametric Study of BCS RF Surface Impedance with Magnetic Field Using Xiao Code, *Proc. SRF 2013 Conf*Paris, France (2013), pp. 444, http://ipnweb.in2p3.fr/srf2013/papers/tup011.pdf

[27] B.P. Xiao, http://arxiv.org/abs/1404.2523

[28] V. Palmieri, 10th Workshop on RF Superconductivity Proceedings, Tsukuba 2001 (Noguchi) p.

[29] A. Gurevich, International SRF Thin Films Workshop, LNL-INFN, 2006 (http://master.lnl.infn.it/thinfilms/)

[30] R. Geng, ILC work

[31] C. Xu, C. E. Reece, and M. J. Kelley, Simulation of Non-linear RF Losses Derived from Characteristic Nb Topography, Proceedings of SRF 2013, Paris, France (2013), pp. 441, http://ipnweb.in2p3.fr/srf2013/papers/tup010.pdf

[32] C. E. Reece and H. Tian, Exploiting New Electrochemical Understanding of Niobium Electropolishing for Improved Performance of SRF Cavities for CEBAF, Proc. XXV Linear Accel. Conf., Tsukuba, Japan (2010), pp. 779-781, http://accelconf.web.cern.ch/AccelConf/LINAC2010/papers/thp010.pdf/

[33] A. Burrill, G. K. Davis, F. Marhauser, C. E. Reece, A. V. Reilly, and M. Stirbet, Production and Testing Experience with the SRF Cavities for the CEBAF 12 GeV Upgrade, Proc. 2nd Int. Part. Accel. Conf., San Sebastián, Spain (2011), pp.26-28, http://accelconf.web.cern.ch/AccelConf/IPAC2011/papers/mooca01.pdf/

[34] Berry, S., et al. "Topologic analysis of samples and cavities: a new tool for morphologic inspection of quench site." 11th workshop on RF Superconductivity. 2003.

[35] Berry, Stéphane, C. Antoine, and M. Desmons. "Surface morphology at the quench site." EPAC. Vol. 4. 2004.

[36] G. Ciovati, Effect of low-temperature baking on the radio-frequency properties of niobium superconducting cavities for particle accelerators, J. Appl. Phys. 96, 1591 (2004), http://dx.doi.org/10.1063/1.1767295

[37] D. Gonnella and M. Liepe, High Q0 Studies at Cornell, Proceedings of SRF 2013, Paris, France (2013), pp. 478, http://ipnweb.in2p3.fr/srf2013/papers/tup027.pdf

[38] A. Romanenko, A. Grassellino, F. Barkov, and J. P. Ozelis, Effect of mild baking on superconducting niobium cavities investigated by sequential nanoremoval, Physical Review Special Topics - Accelerators and Beams 16, 012001 (2013), http://link.aps.org/doi/10.1103/PhysRevSTAB.16.012001

[39] N. R. A. Valles, et al., Record Quality Factor Performance of the Prototype Cornell ERL Main Linac Cavity in the Horizontal Test Cryomodule, Proceedings of SRF 2013, Paris, France (2013), pp. 300, http://ipnweb.in2p3.fr/srf2013/papers/mop071.pdf

[40] P. Ylä-Oijala, *Multipacting analysis and electromagnetic field computation by the boundary integral equation method in RF cavities and waveguides*, University of Kelsinki, 1999

[41] K. Twarowski, L. Lilje, and D. Reschke, Multipacting in 9-cell TESLA cavities, *Proc. 11th Int. Workshop on RF Superconductivity,* Travemunde, Germany (2003), pp. 733-735, http://accelconf.web.cern.ch/AccelConf/SRF2003/paper/thp41.pdf

[42] V. Shemelin, One-point multipactor in crossed fields of RF cavities, *Physical Review Special Topics - Accelerators and Beams* **16**, 102003 (2013), http://link.aps.org/doi/10.1103/PhysRevSTAB.16.102003.

[43] J. Knobloch, *Advanced thermometry studies of superconducting RF cavities*, Cornell University, 1997

[44] C. Lyneis, Y. Kojima, J. P. Turnesure, and N. T. Viet, Electron Loading in L- and S- Band Superconducting Niobium Cavities, (1973), http://accelconf.web.cern.ch/AccelConf/p73/PDF/PAC1973_0101.PDF

[45] P. Kneisel, O. Stoltz, and J. Halbritter, Observations on electron loading in superconducting cavities, *Journal of Applied Physics* **44**, 1785 (1973), http://scitation.aip.org/content/aip/journal/jap/44/4/10.1063/1.1662448

[46] W. Bayer, R. Eichhorn, M. Gopych, H. D. Gräf, J. Hasper, A. Richter, and A. Zilges, X-ray spectroscopy-a new method to investigate field emission in superconducting accelerating cavities, *Nuclear Instruments and Methods in Physics Research Section A:Accelerators, Spectrometers, Detectors and Associated Equipment***575**, 321 (2007)

[47] U. Becker, M. Zhang, and T. Weiland, Two and Three Dimensional Simulations of Dark Current on TESLA-Cavities, Gif-sur-Yvette, France (1995), pp. 397-401, http://accelconf.web.cern.ch/AccelConf/SRF95/papers/srf95c07.pdf/

[48] B. C. Yunn and R. M. Sundelin, Field Emitted Electron Trajectories for the CEBAF Cavity, (1993), pp. 1092-1094, http://accelconf.web.cern.ch/AccelConf/p93/PDF/PAC1993_1092.PDF/

[49] Y. M. Li, K. X. Liu, R. L. Geng, and A. D. Palczewski, Research on Field Emission and Dark Current in ILC Cavities, *Proc. SRF 2013 Conf,* Paris, France (2013), pp. 389-394, http://ipnweb.in2p3.fr/srf2013/papers/tuioa06.pdf/

[50] Field emission and consequences as observed and simulated for CEBAF upgrade cryomodules, 2012, JLAB-TN-12-044

[51] Studies of electromagnetic cascade showers development in the TESLA main linac initiated by electron field emission in RF cavities, 2003, TESLA Report 2003-10.

[52] R. L. Geng and A. C. Crawford, Standard Procedures of ILC High Gradient Cavity Processing at Jefferson Lab, *Proc. 15th Int. Conf. on RF Superconductivity,* Chicago, IL USA (2011), pp. 391-393, http://accelconf.web.cern.ch/AccelConf/SRF2011/papers/tupo015.pdf

[53] B. vanderHorst, A. Matheisen, B. Petersen, S. Saegebarth, and P. Schilling, Update on Cavity Preparation for High Gradient Superconducting Multicell Cavities at DESY, *Proc. 13th Int. Workshop on RF Superconductivity,* Beijing, China (2007), pp. 196-199, http://accelconf.web.cern.ch/AccelConf/srf2007/PAPERS/TUP30.pdf

[54] J. Mammosser, in *ILC cavity qualifications - Americas*, 2007)

[55] F. Furuta, K. Saito, T. Saeki, H. Inoue, Y. Morozumi, Y. Higashi, and T.Higo, High reliable surface treatment recipe of high gradient single cell SRF cavities at KEK, *Proc. 13th Int. Workshop on RF Superconductivity,* Beijing, China (2007), pp. 125-131, http://accelconf.web.cern.ch/AccelConf/srf2007/PAPERS/TUP10.pdf

[56] J. Graber, *High power RF processing studies of 3 GHz niobium superconducting accelerator cavities*, Cornell University, 1993

[57] H. A. Schwettman, J. P. Turneaure, and R. F. Waites, Evidence for surface-state-enhanced field emission in RF superconducting cavities, *Journal of Applied Physics* **45**, 914 (1974)

[58] C. Reece, M. Drury, M. G. Rao, and V. Nguyen-Tuong, Improvement of the Operational Performance of SRF Cavities via In Situ Helium Processing and Waveguide Vacuum Processing, *Proc. 1997 Part. Accel. Conf.,* (1997), http://accelconf.web.cern.ch/accelconf/pac97/papers/pdf/3P034.PDF

[59] H. A. Schwettman, J. P. Turneaure, and R. F. Waites, Evidence for surface-state-enhanced field emission in RF superconducting cavities, *Journal of Applied Physics* **45**, 914 (1974)

[60] C. Reece, M. Drury, M. G. Rao, and V. Nguyen-Tuong, Improvement of the Operational Performance of SRF Cavities via In Situ Helium Processing and Waveguide Vacuum Processing, *Proc. 1997 Part. Accel. Conf.,* (1997), http://accelconf.web.cern.ch/accelconf/pac97/papers/pdf/3P034.PDF

[61] A. Grassellino, et al., Nitrogen and argon doping of niobium for superconducting radio frequency cavities: a pathway to highly efficient accelerating structures, *Superconductor Science and Technology***26**, 102001 (2013), http://stacks.iop.org/0953-2048/26/i=10/a=102001/

[62] A. Grassellino, New Insights on the Physics of RF Surface Resistance and a Cure for the Medium Field Q-Slope, Proc. SRF 2013 Conf, Paris, France (2013), pp. TUIOA03.

[63] D. Gonnella, M. Liepe, and A. Grassellino, Performance of a FNAL Nitrogen Treated Superconducting Niobium Cavity at Cornell, *Proceedings of SRF 2013,* Paris, France (2013), pp. 475, http://ipnweb.in2p3.fr/srf2013/papers/tup026.pdf

[64] G. Ciovati, P. Dhakal, and A. Gurevich, Decrease of the surface resistance in superconducting niobium resonator cavities by the microwave field, *Applied Physics Letters* **104**, 092601 (2014)

[65] H. Padamsee, RF Superconductivity: Volume II: Science, Technology and Applications (WILEY-VCH, Weinheim, 2009)

[66] O. Kugeler, J. Knobloch, and J. M. Vogt, Pathway to a Post Processing Increase in Q0 of SRF Cavities *Proc. Int. Part. Accel. Conf. 2013,*Shanghai, China (2013), pp. 3129-3131, http://accelconf.web.cern.ch/AccelConf/IPAC2013/papers/thobb201.pdf

[67] J. M. Vogt, O. Kugeler, and J. Knobloch, Impact of cool-down conditions at T_c on the superconducting RF cavity quality factor, *Physical Review Special Topics - Accelerators and Beams* **16**, 102002 (2013), http://link.aps.org/doi/10.1103/PhysRevSTAB.16.102002

[68] A. Romanenko, A. Grassellino, O. Melnychuk, and D. A. Sergatskov, Dependence of the residual surface resistance of superconducting radio frequency cavities on the cooling dynamics around T_c, *Journal of Applied Physics***115** (2014) http://scitation.aip.org/content/aip/journal/jap/115/18/10.1063/1.4875655/

[69] D. Gonnella and M. Liepe, Flux Trapping in Nitrogen-doped and 120C Baked Cavities, *Proc. Int. Part. Accel. Conf. 2014,* Dresden, Germany (2014), pp. WEPRI063

[70] N. Wilson and P. Bunch, Magnetic Permeability of Stainless Steel for Use in Accelerator Beam Transport Systems, (1991), pp. 2322-2324, http://accelconf.web.cern.ch/accelconf/p91/pdf/pac1991_2322.pdf/

[71] 1.3 GHz SCRF, Vertical Cavity Testing, KYOCERA CNN and FLNG WLDMT, FNAL Drawing number 4904.010-MC-457301

[71] M. Masuzawa, A. Terashima, and K. Tsuchiya, Magnetic Shielding: Our Experience with Various Shielding Materials, *Proceedings of SRF 2013,*Paris, France (2013), pp. 808, http://ipnweb.in2p3.fr/srf2013/papers/weiod02.pdf

[72] R. L. Geng and P. Kushnick, JLAB-TN-08-05, (2008)

[73] B. Aune, et al., Superconducting TESLA cavities, *Physical Review Special Topics - Accelerators and Beams* **3**, 092001 (2000), http://link.aps.org/doi/10.1103/PhysRevSTAB.3.092001

[74] C. Benvenuti, S. Calatroni, I. E. Campisi, P. Darriulat, M. A. Peck, R. Russo, and A. M. Valente, Study of the surface resistance of superconducting niobium films at 1.5 GHz, *Physica C* **316**, 153 (1999), http://dx.doi.org/10.1016/S0921-4534(99)00207-5

[75] N. Valles, et al., Testing of the Main-Linac Prototype Cavity in a Horizontal Test Cryomodule for the Cornell ERL, Proc. Int. Part. Accel. Conf. 2012, New Orleans, Louisiana (2012), pp. 2387-2389, http://accelconf.web.cern.ch/AccelConf/IPAC2012/papers/weppc075.pdf

[76] W. Weingarton, Progress in thin film techniques, in: Proc. Of 7th workshop on RF superconductivity, Gif-sur-Yevette, France, 1995

[77] T. Wang et al., DC field emission studies, 10^{th} workshop on RF superconductivity, Proceedings of the 10th Workshop on RF Superconductivity, KEK, Tsukuba, Japan, 2001./

[78] K. Saito, P. Kneisel, Temperature Dependence of the Surface Resistance of Niobium at 1300 MHz - Comparison to BCS Theory, in: Proceedings of the 9th Workshop on RF Superconductivity, Santa Fe, New Mexico, USA, 1999.

[79] C. Durand, P. Bosland, J. Mayer, Non Quadratic RF Losses in Niobium Sputter Coated Accelerating Structures, Appl. Superconductivity,IEEE Transactions on 5 (1995) 1107.

[80] J. Halbritter, J. Supercond. 8 (1995) 691

[81] Halbritter, Journal of applied physics 71.1 (1992): 339-343.

[82] I. Kulik, V. Palmieri, Part. Accel. 60 (1998) 257

[83] Halbritter, Journal of applied physics 71.1 (1992): 339-343.

[84] W. Singer, H. Kaiser, X. Singer, G. Weichert, I. Jelezov, P. Kneisel, T. Fujino, K. Saito, Hydroforming of superconducting tesla cavities, in: Proceedings of the 10^{th} Workshop on RF Superconductivity, KEK, Tsukuba, Japan, 2001, FA009

[85] Arbet-Engels, V., et al., Nuclear Instruments and Methods in Physics Research Section A: Accelerators, Spectrometers, Detectors and Associated Equipment 463.1 (2001): 1-8.

[86] C. Benvenuti et al., "Cern Studies On Niobium-Coated 1.5 Ghz Copper Cavities" in: S. Noguchi (Ed.), Proc. of the SRF2001 Workshop, KEK, Tsukuba, 2002, p. 252

[87] B. Bonin et al., in: Proc. of the SRF2003 Workshop, D. Proch ed.

[88] Calatroni, S., et al. Progress of Nb/Cu technology with 1.5 GHz cavities. No. CERN-TS-2004-002-MME. 2003.

[89] J. Halbritter, Supercond. Sci. Technol. 12 (1999) 883

[90] F. Palmer, Surface resistance of Superconductors - Examples from Nb - O system, Proceedings of the 3th Workshop on RF Superconductivity, Argonne, USA, 1988, ANL-PHY-88-1, p. 309.

[91] M. Malev, D. Weisser, Oxygen desorption during niobium sputtering for superconducting RF accelerators, NIM in physics research A 364 (1995) 409

[92] J. Halbritter, in: Proceedings of the 10th Workshop on RF Superconductivity, KEK, Tsukuba, Japan, 2001

[93] Ribeaudeau, Marion. Elaboration et caracterisation de films de niobium deposes sur cuivre. Determination de la resistance de surface de supraconducteurs par thermometrie sous vide. PhD Diss. 1999.

[94] S. Calatroni, 20 years of experience with the Nb/Cu technology for superconducting cavities and perspectives for future developments, in: Proceedings of the 12^{th} Workshop on RF Superconductivity, Cornell University, Ithaca, NY, USA, 2005

[95] Sublet, A., et al., Proceedings of SRF13, Paris, France 2014 (2013).

[96] Nb Coated HIE-ISOLDE QWR Superconducting Accelerating Cavities: From Process Development To Series Production, A. Sublet et al., Proc. of IPAC 2014, Dresden, Germany

[97] G. Bisoffi et al., ALPI QWR and S-RFQ operating experience, in: Proceedings of the 13^{th} Workshop on RF Superconductivity, Peking University, Beijing, China, 2007

[98] A.-M. Porcellato, Nucl. Instr. and Meth. A 382 (1996) 121

[99] R. Russo et al., Supercond. Sci. Technol. 18 (2005) L41

[100] R. Russo et al. IEEE Trans. On Appl. Supercond., Vol. 19, No. 3, June 2009

[101] R. Russo, Report of ARCO Project, Proc. of 10^{th} workshop on RF superconductivity, Tsukuba, Japan, 2001

[102] J. Langner, R. Mirowski, M.J. Sadowski, P. Strzyzewski, J. Witkowski, S. Tazzari, L. Catani, A. Cianchi, J. Lorkiewicz, R. Russo, Vacuum 80 (2006) 1288-1293

[103] R. Russo, L. Catani, A. Cianchi, D. DiGio, R. Nietubyc, M. Sadowski, M. Bruchon, B. Visentin, B. Ruggiero, Nb coating of copper cavities by UHV cathodic arc, in: Proceedings of the 13th Workshop on RF Superconductivity, Peking Univeristy, Beijin, China, 2007, WE101

[104] Xin Zhao, A.-M. Valente-Feliciano, C. Xu, R. L. Geng, L. Phillips, C. E. Reece, K. Seo, R. Crooks, M. Krishnan, A. Gerhan, B. Bures, K. Wilson Elliott, and J. Wright, Large crystal grain niobium thin films deposited by energetic condensation in vacuum arc, J. Vac. Sci. Technol. A 27, 620 (2009).

[105] M. Krishnan, E. Valderrama, C. James, X. Zhao, J. Spradlin, A-M Valente Feliciano, L. Phillips, C. E. Reece, K. Seo, and Z. H. Sung, Phys. Rev. ST Accel. Beams 15, 032001 (2012)

[106] M. Krishnan et al. Proc. of SRF2013,WEIOA02.

[107] D. Horwat and A. Anders, J. Appl. Phys.108 (2010) 123306.

[108] A. Anders, Surf. and Coat. Techn. (205), S2, 2011, pp. S1-S9

[109] J. Andersson and A. Anders, J. Appl. Phys. 111 (2012) 053304

[110] A. Anders, Phys. Rev. Lett. 102, 045003 (2009)

[111] A. Anders et al., TUIOA06, 2011 SRF conference, Chicago, USA

[112] A. Anders Appl. Phys. Lett. 85, 6137 (2004)

[113] A. Anders, R. Mendelsberg, private communication, to be published

[114] G. Terenziani, S. Calatroni, A.P. Ehiasarian, 4th International Conference on Fundamentals and Industrial Applications of HIPIMS (2013), to be published

[115] G. Terenziani, et al., TUP078, SRF2013

[116] R. Vaglio, Particle Accelerators 61, 391 (1998)

[117] S.V.Vonsovsky, Yu.A.Izyumov, E.Z.Kumaev, "Superconductivity of transition metals, their alloys and compounds", Springer-Verlag (1982)

[118] G. Brauer, J. Less-Common Metals 2 (1960) 131

[119] R.W. Guard, J.W. Savage and D.G . Swarthout, Trans. Metall. Soc. ATME 239 (1967) 643], characterized by different T_c [L. Toth, Transition Metal Carbides and Nitrides (Academic Press, New York, 1971), chap. 7.

[120] P. Fabbricatore et al ., J. Appl. Phys . 66 (1989) 5944.

[121] M. Pham Tu et al ., J. Appl . Phys . 63 (1988) 4586

[122] C. Benvenuti et al., Nucl. Instrum. Methods A 336, 1622 (1993)

[123] G.Gemme et al., J.Appl.Phys. 77(1), Jan. 1995

[124] A. Nigro et al., Physica Scripta Vol. 38, 483-485, 198

[125] C. Benvenuti et al. Nucl. Instrum. Methods B 124 (1997) 106-111

[126] A. Nigro et al., Adv. Cryog. Eng. 34, 813 (1988)

[127] R. Di Leo et al. J. of Low Temp. Phys, vol 78, n1/2, pp41-50, 1990

[128] P. Bosland et al., Proceeding of EPAC 1992, p.1316

[129] S. Cantacuzène et al. Proceedings of EPAC 1994, p. 2076

[130] M. Marino, PhD Thesis n ° 2039 (1999), EPFL, Switzerland

[131] M. Marino, Proc. 8th Workshop on RF Superconductivity, October 1997, Abano Terme (Padua), 133/98, vol.IV, p.1076

[132] R.G. Sharma, International SRF Thin Films Workshop, LNL-INFN, 2006, http://master.lnl.infn.it/thinfilms/

[133] A. Godeke, International SRF Thin Films Workshop 2006, INFN-LNL, http://master.lnl.infn.it/thinfilms/ (Lawrence Berkeley National Laboratory. Paper LBNL-62140)

[134] G. Muller et al. Proceedings of the 5th EPAC, London, 1985, p. 2085

[135] M. Peiniger & H. Piel , IEEE Trans. Nucl. Sc. Vol. NS-32, n ° 5, Oct. 85

[136] M. Perpeet et al., IEEE Trans. Appl. Supercond., Vol. 9, n ° .I, June 1999

[137] G. Müller et al., Proceedings of EPAC1996, Institute of Physics Publishing. 3, p.2085 (1997)

[138] G.F.Hardy and J.K. Hulm, Phys. Rev. 87, 884 (1953); 93, 1004 (1954

[139] S. Deambrosis, et al. Physica C 441(2006)108-113

[140] S. Posen and M. Lieppe, Proc. SRF 2013, S. Posen et al., Proc. IPAC 2014

[141] Eremeev et al., Proc. SRF 2013, TUP071.

[142] Nb_3Sn Program For Superconducting Cavities, F. Wohlfarth, Proc. SRF 2013

[143] Jorda, J. L., and J. Muller. "The V_3Si phase Type of formation and homogeneity range." Journal of the Less Common Metals 84 (1982) 39-48.

[144] Gavaler, J. R., M. A. Janocko, and C. K. Jones, Applied Physics Letters 21.4 (1972) 179-180.

[145] J. Nagamatsu et al., Nature 410 (2001) 63

[146] A. Floris et al., Physica C 456, n ° 1-2, (2007) 45-53

[147] X. Xi et al., Physica C 456 (2007) 22-37

[148] B.P.Xiao et al., Supercond. Sci, Technol. 25 (2012) 095006.

[149] Putti, M., et al., Superconductor Science and Technology 23.3 (2010): 034003.

[150] "Artificially engineered superlattices of pnictide superconductor", S. Lee, C. Tarantini, P. Gao, J. Jiang, J. D. Weiss, F. Kametani, C. M. Folkman, Y. Zhang, X. Q. Pan, E. E. Hellstrom, D. C. Larbalestier, and C. B. Eom, Nature Materials, DOI: 10.1038/NMAT3575 (2013)

[151] Characterization of superconducting nanometric multilayer samples for superconducting RF applications: First evidence of magnetic screening effect, C.Z. Antoine et al., Phys. Rev. ST Accel. Beams 13, 121001, Dec. 2010

[152] C.Z. Antoine, IEEE TRANS. ON APPL. SUPERCOND., VOL. 21, NO. 3, JUNE 2011

[153] MULTILAYERS ACTIVITIES AT SACLAY / ORSAY,C. Baumier et al., Proc. Of SRF 2013, Paris

[154] D. B. Beringer, C. Clavero, T. Tan, X. X. Xi,W.M. Roach, and R.A. Lukaszew, "Thickness Dependence and Enhancement of H_{C1} in Epitaxial MgB2 Thin Films," IEEE Trans. Appl. Supercond. 23, 7500604 (2013).

[155] M. Ohring, The Materials Science of Thin Films, 2nd ed. (Academic Press Inc., San Diego, 2002)

[156] D. A. Porter and K. E. Easterling, Phase transformations in Metals and Alloys, 2nd ed. (Nelson Thornes Ltd., Cheltenham, United Kingdom, 2001)

[157] H. J. Frost, Microstructural Evolution in Thin Films, Materials Characterization 32, 257 (1994)

[158] C. V. Thompson, Structure Evolution During Processing of Polycrystalline Films, Annual Reviews of Materials Science 30, 159 (2000)

[159] I. Petrov, P. B. Barna, L. Hultman, and J. E. Greene, Microstructural evolution during film growth, Journal of Vacuum Science and Technology A 21, 117 (2003)

[160] J.S. Colligon, J. Vac. Sci. technol. A13(3), 1995, p. 1649

[161] O. R. Monteiro, Annual Rev. Mat. Sci., vol. 31, pp. 111-137, 2001

[162] A. Anders, Cathodic arcs: from fractal spots to energetic condensation (2008), Ch. 8 pp363-407

[163] Gudmundsson, J. T. "Ionized physical vapor deposition (IPVD) magnetron sputtering discharges." Journal of Physics Conference Series. Vol. 100. No. 8. IOP Publishing, 2008.

[164] Zinsmeister G, Theory of thin film condensation, Thin Solid Films, vol. 2, pp. 497-507, 1968

[164] I. Petrov, P. B. Barna, L. Hultman, and J. E. Greene, Microstructural evolution during film growth, Journal of Vacuum Science and Technology A 21, 117 (2003)

[166] P. B. Barna and M. Adamik, Fundamental structure forming phenomena of polycrystalline films and the structure zone models, Thin Solid Films 317, 27 (1998).

[167] Atomistic Processes in the Early Stages of Thin-Film Growth, Zhenyu Zhang and Max G. Lagally, SCIENCE VOL. 276, 18 APRIL 1997 pp. 377-383

[168] D. W. Pashley, Mat. Sci. Technol. 15 (1999) 2

[169] André Anders, Handbook of Plasma Immersion Ion Implantation and Deposition, John Wiley & sons, inc. New York (2000)

[170] R.A. Lukaszew, PRB 82, 085445, 2010

[171] C. Clavero, D. B. Beringer, R. A. Lukaszew, W. Roach, J. Skuza, C. E. Reece, THPO047,SRF2011

[172] C. Thompson, Ann. Rev. of Mat. Sc., 20, p. 245-268

[173] Lewis B, Anderson J C, Nucleation and Growth of Thin Films, Academic Press, 1978

[174] A. R. Wildes et al., Thin Solid Films, 401 7 (2001).

[175] Smitb JF in : Binary alloy phase diagrams, vol. 3, 2nd ed., Massalski TB, editor, 1990, p.2526

[176] Hutchinson, Journal Applied Physics 36, 270 (1964)

[177] Y. Igarashi and M. Kanayama, J. Appl. Phys. 57, 849 (1985).

[178] T. E. Hutchinson and K. H. Olsen, J. Appl. Phys. 38, 4933 (1967).

[179] D. Beringer, W. M. Roach, C. Clavero, C. E. Reece, R.A. Lukaszew, TH , SRF2011

[180] K. Masek, V. Matolin, Vacuum 61 (2001) 217, 221

[181] E. Bauer and J. H. van der Merwe, Phys. Rev. B 33(6), 3657 (1986).

[182] Gotoh Y, Uwaha M, Arai I. Appl Surf. Sci. 1988;33/34 p. 443.

[183] R. Ramirez, A. Rahman, and I. K. Schuller, Phys. Rev. B 30(10), 6208 (1984).

[184] J. H. Van Der Merwe, Thin Solid Films 74(1), 129?151 (1980).

[185] L. C. A. Stoop and J. H. Van der Merwe, Thin Solid Films 91(3), 257?276 (1982).

[185b] Clavero C. et al., J. Appl. Phys. 112, 074328 (2012).

[186] Hellwig O, Theis-BroK hl K, Wilhelm G, Stierle A, Zabel H., Surf. Sci. 1998;398:379.

[187] I. Langmuir, Phys. Rev. 33, 954 (1929)

[188] M. Moisan, J. Pelletier, Microwave Excited Plasmas, Elsevier Science, (1992)

[189] M. Moisan, J. Pelletier, Physique des plasmas collisionels: application aux décharges haute fréquence, EDP Sciences, (2006)

[190] M.A. Lieberman and A.J. Lichtenberg, Principles of Plasma Discharges and Materials Processing, John Wiley & Sons, New York, USA (2005).

[191] F.F. Chen, Introduction to Plasma Physics and Controlled Fusion Vol. I: Plasma Physics, Plenum, New York, USA (1984), p. 1

[192] F.F. Chen, J.P. Chang, Lectures notes on principles of plasma processing, pp. 1-10, Springer, Los Angeles, (2003)

[193] N.St J. Braithwaite, Introduction to gas discharges, Plasma Sources Science and Technology, Vol. 9(4), pp. 517-527, (2000)

[194] S.M. Rossnagel in J.L. Vossen and Kern (eds.), Thin Film Processes II, Academic Press, New York, USA (1991).

[195] D.M. Sanders, J. Vac. Sci. Technol. A 7, 2339 (1989)

[196] J.R. Roth, Industrial Plasma Engineering Vol. 1: Principles, Institute of Physics Publishing, Bristol, UK (1995).

[197] Y. Okajima, J. Appl. Phys. 51 (1980) 715.

[198] K. S. Sree Harsha, Principles of Physical Vapor Deposition of Thin Films, Elsevier Science, Oxford (2006), p. 566.

[199] D. Depla, S. Heirwegh, S. Mahieu, J. Haemers, R. De Gryse, J. Appl. Phys. 101 (2007) 013301.

[200] P. J. Kelly, R. D. Arnell, Vacuum 56 (2000) 159

[201] J. Musil and S. Kadlec, Vacuum 40, 435 (1990)

[202] U. Helmersson, M. Lattemann, J. Bohlmark, A. P. Ehiasarian, J. T. Gudmundsson, Thin Solid Films 513 (2006) 1.

[203] J. Bøttiger, J. Chevallier, P. Kringhøj, and K. O. Schweitz, Stresses in thin films, Adhesion Aspects of Thin Films 1, 1 (2001).

[204] Broussard Phillip R, Superconducting Film Devices, vol. 3 of Handbook of Thin Film Devices, Academic Press, 2000

[205] Kadlec S, Musil J, Vyskocil H, Hysteresis effect in reactive sputtering: a problem of system stability, J. Phys. D: Appl. Phys., vol. 19, pp. 187-190, 1986.

[206] Schiller S, Beister G, Sieber W, Reactive high rate d.c. sputtering: deposition rate, stoichiometry and features of TiOx and TiNx films with respect to the target mode, Thin Solid Films, vol. 111, pp. 259-268, 1984

[207] Scholl R A, Power Systems for Reactive Sputtering of Insulating Films, Advanced Energy Industries Inc.

[208] Koski K, Holsa J and Juliet P, Voltage controlled reactive sputtering process for aluminium oxide films, Thin Solid Films, vol. 326, pp. 189-193, 1998.

[209] Golans A, Thin-film Thermo-mechanical sensors embedded in metallic structures, PhD thesis, Standford University, December 1999.

[210] J. A. Thornton, The microstructure of sputter-deposited coatings, Journal of Vacuum Science and Technology A 4, 3059 (1986).

[211] B. A. Movchan and A. V. Demchishin, Study of the Structure and Properties of Thick Vacuum Condensates of Nickel, Titanium, Tungsten, Aluminum Oxide and Zirconium Dioxid, Physics of Metals and Metallography (Fizika Metalov i Metalovedenije, USSR) 28, 83 (1969).

[212] J. A. Thornton, Ann. Rev. Mater. Science 7 (1977) 239

[213] J. A. Thornton, Influence of apparatus geometry and deposition conditions on the structure and topography of thick sputtered coatings, Journal of Vacuum Science and Technology 11, 666 (1974).

[214] J. A. Thornton, Influence of substrate temperature and deposition rate on structure of thick sputtered Cu coatings, Journal of Vacuum Science and Technology 12, 830 (1975).

[215] C. Hudson and R. E. Somekh, in Thin Films: Stresses and Mechanical Properties III, Vol. 239 of Materials Research Society Symposium Proceedings, edited byW. D. Nix, J. C. Bravman, E. Arzt, and L. B. Freund (Materials Research Society, Pittsburg, PA, 1992), pp. 145-150.

[216] R. Messier, A. P. Giri, and R. A. Roy, Revised structure zone model for thin film physical structure, Journal of Vacuum Science and Technology A 2, 500 (1984).

[217] P. B. Barna and M. Adamik, Fundamental structure forming phenomena of polycrystalline films and the structure zone models, Thin Solid Films 317, 27 (1998).

[218] Y.P. Purandare et al., J. Vac. Sci. Techn. A 26(2) 288, (2008).

[219] M. Krishnan, et al. Very high residual-resistivity ratios of heteroepitaxial superconducting niobium films on MgO substrates, Supercond. Sci. and Technol., 2011, 24, 115002

[220] Brown IG, Vacuum arc ion sources, Rev. Sci. Instrum. 65 (10): 3061, 1994.

[221] G. Wu et al. Thin Solid Films 2005, 489(1-2), 56-62.

[222] K. Sarakinos, J. Alami, S. Konstantinidis, Surf. & Coat. Technol. 204 (2010), 1661-1684 O. R. Monteiro, Annual Rev. Mat. Sci., vol. 31, pp. 111-137, 2001.

[223] D.K. Brice, J.Y. Tsao, S.T. Picraux, Nucl. Instrum. Methods Phys. Res. B 44 (1989) 68.

[224] W. Eckstein, Computer Simulation of Ion-Solid Interactions, Springer-Verlag, Berlin,1991.

[225] M.M.M. Bilek, D.R. McKenzie, Surf. Coat. Technol. 200 (2006) 4345.G. Carter, Phys. Rev. B 62 (2000) 8376.

[226] L. Hultman, J.E. Sundgren, in: R.F. Bunshah (Ed.), Handbook of Hard Coatings, Noyes, Park Ridge, NY, 2001, p. 108. [69] A. Anders, Thin Solid Films 518, 4087-4090 (2010).

[227] J.M.E Harper et al., Ion Bombardment Modification of Surfaces: Fundamentals and Applications, eds. O. Auciello and R. Kelley, Elsevier, Amsterdam, 1984.

[228] M.R. Wertheimer, M. Moisan, Processing of electronic materials by microwave plasma, Pure and Applied Chemistry, Vol. 66(6), pp. 1343-1352, (1994).

[229] J. Asmussen, Electron cyclotron resonance microwave discharges for etching and thin-film deposition, Journal of Vacuum Science and Techology A, Vol. 7(3), pp. 883 - 893, (1989).

[230] S. Nakayama, ECR plasma for thin film technology, Pure and Applied Chemistry, Vol. 62(9), pp. 1751-1756, (1990)

[231] H. Muta, Investigation of Electron Behaviour in ECR Plasmas Using a Self-Consistent Particle Wave Model, Japanese Journal of Applied Physics, Vol. 38(7B), pp. 4455-4459, (1999)

[232] W. M. Holber, et al., JVST A. Vol.11(6), 1993.

[233] G. Wu PhD thesis, Virginia Tech 2002

[234] Cathodic Arc Deposition of Films, I. Brown, Annual Review of Materials Science Vol. 28: 243-269 (1998).

[235] I.I. Aksenov, Problems of Atomic Science and Technology 2002. No 5. Series: Plasma Physics (8). P. 139-141.

[236] A. Anders et al. Plasma Sources Sci. Technol. 4 (1995) 1-12.

[237] Y. Purandare, et al., Surface and coatings technology, 204 (8), 1158-1162 (2010).

[238] J. Bohlmark et al., J. Vac. Sci. Technol. A 23, 18 (2005).

[239] V. Kouznetsov, et al., Surf. Coat. Technol. 122 (1999) 290.

[240] [A. Anders et al., J. Appl. Phys. 111 (2012) 053304.

[241] Gudmundsson et al. (2012), JVSTA 30030801.

[242] J.M. Andersson, et al., Thin Solid Films 513, 57 (2006).

[243] Alami, et al., J. Vac. Sci. Tech. A 23278 (2005).

[244] 1] R. Russo, Meas. Sci. Technol. 18 (2007) 2299-2313.

[245] Vaglio R, Attanasio C, Maritato L and Ruosi A 1993 Phys. Rev. B 47 15302-3.

[246] Attanasio C et al 2001 J. Phys.: Condens. Matter. 13 3215-21.

[247] L. R. Testardi and L. F. Mattheiss, Phys. Rev. Lett. 41, 1612 (1978).

[248] Valente-Feliciano, A. M. "Nb films: substrates, nucleation & crystal growth." Proc. 15th Int. Conf. on RF Superconductivity. 2011.

[249] Xiao, B., Reece, C., Kelley, M., Physica C: Superconductivity, 2013, 490, 26-31

[250] L. Ozyuzer, J.F. Zasadzinski and K.E. Gray, Cryogenics 38 (1998)911-915.

[251] T. Proslier et al. Appl. Phys. Lett. 92, 212505 (2008).

[252] Wolf, E. L., Principles of Electron Tunneling Spectroscopy. Oxford University Press, New York, 1985.

[253] Proslier, T. et al., IEEE Transactions on, 2009, 19, 1404-1408

[254] Nb measurement Khim, Z. G., Burnell, D. M. and Wolf, E. L., Solid State Commun., 1981, 39, 159.

[255] M. McElfresh, Quantum Design MPMS Application Notes (1994).

[256] B.D. Josephson, Phys. Lett. 1, 251 (1962).

[257] P.W. Anderson and J.M. Rowell, Phys. Rev. Lett 10, 230 (1963).

[258] C. Böhmer, C. Brandstatter, and H. W. Weber, Supercond. Sci. Technol. 10, A1 (1997).

[259] M. Aurino et al. J. Appl. Phys. 98, 123901 (2005).

[260] G. Lamura et al. J. Appl. Phys. 106, 053903 (2009).

[261] B. D. Cullity, Elements of X-Ray Diffraction, 2nd ed. Addison-Wesley (1978).

[262] B. E. Warren, X-ray diffraction, Dover Publications, INC., New York, 1990.

[263] Klug H P and Alexander L E 1974 X-Ray Diffraction Procedures for Polycrystalline and Amorphous Materials 2nd ed. (New York: Wiley).

[264] R. Feidenhans, Surface Structure Determination by X-Ray Diffraction, Surf. Sci. Reports 10 (1989) 105.

[265] L. Kerkeche, A. Layadi, and E. Dogheche, “Physical Properties of RF Sputtered ITO Thin Films and Annealing Effect,” Journal of Physics D: Applied Physics, vol. 39, pp. 184-189, 2006.

[266] Pankov, M. Evstigneev and R. H. Prince, Journal of Applied Physics, vol. 92, no. 8, p. 4255, 2002. 163.

[267] H. Kumazawa, S. Annen, and E. Sada, Journal of Materials Science, vol. 30, no. 18, pp. 4740-4744, 1995.

[268] Schwartz, A. J., M. Kumar, and B. L. Adams. "Electron backscatter diffraction in materials science", 2000.

[269] Goldstein, Joseph I., et al. Scanning electron microscopy and X-ray microanalysis. A text for biologists, materials scientists, and geologists. Plenum Publishing Corporation, 1981.

[270] L. A. Giannuzzi, F. A. Stenie, Introduction to Focused Ion Beams- Instrumentation, Theory, Techniques and Practice, Springer editor.

[271] D. B. Williams and C.B. Carter, “Transmission Electron Microscopy”, 1996.

[272] S. J. Pennycook, “Scanning Transmission Electron Microscopy: Imaging andAnalysis”, Springer, 2011.

[273] R. Egerton, “ Electron energy-loss spectroscopy in the electron microscope”, Springer, 2nd edition 1996.

[274] Agarwal, Bipin K. "X-ray Spectroscopy." Springer series in optical sciences 15 (1979),p. 35-46.

[275] Gillen, Greg, et al. "Secondary ion mass spectrometry SIMS XI." Secondary Ion Mass Spectrometry SIMS XI, by G. Gillen (Editor), R. Lareau (Editor), J. Bennett (Editor), F. Stevie (Editor), pp. 1150. ISBN 0-471-97826-4. Wiley-VCH, May 2003. 1 (2003).

[276] Meyer, E. R. N. S. T. "Atomic force microscopy." Progress in surface science 41.1 (1992),pp. 3-49.

[277] H. Tian, et al. , Appl. Surf. Sci. 257, 4781 (2011).

[278] C. Xu et al., Phys, Rev. ST Accel. Beams 14, 123501 (2011).

[279] C. Xu et al., Phys. Rev. ST Accel. Beams 15, 043502 (2012).

[280] Tompkins, Harland G., and William A. McGahan, Spectroscopic ellipsometry and reflectometry- a user’s guide. New York, Wiley, 1999.

[281] G. Wu, H.L. Phillips, R.M. Sundelin, J. Vac. Sci. Technol., A, Vac. Surf. Films 21 (4) (2003) 842.

[282] M. Lifshitz and V. V. Slyozov, J. Phys. Chem. Solids 19:35 (1961).

[283] Clavero, C., et al. "Strain Effects on the Crystal Growth and Superconducting Properties of Epitaxial Niobium Ultrathin Films." Cryst. Gr. & Des. 12.5 (2012): 2588-2593.

[284] Zhao, Xin, et al., SRF 2011 Proceedings, THPO044

[285] T. Wagner et al., J. Mat. Res. Vol. 11, nº5, pp. 1255-1264 (1996), Mat. Res. Symp. Proc, Vol. 440, pp.151-156, (1997)].

[286] S. Calatroni et al., Influence of the nature of the substrate on the growth of superconducting niobium films, CERN-EST-2000-005-SM.

[287] A. D. Batchelor, et al., Proceedings of Single Crystal Niobium Technology Workshop, Brazil, AIP Conference Proceedings, Melville, NY (2007) p. 72.

[288] G. Ciovati et al., Phys. Rev. ST- Accel. Beams 13 (2010) p. 022002.

[289] P. Maheshwari et al., Symposium on the Superconducting Science and Technology of Ingot Niobium, AIF Conference Proceedings, 1352 (2011) p. 151.

[290] J. E. Mattson, Eric E. Fullerton, C. H. Sowers, and S. D. Bader, J. Vac. Sci. Technol. A 13, 276 (1995).

[291] Martin, D. S., et al. Phys. Rev. B 63.15 (2001): 155403.

[292] E. Cukauskas, W. Carter, and S. Qadri, J. Appl. Phys. 57, 2538 (1985).

[293] Z. Wang and et al., J. Appl. Phys. 79, 7837 (1996).

[294] L. Toth, Transition Metal Carbides and Nitrides (Academic Press, New York, 1971), chap. 7.

[295] V. Buscaglia and et al., J. of All. and Comp. 226, 232 (1995).

[296] V. Zhitomirsky and et al., Thin Solid Films 326, 134 (1998).

[297] Binary Alloy Phase Diagrams, 2nd ed., edited by T.Massalski, H. Okamoto, P. Subramanian, and L. Kacprzak (ASM International, Metals Park, OH, USA, 1990), Vol. 3.

[298] R. Reed-Hill and R. Abbaschian, Physical Metallurgy Principles, 3rd ed. (PWS-Kent Pub., Boston, MA, USA, 1992).

[299] N. Iosad and et al., IEEE Trans. on Appl. Supercond. 11, 3832 (2001)

[300] S. Boelens and H. Veltrop, Surf. and Coat. Technol. 33, 63 (1987)

[301] Handbook of Ternary Alloy Phase Diagrams, edited by P. Villars, A. Prince and H. Okamoto (ASM International, Materials Park, OH, USA, 1995), Vol. 10.

[301] C. Yen and et al., J. Appl. Phys. 38, 2268 (1967).

[302] H. Myoren and et al., IEEE Trans. on Appl. Supercond. 11, 3828 (2001).

[303] U. König, Surf. and Coat Technol. 33, 91 (1987).

[304] T. Shiino et al., Supercond. Sci. Technol. 23 045004 (2010).

[305] A.-M. Valente-Feliciano, et al., THP074, Proc. of SRF conference 2011, Chicago, July 2011.

[306] W.J. Meng, in: James H. Edgar (Ed.), Properties of Group III Nitrides, INSPEC Short Run Press, London, 1994, pp. 22-34.

[307] Ehiasarian, et al., Journal of Applied Physics, 2008, 104, 083305

[308] S. Yoshimori, Physica C 305,281-284(1998).

[309] S. Kuhr, S. Gleyzes, C. Guerlin, J. Bernu, U. B. Hoff, S. Deléglise, S. Osnaghi, M. Brune, J.M. Raimond, S. Haroche, E. Jacques, P. Bosland, B. Visentin, Appl. Phys. Lett. 90, 164101 (2007].

[310] E. Morisaki, H. Fujiyama, Surface and Coatings Technology 98 (1998) 834-838

[311] A. Yonesu, H. Takemoto, M. Hirata, Y. Yamashiro, Vacuum 66 (2002) 275.

[312] C. Boisse-Laporte, O. Leroy, L. de Poucques, B. Agius, J. Bretagne, M.C. Hugon, L. Teulé-Gay, M. Touzeau, Surf. Coat. Technol. 179 (2004) 176.

[313] J. Bretagne, C. Boisse-Laporte, L. de Poucques, G. Gousset, M.C. Hugon, J.C. Imbert, O. Leroy, L. Teulè-Gay, M. Touzeau, P. Vasina, O. Voldoire, in: A.A. Voevodin, D.V. Shtansky, E.A. Levashov, J.J. Moore (Eds.), Nanostructured Thin Films and Nanodispersion Strengthened Coatings, Kluwer Academic Publishers, Dordrecht, 2004, p. 113

[314] T. Kubo, Y. Iwashita, and T. Saeki, Vortex Penetration Field in the Multilayered Coating Model, in Proceedings of SRF2013, Paris, France (2013), p. 427, TUP007

[315] T. Kubo, Y. Iwashita, and T. Saeki, Appl. Phys. Lett. 104, 032603 (2014).

[316] T. Kubo, Y. Iwashita, T. Saeki Proceedings of IPAC14, Dresden, Germany (2014), p. 2522.

List of Figures

List of Tables